THÈSE POUR OBTENIR LE GRADE DE DOCTEUR DE L'UNIVERSITÉ DE MONTPELLIER

En Astrophysique

École doctorale Information, Structures et Systèmes

Unité de recherche UMR 5299, CNRS/UM

Multicomponent simulations of jets and their disks

Présentée par Chadi MESKINI
Le 21 Novembre 2024

Sous la direction de Christophe SAUTY
et Alexandre MARCOWITH

Devant le jury composé de

Ana PALACIOS, Astronome, Université de Montpellier, LUPM	Présidente
Ana Inés GÓMEZ DE CASTRO, Professeure, Université complutense de Madrid	Rapporteure
Christian FENDT, Professeur, Université de Heidelberg	Rapporteur
Paola ROSSI, Astronome chercheuse, INAF Turin	Examinatrice
Jonathan FERREIRA, Professeur, Université Grenoble I	Examinateur
Christophe SAUTY, Professeur, Observatoire de Paris, LUPM	Directeur de thèse
Alexandre MARCOWITH, Directeur de Recherche, CNRS, LUPM	Directeur de thèse

UNIVERSITÉ DE MONTPELLIER

Remerciements

Après cet effort, il est important de reconnaître l'implication et le rôle de chacun. J'aimerais commencer par mes encadrants, Christophe et Alexandre, qui m'ont offert cette opportunité. Je les remercie d'avoir contribué à m'inculquer la démarche scientifique grâce à nos discussions sur les hypothèses ainsi qu'à l'interprétation des résultats. Je les remercie d'avoir été présents, même dans les périodes où leurs charges de travail ne leur permettaient pas de se gratter la tête. Ils resteront tous les deux un modèle d'encadrement.

Outre les aspects scientifiques, je suis reconnaissant pour les discussions politiques, théologiques et pour les anecdotes que nous avons partagées pendant les repas de midi. Leurs personnalités chaleureuses ont contribué à faire de ces trois années de thèse une période agréable à vivre.

Je voudrais remercier ensuite mon jury. Tout d'abord, Ana Inés Gómez de Castro et Christian Fendt pour avoir accepté d'être rapporteurs. J'ai apprécié leurs commentaires et suggestions. Merci à Jonathan Ferreira pour son intérêt pour mon travail, sa minutie, et son accessibilité. Je remercie Paola Rossi d'avoir d'abord été membre de mon comité de suivi de thèse, puis examinatrice. Les questions de Paola, tout au long de nos rencontres, m'ont aidé à mieux présenter mon travail. Pour finir, merci à Ana Palacios d'avoir présidé le jury et pour sa bienveillance.

João Lima et Filipe Gameiro m'ont aidé à comprendre l'importance de la communauté scientifique. Ils m'ont si gentiment accueilli au CAUP et ont accordé de leur temps pour discuter de mon travail.

Il est temps de remercier les amis. Il y a ceux que je connais depuis le début, par le hasard des naissances. D'autres sont venus au fil de l'eau agrémenter ma vie et m'accompagner au quotidien. Ils ont tous une place particulière comme compagnons de route, car j'ai appris d'eux et, de manière ineffable, ils sont liés à cette thèse. Je remercie Morad pour son humeur et son humour. Je remercie Andy pour sa générosité. Je remercie Erwan pour son esprit. Je remercie Hugo pour son empathie. Je remercie Théo pour son éloquence. Je remercie Alice pour ses valeurs. Je remercie Kélian pour sa passion. Je remercie Giacomo pour son rire généreux. Je remercie Victoria pour sa combativité. Je remercie Vincent pour sa complicité. Je remercie Khalil pour son engagement. Je remercie Benjamin pour sa bonne compagnie. Je remercie Juliette pour son regard bienveillant. Je remercie Anaïs pour son sens du rythme. Je remercie Camilla pour son esprit aventurier. Je remercie Joséphine pour sa grâce. À tous ceux

que je n'ai pas mentionnés... je vous remercie pour votre amitié.

Il est important de souligner que les camarades doctorants, en général, et en particulier Hugo, Théo, Alice et Kélian, m'ont permis de souffler quand le rythme de la thèse s'accélérait.

J'aimerais terminer en remerciant ma famille pour le soutien qu'ils m'ont montré et dont eux seuls ont le secret. Merci Roslyn d'être dans ma vie.

Contents

Preamble **1**

1 Young stellar objects and their magnetized environment **3**
1.1 Star formation . . . 3
1.2 T Tauri stars . . . 12
1.3 Circumstellar disks . . . 36

2 Introduction to MagnetoHydroDynamics, equations, waves and numerical tools **45**
2.1 Validity of the MHD approximation . . . 46
2.2 MHD equations . . . 53
2.3 MHD waves . . . 59
2.4 Discontinuities . . . 62
2.5 A brief introduction to the PLUTO code . . . 64

3 Heating sources in the environment of a CTTS **73**
3.1 Elementary ionization processes . . . 73
3.2 Measure of ionization . . . 77
3.3 Ionization sources . . . 83
3.4 Heating and cooling . . . 93

4 Effects of heating on the jet launching and collimation **101**
4.1 Summary of the publication . . . 102
4.2 Introduction . . . 102
4.3 MHD equations and analytical solutions . . . 106
4.4 From analytical solutions to numerical simulations . . . 111
4.5 Results . . . 119
4.6 Discussion . . . 137
4.7 Conclusions . . . 142

5 A complete axi-symmetric system **145**
5.1 Introduction . . . 145
5.2 Including the physics of the accretion disk . . . 148
5.3 Numerical set-up . . . 154

5.4 Results of fiducial simulations results 158
5.5 Adding heating inside the disk 161
5.6 Magnetization and turbulence 163
5.7 Discussion and conclusion 165

6 Conclusion and prospects **169**
6.1 Concluding summary and remarks 169
6.2 Prospects 171

Résumé **175**

A A map of jet and wind tracers **203**

B Additional tables **204**

C ADO-ASO models **206**

Preamble

The cosmogony of the eighteenth century saw the birth of the nebular hypothesis. First published by Immanuel Kant in 1755 (Kant, 2012), this hypothesis attributes the formation of the planetary system to gas and dust revolving around the sun. After clumping, the gas and dust give place to planets. Although obsolete the nebular hypothesis echoes in modern theories. In the 1920s, a dissipative process acting on a disk of matter around the sun is known (Jeffreys, 1924). The viscous friction between adjacent rings of the disk would accelerate the outer ring and decelerate the inner one. Subsequently, the external regions of such disks would migrate away taking the angular momentum imparted by the inner disk while the latter falls towards the star. The equation of evolution for such rings has a known solution (Weizsäcker, 1948).

The paradigm of accretion disks became well established after the discovery of powerful celestial objects like X-ray binaries, quasars, and active galactic nuclei. These compact objects are extremely luminous and needed more than nuclear fusion reactions to justify the displayed radiation. This extraordinary luminosity can only be explained if the energy source is of gravitational origin. The idea of accretion was later used in the context of young stars (Lynden-Bell and Pringle, 1974). During the collapse of a molecular cloud in slow rotation, a young star forms with a surrounding rotating disk. After a first phase of spherical condensation which gives birth to the proto-star, the accretion disk takes over by feeding the central object in mass, thus, in energy, and angular momentum. In total this phase spans over one million years and is referred to as the T Tauri stage.

Universality of accretion disks seems to be paired with the presence of outflows. We observe outflows from compact objects at the center of galaxies or forming stars. These ejections come with different velocities and morphologies. The fast collimated ones are called jets, while slower and wider outflows are called winds. In young forming stars, for the wind component, velocities can reach tens of kilometers per seconds. Jets on the other hand are much faster. They reach hundreds of kilometers per seconds and can go close to the speed of light in exotic objects. Although the properties of winds and jets differ, they describe a common process: an ionized plasma strongly accelerated in the vicinity of a massive object by a thermal and/or magnetic component.

Among the communities of extragalactic objects and stellar formation there is consensus over the interdependence of accretion and ejection. This can be seen by considering only two ingredients - a disk threaded by a magnetic field. The magnetic tension

caused by the rotation applies a torque that brakes the disk. In turn, this brake enables accretion to proceed. Then, the mechanical energy extracted by the magnetic field accelerates plasma creating an outflow. As for collimation, the process happens through the Lorentz force associated with the magnetic field (Ferreira, 1994).

One fundamental aspect to consider is the degree of ionization of the disk. It allows coupling between the magnetic field and the disk. With this coupling magnetohydrodynamic instabilities can grow, resulting in wind launching and inward matter transport. Understanding how ionization rates vary across T Tauri disks is crucial because it directly affects their chemistry, temperature distribution, and dynamics. These rates change significantly with distance from the central star and height above the disk midplane due to differing contributions from various ionization sources.

In this thesis, we will study the effect heating has on the dynamics of jets. Using axisymmetric simulations we can input a net heating rate that beneath hides the microphysics of ionization. We shall constrain the amount of heating possible for jet launching around young stellar objects.

Chapter 1

Young stellar objects and their magnetized environment

Contents

1.1 Star formation 3
1.1.1 From clouds to cores 3
1.1.2 Molecular cloud stability 5
1.1.3 Inside-out collapse 6
1.1.4 Towards the main sequence 7
1.2 T Tauri stars 12
1.2.1 T Tauri physical parameters 13
1.2.2 Outflows and accretion 17
1.2.3 Ejection models, magnetized jets 23
1.2.4 Outflows from an accretion disk 27
1.3 Circumstellar disks 36
1.3.1 A thin disk 36
1.3.2 A viscous thin disk? 40
1.3.3 Turbulence as the driver of viscosity 43

1.1 Star formation

1.1.1 From clouds to cores

Star formation starts at large scales with molecular clouds. Such massive structures are rich in gas and dust with low temperatures, harboring various key features. They consist of molecular hydrogen (H_2), molecules such as CO, and other simple molecular species

that consist of three heavy atoms or less, with a match and mix between H, C, N, O, S (Watanabe et al., 2017). The size of these clouds varies, but star formation process and feedback happen at cloud scales of the order of ~ 100 parsec (pc) (Chevance et al., 2020). Molecular clouds contain two main components, namely, clumps and cores. The hierarchy of these components are represented in Fig.1.1.

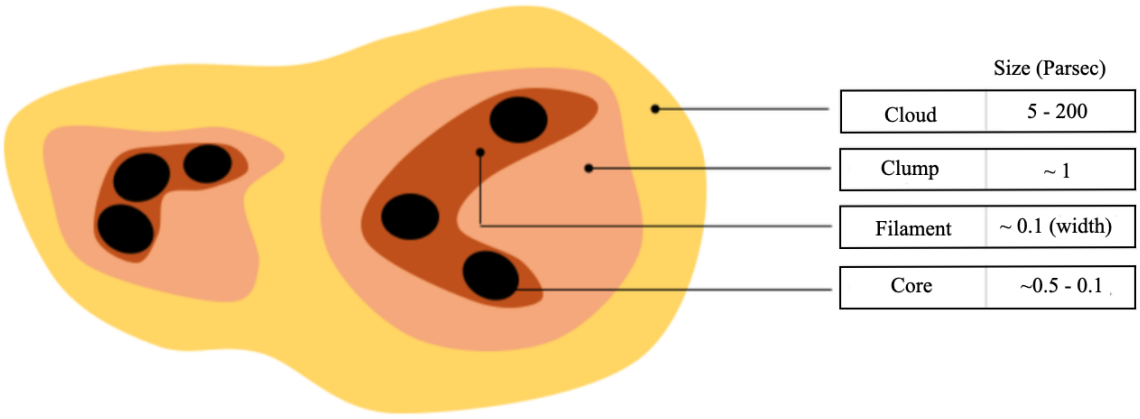

Figure 1.1: Schematic of the structure of a molecular cloud with the typical sizes measured in these objects. Adapted from Valentin Brunn's thesis manuscript (https://theses.fr/s251627)

Clumps form the larger substructures of the cloud with a typical size of 1 pc. Their masses range between $10 - 10^3$ $M_\odot$ (Bergin and Tafalla, 2007) and are the precursor of stellar clusters. They account for a large fraction $(70 - 90\%)$ of stars born in molecular clouds (Lada and Lada, 2003).

The densest and smallest substructure of a molecular cloud is called a core. The dense nucleus goes typically from 1 $M_\odot$ to several solar masses (di Francesco et al., 2007). Gravitational stability of cores is described by Jeans mass and length. They are critical to determine stability of the core (Hennebelle and Chabrier, 2008),

$$M_j = \frac{4\pi}{3}\left(\frac{\pi c_s^2}{G\rho}\right)^{3/2}, \tag{1.1}$$

where ρ is the density, c_s is the sound speed and G the gravitational constant. Above this mass the collapse of clumps begins to form protostars.

For the sake of completeness, there is a last structure linking cores together. This structure has an elongated filament shape. They connect and feed the dense cores (André et al., 2014). The critical mass per unit length for instability to grow in a filament is given by Nagai et al. (1998),

$$M_{crit} = \frac{2c_s^2}{G} \simeq 2.6 \times 10^{17} \frac{T}{100\ \mathrm{K}}\ \mathrm{g/cm}, \tag{1.2}$$

When the filament mass exceeds the critical line mass ($M > M_{crit}$), the structure becomes unstable leading to the formation of dense cores.

Molecular clouds in the Milky way have masses above the Jeans mass defined in Eq.1.1, our galaxy should therefore be extremely unstable. By considering a homogeneous cloud, the free fall time (t_{ff}) can be derived from Newton's second law and results in the following expression,

$$t_{ff} = \left(\frac{3\pi}{32G\rho}\right)^{1/2}. \tag{1.3}$$

If using Eq.1.3 we input an average density of 17 hydrogen atoms/cm^3, then we find a free fall time of $\sim 8 \times 10^6$years. Since the entire molecular gas would be converted into stars during the free fall time, the expected star formation rate should be close to $4000 M_\odot/yr$ if we take the molecular gas in the Milky way to be around $3 \times 10^{10}\ M_\odot$. The observed formation rate, on the other hand, is only $1 - 3\ M_\odot/yr$ (Dobbs, 2013). The magnetic field is responsible for the observed slowing down of star formation. It is also responsible for angular momentum transport, which is a key concept in young stellar objects evolution as well. In Sec.1.1.2, the role of magnetic fields in slowing the collapse is highlighted.

1.1.2 Molecular cloud stability

To get a clearer idea of the mechanism keeping a molecular cloud from collapsing in its entirety we have to look at the Virial theorem. The theorem stipulates the following (Ballesteros-Paredes et al., 2020),

$$2\mathcal{K} + 2\mathcal{U} + \mathcal{W} + \mathcal{M} = \frac{1}{2}\frac{\partial^2 I}{\partial t^2}. \tag{1.4}$$

With $\mathcal{K}$ the kinetic energy, $\mathcal{U}$ the internal energy, $\mathcal{W}$ the gravitational energy, $\mathcal{M}$ the magnetic energy, and finally I the moment of inertia. To say that the long term mass distribution and size does not change implies that there is no variation of the moment of inertia. This transforms Eq.1.4 into $2\mathcal{K} + 2\mathcal{U} + \mathcal{W} + \mathcal{M} = 0$. If observed values for temperature T, magnetic field B, kinetic velocity V, mass M, and radius R are considered, the ratios of each contribution to the gravitational energy are as follows (Stahler and Palla, 2008),

$$\frac{\mathcal{U}}{\mathcal{W}} \sim 0.003 \left(\frac{M}{10^5\ M_\odot}\right)^{-1} \left(\frac{R}{25\ pc}\right) \left(\frac{T}{15\ K}\right), \tag{1.5}$$

$$\frac{\mathcal{M}}{\mathcal{W}} \sim 0.3 \left(\frac{B}{20\ \mu G}\right)^{2} \left(\frac{R}{25\ pc}\right)^{4} \left(\frac{M}{10^5\ M_\odot}\right)^{-2}, \tag{1.6}$$

$$\frac{\mathcal{K}}{\mathcal{W}} \sim 0.5 \left(\frac{V}{4\ km/s}\right)^{2} \left(\frac{M}{10^5\ M_\odot}\right)^{-1} \left(\frac{R}{25\ pc}\right). \tag{1.7}$$

While the internal energy is negligible compared to gravitation, magnetic and kinetic energies are of the order of magnitude of the gravitational energy. We conclude that magnetic fields and turbulence slow down the collapse, and hence slow down star formation.

1.1.3 Inside-out collapse

The structure of molecular clouds is far from homogenous. The center is denser than the outskirt of the cloud, which means the hydrodynamical collapse varies along the radius. The central part of the sphere collapses faster. Looking again at the free fall time, it scales with $\rho^{-1/2}$. This means that the central region contracts at a faster pace than the outer regions. Subsequently, the outer shell looses the pressure support provided by the inner cloud region. Shu (1977) proposed in his seminal work a collapse scenario using a self-similar solution. Numerical hydrodynamical simulations later confirmed the process of collapse (for further details see Larson, 1969, 1981; Hennebelle et al., 2011; Chen and Ostriker, 2014; Chevance et al., 2020; Young, 2023).

Three main distinct phases were confirmed,

- **Free fall phase:** The collapse process exhibits an isothermal behavior, characterized by a timescale comparable to the free-fall timescale. Efficient cooling is facilitated by molecular hydrogen and thermal radiation emitted by dust grains in the infrared spectrum. Subsequent phases follow an adiabatic collapse, as the inner regions of the core reach optical thickness, thereby limiting the efficiency of cooling processes.

- **First core phase:** Following the formation of a stable core spanning a few astronomical units, temperatures exceeding 1000 K cause dust grain evaporation, effectively reducing the medium opacity. As the temperature exceeds 2000 K, molecular hydrogen dissociation occurs, initiating a secondary collapse phase. This transition is attributed to the alteration in the equation of state, disrupting the equilibrium between gravity and internal pressure.

- **Opaque phase:** Once densities are high enough ($> 10^{-2}$ g cm^{-3}) the second collapse halts. As temperatures increase, the dissociation of hydrogen molecules is triggered. This endothermic reaction alters the equation of state, decelerating the temperature increase. Consequently, the pressure fails to rise rapidly enough to sustain hydrostatic equilibrium, leading to a subsequent collapse. Within a short time frame, typically within years, a new equilibrium is reached, resulting in central temperatures on the order of 10^4 K and the formation of the second core. At the end of this phase we are left with a core mass of $\sim 0.1 M_\odot$ (Saigo et al., 2008).

The issue of collapse is far from being fully closed. The initial conditions for core collapse and the processes that connect initial conditions to the outcome of the collapse are not well understood. Observations of the continuum do not help differentiate between collapse hypotheses because density distributions for spherical self-gravitating clouds are too similar (Keto et al., 2015). Observations, though, indicate that cores are supported by thermal instead of magnetic pressure (Di Francesco et al., 2007; Keto et al., 2015).

1.1.4 Towards the main sequence

After the three phases described in Sec.1.1.3, starts the process of accretion. Eventually, it leads to the birth of a star and planets. The accretion phase is characterized by an optically thick core, and the creation of a disk. Contraction and accretion continue until the protostar reaches temperatures high enough for hydrogen burning. This will announce the start of the star journey towards the main sequence. In order to start nuclear reactions, stars need a temperature of $\sim 10^7$ K. By then, a radiative core surrounded by a convective envelope has formed. When a protostar leaves its embedded phase (Fig.1.2b,c) its position can be identified on the Hertzprung-Russell (HR) diagram as the protostar becomes visible at optical wavelengths (Fig.1.2d). We group protostars and pre-main sequence (PMS) stars under the name young stellar objects (YSOs).

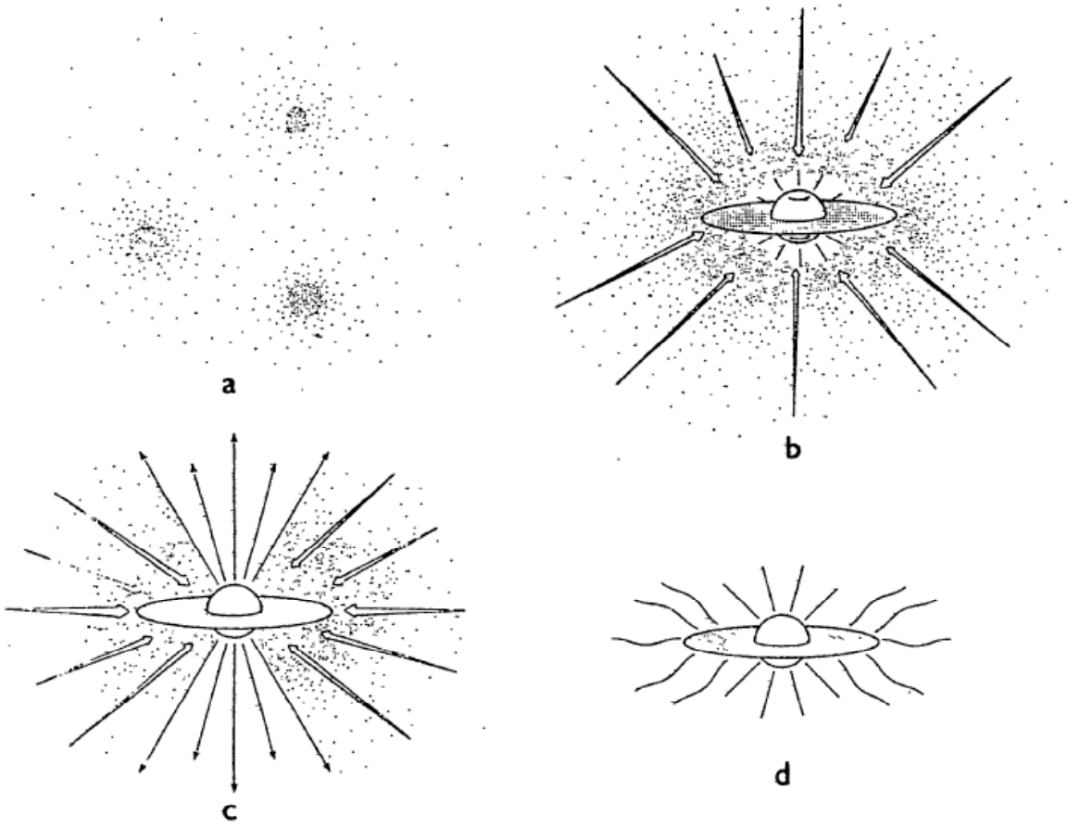

Figure 1.2: Protostar evolution to a system with a visible young star and an accretion disk. (a) The phase where magnetic and turbulent contributions are lost leading to core formation. (b) Inside a cloud core, the protostar forms with a surrounding nebular disk. (c) The star becomes visible with the help of the stellar outflow, and this by pushing material away, creating an unobstructed line-of-sight. (d) All matter from the nebular disk has either been evacuated or settled into a disk. Adapted from Shu et al. (1987).

1.1.4.1 Classification of young stellar objects

Through out their evolution YSOs have different characteristics. Specifically, the central object and the surrounding disk have varying masses shapes and are heated differently. Thus, the temperature profiles change from one epoch to another. Closer material to the YSO will have higher temperatures while cooler disk material will be further away. One very important tracer at hand when studying YSOs is the measured infrared emission. They often exhibit more infrared (IR) than is expected from the photosphere of a PMS star (red line in Fig.1.3). It is without doubt the disk contribution. The bump in Fig.1.3 is the result of thermal emission from dust in the disk. If the environment of a YSO changes with time, then it is bound to appear in its thermal profile.

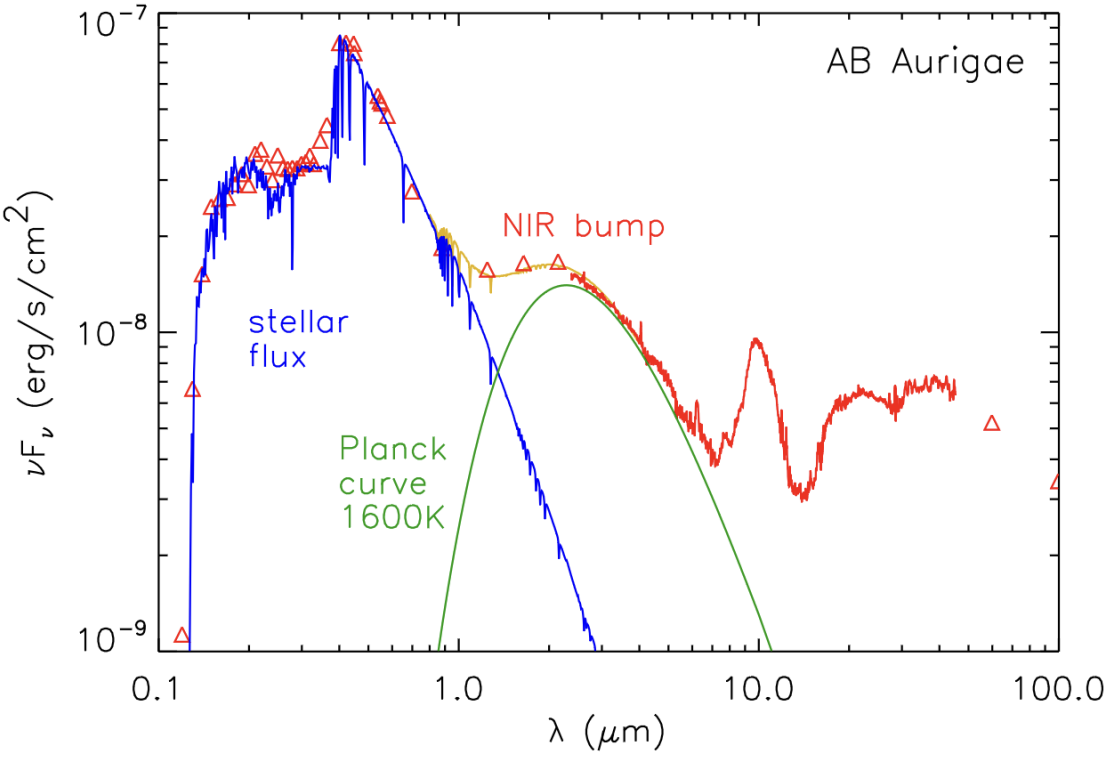

Figure 1.3: The spectral energy distribution of the Herbig Ae star AB Aurigae. Red is the measured emission. Blue is the stellar spectrum predicted with a Kurucz stellar atmosphere model. The excess of flux above the atmosphere (the "infrared excess") is the thermal emission from the dust in the disk. The emission in the near infrared clearly has a bump-like structure, and is often called the "near infrared bump". In green a Planck curve at a temperature of 1600 K is plotted over. The golden curve is the sum of the Planck curve and the stellar atmosphere. Caption and figure taken from Dullemond and Monnier (2010).

Based on this empirical discovery, Lada and Wilking (1984) devised a YSO classification scheme using the IR excess. The IR excess index provides information on the

spectral energy distribution (SED), specifically its slope, which is defined as,

$$\alpha_{IR} \equiv \frac{d \log \nu F_\nu}{d \log \nu} = \frac{d \log \lambda F_\lambda}{d \log \lambda}, \tag{1.8}$$

where ν is the frequency and νF_ν is the flux density. Usually, the slope of the SED is measured between 2 μm and 25 μm. According to Lada and Wilking (1984), Lada (1987), Andre et al. (1993), and Greene et al. (1994) four main classes ensue.

Class 0: In this class YSOs are deep inside their parent cloud and cannot be observed through visible light (from 0 to 10^4 years). Hence, the envelope dominates the spectrum and takes the shape of a gray body with a peak at $\sim 100\mu$m. At this stage there is no certainty as to whether a star exists or not (Contopoulos and Sauty, 2001). Although not visible in the optical lines, they present strong sub-mm emission (Andre et al., 1993). YSOs in this class have an infalling envelope and display strong jets (Fig.1.4). Accretion rate is measured, through bolometric luminosity ($L_{acc} \sim L_{bol}$), at a rate of $10^{-5}\ M_\odot/yr$ (Bontemps et al., 1996).



Figure 1.4: The James Webb Space Telescope provides a detailed view of the embedded Class 0 object, Herbig-Haro 211, in high-resolution near-IR. It reveals intricate details of a young stellar outflow, showing a series of bow shocks extending left and right, driven by a bipolar jet. Infrared emissions from molecular hydrogen, carbon monoxide, and silicon monoxide illuminate these outflows, allowing Webb to map their structure. Credit: ESA/Webb, NASA, CSA

Class I: Here the YSO exhibits a rise in α_{IR}, particularly in mid-IR. $\alpha_{IR} > 0.3$ indicates the presence of a large amount of material around the protostar. The circumstellar material is infalling towards the star, with $\dot{M}_{acc} \sim 10^{-7} - 10^{-6}\ M_\odot/yr$ (Antoniucci et al., 2008). Class I has a life time of 10^5 years. Between class I and class II, Greene et al. (1994) introduced the flat spectrum phase. Its index lays between $-0.3 < \alpha_{IR} < 0.3$.

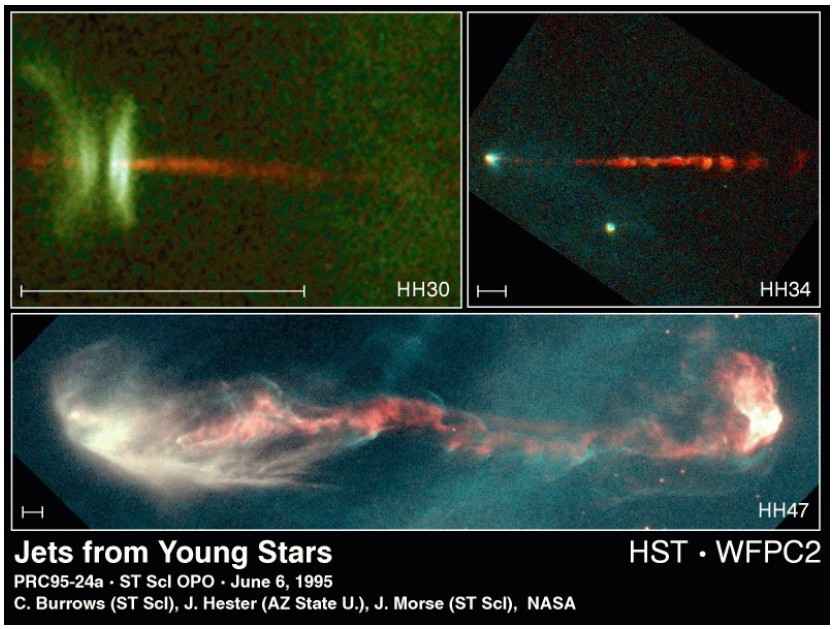

Figure 1.5: Three Hubble Space Telescope images of Class I objects, namely, HH30, HH34 and HH47. For HH30, the accretion disk is clearly visible. HH34 shows the region of shocks between the jet and the interstellar medium. In the case of HH47, the counter jet is not observed as it moves away hidden by the molecular cloud hosting the emitting star.

Class II: Class II YSOs with $-1.6 < \alpha_{IR} < 0.3$ exhibit a milder infrared excess. These YSOs are typically linked with classical T Tauri stars (CTTS) and are believed to be in a phase where a circumstellar disk still exists and is connected to the star magnetosphere. The infalling envelope surrounding them has mostly dissipated and accretion proceeds at $\dot{M}_{acc} \sim 10^{-8}\ M_{\odot}/yr$. Classical T Tauri stars are recognized by prominent hydrogen emission lines, often accompanied by other significant features like Ca II, He I, and Fe II (Garufi et al., 2019). These spectral characteristics indicate an active accretion process, where material from the circumstellar disk accrete onto the star surface.

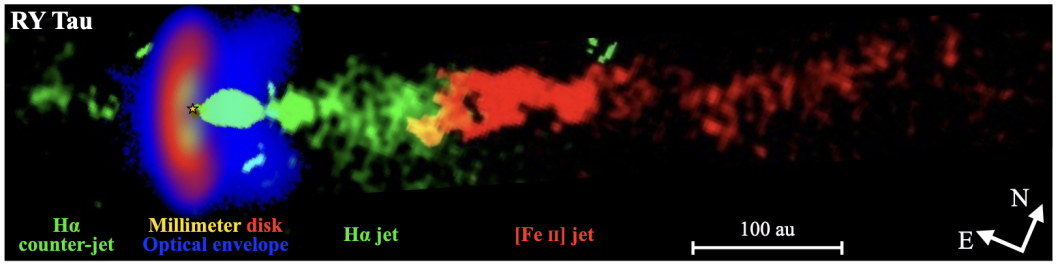

Figure 1.6: Composite image of RY Tau comparing the datasets of sphere superimposed onto the disk seen in the millimeter by ALMA. The jet is traced by H_{α}. Taken from Garufi et al. (2019).

Class III: At $\alpha_{IR} < -1.6$, the disk starts to disperse accompanied by a ceasing of accretion activity. In this phase, YSO are associated with weak-linked T Tauris (WTTS). The IR excess is attributed to a mostly dissipated or optically thin disk. Class III stars often cannot be distinguished from main sequence stars on IR excess alone (Kang et al., 2017). The SED is dominated by emission from the star and spectra from WTTS lack strong emission lines. While WTTS are less affected by accretion phenomena compared to CTTS, they still demonstrate magnetic activity, including chromospheric and coronal emissions. These activities are sustained by their convective interior and rapid rotation (Montmerle et al., 2000; Güdel and Telleschi, 2007).

The transition between CTTS and WTTS is influenced by factors such as initial mass, angular momentum and magnetic fields. No study so far proves that class III are systematically older than class II stars. A study by Spezzi et al. (2011) shows that the class III population dominate in older Lupus clouds compared to younger ones where Class II are predominant, indirectly addressing the question of whether Class III is in a different stage of evolution. Multi-wavelength observations and detailed modeling are crucial for understanding the interaction between stars and their circumstellar environments during early stellar evolution. In that view, this thesis concentrates on the T Tauri stage, specifically class II stars.

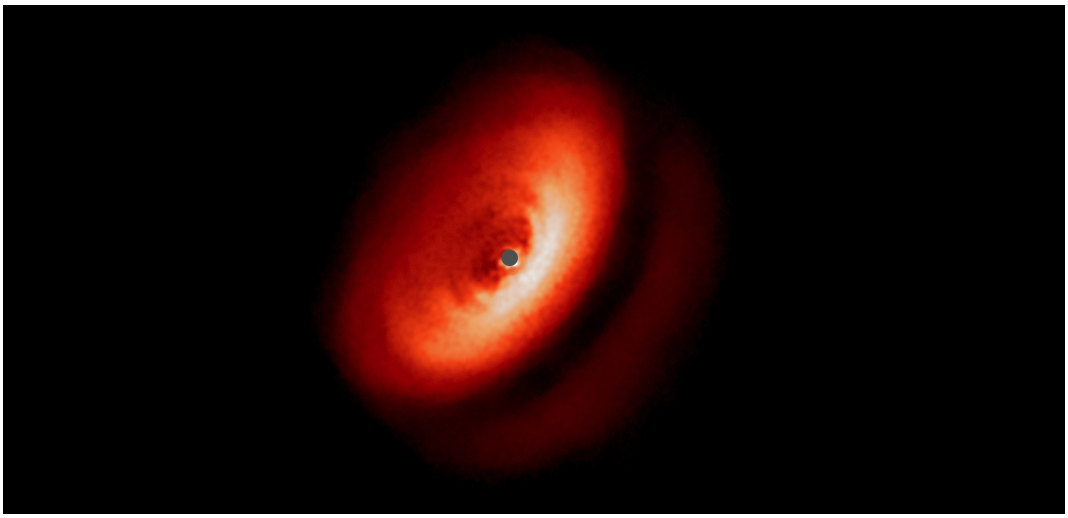

Figure 1.7: Image of the disk surrounding IM Lupi, marked by a gray circle at the center. This image was taken by the VLT. credit: ESO/H. Avenhaus et al./DARTT-S collaboration.

A too simple classification: This classification scheme helps understanding YSO evolution based on their observable SED properties. As YSOs evolve, their infrared excess and SED slope change, indicating the dissipation of circumstellar material and transition from envelope to disk dominance (Sicilia-Aguilar et al., 2010; Kang et al., 2017). However, interpreting YSO classification is complex due to factors like inclination angle (White et al., 2007), dust properties, and presence of outflows (Großschedl et al., 2019). Robitaille et al. (2006) point out the importance of viewing angle as it

can lead to an incorrect classification. Older YSOs with a thick disk can be misconstrued as a class I when viewed close to the mid plane of the disk (strong inclination i). According to White et al. (2007), $30 - 50\%$ of class II stars in the Taurus-Auriga cloud are wrongly identified as class I due to their inclination.

Other alternatives were proposed to sort YSOs (Robitaille et al., 2006; Van Kempen et al., 2009; Kang et al., 2017). They rely on mass ratios between envelope, disk, and star using sub-mm emissions. This classification is by construction less vulnerable to inclination effects. In addition, Van Kempen et al. (2009) proposed a further tracer that uses the presence of molecules, such as HCO+, in the envelope. These methods are more representative of the evolution, but less used than the α_{IR} spectral index.

1.1.4.2 Processes linked to a young stellar object evolution

When migrating towards the main sequence, YSOs experience a number of key events that model their emission, shape, and environment. First, during the protostellar phase, the protostar gains mass by accreting material from its surrounding envelope, influencing its final mass, angular momentum, and other properties as it evolves into a main sequence star. As the protostar accretes matter and grows in mass, its internal structure evolves, contracting and heating up, leading to increased core temperature and pressure. Accretion often triggers the formation of bipolar flows and jets. These structures help to remove excess angular momentum from the system and regulate the accretion process.

As the protostar continues to accrete material from its surrounding envelope, the envelope mass decreases, reducing its optical depth. This decrease in optical depth allows radiation from the central protostar to escape more easily. Eventually, the envelope is fully dissipated due to a combination of accretion, radiative feedback, and outflows. This reveals the central protostar and the surrounding disk.

Deuterium is one of the elements generated during the Big Bang. It starts burning at temperatures above 10^6 K (Palla and Stahler, 1999). In low mass stars ($< 1M_\odot$), accretion provides a stable supply of deuterium fuel while fusion drives convection. In higher mass stars ($> 2M_\odot$) the fusion depletes the core, and deuterium burning only happens on the surface since material continues to accrete (Stahler and Palla, 2008). The energy produced stabilizes the protostar as it slows down contraction. Finally, the disk disperses when most of the material has been accreted through viscous accretion or evacuated with the help of photoevaporation and magnetised outflows. This happens over a few million years.

1.2 T Tauri stars

T Tauri stars (TTS) are named after T Tauri, which is a variable Sun-like star in the Taurus constellation. First observed by John Hind (Hind, 1852), it was later studied by Joy (1945) and Herbig (1962). Their emission spectra is similar to the emission of the solar chromosphere. In this class, TTS have masses that can reach 3 $M_\odot$ and ages

between 1 and 10 million years. They also present irregular brightness variations, with peculiar spectral properties (Herbig, 1962). Historically, to account for observations of Hα, and Ca II emissions in the spectrum, several models were developed. Between accretion, presence of a strong chromosphere, spherical winds, there was a rapid convergence on the accretion disk paradigm with the presence of outflows.

1.2.1 T Tauri physical parameters

1.2.1.1 Mass and age

A method to determine masses and ages of T Tauris is to compare PMS evolution tracks with their position on the Hertzprung-Russell (HR) diagram. In this diagram, where luminosity is plotted against temperature, the track a young star evolves along appears as a nearly vertical curve. Once a protostar completes its contraction phase and evolves into a T Tauri star, it maintains a high level of luminosity. The star then continues to contract, but at a much slower rate. During this slow contraction, it follows the Hayashi track downward, decreasing significantly in luminosity while maintaining roughly the same surface temperature. This continues until either a radiative zone develops, causing the star to transition to the Henyey track, or enters the main sequence after nuclear fusion begins.

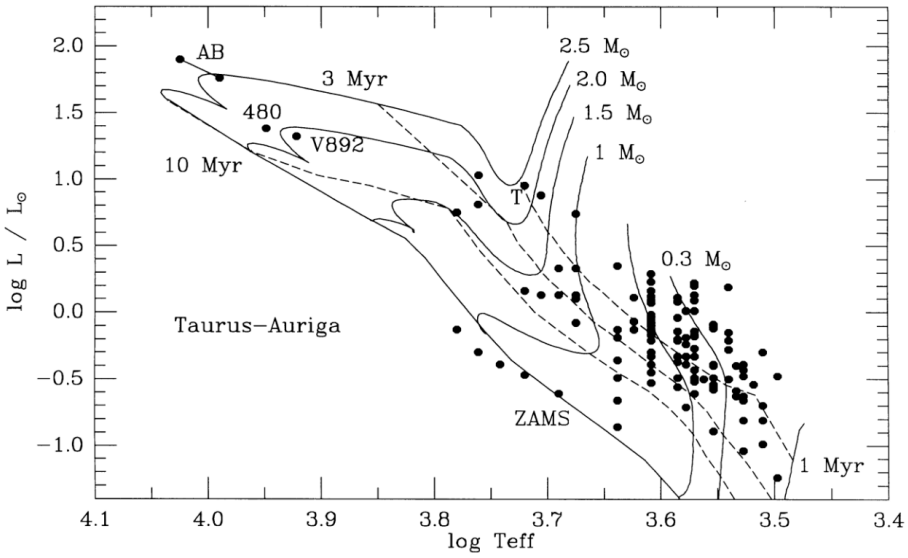

Figure 1.8: The HR diagram of objects in the Taurus molecular cloud features stellar evolution tracks for the pre-main sequence, shown as solid lines. Stars with lower masses (i.e., lower T_{eff}) follow nearly vertical paths known as Hayashi tracks until they reach the main sequence. The dashed lines, labeled with ages, represent isochrones at different stages of stellar evolution. (Hartmann et al., 1998)

As can be seen in Fig.1.8, for a fixed temperature a large spread of luminosities

is observed, even with advanced analysis methods (Herczeg and Hillenbrand, 2015; Alcalá et al., 2017). An - a priori - assumption to determine the age of a cluster is that all its stars are of the same age. The luminosity spread could indicate a real age spread or be due to unaccounted-for mechanisms. Recent Gaia-based analyses support the notion of an age spread in specific regions, particularly between the population partially embedded in the cloud and the one that surrounds it (Esplin and Luhman, 2022).

A PMS position on the HR diagram can be affected by numerous assumptions, such as stellar spots (Somers et al., 2020), the presence of magnetic fields (Feiden, 2016), and atmospheric convection and metallicity (Baraffe et al., 2015). All these models produce diverse mass constraints. Simon et al. (2019) and Braun et al. (2021) find masses in the range of $M_\star \sim 0.4 - 1\ M_\odot$ and $M_\star \sim 0.6 - 1.3\ M_\odot$, respectively. They show that evolution models with magnetic fields are in better agreement with masses determined through Newton's inverse square (dynamical masses). In contrast, models not including a magnetic contribution align better with lower mass stars (Braun et al., 2021).

1.2.1.2 Accretion rates

Accretion proceeds typically in young stars within an age range of $1 - 10$ million years, and masses between $\sim 0.2 - 2\ M_\odot$ (Hartmann et al., 2016). For accretion to happen, material from the disk – composed of gas and dust – is transported to the star. The exact process of mass and angular transport is not yet precisely known and is likely a mix of wind and viscous driven accretion. Within ~ 0.1 au of the central star, the disk temperature exceeds 1,000 K due to stellar radiation, leading to the sublimation of dust (Hartmann et al., 2016). This critical zone, known as the dust sublimation radius, is where the inner edge of the disk emits the absorbed energy, significantly contributing to the near-IR excess observed. Beyond this region, up to roughly 1 au, the inner disk is responsible for generating a bipolar flow or jet, fueled by the accretion process. This process is guided by magnetic field to the star surface. At the same time, these fields truncate the disk at a few stellar radii. The heat produced in accretion funnels reaches 8000 K, which leads to broad Hα emission lines. Heating in this region is presumably from radiation originating from the star, and of magnetic origin. Magnetic field lines connected to the disc channel material toward the star at nearly free-fall velocities. As the gas accelerates to around 300 $km\,\mathrm{s}^{-1}$, it creates a shock upon impact with the stellar photosphere, heating the gas to temperatures around 10^6 K. Most of the resulting X-ray emission is absorbed and re-emitted at lower temperatures, producing strong ultraviolet-optical continuum excesses and some relatively narrow emission lines.

As outlined by Fischer et al. (2023) to measure accretion one can use proxy emission lines as diagnostics. This method calibrates line fluxes corrected for extinction to accretion shock models. An other technique is to directly model the continuum excess emission. This implies a precise knowledge of the accretion geometry, the temperature structure, and the stellar parameters (Hartmann et al., 2016). In total, accretion disks roughly provide between $\sim 10^{-10} - 10^{-7}\ M_\odot\,\mathrm{yr}^{-1}$ (Hartmann et al., 2016; Manara et al.,

2016).

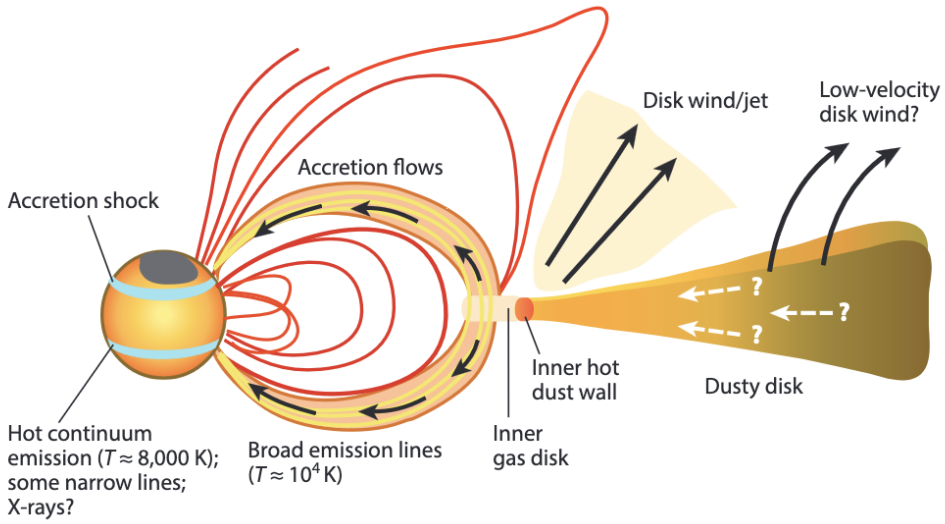

Figure 1.9: Schematic view of a young star accreting from a disk through the stellar magnetosphere. (Hartmann et al., 2016)

1.2.1.3 Magnetic fields

T Tauri stars with a solar mass typically exhibit averaged magnetic field strengths between 1 and 2 kG (Johns-Krull, 2007; Donati and Landstreet, 2009). This strength is sufficient to cause magnetospheric truncation radii near co-rotation if the field were purely dipolar. However, a significant portion of the magnetic field is arranged in quadrupolar and higher-order configurations, with small-scale fields distributed across the entire stellar surface (Donati et al., 2008). This results in a considerable weakening of the dipolar component. Caution ought to be taken as most of these reported results stem from isolated sources, with highly active periods similar to the Sun. The dipolar field structure is a good representation of the field configuration in the objects we simulated in this thesis.

To construct the global structure of the magnetic field, Zeeman-Doppler techniques are used. They involve analyzing the polarisation of photospheric lines and, in particular, narrow line components. From these techniques magnetic fields have been identified as being strong, multipolar, and accretion spots that predominantly favor the poles (Donati et al., 2008). Some field lines may become twisted as a result of the differential rotation between the disk and the star, resulting in an outward bulge, when this bulge open matter is ejected. These processes can lead to the occurrence of highly intense flaring events observed in X-rays (Getman et al., 2008; Getman and Feigelson, 2021).

MHD simulations, conducted in both two and three dimensions for rotating stars with an angle between the rotation axis of the star and the dipolar magnetic field (see Fig.1.10) reveal that matter is funneled toward the star through two distinct paths at

high tilt angles and through multiple channels at low tilt angles. These simulations demonstrate that factors such as the distribution of hot spots, their temperature and density distribution vary depending on the tilt angle and the mass accretion rate. Specifically, there is an inverse relationship between the density of a spot and the proportion of space each density occupies (Romanova et al. 2014 and references therein).

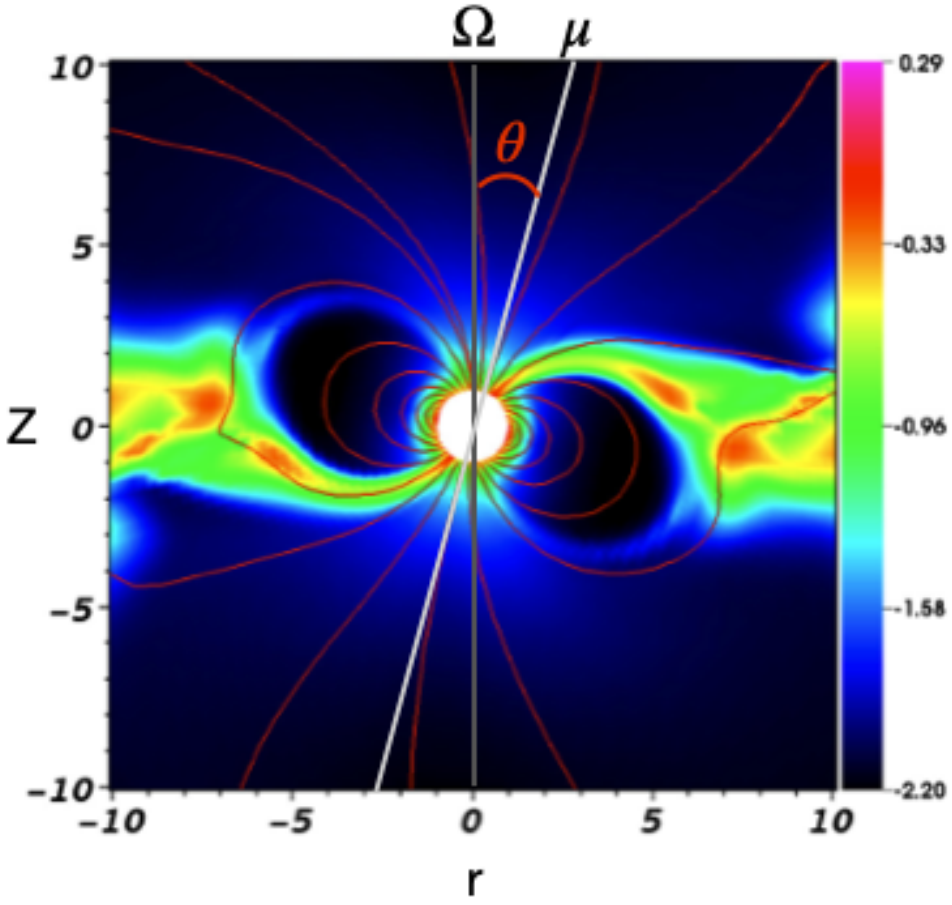

Figure 1.10: Accretion with the stellar rotation axis Ω and the dipolar magnetic axis μ are separated by an angle θ. Adapted from Alencar et al. (2012).

In some cases, this leads to well-structured funnel flows in a stable accretion regime (Kurosawa and Romanova, 2013). As the flow approaches the stellar surface, strong octupolar fields alter the material trajectory. The point where the flow meets the stellar surface, known as the flow footpoint, is located at high latitudes when both dipolar and octupolar fields dominate. However, if quadrupolar or higher-order fields are more prominent, the footpoint is located at mid-latitudes (e.g., Romanova et al. 2011; Johnstone et al. 2014).

1.2.2 Outflows and accretion

1.2.2.1 Opening angles

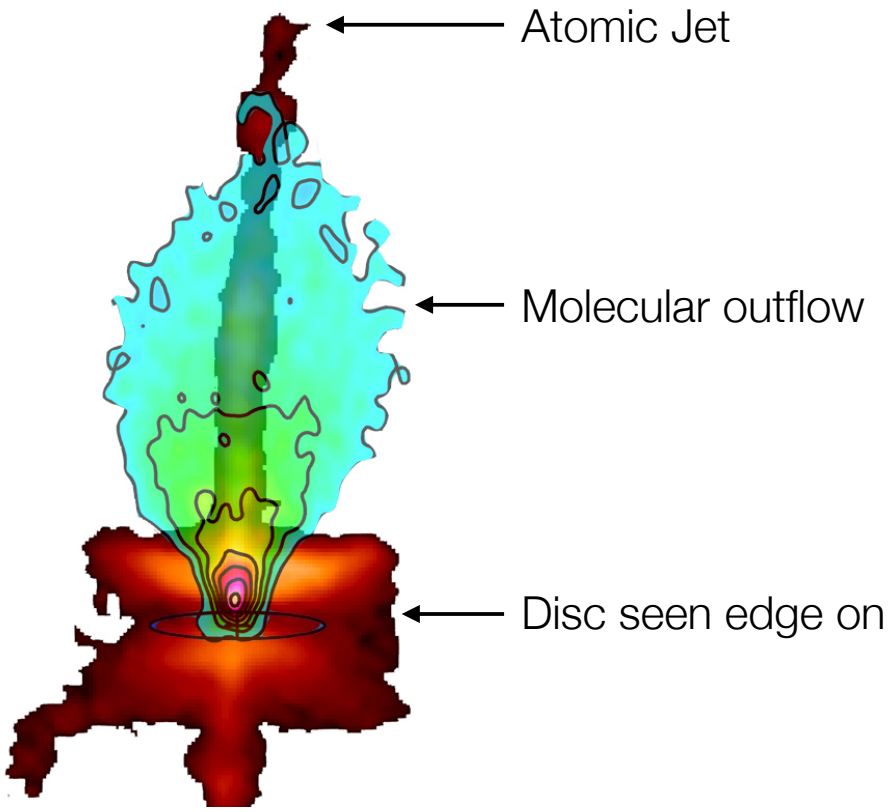

Figure 1.11: A disk and an atomic jet observed by Hubble telescope superimposed with a molecular wind observed by ALMA. From Lesur (2021).

Thanks to adaptative optics and observations from the Hubble telescope, and now from the James Webb telescope, a large number of TTS jets have been captured with great details (e.g., Burrows et al. 1996; Dougados et al. 2000; St-Onge and Bastien 2008; Agra-Amboage et al. 2009; Agra-Amboage et al. 2011, 2014; Harsono et al. 2023). Observations can resolve the transverse structure of jets. By doing so, they reveal a layered onion-like composition. The first layer, at the axis, is the high-velocity component (HVC) with velocities that reach 400 km/s. The second layer, surrounding the first layer, is a low-velocity component (LVC) associated with less collimated outflows from the accretion disk. An example of this structure is displayed on Fig.1.11. This composite image reveals a jet that is poor in molecules surrounded by winds only visible at the base of outflows (Louvet et al., 2018). Even though molecular outflows are very prominent around class 0 and I YSO reaching $0.1 - 0.3$ pc, these outflows are more diffuse in class II environment. Contrary to class 0 and I stage where outflows speed

up proportionally with distance (Lada and Fich, 1996), in class II the jet velocity is constant with height (Louvet et al., 2018).

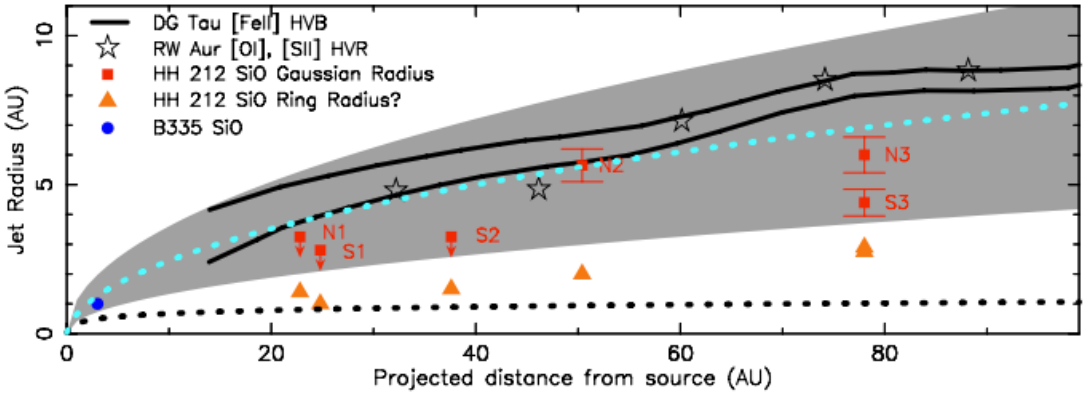

Figure 1.12: Plot of the observed jet radius versus the distance from the central source. DG Tau data from Agra-Amboage et al. (2011), RW Aur from Woitas et al. (2002), HH 212 from Lee et al. (2017a), and B335 from Bjerkeli et al. (2019). The gray area shows that the jet radius increases roughly parabolically with distance. Caption and figure from Lee (2020).

The collimation does not depend on the mass of the envelope Cabrit (2007), or at least very marginally in class 0 YSOs. This was made clear by ALMA and the VLT. Measures of jet radii of different class of YSO show similar values be it for class 0 or class II (Fig.1.12). The origin of these outflows is the inner disk (≤ 1 au) and are extremely collimated, with angles lower than 5 degrees for distances from the star larger than 20 au. Let us consider the idea of a recollimation induced by the outer envelope of a TTS with a jet of mass loss $\dot{M}_j = 10^{-8}\ M_\odot\,\mathrm{yr}^{-1}$, a velocity $v_j = 300\ km\,\mathrm{s}^{-1}$, and a temperature $T = 10$ K. Barral and Canto (1981) show that after some distance along the polar axis z, the pressure of the jet drops. The external pressure could in principle reconfine it. In that case, for recollimation to happen the pressure should be,

$$P \sim 5 \times 10^{-5}\ \mathrm{g\ cm^{-1}\ s^{-2}} \left(\frac{\dot{\mathrm{M}}_\mathrm{j}}{10^{-8}\ \mathrm{M_\odot\,yr^{-1}}}\right) \left(\frac{\mathrm{v_j}}{300\ \mathrm{km\,s^{-1}}}\right) \left(\frac{\mathrm{z}}{50\ \mathrm{au}}\right)^{-2}. \tag{1.9}$$

This results in a density $n > 2.4 \times 10^9\ \mathrm{cm^{-3}}$ which is around 600 times higher than what is observed (e.g., Hartigan et al. 1995; Gómez de Castro and Verdugo 2001). We can conclude that pressure alone cannot confine the jet. The most probable candidates of collimation are of magnetic origin. With high angular resolution observations in the years 2000, the necessity of a magnetized outflow has been established.

1.2.2.2 Outflow/Inflow tracers

CTTS have pronounced ultraviolet and optical emission lines, for instance, Balmer lines, neutral and ionized metal lines. Two easily identifiable lines characteristic to

YSOs are Hα and the Lithium line, respectively identified at 6563 Å and 6708 Å. Hα with broad profiles originate from an extended region in the magnetosphere (Calvet et al., 1984), which includes the stellar surface and the base of accretion (Dodin, 2015). Depending on the line of sight, an observer may also detect blueshifted or redshifted Balmer absorption lines. The sense in which they are shifted indicates the inflow or outflow signature, respectively. The presence of forbidden lines, e.g, $[OI]$ 630 nm, $[SII]$ 671.6 nm, etc, is indicative of a low density medium ($\sim 10^4 - 10^5$ cm^{-3}) within the jet emitting regions (Hartigan et al., 1995). A worth noting difference between CTTS and WTTS is the lack of strong emission lines in the case of WTTS (Stahler and Palla, 2008). This behavior is observed when the disk has dispersed in YSOs with ages above 10 million years.

Emission lines do not show a stable behavior. Emission variability happens on a time scale of a few hours to a day (Chou et al., 2013; Petrov et al., 2019). To explain this variability, Herbst et al. (1994) advanced three reasons. First, it could be due to cold spots that develop because of magnetic activity in WTTS. Second, CTTS exhibit hot spots on their surfaces as a result of ongoing accretion of circumstellar material. Hot spots have a shorter lifespan compared to cold spots. Third, both CTTS and WTTS experience obscuration of the central star caused by circumstellar dust, leading to an increase in visual extinction along the line of sight. In chapters 4 and 5, we present the results of simulations where, in certain cases, failed wind start to accrete again at higher altitudes. This surface accretion may explain the increase if visual extinction as dust would be transported closer to the star by the inflow.

1.2.2.3 Linking ejection and accretion

Outflows are now observed from many young stellar objects of different masses and evolutionary phases. However, they are always associated with accretion disks around the young stellar object (Ray and Ferreira, 2021). This suggests that an accretion disk is necessary for a jet to be launched. Additionally, there is a correlation between the forbidden line luminosity of [OI] and the infrared excess (Cabrit et al., 1990), linking the jet mass loss rate with the disk mass accretion rate. Hartigan et al. (1995) explicitly calculated these correlations, using line veiling to compute the mass accretion rate. The value obtained with this method can then be compared to the value obtained using the infrared excess. The authors measured the jet velocity and estimated its density using forbidden line emission, from which they computed the mass loss rate. The mass loss rate was shown to be highly correlated with the mass accretion rate. Typical ratios between jet mass loss and accretion rates range from 1% to 10% (Hartigan et al., 1995; White and Hillenbrand, 2004; Cabrit, 2007; Nisini et al., 2018). We emphasis this correlation by showing in Fig.1.13 the evolution of ejection with accretion which again demonstrates the strong link between the two processes.

With this ratio, we can estimate the magnetic lever arm, λ (Eq.1.10). In simple terms, the lever arm λ measures the angular momentum of the outflow and can be linked to the jet terminal velocity, assuming angular momentum is conserved along a

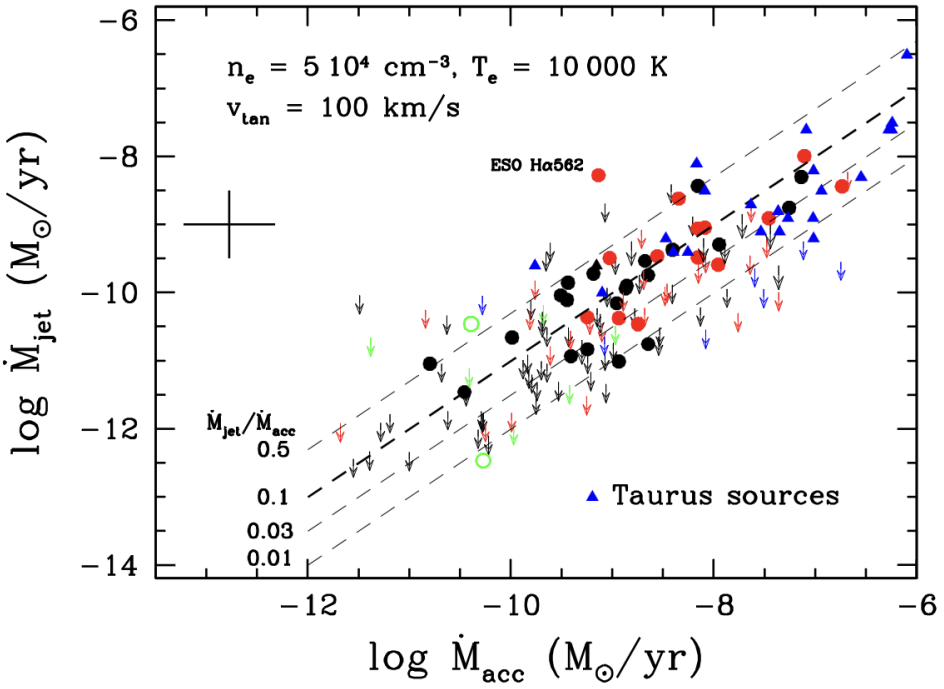

Figure 1.13: Measured accretion versus mass ejection. The colors indicate the cloud from which the sources originate. In total 131 TTS have been probed. A large dispersion is noticed around the value $\dot{M}_j \sim 0.1\dot{M}_\odot$. Adapted from Nisini et al. (2018).

streamline. To be noted that this estimation applies only to magnetocentrifugal winds, and is an upper limit value as it means that all the angular momentum of the disk is transferred to the wind. λ is defined as (Shu et al., 2000; Pudritz et al., 2007),

$$\lambda \equiv \frac{\Omega_A \varpi_A^2}{\Omega_0 \varpi_0^2} \sim \left(\frac{\varpi_A}{\varpi_0}\right)^2 \simeq \frac{\dot{M}_{acc}}{\dot{M}_j}, \tag{1.10}$$

where Ω_0 and Ω_A are the rotational frequencies at the disk surface and the Alfvén surface (where the plasma reaches the wave speed defined as $v \equiv B/\sqrt{4\pi\rho}$) respectively. ϖ_0 is the radius at which the jet is launched from the disk, and ϖ_A is the radius where the magnetic field crosses the Alfvén surface along a streamline launched from ϖ_0.

According to current magneto-centrifugal models, where angular momentum is transported by magnetic fields, the asymptotic jet velocity can be expressed as (Blandford and Payne, 1982),

$$v_j \sim \sqrt{2\lambda - 3} V_K. \tag{1.11}$$

Here V_K is the speed at which the centrifugal and gravitational forces are equal, $V_K = \sqrt{GM/\varpi} = \Omega\varpi$.

We can go further and express the jet launching radius, r_0, in terms of the lever arm, jet velocity, v_j, and mass of the central engine, $M_\star$. Going from Eq.1.11 we can

find the launching radius,

$$\varpi_0 \sim (2\lambda - 3)\frac{GM_\star}{v_j^2} \tag{1.12}$$

1.2.2.4 Jet rotation

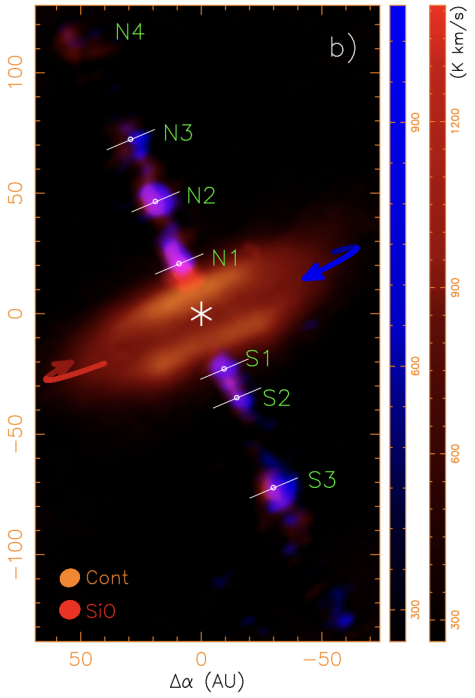

Figure 1.14: Observation of HH212 jet with ALMA (Lee et al., 2017a). Represented here, the blue and red shifted components of the jet. The jet rotation is consistent with the disk rotation.

Measuring the jet rotational frequency is an essential key to understanding the jet kinematics. It enables an accurate determination of the specific angular momentum contained in the jet. Subsequently, it will help differentiate between ejection models. Previously, a hint of the jet rotation was inferred for T Tauri from [OI], [NII], [SII] lines. The velocity resolution is $\sim$ 25 $km\,s^{-1}$ pixel^{-1}, with a spatial resolution of $\sim$ 7 au pixel^{-1} (Bacciotti et al., 2002; Coffey et al., 2007). From these measurements, the specific angular momentum is found to be up to a few 100 au.km s^{-1}, which suggests a launching radius of $0.2 - 1$ au (Coffey et al., 2007). However, these measurements are obtained from a shocked medium, leading to an important uncertainty if the shock structure is not resolved. Coffey et al. (2012) later found that the rotation signature observed in RW Aur jet is likely false. In fact, jet precession and asymmetric shock structures can both produce a velocity gradient which are too similar to a jet rotational signature.

To effectively resolve the highly collimated and narrow jets, a spatial resolution better than 10 au is necessary (Lee, 2020). Additionally, a velocity resolution of approximately 1 $km\,s^{-1}$ is required to detect the small rotation speeds within the jets. Crucially, we need to focus on the innermost regions of the jet where internal shocks have not yet significantly developed, where interactions with surrounding and cavity material are minimal, and where jet precession effects are not prominent. This ensures the preservation of the rotational signature, allowing any observed velocity gradient across the jet axis to be attributed to the rotation of the jet. Moreover, it is important to measure at altitudes high enough and avoid pointing the instruments too close to the central source, as the jet radius decreases towards the center, making the jets unresolvable with current instruments. One of the most convincing rotation evidence is provided by ALMA thanks to an angular resolution of 8 au (Fig.1.14). For HH212 jet, a class 0, Lee et al. (2017a) determined a specific angular momentum of 10 au $\mathrm{km\,s^{-1}}$ in the molecular outflow.

At the foot point of the jet emitting disk the launching radius can be inferred from the measure of the specific angular momentum and jet velocity at a large distance from the central source. A value for the launching radius is obtained by assuming a conservation of energy and angular momentum along the field line (Lee, 2020). We can in addition assume that winds have enough energy to escape the gravitational pull of the star. With all these assumptions Anderson et al. (2003) provided a relation between angular momentum and jet launching radius at the foot point of the magnetic field line,

$$\varpi_0 \sim 0.7 \text{ au} \left(\frac{\mathrm{l_j}}{100 \text{ au km s}^{-1}}\right)^{2/3} \left(\frac{\mathrm{v_j}}{100 \text{ km s}^{-1}}\right)^{-4/3} \left(\frac{\mathrm{M_\star}}{1 \text{ M}_\odot}\right)^{1/3}, \tag{1.13}$$

where l_j is the specific angular momentum and v_j the velocity of the jet. In the case of a TTS with $l_j = 100$ au $\mathrm{km\,s^{-1}}$, $v_j = 300\ km\,s^{-1}$, and a stellar mass $M_\star = 2M_\odot$, the launching radius is ~ 0.2 au. This results in a lever arm of $\lambda \sim 6.5$ (see Eq.1.12), indicating that for TTS the jet specific angular momentum is around 6 times higher than the disk. The lever arm as defined here is sensitive to the amount of angular momentum. If we increase the specific angular momentum to $l_j \sim 200$ au $\mathrm{km\,s^{-1}}$, the lever arm also increase, $\lambda \sim 11$. This emphasizes the importance of a good jet rotation measure and identification of launching radii.

Sauty et al. (2012), have shown however that to determine the total angular momentum transported in the jet, it is not enough to measure the rotational speed. In fact, counter rotation can be obtained even if the total angular momentum is conserved. This is because the magnetic field can take part of the angular momentum. Indeed, if the jet decelerates, counter rotation is expected under some specific condition, while remaining super-Alfvénic.

1.2.2.5 Shock formation

Studying the formation of knots and bow shocks in molecular jets provides crucial insights into the origins of these jets. Observations of molecular jets such as HH 211

(Gueth and Guilloteau, 1999; Lee et al., 2010), HH 212 (Lee et al., 2008, 2015), and L1448C (Hirano et al., 2010) show that these jets appear continuous in their inner regions, suggesting continuous jet ejection at the base. The roughly equal spacing between knots and bow shocks observed in some jets indicates that these features are produced by quasi-periodical variations in ejection.

Knots and bow shocks, well-detected in molecules like SiO and H2, are very similar to those observed in optical jets (Ray et al., 2007; Hartigan et al., 2011; Bally, 2016). This implies that these features do not merely result from quasi-periodical ejections of enhanced jet densities, as such ejections alone would not produce shocks (Frank et al., 2014). Instead, there must also be quasi-periodical variations in ejection velocity, leading to the formation of shocks when faster jet material catches up with slower material (Matsakos et al., 2009). A simple form of this velocity variation could be sinusoidal, possibly induced by orbital motion of perturbations, or by the stellar activity. An eccentric orbit could further enhance this effect by causing increased accretion and mass-ejection rates (Reipurth, 2000; Benisty et al., 2013).

1.2.3 Ejection models, magnetized jets

As mentioned before, given the jet opening angles do not vary with the gas pressure of the outer envelope, collimation cannot be caused by an ambient cold external layer. What about a heated atmosphere? Cabrit (2007) showed using observations that a thermal pressure from the disk cannot collimate the jet either. However, there are also theoretical arguments in the same sens, see Sauty and Tsinganos (1994) for instance. For the jet to be contained without obscuring the star, a temperature higher than 6000 K needs to be provided, and the confining force has to act on the jet up to $\sim$ 10 au. If thermal pressure is not enough, can magnetic pressure replace it? Going from Eq.1.9 and replacing P with $B^2/2$ to get magnetic pressure, we obtain the following,

$$B \sim 10 \text{ mG} \left(\frac{\dot{M}_j}{10^{-8}\ M_\odot \text{ yr}^{-1}} \right)^{1/2} \left(\frac{v_j}{300 \text{ km s}^{-1}} \right)^{1/2} \left(\frac{z}{50 \text{ au}} \right)^{-1}. \tag{1.14}$$

Observations, on the other hand, show that magnetic fields in protostellar cores are two to three orders of magnitude lower (Lee et al., 2017b). This, in turn, excludes the envelope magnetic pressure as producing collimation, but not turbulent magnetic pressure. Another candidate is collimation by winds created from photo-evaporation. Although, densities and temperatures from this process are insufficient (Font et al., 2004; Wang and Goodman, 2017b).

As we exhaust possible collimation sources, it becomes clearer that confinement is self-induced. Magnetic fields are able to collimate outflows through magnetohydrodynamic (MHD) self-collimation. Transported by the jet itself, magnetic fields span from the launching radius at the base of the disk to the collimation and propagation zones. The source of magnetization is also easy to explain. Since stellar formation happens through the collapse of magnetized clouds, the disk is expected to have large

scale magnetic fields (Li et al., 2014). Subsequently, this magnetic configuration would be maintained through disk dynamo and field lines advection. A consensus has been reached on the primary role of the magnetic fields on jet launching and collimation. Further studies concentrated on constraining the ejection region.

By extending the trend of jet opening angles to the source - the surface of the accretion disk - observations show that the launching region is lower than 1 au (Fig.1.12). Even in observations with the highest resolution, disks are not resolved close to the central engine, which leaves the question of the jet launching radius open. Models, developed to tackle this problem, make use of different magnetic configurations. We will describe them hereafter.

1.2.3.1 Stellar winds

Magnetic field lines anchored in the central star and open at the pole can eject a stellar wind. Since Class II stars have a rotation speed of about 10% of the Keplerian speed at the ejection radius, the acceleration of such winds is not solely magneto-centrifugal but also requires an additional gradient of thermal and turbulent pressure during the ejection (DeCampli, 1981; Pantolmos and Matt, 2017). Nevertheless, the poloidal magnetic field helps to collimate the stellar wind below the Alfvén radius, once ejection has occurred (Sauty et al., 2002), and by the toroidal field above.

Stellar winds could explain the slowing down of stellar rotation. For example, in the Sun, angular momentum is removed by stellar winds. A promising model is the accretion-powered stellar winds (APSW) proposed by Matt and Pudritz (2005). According to this model, these outflows are sustained by a fraction of the energy released by accretion processes. The authors suggest that if the mass loss rate in the stellar winds is around 10% of the accretion rate, it would be sufficient to counteract the star spin-up. Further, Matt and Pudritz (2008) propose that if stellar winds are powered by accretion, the mass loss rate of the wind should be 60% or less of the accretion rate. Zanni and Ferreira (2010) show, however, that the APSW scenario has difficulty explaining all stellar outflows and braking contribution. For APSW to work much more UV luminosity has to be emmited than what is observed. Beyond this threshold, accretion cannot adequately power the wind. The stellar wind struggles to achieve the ejection-to-accretion ratio (~ 0.1) observed in jets (Cranmer, 2009; Pantolmos et al., 2020). Alone this process may not explain the entire jet mass loss, but it serves as a good angular momentum extractor. Sauty et al. (2011) show that stellar winds can act as a spin-down mechanism and efficiently break the rotation of the star. Sauty et al. (2022) and Meskini et al. (2024) later show that the solution is stable no matter the accretion profile or disk wind.

1.2.3.2 Extended disk winds

Extended winds require a poloidal magnetic field anchored in the disk over a wide range of radii (Ferreira, 1997), see Fig.1.15a). The disk material is ejected and accelerated

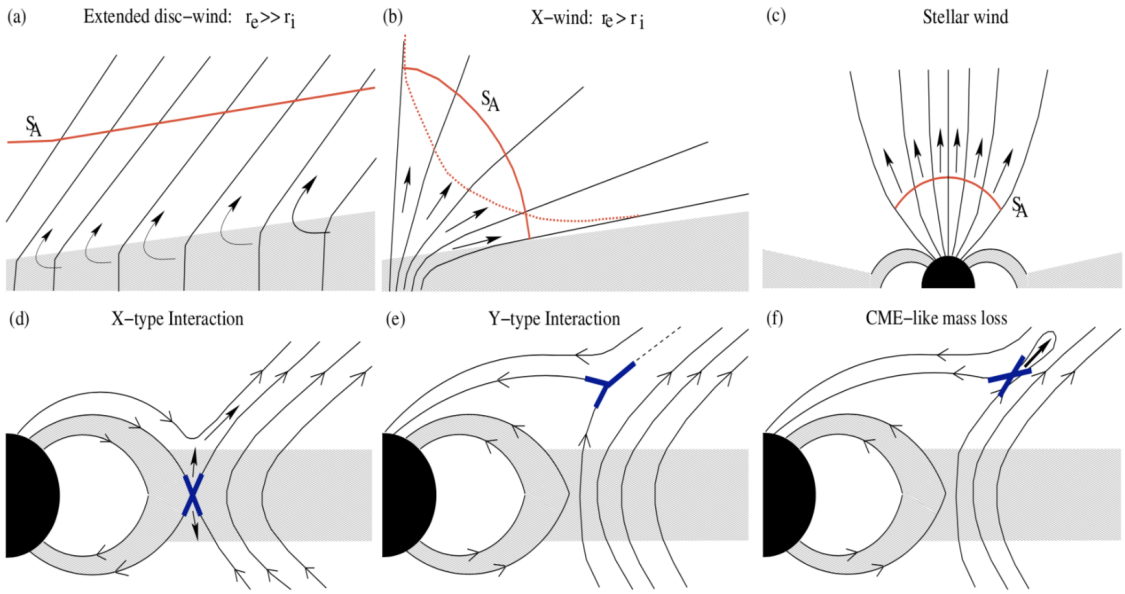

Figure 1.15: Different ejection models and types of magnetic interactions between the disk and the magnetosphere. (Ferreira et al., 2006)

by the magneto-centrifugal ejection process. Such models are self-collimated by the toroidal magnetic field of the external field lines and can thus very effectively reproduce the quasi-cylindrical appearance of jets. These models can also efficiently reproduce the observed ratio between the ejection rate and the accretion rate onto the central star. Extended winds can replicate the "onion shell" kinematic structure observed in the Class II star DG Tau. The innermost regions would produce the highest velocities, while the outer regions correspond to lower velocities (Agra-Amboage et al., 2011). Note that Casse and Ferreira (2000) showed that heating is an important contributor in ejection and disk structure. More recently, Jacquemin-Ide et al. (2021) showed that turbulent pressure also acts as an outflow enhancer. This entails that ejection from extended disk winds cannot solely be a result of magnetocentrifugal processes.

In parallel to the analytical approach, numerical MHD simulations were the object of an increasing interest. Initial attempts did not consider the disk, instead they computed jet acceleration and propagation with fixed boundary conditions imposing launching conditions (e.g., Ouyed and Pudritz 1997a). This methodology enables studying the jet at large scales allowing to relate magnetization and jet mass loss for instance (Anderson et al., 2005; Pudritz et al., 2006; Fendt, 2006). Nonetheless, to study feedback effects on the disk, one needs include the disk structure (Casse and Keppens 2002, 2004; Zanni et al. 2007; Tzeferacos et al. 2009; Murphy et al. 2010; Stepanovs and Fendt 2016; Mattia and Fendt 2020a,b, 2022; Jannaud et al. 2023, to cite only a few).

1.2.3.3 X-winds

In X-winds (fig.1.15b), the ejection is also magneto-centrifugal, similar to extended disk winds. The main distinction lies in where the field lines are anchored. In the context of the X-wind model, all ejection originates from stellar field lines that have been disconnected from the central star at the truncation radius (Shu et al., 1994). Since the magnetic field is concentrated at a specific point, the field lines are much more open initially compared to disk wind models. However, the field lines are quickly collimated by the toroidal magnetic field. This model can also effectively reproduce the quasi-cylindrical density profiles observed in jets (Shu et al., 1995), although it produces a narrow range of terminal velocities. It accurately replicates the morphology and dynamics of the RW Aur jet (Liu and Shang, 2012). Similar to the extended disk wind, the X-winds can also achieve the observed accretion/ejection ratio.

X-winds are expected to be the dominant component in YSO jets in this model, and this in terms of appearance, power, and mass flux. These winds carry away sufficient angular momentum to prevent the star from being spun up by the accreting material, ensuring a zero net torque condition. However, this model has its drawbacks. Observed jet dynamics are inconsistent with the model predictions. For instance, there is a steep horizontal decline of the poloidal velocity (Cabrit, 2007). In addition, since accretion deposits angular momentum at the base of the accretion funnel, X-winds need to carry all the excess momentum. This requires a very efficient viscous process (Ferreira and Casse, 2013). Referring to 2D and 3D simulations, they all show that the truncation radius is smaller than the co-rotation radius (e.g., Romanova et al. 2002; Zanni and Ferreira 2009; Romanova et al. 2012). Although, some ejections happen at the truncation radius they are non-stationary.

Another scenario exists where magnetic fields of the disk parallel to the stellar magnetic moment result in a magnetic X-point (Ferreira et al., 2000). This configuration is called reconnection X-wind (ReX-wind). In this process, disk material is lifted above the X-point by a strong Lorentz force and is loaded into the open magnetic field lines. As pointed out by Ferreira et al. (2006), even though ReX-winds and X-winds both emerge from the corotation radius (i.e., the radius where the disk and the star spin at the same rate) there is a fundamental difference between the two models. First, ejection from ReX-winds is unsteady and is seen as a series of bullets rather than a continuous laminar flow. Second, X-winds are less efficient at breaking the accreting star. Last, the disk has to be threaded by a large scale magnetic field in the case of ReX-winds.

1.2.3.4 Star-disk interaction

Models presented on the second row of Fig.1.15 are non-stationary ejections due to star-disk interaction (SDI). In Fig.1.15d, we have X-wind reconnection where magnetic lines are parallel, and coronal mass ejections where the lines are in an anti-parallel configuration (Fig.1.15e). Magnetospheric ejections result from a series of events including expansion, disconnection, and reconnection of magnetic field lines. Differences in angular velocities between the star and the disk cause the magnetic field lines to

inflate. This process leads to material being ejected towards the interstellar medium during disconnection events.

In the 1990s, Goodson et al. (1997) successfully simulated these outflows and suggested their potential cyclic nature. Later, Zanni and Ferreira (2013) simulated multiple cycles of magnetospheric ejections (MEs) arising from the interaction between the stellar dipolar magnetic field and the circumstellar disk. They found that MEs not only regulate stellar rotation by removing angular momentum from the inner disk region but also by directly extracting it from the star due to differential rotation. These ejections propagate between the stellar wind and disk wind regions. the frequency of these events are high, with multiple MEs happening in a short period of time.

1.2.4 Outflows from an accretion disk

1.2.4.1 Magneto-centrifugal ejection

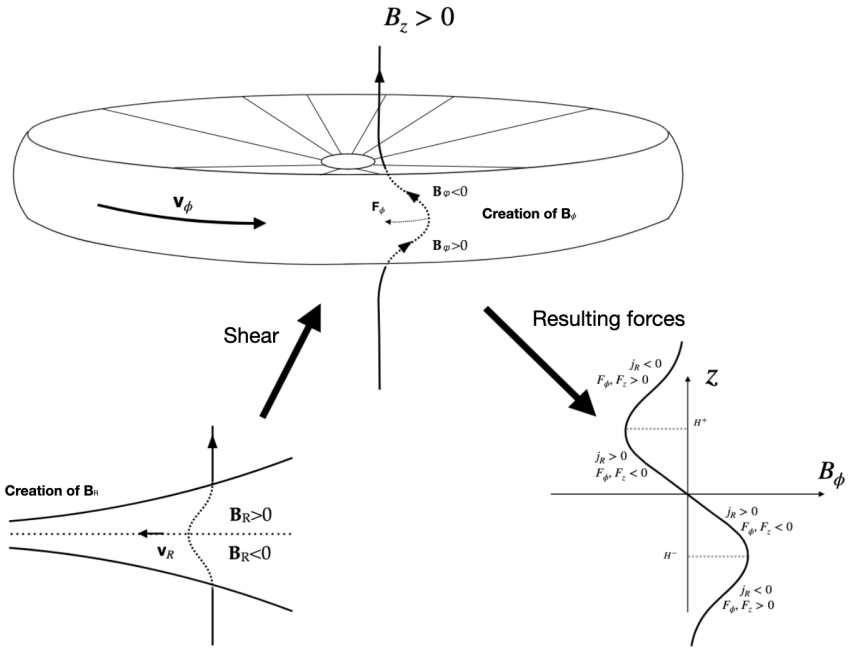

Figure 1.16: Sketch of an initially vertical magnetic field modified by a Keplerian disk. In this plot $R \equiv \varpi$. Taken from Aloïs De Valon thesis manuscript (https://theses.hal.science/tel-03597792).

Magneto-centrifugal ejection is at the origin of all magnetized ejection models described in Sec.1.2.3. First proposed by Blandford and Payne (1982) to explain winds from cold disks, this mechanism necessitates a large scale poloidal magnetic field. As the disk rotates, the magnetic field rolls around the axis creating a toroidal field. In turn this new component applies a force that slows down the disk, facilitating accretion.

Since the field lines are inclined at the surface of the disk, the Lorentz force produced expel matter out of the disk, which creates the winds. In this model, the wind extracts angular momentum through magnetic fields. The transfer of momentum is characterized by the magnetic lever arm, which is a measure of the specific angular momentum in the wind to the specific angular momentum at the ejection radius (see Eq.1.10).

Jet launching is closely linked to the physics inside the disk. Ferreira and Pelletier (1995) described the mechanism of ejection and extraction of angular momentum (resumed in Fig.1.16). The initially vertical magnetic field lines are distorted by radial accretion in the disk, creating a radial magnetic field B_ϖ. This radial field is then sheared by the Keplerian flow, generating a toroidal magnetic field $B_\phi < 0$ in the upper half-plane of the disk. This induces a current j_R, resulting in a vertical Lorentz force $j_\varpi B_\phi$ and an azimuthal Lorentz force $-j_\varpi B_z$. The force F_ϕ corresponds to the magnetic tension of the field lines. It is negative in the disk, indicating that the magnetic field brakes the disk due to the magnetic tension opposing the deformation of the field lines. This induces radial accretion and sustains the radial magnetic field B_ϖ. The Lorentz force $j_\varpi B_\phi$ corresponds to the magnetic pressure $-\partial_z {B_\phi}^2$. This magnetic pressure is created when the field lines are wound in the toroidal direction by the disk. It is positive above the disk surface, ejecting matter vertically, while below the disk surface, it is negative. The disk is compressed by the wind, which relies on the lower regions to be launched.

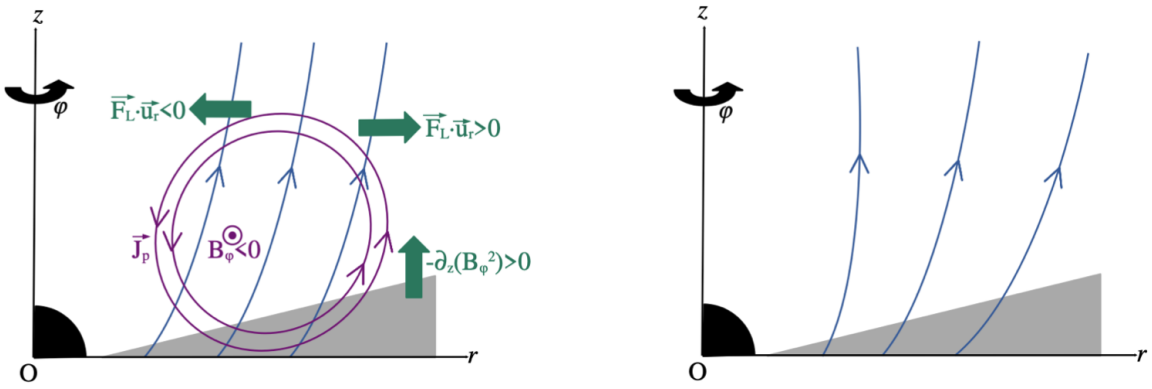

Figure 1.17: Schematic of the forces at play which recollimate magnetic field of the disk. In blue are the poloidal magnetic field lines, initially vertical, but subsequently bend under the influence of accretion. In grey is the accretion disk, in Keplerian rotation around the axis Oz. The rotation velocity v_ϕ is in purple, as well as the subsequent toroidal magnetic field B_ϕ and poloidal current loops j_p. In green are the Lorentz force $F_L = \frac{1}{c} j \times B$ and magnetic pressure gradient $-\nabla {B_\phi}^2$. here, $r \equiv \varpi$. Adapted from Thomas Jannaud's thesis manuscript (https://theses.hal.science/tel-04480257).

The emergence of a toroidal magnetic field helps launching the plasma and plays a crucial role in the jet collimation. Rotation induces an electric field $E_i = v_\phi \times B_z$, along the v_ϖ direction in the disk. The associated current density j_p is shown in purple in the

left plot in Fig.1.17. Due to the current closure condition $\nabla \cdot j = 0$, counterclockwise current loops form. The resulting Laplace force $j_p \times B_\phi$ is directed inwards along $-v_\varpi$ on the innermost magnetic field lines, initiating jet collimation. In the right panel of Fig.1.17, these magnetic field lines are collimated, while the outer field lines open up.

To better understand jet launching using magnetic fields one can use the bead on a rigid wire analogy. Although as shown before, jet ejection is inherently magnetic, we can use a mechanical analogy for explaining the ejection. Since outside the disk magnetic diffusivity is negligible, the plasma follows the flux freezing condition. Thus, we are in the ideal MHD regime. This implies that the velocity and magnetic fields are parallel. Hence, the plasma follows the magnetic fields as if it was on a rigid wire, at least close to the launching region. As given by Blandford and Payne (1982), the energy potential describes a bead subject only to centrifugal and gravitational forces at a cylindrical radius, r_0, of the disk,

$$\Phi(\varpi, z) = -\frac{GM}{\varpi_0}\left(\frac{1}{2}\frac{\varpi^2}{\varpi_0^2} + \frac{\varpi_0}{(\varpi^2 + z^2)^{1/2}}\right). \tag{1.15}$$

The bead is co-rotating with a Keplerian disk and the potential is expressed in cylindrical coordinates. The purpose here is to determine the conditions under which the bead can be flung out the disk. To make the analysis easier, we will use spherical coordinates, replacing ϖ and z by a new coordinate system where $\varpi = \varpi_0 + R\sin\theta$ and $z = R\cos\theta$. Here, R is the spherical radius of the wire, and θ its colatitude. To know at what angle launching happens, we have to compute the second derivative of the potential energy,

$$\left(\frac{\partial^2}{\partial R^2}\Phi(R,\theta)\right)_\theta = -\frac{GM}{\varpi_0}\left(\frac{\sin^2\theta}{\varpi_0^2} + \frac{\varpi_0(2R^2 - \varpi_0^2 + 3\varpi_0^2\sin^2\theta + 4\varpi_0 R\sin\theta)}{(\varpi_0^2 + 2\varpi_0 R\sin\theta + R^2)^{5/2}}\right), \tag{1.16}$$

and by anchoring the wire at $\varpi = \varpi_0$ and $z = 0$, then choosing the bead to release at rest from ϖ_0, we impose $R = 0$. Subsequently, Eq.1.16 transforms into,

$$\left(\frac{\partial^2}{\partial R^2}\Phi(R,\theta)\right)_{\theta,R=0} = \frac{GM}{\varpi_0^3}\left(1 - 4\sin^2\theta\right). \tag{1.17}$$

It is now clear through Eq.1.17 that if $\theta > \pi/6$ the equilibrium is stable and the bead stays on the disk. On the other hand, if $\theta < \pi/6$ the bead leaves the disk with a trajectory imposed by the wire. In other words, if the angle between the polar axis and the magnetic field is larger than $\sim 33°$ a jet can be launched to infinity from a magnetic field that is rigid up to the Alfvén surface. In Fig.1.18, Blandford and Payne (1982) show the space where a bead can be ejected, which illustrates the analysis we have done so far.

1.2.4.2 Theory of magnetized jets

To describe magnetized jets we use the MHD formalism since we are dealing with fluids that evolve with a magnetic field (a detailed description is reserved for chapter 2).

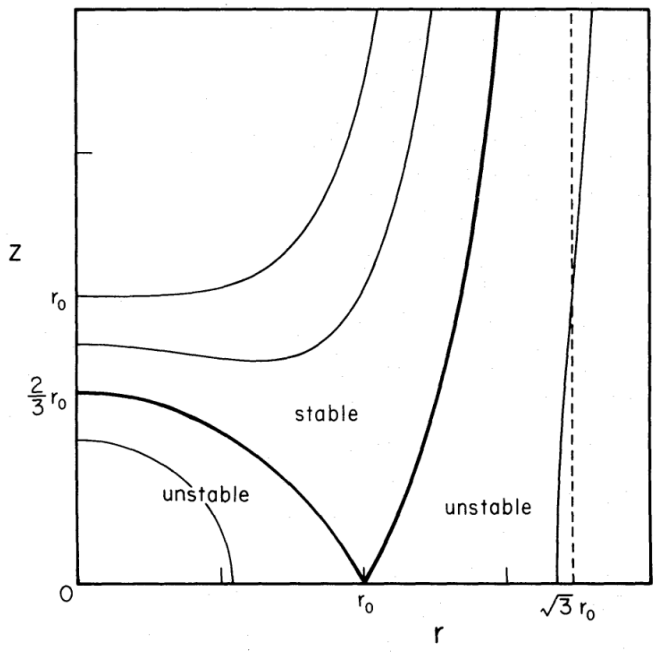

Figure 1.18: Plot of the isopotential in terms of cylindrical coordinates. The plot is of plane perpendicular to the disk. The dashed line at $r = \sqrt{3}r_0$ is the asymptote of the marginal stability isopotential. Here $r \equiv \varpi$ in the main text. Taken from Blandford and Payne (1982).

Although magneto-centrifugal ejection give birth to multiple models with varying dynamics and morphologies, three conservation laws, in the form of three free integrals, emerge in axisymmetric and stationary outflows along a constant magnetic surface. The three conserved quantities are the total specific energy (E), the specific angular momentum (L), and the co-rotation frequency of a magnetic field (Ω),

$$E = \frac{1}{2}v^2 - \frac{B_\phi B_p \Omega \varpi}{4\pi\rho v_p} + h + \Phi_{grav} - \mathcal{H}, \tag{1.18}$$

$$L = \varpi\left(v_\phi - \frac{B_\phi B_p}{4\pi\rho v_p}\right) = \lambda\Omega\varpi_0^2, \tag{1.19}$$

$$\Omega = \frac{1}{\varpi}\left(v_\phi - \frac{B_\phi v_p}{B_p}\right). \tag{1.20}$$

Eq.1.18 shows the energy inputs to consider when dealing with a magnetized plasma subject to gravity and heating. The first two terms describe the kinetic and magnetic contributions. h is the enthalpy and Φ_{grav} the gravitational potential. Last, we have $\mathcal{H}$, a term that accounts for heating sources not included in the models (i.e., Alfvén waves, turbulent heating).

Specific angular momentum (Eq.1.19) can be stored in two ways, in the rotational velocity v_ϕ or in the toroidal magnetic field. The final equation (Eq.1.20) describes the angular frequency of the magnetic field lines. For a disk wind, this angular frequency is equal to the angular frequency of the disk at the ejection radius. The morphology of the disk wind is determined by solving the transverse magnetic equilibrium, governed by the Grad-Shafranov equations. We can, nonetheless, determine the dynamics of winds, expressed by the magnetic lever arm and the launching radius.

By changing of reference frame, we can cancel the magnetic terms since they compensate. We place ourselves in the co-rotationg frame by combining the three equations described above, which leads to,

$$\begin{aligned} F &= E - L\Omega \\ &= \frac{1}{2}v^2 - v_\phi \Omega \varpi + h + \Phi_{grav} - \mathcal{H}. \end{aligned} \tag{1.21}$$

By invoking the conservation property, the specific energy at infinity is equal to the specific energy at the base of the outflow ($F = F_{\varpi_0}$). If additionally, we define the lever arm as the quantity λ_ϕ linking ϖv_ϕ and $\varpi_0 V_{k,\varpi_0}$, we can express the poloidal velocity at infinity using quantities at the base of the outflow . We write,

$$\varpi v_\phi = \lambda_\phi \varpi_0 V_{K,\varpi_0} \tag{1.22}$$

$$v_{p,\infty} = V_{K,\varpi_0}\sqrt{2\lambda_\phi - 3 + \beta} \tag{1.23}$$

$$\beta = 2(h_0 - h + \mathcal{H})/V_{K,\varpi_0}^2 \tag{1.24}$$

We get Eq.1.23 using the fact $v_p >> v_\phi$ at infinity, and that asymptotically, gravitation is also negligible. When $v_\phi >> (B_\phi B_p/4\pi\rho v_p)$, all the angular momentum is transferred to the plasma, because Eq.1.22 and Eq.1.19 would be equal, leading to $\lambda_\phi = \lambda$. In that sens, λ_ϕ represents a lower limit to λ. β contains all the heating input. Neglecting this term puts us in the cold disk hypothesis and all the dynamics would be described by $\sqrt{2\lambda_\phi - 3}$.

1.2.4.3 Dependence of the launching radius on the heating input

Anderson et al. (2003) was able to locate the launching radius in the case where the thermal effects are neglected. Going back to Eq.1.21, and considering $V_{K,\varpi_0} >> v_{p,\varpi_0}$ and $v_{\phi,\varpi_0} \sim V_{K,\varpi_0}$ at the base of the flow, we have,

$$\begin{aligned} F &= \frac{v_\phi^2}{2} - \varpi_0 v_\phi \Omega + \Phi_{grav} \\ &\sim -\frac{3}{2}V_{K,\varpi_0}^2 \end{aligned} \tag{1.25}$$

Now by equating this value with the specific energy at infinity we get,

$$\varpi_\infty v_{\phi,\infty}\Omega - \frac{3}{2}(GM\Omega_0)^{2/3} - \frac{v_{p,\infty}^2}{2} \sim 0. \tag{1.26}$$

By measuring the poloidal velocity and specific angular momentum we can determine Ω_0 and by extension $\varpi_0 = (GM/\Omega_0^2)^{1/2}$.

It is not possible to determine a launching radius and lever arm when $\beta \neq 0$, as we would have three unknowns for two equations. To gauge how the launching radius ϖ_0,

and the lever arm λ change with heating input, we need to fix ϖv_ϕ and v_p. Then by varying β between 0 and 1 we get a better feel of how heating can influence launching radius and lever arm values. For high values of λ, a value of $\beta = 1$ is negligible compared to $2\lambda - 3$. When, on the other end, λ approaches unity, β heavily biases the value of ϖ_0. As can be seen in Fig.1.19, an underestimation of up to 80% occurs when $\lambda \sim 1.5$.

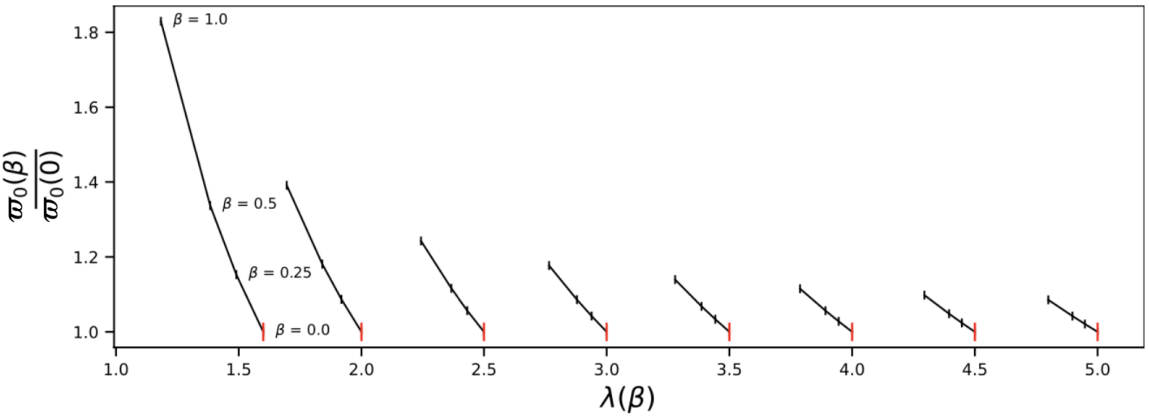

Figure 1.19: Plots of the launching radii and lever arms as functions of β. Modified from Aloïs De Valon's thesis manuscript (https://theses.hal.science/tel-03597792).

The influence of thermal and/or wave gradients β on the poloidal velocity of jets from Keplerian accretion disks is minimal and can be neglected. A Keplerian rotation requires a negligible radial pressure gradient within the disk. Consequently, the enthalpy at the disk surface always verifies,

$$\frac{h_0}{V^2_{K,\varpi_0}} << 1. \tag{1.27}$$

Ferreira and Casse (2004) show that a β of a few percent only can produce highly heated disk jets, where temperatures reach up to 10^5 K. Although thermal effects have no measurable effect on jet poloidal velocities, they do have a significant effect on mass loading and, consequently, jet kinematics (Ferreira et al., 2006).

1.2.4.4 Mass flux

In jet emitting disk models accretion depends on the ejection efficiency. Accretion and ejection are linked in this model by allowing accretion rate to be a function of the radius ϖ. The accretion rate writes as a power-law of ϖ,

$$\dot{M}_{acc} \propto \varpi^{\xi}. \tag{1.28}$$

ξ, here, is the ejection efficiency parameter and lies between 0 and 1. The higher ξ is, the more matter is ejected. $\xi = 0$ corresponds to no mass loading in the jet when no additional contribution, such as heating, is considered. It is also closely linked to

the lever arm. For accretion dominated by a vertical extraction of angular momentum (Ferreira, 1997), we have,

$$\lambda \sim 1 + \frac{1}{2\xi}. \tag{1.29}$$

Since observations of v_ϕ and v_p provide a lower limit on the lever arm, it therefore also provides an upper limit on accretion. In the case of extended winds, mass loss of the winds is given in the ejection region between ϖ_{in} and ϖ_{out} (mass conservation),

$$\dot{M}_{wind} = \dot{M}_{acc}(\varpi_{out}) - \dot{M}_{acc}(\varpi_{in}), \tag{1.30}$$

Consequently,

$$\frac{\dot{M}_{wind}}{\dot{M}_{acc}} \leq \left(\frac{\varpi_{out}}{\varpi_{in}}\right)^{\frac{2}{\lambda_\phi - 1}} - 1 \tag{1.31}$$

1.2.4.5 Distinguishing between magnetized models

It is hard to constrain the efficiency of stellar winds in launching jets. Observations do not produce a good measure of the specific angular momentum because of the lack of a good velocity resolution. Thus, we cannot look into regions close to launching and with small jet radii. Without this, a proper analysis of stellar wind contribution is out of reach. In the case of stellar winds, the plasma is essentially pressure driven, and so the ejected material derives most its energy from β, although, magnetic fields are responsible for jet collimation. We will focus here on disk wind models, namely, X-Winds and extended disk winds.

The initial self-similar solutions for disk winds (Blandford and Payne, 1982; Ferreira, 1997) are cold, have high lambda values between $30 - 50$, and require strong magnetic fields ($\mu = (B^2/4\pi P) = 1$). Casse and Ferreira (2000) managed to reduce the lambda values to approximately 2 by applying significant surface heating ($\beta \sim 1.7$). Recently, solutions with low magnetic fields ($\mu \sim 10^{-7}$) have been obtained (Stepanovs and Fendt, 2016; Jacquemin-Ide et al., 2019; Lesur, 2021). These three studies particularly explored the parameter space in Fig.1.20. The steady-state solutions shown in Fig.1.20 achieve extremely low lambda values ($\lambda \sim 1.5$) while maintaining the cold hypothesis.

Several numerical simulations of disk winds have been produced. Ideal MHD simulations (Zhu and Stone, 2018; Jacquemin-Ide et al., 2021) achieve lambda values around $\lambda \sim 5 - 10$. The ideal MHD assumption is justified for describing the well-ionized inner regions of the disk (within 1 au). However, non-ideal effects must be considered to realistically describe the outer regions. Numerous simulations have been conducted under the non-ideal hypothesis (e.g. Béthune et al. 2016; Wang et al. 2019; Bai 2017). Notably, Béthune et al. (2016) achieve very low lambda values ($\lambda \sim 1.4$) and require heating ($\beta \sim 0.2$) to go beyond the point where the plasma becomes super Alfvénic.

As mentioned above, the X-wind model was introduced through a series of papers (e.g., Shu et al. 1994; Shu et al. 1995). In this model, the disk is assumed to be non-magnetized, with all the magnetic fields originating from the star. These fields are

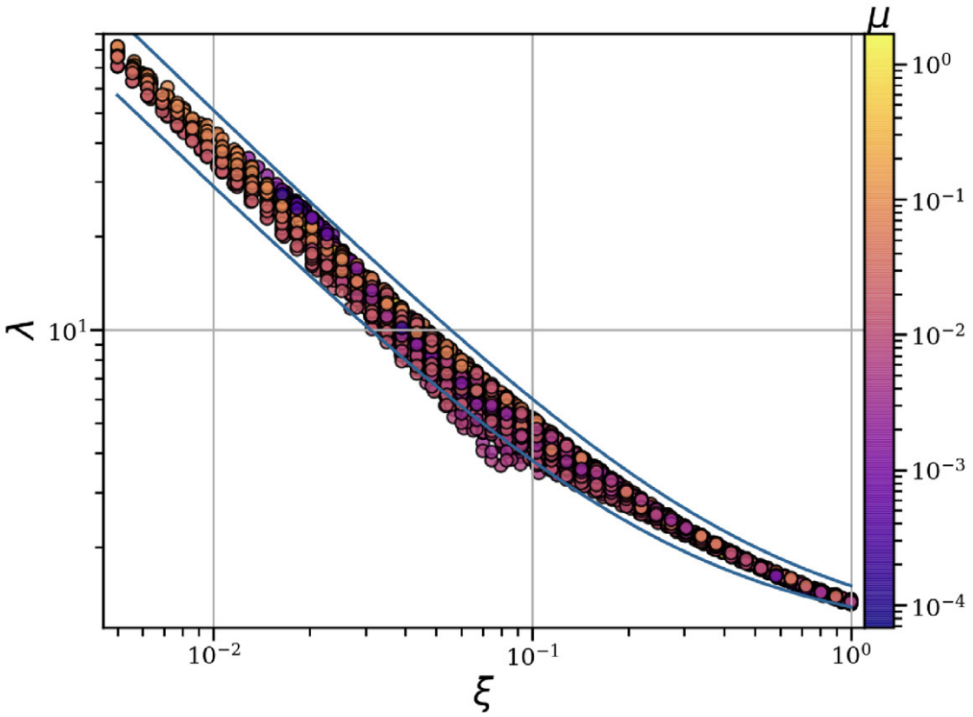

Figure 1.20: Dependence of λ on the ejection index and magnetization. Jacquemin-Ide et al. (2019).

concentrated at the radius ϖ_X, which is close to the co-rotation radius where the magnetosphere truncates the disk. Unlike the extended disk wind model, the parameters λ and ϖ_0 are much more tightly constrained. The X-wind model also assumes $\lambda \sim 3-5$ and $\beta = 0$. For a central star with a solar mass, this model can achieve poloidal velocities of around 300 $km\,\mathrm{s}^{-1}$ and specific angular momenta of approximately 30 au km s^{-1}. A major difference from the disk wind model is that the X-wind model has only a single ejection radius by definition. Consequently, it is challenging to explain the strong radial stratification in velocities observed in the jets.

In Fig.1.21, the asymptotic angular momentum as a function of terminal velocity are plotted for various jet-like outflows. Ferreira et al. (2006) use these values to constrain the ejection radii and the magnetic lever arm. The results indicate that the λ values are constrained between 4 and 12, consistent with an MHD-driven disk wind Casse and Ferreira (2000). The authors conclude that the most likely model to explain the observed jet behavior is the extended disk wind, while not excluding a stellar contribution. Most of the mass however would be from the disk according to the authors. The space stellar models occupy in Fig.1.21 is inferred from observations. Hence, some caution is in order with too definitive conclusions. First, the measured jet rotations in T Tauri stars are tentative and need refining. In the case of RW Aur for instance, rotation evidence were retracted and are likely due to other effects.

Second, a substantial contribution of stellar winds and X-Winds is still possible close

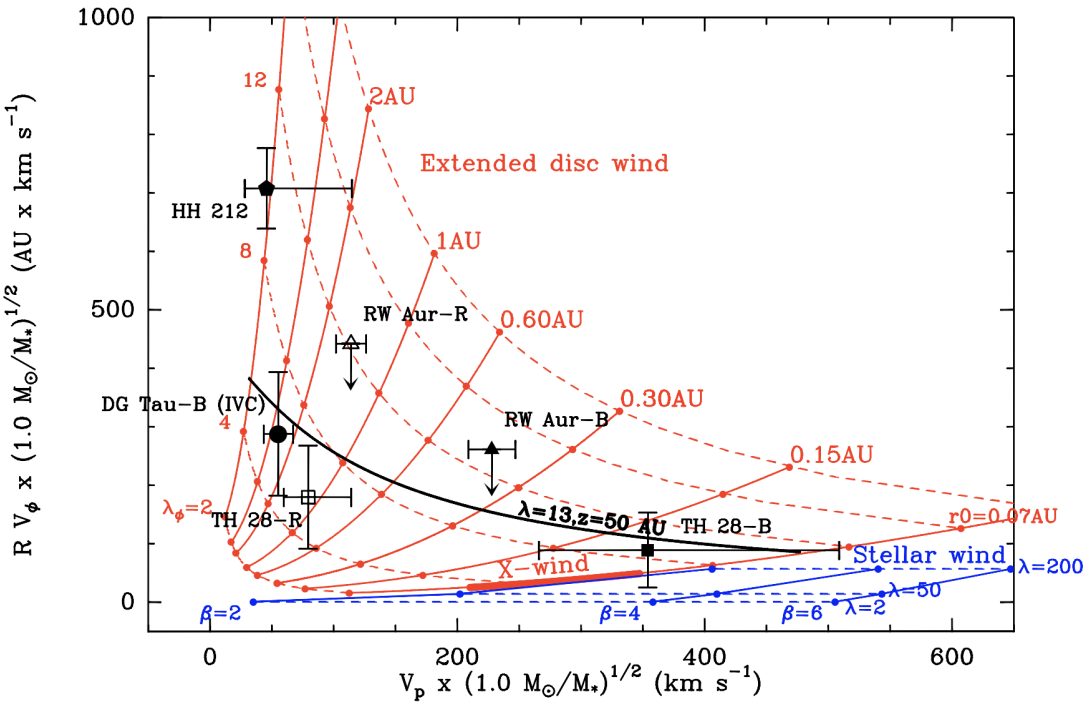

Figure 1.21: Comparison of predicted specific angular momentum and poloidal velocities with observations of T Tauri jets. From Ferreira et al. (2006).

to launching radius and might become negligible compared to disk emitted jets at large scales. Jets are inherently multi-component objects.

1.2.4.6 Photo-evaporative winds

Models of photo-evaporative winds are almost as old as magnetized winds (Bally and Scoville, 1982). In these models winds are generated through radiation of surface disk material. Subsequently, The excess thermal energy acquired by these shallow layers can help disk material escape the gravitational potential, thus generating outflows where the terminal speed is estimated to be $2-3$ times the sound speed, c_s (Hollenbach et al., 1994). Compared to MHD disk winds, the photo-evaporative winds are very slow (≤ 10 km s^{-1}), and the momentum extracted from the disk is equal to the specific angular momentum at the launching radius. This entails that for accretion to proceed, photo-evaporative winds need a viscous accretion disk. Once material is ejected the lack recollimation processes results in wide and conical outflows. These models are excellent candidates for describing low-velocity and low-ionization ejections, such as molecular outflows.

Although photo-evaporation is conceptually straightforward, it quickly becomes very complex to model. The complexity originates from the difficulty to model the physical heating sources. In the case of photo-evaporation there are three distinct sources, namely, X-ray ($0.1-10$ keV), Extreme UV ($13.6-100$ eV), and Far UV ($6-13.6$ eV).

Each process has its own penetration range and energy deposit rate. We will describe these processes in detail in chapter 3. Our aim however is to characterize the physical processes available to heat the disk and its atmosphere. For more information about photo-evaporative winds refer to Wang and Goodman (2017a), and for a comparaison between magnetically and thermally driven disk winds refer to Rodenkirch et al. (2020) and Rodenkirch and Dullemond (2022). We will not delve into the topic of photo-evaporative winds, instead concentrating on MHD outflows.

1.3 Circumstellar disks

1.3.1 A thin disk

1.3.1.1 A disk interacting with magnetic fields

An accretion disk is a complex object (Fig.1.22) which internal structure is hard to probe. Understanding its evolution entails constraining surface and internal processes. The early history of its formation is also a significant factor in the disk structure, namely, infall (Cameron, 1978; Popham and Narayan, 1992; Padoan et al., 2005; Lesur et al., 2015), and self-gravity (e.g., Kratter and Lodato, 2016). In class II YSO, an important parameter that describes the disk evolution is the strength of the magnetic field. Parametrized by the plasma β_p, it characterizes the ratio between the thermal and magnetic pressure,

$$\beta_p = \frac{2}{\mu} = \frac{8\pi P_{gas}}{B_z^2}. \tag{1.32}$$

The lifetime of a disk is heavily dictated by the strength of B_z, at least theoretically. With a plasma β_p approaching zero (i.e., very strong magnetic fields), the magnetic braking is dominant, which shortens the disk lifespan. Conversely, when β_p tends towards infinity, the evolution is slow. In cases where $\beta_p >> 10^5$, the disk is influenced by hydrodynamical instabilities, like the vertical shear instability (Nelson et al., 2013; Flock et al., 2020), the convective, and zombie vortex instabilities (Lesur et al., 2023). For weak vertical magnetic fields, with β_p between $10^3 - 10^5$, we can already see an important contribution in turbulent and laminar MHD transport compared to non-magnetized disks (Simon et al., 2013; Lesur, 2021). They extract angular momentum and contribute to mass loss via MHD winds (Bai and Stone, 2013). Points of interest ensue from this framework, and relate to the driver of the disk evolution. Since two angular momentum transport mechanisms exist in an accretion disk (turbulent transport, MHD winds), it is important to quantify the contribution of each. The second point of interest relates to the primary turbulence driver. Both hydrodynamical and MHD processes generate turbulence, and the contribution of each must be determined.

Fundamentally, all MHD transport processes depend on the parameter plasma β_p. While there are one-dimensional effective theories for this parameter (Leung and Ogilvie, 2019), they have yet to be fully validated through simulations. Adding to the complexity, as highlighted in the previous section, there is no standard tracer that

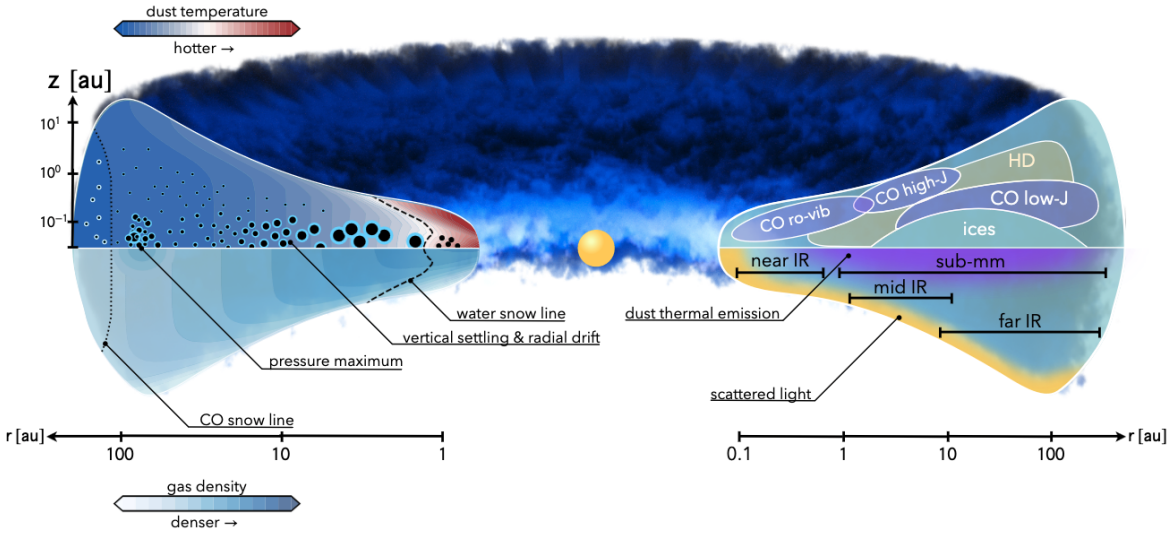

Figure 1.22: Sketch of the physical and chemical structure of $1 - 5$ Myr old accretion disk around a Sun-like star. From Miotello et al. (2023).

directly measures gas surface density. Comparisons based on observations require intermediate steps involving dust evolution models (Birnstiel et al., 2012) or chemical models (e.g., Woitke et al. 2016), which introduce additional uncertainties.

For the disk to be linked to the magnetic fields, the former needs to be ionized enough since the magnetic field acts on charge carriers. The first source of ionization is the star itself. It only acts on small radii of ~ 0.1 au and less. The second is the accretion which releases heat also raising the temperature, thus the degree of ionization (Mohanty et al., 2018). Although, It is not clear if the ionization is sustained deep in the disk or only superficial. Non-thermal ionization processes also exist, such as X-rays (Glassgold et al., 2012), far-UV photons emitted by accretion layers and the corona (Igea and Glassgold, 1999; Perez-Becker and Chiang, 2011), cosmic rays (Umebayashi and Nakano, 1981; Rab et al., 2017), and a very promising source that can ionize deep inside the disk up to $\sim$ 0.2au in form energetic particles created after reconnection phenomena (Brunn et al., 2023, 2024). In chapter 3 we present a detailed overview of the ionization and heating processes that are likely at play in YSOs.

1.3.1.2 Surface density

Angular transport in accretion disk has garnered a significant amount of attention. Here after we will describe the turbulent viscous thin disk using the pseudo-viscosity α parameter introduced by Shakura and Sunyaev (1973). The structure of accretion disks of TTS is described by a geometrically thin and optically thick disc model, composed of gas and dust. In essence, studying transport of angular momentum is similar to studying convection in stellar interiors as both are described by a diffusion-type equation (see Eq.1.42 and text after). The key is to link radial stresses to quantities like the disk

surface density Σ, thickness h, rotation rate Ω, magnetic diffusivity, and magnetic field strength (Lesur, 2021).

To describe the disk evolution, we will examine mass and angular momentum conservation for a differential ring at radius ϖ and thickness $d\varpi$. While assuming the disk has an axisymmetric structure, its surface density is described by $\Sigma(\varpi)$, which is the integral of mass density $\rho(\varpi, z)$ over the disk height,

$$\Sigma(\varpi) = \int_{-h}^{h} \rho(\varpi, z) dz. \tag{1.33}$$

This simplification is possible because we assume a thin disk approximation. We also need the radial velocity denoted by $v_\varpi(\varpi)$, where a positive value indicates an outward direction and a negative one refers to accretion. For a ring located at a radius ϖ, the flow rate at the inner edge is,

$$\dot{M}_{\text{inner}} = 2\pi\varpi\Sigma(\varpi)v_\varpi(\varpi). \tag{1.34}$$

At the outer edge we have to add the ring thickness $d\varpi$,

$$\dot{M}_{\text{outer}} = 2\pi(\varpi + d\varpi)\Sigma(\varpi + d\varpi)v_\varpi(\varpi + d\varpi). \tag{1.35}$$

The difference between the flow rates at ring ϖ and ring $d\varpi$ give the mass change rate,

$$2\pi\varpi d\varpi \frac{\partial\Sigma}{\partial t} = \dot{M}_{\text{inner}} - \dot{M}_{\text{outer}}. \tag{1.36}$$

Substituting these expressions, we obtain,

$$\varpi\frac{\partial\Sigma}{\partial t} = -\frac{(\varpi + d\varpi)\Sigma(\varpi + d\varpi)v_\varpi(\varpi + d\varpi) - \varpi\Sigma(\varpi)v_\varpi(\varpi)}{d\varpi}, \tag{1.37}$$

then we deduce the vertical continuity equation for mass,

$$\varpi\frac{\partial\Sigma}{\partial t} = -\frac{\partial}{\partial\varpi}(\varpi\Sigma v_\varpi). \tag{1.38}$$

If we represent the rotation frequency with Ω, then the angular momentum per unit area is $\varpi^2\Omega\Sigma$. The conservation of angular momentum considers the torques acting on the ring. Since a force is applied off center of mass a torque acts on the body and rotates it. The equation for angular momentum conservation in a thin disc, can be written as,

$$\varpi\frac{\partial}{\partial t}\left(\varpi^2\Omega\Sigma\right) + \frac{\partial}{\partial\varpi}\left(\varpi^2\Omega \times \varpi\Sigma v_\varpi\right) = \frac{1}{2\pi}\frac{\partial\tau}{\partial\varpi}. \tag{1.39}$$

On the right hand side of Eq.1.39, we can see that if the derivative of the torque along ϖ is equal to zero then angular momentum stays constant. Otherwise, there would be a differential torque along the annulus.

Shakura and Sunyaev (1976) made assumptions on viscosity to further simplify the problem at hand. The simplest assumption is that the torque comes from viscous interactions within the disk. Without describing viscosity in details yet, the torque τ can be expressed as,

$$\tau = 2\pi\varpi^3 \times \nu\Sigma\frac{\partial\Omega}{\partial\varpi}. \tag{1.40}$$

Here, ν is the turbulent dynamic viscosity. Eq.1.40 is the product of three terms. An integration term around the disk, $2\pi\varpi$ (i.e., the circumference of the annulus). The second term is the viscous force per unit length, $\nu\varpi\Sigma(d\Omega/d\varpi)$. The last term is the lever arm, ϖ. The viscosity being proportional to $d\Omega/d\varpi$ reflects the fact that a disk in solid rotation cannot produce viscous torques. Only when $d\Omega/d\varpi \neq 0$ can the disk feel viscosity. Now, by substituting the torque expression in Eq.1.39 and using the mass continuity presented in Eq.1.38, we obtain,

$$\frac{\partial\Sigma}{\partial t} = -\frac{1}{\varpi}\frac{\partial}{\partial\varpi}\left[\left(\frac{\partial}{\partial\varpi}\left(\varpi^2\Omega\right)\right)^{-1}\frac{\partial}{\partial\varpi}\left(\varpi^3\nu\Sigma\frac{d\Omega}{d\varpi}\right)\right]. \tag{1.41}$$

The purpose of these manipulations is to eliminate v_ϖ, and hence reduce sources of complexity. The evolution is described in terms ϖ, ν, and Σ. In the specific case where the disk is in Keplerian rotation, the evolution equation reduces to,

$$\frac{\partial\Sigma}{\partial t} = \frac{3}{\varpi}\frac{\partial}{\partial\varpi}\left[\varpi^{1/2}\frac{\partial}{\partial\varpi}\left(\nu\Sigma\varpi^{1/2}\right)\right]. \tag{1.42}$$

It is now clear that the temporal evolution of disk density has the form of a diffusion equation ($\partial_t f \propto \partial_x^2 f$).

1.3.1.3 Steady state disk structure

In steady-state conditions, the structure of a non-magnetized thin disk is governed by the conservation of radial and angular momentum, along with the assumption that vertically, the stellar gravity is balanced by the gas pressure gradient, resulting in hydrostatic equilibrium. To study this, we consider a disk ring at a distance ϖ from the star, with material flowing in and out of this ring with a radial velocity v_ϖ. The equation governing radial momentum conservation for a steady-state flow is then given by,

$$v_\varpi\frac{\partial v_\varpi}{\partial\varpi} - \frac{v_\phi^2}{\varpi} = -\left(\frac{1}{\rho}\frac{\partial P}{\partial\varpi} + \frac{GM}{\varpi^2}\right) \tag{1.43}$$

The terms in the above equation result from four contributions, namely, the radial mass flow, the centrifugal force, the gas pressure, and gravity. Since the pressure typically decreases when increasing radius, the first term on the right is almost always negative. This negative value indicates that gas pressure opposes the gravitational force, causing the gas to rotate at sub-Keplerian orbital velocities.

We ,now, determine the surface density in the case where accretion proceeds and is determined by,

$$\dot{M}_{acc} = -2\pi\varpi\Sigma v_{\varpi}. \tag{1.44}$$

Going back to Eq.1.39 and replacing the expression of the torque τ (Eq.1.40), we have,

$$\frac{\partial}{\partial\varpi}\left(\varpi v_{\varpi}\Sigma\varpi^2\Omega\right) = \frac{\partial}{\partial\varpi}\left(\nu\Sigma\varpi^3\frac{d\Omega}{d\varpi}\right). \tag{1.45}$$

The left hand side describes the radial change in angular momentum and the right hand side is a consequence of viscous torques. subsequently, integrating this equation results in the following expression,

$$\nu\Sigma\frac{d\Omega}{d\varpi} = \Sigma v_{\varpi}\Omega + \frac{Cst}{2\pi\varpi^3}, \tag{1.46}$$

and by evaluating at the point where $d\Omega/d\varpi$ vanishes we can determine the value of the constant. It results in the following,

$$\begin{aligned} Cst &= -2\pi\Sigma v_{\varpi}\Omega\varpi^3 \\ &= \dot{M}_{acc}\varpi^2\Omega. \end{aligned} \tag{1.47}$$

We finally have for $\Omega = \sqrt{GM/r^3}$,

$$\Sigma = \frac{\dot{M}_{acc}}{3\pi\nu}\left(1 - \sqrt{\frac{\varpi_{in}}{\varpi}}\right) \tag{1.48}$$

In the case where $\varpi_{in} << \varpi$, the equation above transforms into $\dot{M}_{acc} = 3\pi\nu\Sigma$. This underscores the central role that the viscosity ν plays in both mass distribution and the accretion mechanisms within the disk.

1.3.2 A viscous thin disk?

With the mean free path λ of particles in the disk we can determine the molecular viscosity. The frequency of interactions between molecules is,

$$\nu_m \sim \lambda c_s = \frac{1}{n\sigma}c_s, \tag{1.49}$$

n here is the particle density and σ is the cross section of particles which we approximate as being equal to $\sim 10^{-15}$ cm^2 (Stahler and Palla, 2008). If we additionally approximate $n \sim 10^{12}$ cm^{-3}, and $c_s \sim 10^4$ cm/s, we get the following order of magnitude for molecular interactions,

$$\nu_m \sim \frac{10^4}{10^{12}\times 10^{-15}} = 10^7 cm^2/s. \tag{1.50}$$

If we estimate the diffusion time scale t_ν at a radius $r = 10$ au, we get,

$$t_\nu = \frac{r^2}{\nu_m} \sim 7 \times 10^{13}\ years. \tag{1.51}$$

The typical evolutionary timescale of the disk is of the order of a few million years, so this molecular viscosity timescale is more than tens of millions of times longer than the lifetime of the disk. We can immediately rule out this type of viscosity, as the main turbulence driver in the disk. Moreover, if we look at the Reynolds number (Re) which describes the ratio of inertial forces to viscous forces, we find high values,

$$Re = vL/\nu \sim 10^{11}. \tag{1.52}$$

v and L are the characteristic velocity and length in the disk, respectively. In essence, Re defines whether a fluid is laminar or turbulent. These high values indicate a very turbulent flow, it is thus necessarily turbulence that drives angular momentum transport in the disk. We need to identify potential instabilities capable of generating turbulence that exceed the levels produced by molecular viscosity.

1.3.2.1 α-disk prescription

Shakura and Sunyaev (1973) who first introduced the α-disk prescription based on dimensional considerations, proposed that,

$$\nu = \alpha c_s h. \tag{1.53}$$

The geometry of the flow sets the largest turbulent scales, one can use the vertical scale height (h) of the gas as a representative scale. Using the same dimensional analysis, the sound speed which is the characteristic velocity of the turbulent motions, can be expressed as $c_s = (h/\varpi)v_\phi$ because the sound speed is negligible compared the orbital speed. Hence, we can write the viscosity as shown in Eq.1.53, where α sets the intensity of viscosity and is ≤ 1.

We can now express viscosity using the disk parameters to estimate the efficiency of angular momentum transport and, consequently, mass accretion onto the central star. This approach also allows us to determine the value needed of α to match the observed timescale of disk evolution. Same as in Eq.1.51, we can express the viscous timescale as,

$$t_\nu = \left(\frac{h}{\varpi}\right)^{-2} \frac{1}{\alpha\Omega}. \tag{1.54}$$

By filling in the evolution time scale as 10^9 years at 50 au, and assuming a thin disk with the ratio $h/\varpi \sim 0.1$, Eq.1.54 yields an $\alpha \sim 10^{-2}$.

Another way to reach the temporal evolution of the surface density as expressed in Eq.1.42 is using Navier-Stokes' equations (Lodato, 2008). In this method ν is associated

with a viscous stress tensor, which simplifies in vertical shear viscosity to only one non-zero term (ϖ, ϕ). Integrating the stress tensor yields,

$$T_{\varpi\phi} = \nu\varpi\Sigma\frac{d\Omega}{d\varpi}. \tag{1.55}$$

By identifying the previous equation with the α-disk prescription, we deduce a link between α and the parameters of a turbulent flow. Assuming the disk is magnetized and subject to gravity, we can express α as such,

$$\alpha = \left\langle \frac{\delta v_\varpi \delta v_\phi}{c_s^2} - \frac{B_\varpi B_\phi}{4\pi c_s^2} - \frac{g_\varpi g_\phi}{4\pi G\rho c_s^2} \right\rangle \tag{1.56}$$

The angle brackets indicate a temporal average on α. Notice that the last term is only important when studying a massive disk. In the case of class II stars, we can neglect this term. Eq.1.56 introduces hydrodynamic, magnetic, and gravitational stresses. It is a way of reframing the α parameter as an efficiency indicator of how turbulence transports angular momentum, instead of an input parameter that describes the thin disk (Lesur, 2021).

1.3.2.2 MRI driven turbulence

A disk only subject to hydrodynamical processes can go through turbulent phases. Whether the turbulence grows is another story. For that purpose we turn to Rayleigh criterion, namely, for a thermal instability to grow we need,

$$\frac{d(\varpi^2\Omega)}{d\varpi} < 0. \tag{1.57}$$

This criteria is not respected for Keplerian disks. In such disks, angular momentum increases with the disk radius, making them stable to hydrodynamical turbulence in the linear phase. Although, in the non-linear case hydrodynamical turbulence could also produce a turbulent disk with an α between $\sim 10^{-4}$ and 10^{-2} (Hersant et al., 2005).

Magnetic field lines act as springs connecting different rings within the disk. This effect increases the velocity difference between the two adjacent rings. This leads to the creation and growth of an instability called the magneto-rotational instability (MRI). A necessary condition for an accretion disk with a magnetic component to be linearly unstable is that the orbital velocity decreases with radius $d\Omega/d\varpi < 0$ (Balbus and Hawley, 1991). In this case Keplerian disks satisfy this condition, making them sensitive to MHD instabilities.

In a disk influenced by a vertical magnetic field, MRI produces solutions where vertical disk layers alternately move inward or outward. When averaged vertically, these motions do not result in net angular momentum transfer. Understanding the full complexity of MRI requires numerical simulations, which is an active area of research. Most models suggest that magnetic stresses are the primary drivers, with typical efficiencies for MRI-driven angular momentum transfer characterized by α values ranging from 10^{-3} to 10^{-2}.

1.3.3 Turbulence as the driver of viscosity

The founding work by Shakura and Sunyaev (1973) paved the way for effective viscosity models of accretion disks, where accretion results from turbulence within the disk that drives angular momentum transport radially outwards. A key discovery by Balbus and Hawley (1991) identified MRI as a mechanism capable of generating such turbulent transport. MRI induces robust magnetized turbulence from vertical or toroidal magnetic fields, driving angular momentum transport through turbulent torques. The strength of this turbulent torque is quantified by the Shakura-Sunyaev α parameter, which controls the turbulent viscosity and torque.

Accurately assessing the non-linear saturation of MRI required advancements in numerical methods. The shearing box model, developed for this purpose, isolates the essential elements of MRI—shear and magnetic fields. Using this method, Hawley et al. (1995) explored the growth and saturation of MRI in non-stratified simulations, confirming the theoretical predictions by Balbus and Hawley (1991). These studies showed that MRI produces vertical oscillatory structures, known as channel modes, which grow in amplitude over time. However, these structures are disrupted by secondary instabilities, leading to fully developed turbulence.

Hawley et al. (1995) further demonstrated that MRI-driven turbulent torque scales with the mean magnetic field strength, particularly with the magnetization level. They found MRI to be strongest with a vertical magnetic field rather than a toroidal one.

Gammie (1996) introduced the dead-zone model for protoplanetary disks, proposing that weak ionization in the outer cold regions ($\varpi > 1$ au) leads to significant Ohmic resistivity, quenching MRI and confining accretion to the disk surface, where stellar radiation ionizes the gas. Subsequent studies (Wardle, 1999; Kunz and Balbus, 2004; Mattia and Fendt, 2022) and numerical experiments (Bai and Stone, 2011) confirmed that non-ideal MHD effects stabilize MRI in the outer disk regions, restricting MRI-driven turbulence to the inner regions ($\varpi < 1$ au).

In the presence of a net vertical magnetic flux, the magnetic field growth eventually saturates, halting the MRI (Murphy and Pessah, 2015; Hirai et al., 2018). These saturated MRI conditions are found in both the inner and outer regions of accretion disks (Parkin, 2014; Suzuki and Inutsuka, 2014; Zhu and Stone, 2018). Fully saturated MRI turbulence results in an angular momentum transport coefficient α ranging from 0.01 to 1, depending on the initial magnetic field strength and topology. For instance, Salvesen et al. (2016) found $\alpha \sim 11\beta^{-0.53}$ for $10 < \beta < 10^5$ in stratified shearing box simulations threaded by a vertical field, suggesting α is roughly proportional to B_p.

While this result holds in "ideal" MHD, the magnetic Prandtl number $\mathcal{P}_m$, which is the ratio of viscous to magnetic diffusion rates, is expected to be very small in disks, even in regions where ideal MHD applies. This small $\mathcal{P}_m$ regime was investigated using non-stratified high-resolution simulations, achieving convergence for the first time (Meheut et al., 2015) with a value of $\alpha \sim 10^{-2}$ and $\beta \sim 10^3$. However, this value of β is relatively small for standard disks (Thi et al., 2019). Indeed, MRI simulations in the low Prandtl number limit show turbulent decay (Mamatsashvili et al., 2020) and do not sustain

turbulence. It should be kept in mind that these studies take interest for disks far from the star. The magnetic Prandtl number within disks in the vicinity of the star is high enough to not present with turbulent decay. As mentioned before values of α between 10^{-3} and 10^{-2} are for when MRI is driven by a toroidal field configuration. For large scale vertical field, the max value of α can reach unity. Lesur et al. (2013) specifically demonstrate that large-scale MRI modes, which dominate strongly magnetized discs ($\beta \sim 10$), inherently generate magnetically driven outflows.

To explain accretion in the outer regions of protoplanetary disks, theoreticians revisited the work of Blandford and Payne (1982) and integrated the disk wind component into shearing box simulations. Initial unstratified simulations with vertical magnetic fields could not sustain winds due to high magnetic pressures disrupting the disk structure, see Stone et al. (1996). However, stable ideal-MHD shearing box simulations of vertically stratified disks with vertical magnetic fields were eventually achieved by Suzuki and Inutsuka (2009), thanks to robust numerical techniques and carefully designed boundary conditions.

These simulations enabled the computation of outflows from MRI-active accretion disks. Subsequent studies (e.g.,Fromang et al. 2013; Lesur et al. 2013; Pantolmos et al. 2020; Jacquemin-Ide et al. 2021) examined both highly and weakly magnetized disks launching magnetized outflows, revealing structures similar to Ferreira (1997) solutions, where laminar magneto-centrifugal winds are launched from turbulent accretion disks. Moreover, Jacquemin-Ide et al. (2021) highlighted using 3D global simulations the importance of the turbulent magnetic pressure in accretion disks.

Chapter 2

Introduction to MagnetoHydroDynamics, equations, waves and numerical tools

Contents

2.1 Validity of the MHD approximation 46
2.1.1 Characteristic lengths and interaction time 46
2.1.2 Plasma approximation 51
2.2 MHD equations 53
2.2.1 Mass conservation 54
2.2.2 Momentum conservation 55
2.2.3 Fluid equations 56
2.2.4 Magnetic effect 56
2.2.5 Energy equation 58
2.3 MHD waves 59
2.3.1 MHD waves, linear analysis of MHD equations 59
2.3.2 Characteristic velocities 60
2.4 Discontinuities 62
2.4.1 Recollimation 62
2.4.2 Recollimation shocks 63
2.5 A brief introduction to the PLUTO code 64
2.5.1 Finite volume method 65
2.5.2 Riemann problem 66

2.5.3 Riemann solvers 66
2.5.4 Divergence-free condition 68
2.5.5 Limiters 70
2.5.6 Heating/cooling module 71

2.1 Validity of the MHD approximation

MHD offers a large-scale description of partially or fully ionized gases. For these plasmas to be described macroscopically, the characteristic lengths of the plasma—specifically, the characteristic lengths of the magnetic and electric fields—must be significantly greater than the lengths associated with microscopic phenomena. The mean free path of a particle must be very short relative to the characteristic variation of the electromagnetic field. The lengths that describe microscopic processes vary depending on the types of plasma found throughout the Universe.

MHD as an approach is non-linear since outflows impact magnetic fields, which in turn modify the outflows through non-linear equations. This approach enables - through a set of simplifying hypotheses - a reliable description of astrophysical jets. We will start this chapter by introducing the characteristic scales

2.1.1 Characteristic lengths and interaction time

2.1.1.1 Quasi-neutrality hypothesis

Essentially, theories describing the evolution of plasmas all rely on the important notion of quasi-neutrality. In a plasma, matter is composed of negatively and positively charged components. This makes the fluid present as electrically neutral at a macroscopic scale. The neutrality is an average behavior seen at large scales. Consequently, unlike for neutral gases where interaction are binary and forces have a short range, plasmas feel the Coulomb force which is theoretically infinite as it decreases with $1/r^2$, where r is the distance between charges. Every charge in the fluid interacts simultaneously with a number of its neighbors. This collective behavior of charges is an essential characteristic of plasmas.

We can show the importance of the electrostatic force in shaping the plasma by estimating its effect on a charged lightweight particle. A deviation from neutrality in a sphere with volume V leads to a potential of the form (in CGS units),

$$\Phi(r) = \frac{(q_e N_e + q_i N_i)V}{r}, \tag{2.1}$$

q and N are the charge and density of electrons and ions, respectively. We assume the densities of each species uniform in the sphere, and that ions are still and only electrons move - an assumption warranted by the fact that ions are much heavier than electrons.

This potential is associated with an electric filed E, thus a force, which will apply to an electron of charge $q = -e$. The acceleration that ensue is as follows,

$$a = \frac{1}{m} f(r) = -\frac{e}{m}\frac{\Phi(r)}{r} = -\frac{e}{m}\frac{(q_e N_e + q_i N_i)V}{r^2}. \tag{2.2}$$

If we let the populations of electrons and ions deviate from neutrality by a factor of 1/100 (i.e. $|N_i - N_e|/N_e = 1/100$) in a sphere of 1 cm with a density of 10^{11} cm^{-3} results in an acceleration of $a \sim 1 \times 10^{27}$ cm/s^2. This acceleration is very high, consequently, correction for quasi-neutrality deviation is almost instantaneously addressed by electrons. This shows the natural tendency of plasmas to stay neutral.

2.1.1.2 Debye length

Negative charges are attracted to positive ones, and vice versa. This natural tendency means that, statistically, any charge will surround itself with a surplus of charge of the opposite sign, forming what is known as the Debye cloud. Every electron in the cloud surrounding an ion enters and leaves this cloud in a very short amount of time. In fact, this process is both dynamical and statistical, and represents a balance between two antagonistic tendencies, the Coulomb force, which tends to bring the electrons closer to the central ion, and thermal agitation, which tends to smooth out all accumulations of charge. Thus, this incessant motion of charges limits the range of the electrostatic interaction generated by a given particle. To estimate the range of the electrostatic potential of a particle, we will first estimate the spatial distribution of particles of each species around the considered particle.

Considering a chemical species α with a charge q_α and an electrostatic potential $\Phi(r)$, its potential energy would be $q_\alpha \Phi$. Plasma particles follow a Maxwell-Boltzmann statistical distribution, thus, density of the specie n_α around a particle is,

$$n_\alpha(r) = n_{\alpha,0} \exp\left(-\frac{q_\alpha \Phi(r)}{k_B T}\right). \tag{2.3}$$

$n_{\alpha,0}$ is the density of species α at infinity, where $\Phi(r) \to 0$. Depending on the sign of the charge, the population will either grow or diminish. For the plasma to stay ionized, the thermal energy has to be much larger than the potential electrostatic energy, $|q_a \Phi(r)| \ll k_B T$. Otherwise, the electrons would be recaptured. This allows to simplify the expression of $n_\alpha(r)$,

$$n_\alpha(r) \simeq \sum_\alpha n_{\alpha,0}\left(1 - \frac{q_\alpha \Phi(r)}{k_B T}\right). \tag{2.4}$$

The total charge density of the plasma can be expressed as, $\rho = \sum_\alpha n_\alpha q_\alpha$. Subsequently, the electrostatic potential is given by Poisson's equation,

$$\Delta\Phi(r) + 4\pi\left[\rho(r) + q\delta(r)\right] = 0. \tag{2.5}$$

Here q is the charge of the particle at $r = 0$ with a Dirac delta function as its density distribution. Going back to Eq.2.4, we can neglect the first term $\sum_\alpha q_\alpha n_{\alpha,0} = 0$ because the plasma is globally electrically neutral. Eq.2.5, then becomes,

$$\Delta\Phi(r) - 4\pi\left[\sum_a \frac{n_{a0}q_a^2\Phi(r)}{k_BT} + q\delta(r)\right] = 0 \tag{2.6}$$

We define the Debye length λ_D as the characteristic length of interaction,

$$\lambda_D^2 = \frac{1}{4\pi}\sum_a \frac{k_BT}{n_{a0}q_a^2} = \sum_a \lambda_{D,a}^2. \tag{2.7}$$

To solve Eq.2.6 which is a differential equation, we apply a Fourier transform. We can easily show that $\Delta\hat{\Phi}(\mathbf{k}) = -k^2\hat{\Phi}(\mathbf{k})$ by crossing to the phase space,

$$\hat{\Phi}(\mathbf{k}) = \iiint \Phi(\mathbf{r})e^{-i\mathbf{k}\cdot\mathbf{r}}\, d^3r. \tag{2.8}$$

We then have the following in the Fourier space,

$$\hat{\Phi}(\mathbf{k}) = 4\pi q\frac{\lambda_D^2}{1 + k^2\lambda_D^2} \tag{2.9}$$

To finally obtain the potential energy, we need to apply the inverse Fourier transform, which is,

$$\Phi(\mathbf{r}) = \frac{1}{(2\pi)^3}\iiint \hat{\Phi}(\mathbf{k})e^{i\mathbf{k}\cdot\mathbf{r}}\, d^3k. \tag{2.10}$$

The equation above simplifies greatly by choosing the spherical coordinates. In this system of coordinates we can orient the sphere so that $\theta = 0$ and $\mathbf{k}\cdot\mathbf{r} = k_r r\cos\theta$. This cancels the dependence on ϕ and trivially bears a factor of 2π. The integral is then,

$$\begin{aligned}\Phi(r) &= \frac{1}{(2\pi)^2}\int_0^\infty \frac{4\pi q\lambda_D^2}{ir}\left[\frac{k_r e^{ik_r r\cos\theta}}{1 + k^2\lambda_D^2}\right]_0^\pi dk_r \\ &= \frac{1}{4\pi^2}\int_0^\infty \frac{4\pi q\lambda_D^2}{ir}\frac{k_r sin(k_r r)}{1 + k^2\lambda_D^2}dk_r \\ &= \frac{1}{4\pi^2}\int_{-\infty}^\infty \hat{\Phi}(\mathbf{k})\frac{k_r e^{ik_r r}}{r}dk_r\end{aligned} \tag{2.11}$$

We get Eq.2.11 since the integrand is an even function. This equation presents a singularity on the imaginary axis when $k = i/\lambda_D$, thus we can use the residue theorem,

$$\int_{-\infty}^\infty \hat{\Phi}(\mathbf{k})\frac{k_r e^{ik_r r}}{r}dk_r = 2i\pi\text{Res}\left(\frac{\hat{\Phi}(k)k_r e^{ikr}}{r}, \frac{i}{\lambda_D}\right) \tag{2.12}$$

By definition the residue theorem says that we can substitute computing the integral by determination of a limit,

$$\text{Res}\left(\frac{\hat{\Phi}(k)k_r e^{ikr}}{r}, \frac{i}{\lambda_D}\right) = \lim_{k_r \to i/\lambda_D}\left\{\frac{-iq\lambda_D k_r e^{ikr} r}{\pi r(1-ik_r\lambda_D)}\right\}. \tag{2.13}$$

We finally substitute for the values we found and obtain the expression of the electrostatic energy potential generated by a particle,

$$\Phi(r) = \frac{q}{r} exp\left(-\frac{r}{\lambda_D}\right). \tag{2.14}$$

This electrostatic potential shows a modification when compared to the potential of the same particle isolated in a vacuum. An exponential decay factor appears due to the presence of plasma electric charges of opposite sign in the immediate vicinity of the particle under consideration. This means that the range of electrostatic influence of a charged particle in plasma is spatially limited to a length equivalent to the Debye length. Typically, in natural plasmas the Debye length can take values from 10^{-11} m in the Solar core to 10^2 m in the Earth magnetosphere. This length varies with density and temperature as can be explicitly seen in Eq.2.7. We show in Fig.2.1 the Debye length of plasma used to simulate the jets and accretion disks in this thesis.

2.1.1.3 Plasma frequency

Under the effect of an external perturbation (electromagnetic field, wave, shock, etc.), the electrons are locally set in motion, creating a deviation from the stationary value of the density, which we denote as δn_e. This displacement of electrons then generates an electric field that satisfies the Maxwell-Gauss equation $\nabla \cdot \delta\mathbf{E} = -4\pi e\delta n_e$. The continuity equation for electric charges indicates that,

$$-e\frac{\partial \delta n_e}{\partial t} + \nabla \cdot (\delta\mathbf{J}) = 0 \tag{2.15}$$

The induced current by the electron displacement is $\delta\mathbf{J} = -n_e e\delta\mathbf{v_e}$, with $\mathbf{v_e}$ the group velocity of the electrons after being perturbed. Newton's equation of motion enables to link what we have presented so far,

$$\frac{\partial \delta\mathbf{v}_e}{\partial t} = -\frac{e}{m_e}\delta\mathbf{E} \tag{2.16}$$

Here, an important assumption should be noted, we neglect the contribution of electronic pressure forces that could add to the balance. It should be kept in mind that this expression is only valid for cold, non-correlated plasmas. The derivative of Eq.2.15 with respect to time gives,

$$-e\frac{\partial^2 \delta n_e}{\partial t^2} + \nabla \cdot \left(n_e \frac{e^2}{m_e}\delta\mathbf{E}\right) = 0 \tag{2.17}$$

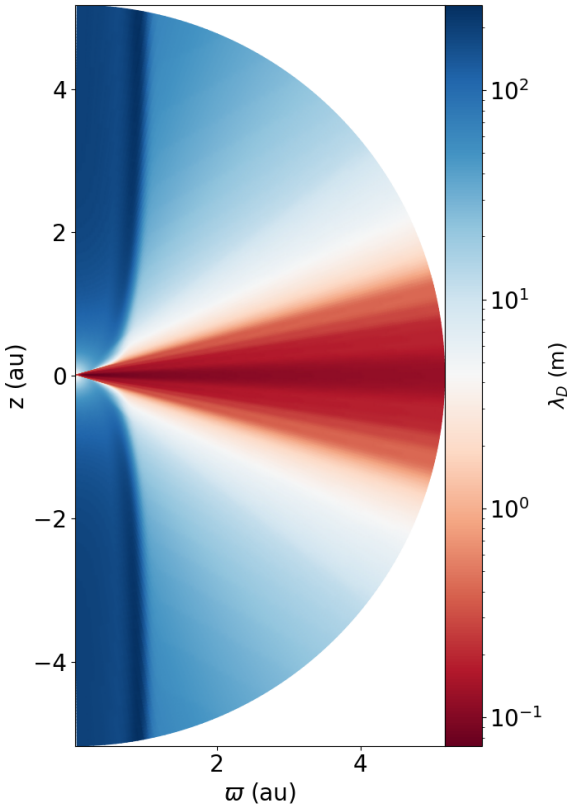

Figure 2.1: Plot of the Debye length of the plasma we use to initialize jet and disk simulations in chapter 5.

To linearize this expression, we assume that the electronic displacement is of low amplitude, which does not disturb the electron density beyond a minor perturbation. This corresponds to a displacement of the electrons over a distance much smaller than the wavelength of the created electric field. If this condition is fulfilled, then it follows that,

$$\frac{\partial^2 \delta n_e}{\partial t^2} + \left(\frac{n_e e^2}{\varepsilon_0 m_e} \right) \delta n_e = 0 \tag{2.18}$$

This equation is similar to a harmonic oscillator with characteristic oscillation that is defined as,

$$\omega_{pe}^2 = \frac{4\pi n_e e^2}{m_e} \tag{2.19}$$

This pulsation characterizes the oscillatory motions of the electrons at the plasma frequency. These oscillations arise from the fact that following a slight collective displacement of the electrons, they experience a restoring force from the ions that tends to bring them back to an equilibrium position, similar to a harmonic oscillator. From the point of view of an electron crossing the Debye sphere of a proton, this plasma frequency is

directly related to the transit time of the sphere,

$$\tau_e^2 = \frac{\lambda_D^2}{v_e^2} = \frac{k_B T}{4\pi n_e e^2 v_e^2} \sim \frac{1}{\omega_{pe}^2}. \tag{2.20}$$

v_e, here, is the electron thermal speed. The individual motion of electrons is dominated by thermal effects, which, if no other phenomena were present, would render the electronic distribution isotropic with electrons having ballistic trajectories in all directions. The electrostatic attraction of ions on electrons maintains small statistical density fluctuations by creating these oscillations. Electrons experience, along their trajectory, these ion-induced electric fields that successively slow them down and accelerate them, giving rise to this collective oscillatory motion. However, it is important to keep in mind that we have assumed that we could neglect the thermal pressure of the plasma in the description of the oscillations. This assumption is quite restrictive as it corresponds to a plasma with electron temperature approaching zero, which is hardly compatible with a non-correlated plasma.

2.1.2 Plasma approximation

A number of hypotheses hide beneath the use of the plasma approximation. They define necessary criteria for plasma to exist. There are mainly four approximations to make.

Debye length - A necessary and obvious condition is that the dimensions of the system under study must be much larger compared to the Debye length. Otherwise, there is not enough space for collective - statistical - effects to exist, and the set of particles does not constitute a plasma. If we assume that the dimension of the system is L, then we must have the relation,

$$L >> \lambda_D. \tag{2.21}$$

Screening - It is a statistical phenomena where a large number of particles needs to be inside the Debye sphere. This condition writes,

$$n_e V = n_e \lambda_D^3 >> 1. \tag{2.22}$$

This relation allows the use of a quasi-fluid model to describe the plasma and demonstrates that the Debye length is much larger than the average distance between two particles. In this case we can show that the thermal energy is negligible compared to the interaction energy. This inequality means from a thermodynamic point of view that the plasma approaches a perfect gas. We can therefore use the classical ideal gas law, $p = nk_B T$, to define the internal pressure of the plasma. In some cases, electrons and ions are separately in equilibrium with $T_e \neq T_i$, such that this formula applies for each species of particles using the partial pressures p_e and p_i.

Neutrality - Electron and ion densities need to be equal in proportion as was outlined in Sec.2.1.1.1. In a way, this criterion logically results from the first one ($L >> \lambda_D$). If the system is much larger than the Debye's length, then necessarily quasi-neutrality must be ensured at least on large scales.

Collisions with neutrals - The plasma frequency ω_{pe} was determined by completely neglecting the influence of neutrals. It is clear that collisions of electrons with this population can only disturb, or even destroy, any collective electron oscillation. For these oscillations to exist, it is necessary that the electron-neutral collision frequency, denoted by ν_c, be lower than the plasma frequency. The average time between two electron-neutral collisions must be much greater than all characteristic time scales of plasma parameter variations. Otherwise, the electrons will be forced to follow the dynamics of the neutrals, and the plasma should instead be considered as a neutral gas.

2.1.2.1 Jet plasma

Let us consider temperatures and densities in the case of YSO jets. In terms of temperatures we will choose $T = 10^4$ K (Bally et al., 2007), and a density of $n = 10^3$ cm^{-3} values typically observed in jets. If the plasma is fully ionized, then the density gives a good estimate of electron density. If, on the other hand, the plasma is in a poor ionization state, then the observed densities are representative of the neutral population. By considering a fully ionized plasma, we estimate $n = n_e = 10^3$ cm^{-3} and $T = T_e = 10^4$ K. This yields to the following,

$$\frac{\lambda_D}{\varpi_j} \sim 10^{-13}, \quad \frac{\lambda_D^{-3}}{n_e} \sim 10^{-12}. \tag{2.23}$$

Here ϖ_j is the radius of the jet, with a typical value of ~ 10 au asymptotically.

2.1.2.2 Disk plasma

Same as the jet, for the disk to be in the fluid approximation collisions between electrons and ions must be frequent enough. The added difficulty in the disk is the ionization of the structure. Determining the ionization fraction in disks is complex. In the inner regions of these disks, thermal ionization of alkali metals is the primary source (Armitage, 2011), therefore the metallicity of the gas needs to be well constrained. In the outer regions of the disk, other sources are at play such as the stellar X-ray emission, the cosmic rays and/or the turbulent heating (Lesur, 2021). Because of the low ionization degree in the outer regions, non-ideal effects are to be considered, like, Hall effect, ambipolar diffusion, and Ohmic resistivity (Gammie, 1996).

Concerning the non-ideal diffusivities at play, we can use a simplified case to better understand where each effect is most dominant. In this simplified case, only two charged particle species are considered, namely, ions and electrons. Whether it is ohmic diffusion, Hall diffusion, or ambipolar diffusion, they all have an associated magnetic

diffusivity term. We start our analysis from their expressions as expressed in Lesur (2021),

$$\begin{aligned}\eta_O &= \frac{cB}{4\pi e n^+}\frac{1}{\mu_h^e - \mu_h^i},\\ \eta_H &= \frac{cB}{4\pi e n^+}\frac{\mu_h^e + \mu_h^i}{\mu_h^i - \mu_h^e},\\ \eta_A &= \frac{cB}{4\pi e n^+}\frac{\mu_h^i \mu_h^e}{\mu_h^i - \mu_h^e}.\end{aligned} \tag{2.24}$$

Here n^+ is the ionization fraction. μ_h^e and μ_h^i represent the Hall parameter for electrons and ions, respectively (Wardle and Ng, 1999),

$$\mu_h^{ei} \equiv \frac{q^{ei} B}{\gamma^{ei} \rho m^{ei} c} \tag{2.25}$$

In simple terms, this parameter represents the ratio between gyrofrequency of a species to the species-neutral collision frequency. We notice that all diffusive terms are inversely proportional to the ionization fraction, n^+. Hence, in the limit of ideal-MHD these terms vanish and the magnetic field is in frozen-in conditions. Except for Ohmic diffusion, both Hall and ambipolar effects depend on the magnetic field ($\eta_H \propto B$ and $\eta_A \propto B^2$). It is important to note that in the case where the species have the same masses, the Hall effect does not contribute as it vanishes.

In the case where charge carriers are composed of electrons and ions, we have $|\mu_h^e| >> |\mu_h^i|$ (Lesur, 2021). It entails that $\eta_O \propto |\mu_h^e|^{-1}$ and $\eta_A \propto |\mu_h^i|$. It follows that Ohmic effects are due to electron-neutral while ambipolar diffusion is on the contrary a result from ion-neutral collisions. We can distinguish between three cases. First, Ohmic diffusion dominates where $|\mu_h^i| < |\mu_h^e| < 1$. If $|\mu_h^i|$ is below unity while $|\mu_h^e|$ is above, the Hall effect dominates. Last, where $1 < |\mu_h^i| < |\mu_h^e|$ the system is predominantly ambipolar. From this, we can clearly draw a picture of what process is preponderant given the density of the neutral species and the intensity of the magnetic field.

2.2 MHD equations

The MHD equations are obtained by integrating the kinetic equations that rule the evolution of charged particles over the collisional invariants, mass, momentum and energy. We start establishing the link between the microscopic Boltzmann equations and the macroscopic fluid equations.

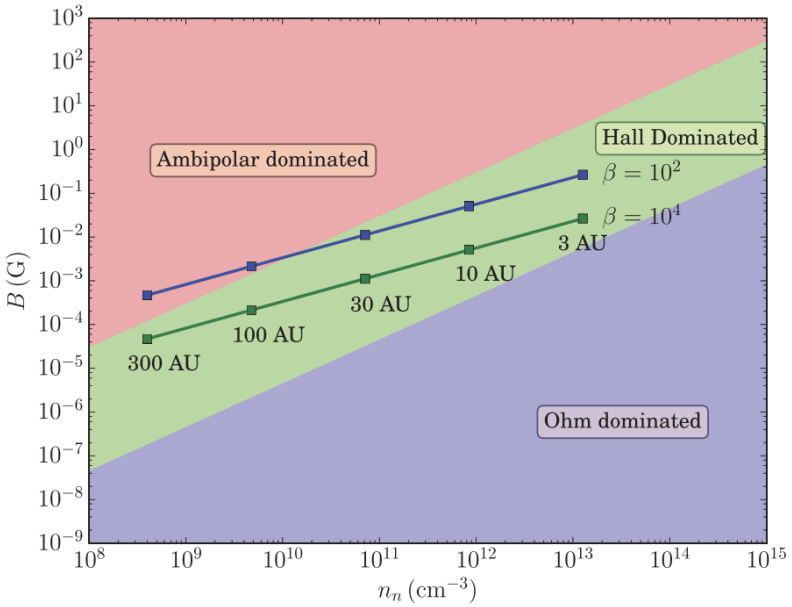

Figure 2.2: Plot of the non-ideal regimes as a function of the neutral density and the magnetic field strength, computed for a plasma under the assumption that $T < 100$ K. The blue and green lines show the typical values of β_p at the disk midplane. Lesur (2021).

2.2.1 Mass conservation

For a species α the key variables are the distribution functions f_α, which evolve following Boltzman equation,

$$\frac{df_\alpha}{dt} = \frac{\partial f_\alpha}{\partial t} + \mathbf{V}_\alpha \cdot \nabla_{\mathbf{x}} f_\alpha + \frac{\mathbf{F}}{m_\alpha} \cdot \nabla_{\mathbf{V}} f_\alpha = \sum_\beta \mathcal{C}_{\alpha\beta}, \tag{2.26}$$

with $\mathbf{V}$ and $\mathbf{x}$ the variables in the phase space. They represent the velocity and position of a particle, respectively. Here, $\mathbf{F}$ is the force applied to a particle α, $\mathbf{F} = q_\alpha(\mathbf{E} + \mathbf{V}_\alpha \times \mathbf{B}/c) - m_\alpha \nabla \Phi_{grav}$. The collision operator takes into account collisions with other species. It must follow conservation of particle numbers which implies,

$$\begin{aligned} \sum_\beta \int \mathcal{C}_{\alpha\beta}\ d^3\mathbf{V}_\alpha = 0, \\ \sum_\beta \int \mathbf{V}_\alpha\ \mathcal{C}_{\alpha\beta}\ d^3\mathbf{V}_\alpha = 0. \end{aligned} \tag{2.27}$$

From the zeroth-order moment of Eq.2.26 and Eq.2.27 we have,

$$\frac{\partial n_\alpha}{\partial t} + \nabla \cdot (n_\alpha \mathbf{v}_\alpha) = 0. \tag{2.28}$$

In contrast to $\mathbf{V}_\alpha$, which is the velocity of a particle α, $\mathbf{v}_\alpha$ is the macroscopic velocity. In this equation we used the following,

$$n_\alpha \mathbf{v}_\alpha = \int \mathbf{V}_\alpha f_\alpha d^3\mathbf{V}_\alpha. \tag{2.29}$$

We find the classical conservation laws where the temporal variation of a quantity is expressed by the divergence of a flux. It should be noted that the mass conservation equation is very easily obtained thanks to the relationship between the density n_α and the mass density $\rho_\alpha = n_\alpha m_\alpha$.

2.2.2 Momentum conservation

Using the first-order moment, we can integrate Boltzmann equation (Eq.2.26) in order to get,

$$m_\alpha \int \mathbf{V}_\alpha \frac{df_\alpha}{dt} d^3\mathbf{V}_\alpha = \int \mathbf{V}_\alpha \mathcal{C}_{\alpha\beta} d^3\mathbf{V}_\alpha = \Pi_\alpha. \tag{2.30}$$

$$\begin{aligned}\Pi_\alpha = m_\alpha \frac{\partial n_\alpha \mathbf{v}_\alpha}{\partial t} + m_\alpha \nabla \cdot \int f_\alpha [(\mathbf{V}_\alpha - \mathbf{v})(\mathbf{V}_\alpha - \mathbf{v}) + \mathbf{V}_\alpha \mathbf{v} - \mathbf{v}\mathbf{v}] d^3\mathbf{v}_\alpha \\ + \int \mathbf{v}_\alpha \mathbf{F} \frac{\partial f_\alpha}{\partial \mathbf{v}_\alpha} d^3\mathbf{v}_\alpha\end{aligned} \tag{2.31}$$

Rearranging the above equation we have,

$$\frac{\partial(\rho_\alpha \mathbf{V}_\alpha)}{\partial t} + \nabla \cdot \overline{\overline{P}}_\alpha + \rho_\alpha \nabla \cdot (\mathbf{V}_\alpha \mathbf{v} + \mathbf{v}\mathbf{V}_\alpha - \mathbf{v}\mathbf{v}) - n_\alpha q_\alpha (\mathbf{E} + \mathbf{V}_\alpha \times \mathbf{B}/c) + \rho_\alpha \nabla \Phi_G = \mathbf{\Pi}_\alpha \tag{2.32}$$

$\mathbf{v}$ is the bulk macroscopic velocity of the fluid, $\mathbf{v} = \sum \rho_\alpha \mathbf{v}_\alpha / \sum n_\alpha m_\alpha$. $\overline{\overline{P}}_\alpha$ is the total pressure tensor that contains the thermal pressure, on the diagonal, and the viscous stress effects on the non diagonal elements. It is defined as,

$$\overline{\overline{P}}_\alpha = \int m_\alpha f_\alpha (\mathbf{V}_\alpha - \mathbf{v})(\mathbf{V}_\alpha - \mathbf{v}) d^3\mathbf{V}_\alpha. \tag{2.33}$$

As can be seen, the momentum equation depends on the collision rate between species. Determining the collision rate is not an easy task, to overcome this difficulty we adopt a one fluid description of all species with the mean fluid representing the barycentric mean of all species. A very interesting property of this equation is that it is valid no matter the pressure profile. We use this property to study jet ejection and collimation in chapter 4. The pressure is not necessarily restricted to the kinetic term but may include other components such as non-thermal effects. Although we retrieve an effective temperature out of simulations it provides an appealing freedom in studying non-thermal sources of ionization. Indeed, as we will see later in chapters 3 and 4 ionization can stem from non-thermal particles which contribute to heating plasma. Nonetheless, the pressure added by such processes do not linearly add to the plasma pressure. In other terms, the total temperature retrieved from the simulations is overall an upper limit to the true gas temperature. However, it is only noticeable in very low density regions.

2.2.3 Fluid equations

By summing over all the species present in the plasma we can retrieve the mean fluid behavior. Since electrons are less massive than ions, in practice, we are describing a fluid with a density that is set by the ion population, mainly the protons,

$$n \equiv n_i \sim n_e \quad , \quad \rho = n_i m_i + n_e m_e = n(m_i + m_e) \sim n_i m_i. \tag{2.34}$$

As for the velocity, ions describe the bulk velocity. Let us introduce the mean quantities of the fluid in a generic form,

$$\begin{aligned} \rho &= \sum_\alpha n_\alpha m_\alpha, \\ \mathbf{v} &= \frac{\sum_\alpha \rho_\alpha \mathbf{v}_\alpha}{\rho}, \\ \overline{\overline{P}} &= \sum_\alpha \overline{\overline{P}}_\alpha, \\ \mathbf{J} &= \sum_\alpha n_\alpha q_\alpha \mathbf{v}_\alpha, \end{aligned} \tag{2.35}$$

This immediately transforms mass and momentum conservation as follows,

$$\frac{\partial \rho}{\partial t} + \nabla \cdot (\rho \mathbf{v}) = 0, \tag{2.36}$$

$$\frac{\partial \rho \mathbf{v}}{\partial t} + \nabla \cdot \overline{\overline{P}} + \nabla \cdot (\rho \mathbf{v}\mathbf{v}) = \frac{1}{c}\mathbf{J} \times \mathbf{B} - \rho \nabla \Phi_{grav}. \tag{2.37}$$

To go back to the familiar Navier-Stokes equation, we can rewrite the third term on the left-hand side of Eq.2.37, $\nabla \cdot (\rho \mathbf{v}\mathbf{v}) = \nabla \cdot (\rho \mathbf{v})\mathbf{v} + \rho(\mathbf{v} \cdot \nabla)\mathbf{v}$. By injecting this expression in Eq.2.37, we obtain,

$$\rho \left(\frac{\partial \mathbf{v}}{\partial t} + \mathbf{v} \cdot \nabla \mathbf{v} \right) = -\nabla \cdot \mathbf{P} + \frac{1}{c}\mathbf{J} \times \mathbf{B} - \rho \nabla \Phi_{grav} \tag{2.38}$$

The fluid in a Keplerian disk exhibits differential rotation around the central object. The velocity difference between two adjacent rings in the disk causes viscous friction, which slows down the inner ring while accelerating the outer ring. This interaction results in a radial transfer of angular momentum and the generation of heat. Given that the trajectory of matter in a thin or even moderately thick disk is primarily circular, the most significant viscous stresses are those that work to slow down this rotational motion.

2.2.4 Magnetic effect

To the hydrodynamical equations presented previously we need to add the magnetic contribution. Given that they impact charged particles, the plasma needs to be sufficiently ionized. The main challenge arises from the interplay between the plasma motions governed by the magnetic field and the magnetic field itself, which also depends

on the plasma movements. Ohm's law is the relation that links the electromagnetic field to the current flowing through the fluid. It is an important step to determine the temporal evolution of the electric field. To establish this relation, let us examine the equation describing the dynamics of electrons. In this equation, we can neglect the inertial terms due to the low mass of electrons compared to that of ions,

$$0 = -\nabla P_e - n_e e(\mathbf{E} + \frac{1}{c}\mathbf{v}_e \times \mathbf{B}) - n_e m_e \nu_{ei}(\mathbf{v}_e - \mathbf{v}_i). \tag{2.39}$$

We take into account a mean linearized approximation with a collision frequency averaged on the distribution function for describing electron-ion collisions, represented by the last term of Eq.2.39, where ν_{ei} is the collision rate. Using the definition of current, $\mathbf{J} = n_e m_e(\mathbf{v_e} - \mathbf{v_i})$, we can rewrite this equation as follows,

$$\mathbf{E} + \frac{1}{c}\mathbf{v} \times \mathbf{B} = -\frac{\nabla P_e}{n_e e} + \frac{1}{\sigma}\mathbf{J} - \frac{1}{c}\frac{\mathbf{J} \times \mathbf{B}}{n_e e}. \tag{2.40}$$

To determine if one of these terms is dominant compared to the others, we use MHD ordering. This ordering is based on the hierarchy of characteristic lengths and velocities. First, we denote l_0 as the characteristic length of magnetic field variation. The current is then defined as $J \sim cB/l_0$. The wavelength of perturbations generated by ion oscillations is defined as $r_0 = v_A/\omega_{ei}$. To satisfy the MHD ordering, this length must satisfy $l_0 >> r_0$, where the characteristic velocity of this medium is the Alfvén velocity v_A. Both the pressure generated by the current, represented by the first term of the right-hand side, and the last term which describes the Hall effect are negligible since they both verify r_0/l_0. Finally we get the generalized Ohm's law,

$$\mathbf{E} + \frac{1}{c}\mathbf{v} \times \mathbf{B} = \frac{\mathbf{J}}{\sigma}. \tag{2.41}$$

with $c^2/(4\pi\sigma) = \eta_m$ the turbulent magnetic resistivity of the medium. In the case of highly conducting plasma, $\mathbf{E} = -\mathbf{v} \times \mathbf{B}/c$. By combining Eq.2.41 with Maxwell's equations we retrieve the induction equation,

$$\frac{\partial \mathbf{B}}{\partial t} = \nabla \times (\mathbf{v} \times \mathbf{B}) - \eta_m \nabla \times (\nabla \times \mathbf{B}). \tag{2.42}$$

In the case of ideal-MHD $\eta_m \to 0$, subsequently, only the first term on the right-hand side would persist. We now have a continuity equation, a momentum equation and an induction equation for magnetic fields. In the last equation, turbulence made its appearance at the level of magnetic diffusion, while in the momentum equation turbulence lies in the viscous stress tensor. This phenomenon is in fact involved in all transport coefficients. These coefficients could be computed by integrating second-order moment Boltzmann equation. However, with this approach we need to know the collision operator which is not the case.

2.2.5 Energy equation

To close the system composed of Eq.2.36,2.38,2.42 an additional equation needs to be considered. One can either use the polytropic Equation of State (EoS) assumption, namely,

$$\frac{dP\rho^{-\gamma}}{dt} = 0, \tag{2.43}$$

where γ is the ratio of the specific heats which in such case gives the adiabatic EoS ($\gamma = 5/3$). If we choose $\gamma \sim 1$ we would be in the isothermal case. We can also use the energy equation. The conservation of energy can be expressed in many forms. We start from the exact energy equation that uses entropy, and then retrieve an explicit formulation in terms of density, pressure, and velocity,

$$\rho T \frac{ds}{dt} = \Gamma - \Lambda. \tag{2.44}$$

Here, s is the specific entropy. Γ and Λ are the heating and cooling sources, respectively. We can rewrite the left hand side of Eq.2.44 with the help of the first law of thermodynamics,

$$du = Tds - Pd(\frac{1}{\rho}), \tag{2.45}$$

u is the internal energy, and since we take the equation of state of an ideal gas, we can write u as,

$$u = \frac{P}{(\gamma - 1)\rho}, \tag{2.46}$$

which, if coupled with Eq.2.45, gives,

$$Tds = \frac{1}{\gamma - 1}\left(dP - \gamma\frac{P}{\rho}d\rho\right). \tag{2.47}$$

Finally using the total derivative, $d/dt \equiv \partial_t + \mathbf{v}\cdot\nabla$, we get,

$$\frac{\partial P}{\partial t} + v\cdot\nabla P + \gamma P\nabla\cdot\mathbf{v} = \Gamma - \Lambda. \tag{2.48}$$

Heating processes depend on the considered medium. In jets, where plasma can be described by ideal-MHD, heating due to viscosity does not contribute while external ionization sources dominate the heating profile. In the disk, on the other hand, turbulent viscosity and turbulent resistivity are far from negligible. Inelastic collisions between particles can be expressed as (Landau and Lifschitz, 1989),

$$\Gamma_v = \rho\nu_v(r\nabla\Omega)^2 \tag{2.49}$$

where ν_v is the macroscopic viscosity transport coefficient. Resistivity is also at play and intervenes as energy dissipation by Joule effect. The physical interpretation of this resistivity is that the electric field induces motions of the charged fluid, which encounter

resistance due to friction between the fluid particles. These frictions generate heat. The analytical form of this heating is,

$$\Gamma_{ohm} = {}^t\mathbf{J}\overline{\overline{\eta}}_m\mathbf{J} \tag{2.50}$$

The cooling process, Λ, is primarily driven by radiative losses. The formulation of the radiative flux depends on the optical opacity regime of the plasma. Specifically, if the plasma is optically thick or optically thin, the formulation of the radiative flux differs significantly. In its general form radiative losses are written as, $\nabla \cdot \mathbf{S}$, where $\mathbf{S}$ is the radiative flux, which analytical expression is undetermined. Other phenomena can be considered as cooling terms. However, they primarily serve to transport and redistribute the released heat to different regions of the disk. These phenomena include convection and conduction. For a classical fluid, energy conduction follows a Fourier-type law,

$$\mathbf{q}_{cond} = -\overline{\overline{K}}.\nabla T. \tag{2.51}$$

As we can deduce from studies on heating exchange rates around the Sun, finding an accurate energy equation that takes into account the microphysics is out of reach at the moment. So instead of explicitly finding heating and cooling expression that best describe the jet dynamics, we choose the reverse approach by parametrizing $\Gamma - \Lambda$. This method set constrains on the heating intensity as well as where the bulk of heating resides. We discuss this in more details in chapter 4.

2.3 MHD waves

2.3.1 MHD waves, linear analysis of MHD equations

Using linear perturbation theory, we can explicit the waves that are allowed to propagate in a magnetized static plasma. We decompose density, pressure, the magnetic field, and velocity into a mean component (index 0), plus a small perturbation of the quantity (index 1) as follows,

$$\rho = \rho_0 + \rho_1, \quad P = P_0 + P_1, \quad B = B_0 + B_1, \quad \mathbf{v} = \mathbf{v}_1. \tag{2.52}$$

To obtain the wave solution of the MHD equations we assume the perturbations are proportional to $e^{i(\mathbf{k}\cdot\mathbf{r}-\omega t)}$, with $\mathbf{k}$ the wave vector and ω the wave frequency. This procedure leads to,

$$\omega\rho_1 - \rho_0(\mathbf{k}\cdot\mathbf{v}_1) = 0, \tag{2.53}$$

$$\omega\rho_0\mathbf{v}_1 - P_1\mathbf{k} + \frac{1}{4\pi}(\mathbf{k}\times\mathbf{B}_1)\times\mathbf{B}_0 = 0, \tag{2.54}$$

$$\omega\mathbf{B}_1 - \mathbf{k}\times(\mathbf{v}_1\times\mathbf{B}_0) = 0, \tag{2.55}$$

$$\frac{P_1}{P_0} - \Gamma\frac{\rho_1}{\rho_0} = 0. \tag{2.56}$$

Injecting these equations in the linearized equation of motion, we get,

$$\left[\omega^2 - \frac{(\mathbf{k}\cdot\mathbf{B}_0)^2}{4\pi\rho_0}\right]\mathbf{v}_1 = \left[\left(\frac{\gamma P_0}{\rho_0} + \frac{\mathbf{B}_0^2}{4\pi\rho_0}\right)\mathbf{k} - \frac{\mathbf{k}\cdot\mathbf{B}}{4\pi\rho_0}\mathbf{B}_0\right](\mathbf{k}\cdot\mathbf{v}_1) - \frac{(\mathbf{k}\cdot\mathbf{B}_0)(\mathbf{v}_1\cdot\mathbf{B}_0)}{4\pi\rho_0}\mathbf{k}. \tag{2.57}$$

Using Cartesian coordinates, and without loss of generality, we additionally set $\mathbf{B}_0 = B_0\mathbf{e_z}$ and θ the angle between $(\mathbf{k}, \hat{\mathbf{B}}_0)$. To compute the dispersion equation, we need to find the non-trivial solution for $\mathbf{v}$ that satisfy $\det(\mathcal{M}) = 0$, where $\mathcal{M}$ is the 3×3 matrix shown on the left hand side of Eq.2.58. This translates into computing the determinant of the following matrix,

$$\begin{pmatrix} \omega^2 - k^2v_A^2 - k^2c_s^2\sin^2\theta & 0 & -kc_s^2\sin\theta\cos\theta \\ 0 & \omega^2 - k^2v_A^2\cos^2\theta & 0 \\ -k^2c_s^2\sin\theta\cos\theta & 0 & \omega^2 - k^2c_s^2\cos^2\theta \end{pmatrix}\begin{pmatrix} v_x \\ v_y \\ v_z \end{pmatrix} = \begin{pmatrix} 0 \\ 0 \\ 0 \end{pmatrix} \tag{2.58}$$

Here, v_A is the Alfvénic velocity, and $c_s = \sqrt{\gamma P/\rho}$ the sound speed. The determinant yields the following dispersion equation,

$$(\omega^2 - k^2v_A^2\cos^2\theta)(\omega^4 - \omega^2k^2(v_A^2 + c_s^2) + k^4v_A^2c_s^2\cos^2\theta) = 0. \tag{2.59}$$

Three solutions result from Eq.2.59. the first is shear Alfvén waves,

$$\omega = \pm kv_A\cos\theta. \tag{2.60}$$

then there is the magnetosonic waves,

$$\omega_\pm = \frac{k}{\sqrt{2}}\left(v_A^2 + c_s^2 \pm \sqrt{(v_A^2 + c_s^2)^2 - 4v_A^2c_s^2\cos^2\theta}\right)^{1/2}. \tag{2.61}$$

2.3.2 Characteristic velocities

2.3.2.1 Critical points

The fast magnetosonic speed is defined as $V_+ \equiv \omega_+/k$ and the slow magnetosonic as, $V_- \equiv \omega_-/k$. Fast waves are magneto-acoustic perturbations that propagate in a nearly isotropic manner. Slow waves also convey magneto-acoustic information but do so in a highly anisotropic manner, following the magnetic field lines. Alfvén waves, being purely magnetic perturbations, bend the magnetic field lines without compressing them and do not disturb the plasma density.

In the case of ideal-MHD and specifically for disk and stellar wind models, each magnetic field can cross the slow, Alfvén, and fast critical points, depending on the ejection conditions. These critical surfaces are associated with physical characteristic of the problem. To cross a critical point, some parameters are required to be free. The slow-magnetosonic determines the mass flux emitted from the disk. A high jet mass flux lowers this critical point, bringing it closer to the disk, while a low ejected mass

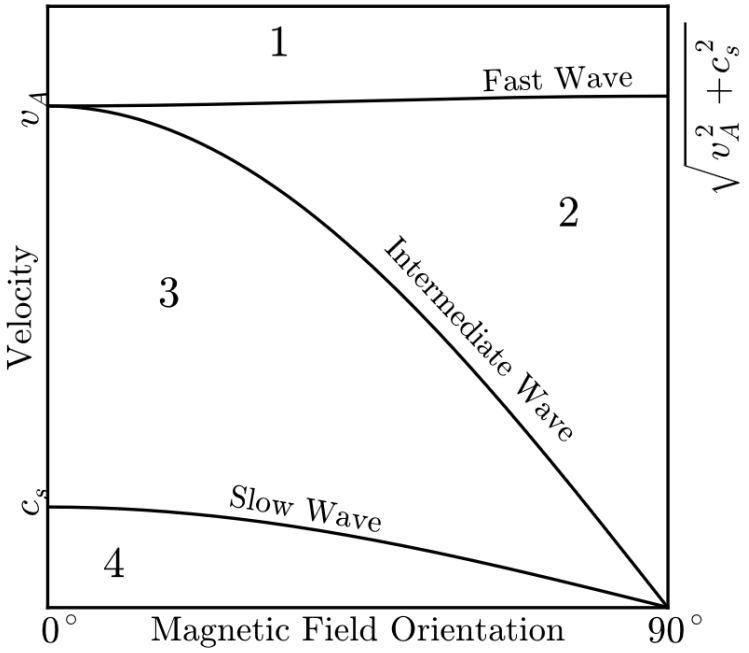

Figure 2.3: MHD wave velocities plotted as functions of θ. this plot is for $v_A > c_s$ which is the case for MHD jets. The wave speeds delineate the regions marked $1 - 4$. Lehmann et al. (2016).

raises it higher in the flow. Alfvén surface crossing sets the angular momentum of the flow. And finally, the fast-magnetosonic sets the total energy E of the flow. Finding solution for wind models is inherently an iterative process.

In the disk where resistivity needs to be included, the determinant equals zero when (Ferreira, 1994),

$$v^2(v^2 - c_s^2) = 0. \tag{2.62}$$

Ferreira (1994) showed that when resistivity is included, $\det(\mathcal{M}) = 0$ does not contain MHD critical velocities. The first critical surface is at the equatorial plane. The flow velocity is zero, and all the possible axisymmetric stationary solution go through this critical point. Making this point useless in finding disk solutions. The second critical surface is purely sonic - counterintuitive, as the dominant component in the disk is the magnetic field. Nonetheless, resistivity introduces diffusion, reducing the role of magnetic fields. It follows that magnetosonic waves are damped in the presence of resistivity.

2.3.2.2 The real critical surfaces

Determining the position of the critical points is not as straightforward as determining where the ratio of the flow velocity to the MHD characteristic velocity is equal to one. Tsinganos et al. (1996) showed that in self-similar flows the critical surfaces correspond

to the slow and fast characteristic velocities, but in the direction perpendicular to the separatrix. It confirms that the only critical point is the modified one (Bogovalov, 1994; Sauty et al., 2004). For self similar flows, because of self similarity it is perpendicular to the self similar symmetry direction. Matsakos et al. (2008) who showed that when a shock forms in the super-fast region, the shock front collapses on the separatrix or critical surface. There, the perpendicular velocity is equal to the fast. Fig.2.4 shows where the real critical separatrices are, named SMSS for the slow magnetoacoustic and FMSS for the fast magnetoacoustic.

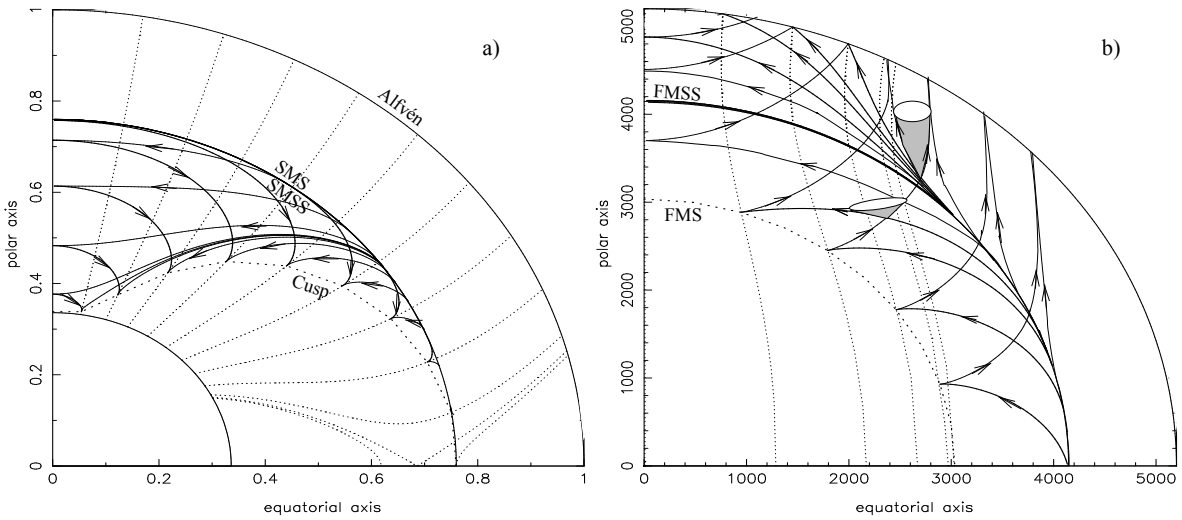

Figure 2.4: In the left plot the slow magnetoacoustic separatrix surface (SMSS) is just before the slow magnetoacoustic surface (SMS). In the right plot the fast magnetoacoustic separatrix surface (FMSS) is above the fast magnetoacoustic surface (FMS) at about R = 3000. Arrows indicate the direction of MHD signal propagation.

This result was found for the self-similar solution, but a confirmation of the general nature of this result is briefly discussed in section.4.5.6 where we show and analyse the standing recollimation shocks present in our simulations. Particularly, the shock front was found to match the real fast critical surface defined by the perpendicular velocity component as argued by Bogovalov (1994) and Tsinganos et al. (1996). Indicating the propagation of matter is delimited by a cone which side is set by the critical surface.

2.4 Discontinuities

2.4.1 Recollimation

Magnetically dominated jets have two mechanisms of collimation. Both involve a plasma threaded by a magnetic field and an electric current. First, we have the z-pinch, where the current **j** is directed along the axis of the jet and the magnetic field **B** is toroidal. A hoop-stress appears due this mechanism and acts on jet collimation. The

second mechanism is called θ-pinch. In this configuration it is now $\mathbf{j}$ that is toroidal, and $\mathbf{B}$ runs along the jet axis. Both cases apply a Lorentz force that collimates the jet.

The toroidal and poloidal components of the magnetic field can be shown to be proportional to ϖ^{-1} and ϖ^{-2}, respectively. This is deduced from the current density ϖB_ϕ, and magnetic flux $\pi\varpi^2 B_z$ since both are conserved along the flux tube. As the altitude increases, the poloidal magnetic field decreases faster, leaving the toroidal component to dominate early in the jet. This implies that the electric current is created by the toroidal component of the magnetic field. The direction of the current on the jet axis has to be towards the central star (-$\mathbf{e}_z$), since the magnetic toroidal field is along -$\mathbf{e}_\phi$ due to differential rotation.

Three scenarios emerge from the z-pinch mechanism at the level of a jet emitted from the accretion disk. To get a sense of the possible current configurations we can look the integrated current I,

$$I = 2\pi \int_{\varpi_i}^{\varpi_e} \varpi j_z d\varpi = I_0 \left[1 - \left(\frac{\varpi_i}{\varpi_e}\right)^{\mathcal{A}}\right]. \tag{2.63}$$

Here, ϖ_i and ϖ_e are the internal and external jet radii, and I_0 the current intensity at the polar axis ($I_0 < 0$). Depending on the value of $\mathcal{A}$ the confinement current can either start at jet launching radii or, inversely, close on the disk surface. In the case where $\mathcal{A} < 0$, I is positive an thus the jet transports current outwards. If $\mathcal{A} > 0$, I is negative and the current originates from an external region of the disk then it closes at smaller radii. Last, if $\mathcal{A} = 0$, no current is transported by the jet and all the confining current originates from an outer cocoon. Ultimately, collimation is set by the asymptotic values of the current. Regardless of the value of the asymptotic current, it should be separated from the accelerating current connected to the source by a recollimation shock (Jannaud et al., 2023).

2.4.2 Recollimation shocks

Thanks to the conservation equations of MHD and by assuming a steady state, we can derive shock conditions. A shock is a discontinuity that happens when a subsonic flows become supersonic. A shock needs to verify the Rankine-Hugoniot (RH) jump conditions (Rankine, 1870; Hugoniot, 1887). These conditions described originally hydrodynamical shocks, nonetheless, they can be generalized to describe the conditions of a shock happening in a magnetized environment (Kennel et al., 1989). RH jump conditions with the presence of a magnetic field give,

$$\left[\rho \mathbf{v}_\parallel\right]_1^2 = 0, \tag{2.64}$$

$$\left[\rho v_\parallel^2 + P + \frac{B_\perp}{8\pi}\right]_1^2 = 0, \tag{2.65}$$

$$\left[\rho v_\parallel \mathbf{v}_\perp - \frac{B_\parallel \mathbf{B}_\perp}{4\pi}\right]_1^2 = 0, \tag{2.66}$$

$$\left[\rho v_{\parallel}\left(\frac{v^2}{2}+H\right)+\frac{v_{\parallel}B_{\perp}^2}{4\pi}-\frac{B_{\parallel}(\mathbf{B}_{\perp}\cdot\mathbf{v}_{\perp})}{4\pi}\right]_1^2=0, \tag{2.67}$$

$$\left[\mathbf{B}_{\parallel}\right]_1^2=0, \tag{2.68}$$

$$\left[(\mathbf{v}\times\mathbf{B})_{\perp}\right]_1^2=0, \tag{2.69}$$

with $[...]_1^2$ the difference between post- and pre- shock environment. H is the enthalpy and $\perp$, $\parallel$ symbols define the normal and tangential components to the shock surface. Consequently, these jump conditions lead to a change in the geometry of the magnetic field across a shock front, which is different for each shock family. For fast shocks, the component of the magnetic field perpendicular to the direction of propagation, $B_{\perp}$, increases from its pre-shock to post-shock value. For intermediate shocks, $B_{\perp}$ changes sign due to the rotation of the magnetic field within the shock front. For slow shocks, $B_{\perp}$ decreases. This behavior is schematically shown in Fig.2.5. Matsakos et al. (2008) showed that the shocks occurring at the jet axis superimpose on the modified fast critical surface.

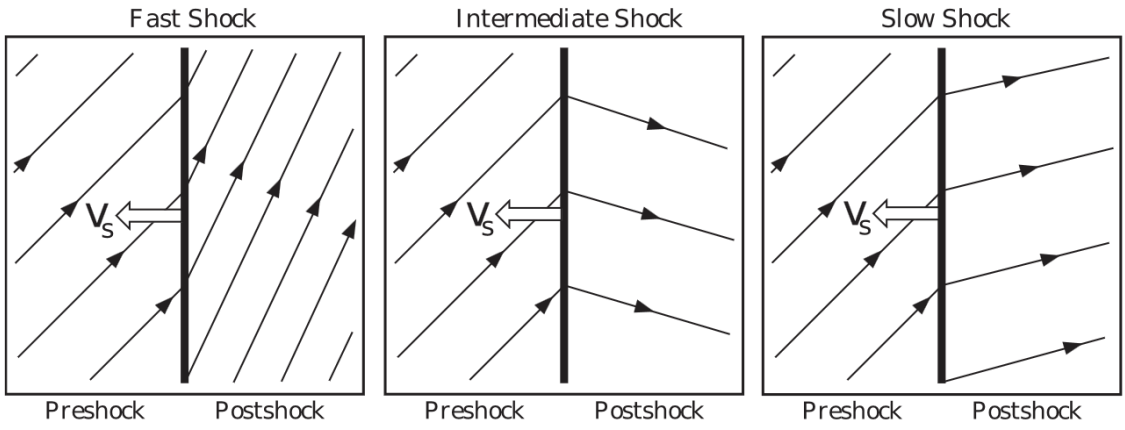

Figure 2.5: Schematic of the orientation of the magnetic field according to the types of shock. In this schematic V_s is the shock velocity. The effect of the three classes of MHD shock waves on magnetic field orientation is as follows: Fast shocks (left) increase the angle between the field and the shock normal, intermediate shocks (middle) reverse the angle sign, and slow shocks (right) decrease the angle. Consequently, the magnetic field strengthens over fast shocks and weakens over slow shocks. Taken from Lehmann et al. (2016)

2.5 A brief introduction to the PLUTO code

We would like to acknowledge the PLUTO team who have developed and maintained the code. We relied on the PLUTO manual for this section.

2.5.1 Finite volume method

MHD equations describe highly nonlinear problems that cannot be solved analytically. Nevertheless, these equations can be numerically resolved with computational schemes that capture plasma flows. The finite volume method consists of discretizing the domain over which flow equations are solved. This is accomplished by juxtaposing small volume elements in order to cover the entire computational box. Each box of the grid takes the average of the physical quantities that have evolved over time. In order to use this method, the evolution equations need to be writen in conservative form, i.e.,

$$\frac{\partial U}{\partial t} + \nabla \cdot \mathbf{F} = \sigma, \tag{2.70}$$

where U represents density, $\mathbf{F}$ density flux, and σ a source term. Averaging over a volume element, we get,

$$\frac{\partial}{\partial t}\int_{\mathcal{V}} U d\mathcal{V} + \int_{\mathcal{S}} \mathbf{F} \cdot d\mathcal{S} = \int_{\mathcal{V}} S d\mathcal{V}. \tag{2.71}$$

Thus, computing the time evolution of U simplifies to finding the flux $\mathbf{F}$ at the faces of the elementary volume. With this method, the conservative variables are naturally conserved to machine precision, enabling highly accurate determination of shocks. The accuracy of the solution depends on the estimation of the flux at the surface, consequently we can further write Eq.2.71 as follows,

$$\frac{\partial U_n}{\partial t} + \sum_{i=1}^{n} F_i S_i = \sigma. \tag{2.72}$$

Here U_n is the integrated value of U which is unknown in the cell. More explicitly, U, F, and σ are,

$$U = \left(\rho,\ \rho\mathbf{v},\ P\rho^{-\gamma},\ \mathbf{B}\right)^T, \tag{2.73}$$

$$\mathbf{F} = \begin{pmatrix} \rho\mathbf{v} \\ \rho\mathbf{v}\mathbf{v} + \overline{\overline{P}} - \mathbf{B}\mathbf{B} \\ P\rho^{-\gamma}\mathbf{v} \\ \mathbf{v}\mathbf{B} - \mathbf{B}\mathbf{v} + \overline{\overline{\eta}}_m \nabla \times \mathbf{B} \end{pmatrix}^T, \tag{2.74}$$

$$\sigma = \left(0,\ -\rho\nabla\Phi,\ \Gamma - \Lambda, 0\right)^T. \tag{2.75}$$

To compute F we need primitive variable which are ρ, P, $\mathbf{v}$, and $\mathbf{B}$. The transition from the conservative to the primitive form is delicate as it necessitates the use of limiters that ensure the quantities do not diverge or assume negative non-physical values (for instance, in the case of pressure and density). Computing the flux passing cell interfaces is equivalent to solving a Riemann problem, which we shall introduce now.

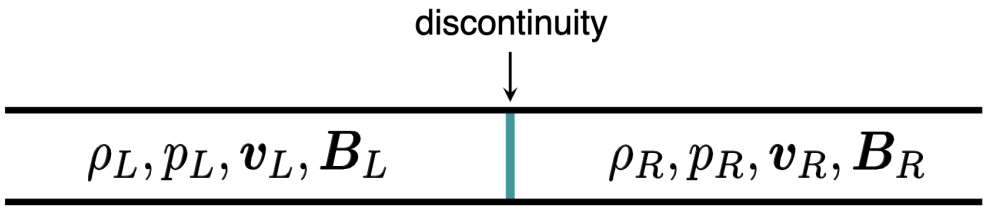

Figure 2.6: An initial value problem for the initial conditions, which consist of the constant states separated by a discontinuity.

2.5.2 Riemann problem

It is a one-dimensional problem that seeks to solve hyperbolic equations with a discontinuity (Fig.2.6), such that,

$$\frac{\partial U}{\partial t} + \frac{\partial F}{\partial x} = 0, \quad \text{with } U_0 = \begin{cases} U_L & x < x_0 \\ U_R & x > x_0 \end{cases} . \tag{2.76}$$

U_0 is the value located at the discontinuity, x_0. Depending on the solver used, this equation can be solved exactly. In PLUTO, solving this problem is central to follow the flow dynamics. A detailed study shows that characteristic waves appear and propagate the information about the system at the discontinuity. Each wave is associated with a characteristic velocity (illustrated in Fig.2.7). For fluid equations, three waves are necessary to carry information through the system - two sonic waves in addition to an entropy wave. In hydrodynamics, the entropy wave ensures the uniqueness of the solution. While for ideal-MHD, seven waves are needed - two Alfvén waves, two slow magnetosonic waves, two fast waves, and finally an entropy wave.

If the system is linear and the velocity of the waves do not depend on U, one can use the method of characteristics. This method involves finding the linear combinations of conservative variables, which are advected at the waves speeds along characteristic curves. These are, by definition, the eigenvectors associated with the eigenvalue of the Jacobian matrix $\partial F/\partial U$. The regions of space that have not yet received information from the waves remain in their initial state. The regions that have received information are in a state that is a linear combination of the eigenvectors. The final solution is obtained by summing all these contributions. If, on the contrary, we are dealing with a non-linear system, interactions between the waves have to be taken into account. Each wave can have a different nature, i.e, a shock, a refraction, etc. This greatly adds to the complexity of the problem.

2.5.3 Riemann solvers

There is a number of Riemann solvers each with their advantages and drawbacks. For an exhaustive presentation of these solvers one can read Massaglia et al. (2008). Exact solvers are computationally expensive. To circumvent this limitation, approximate

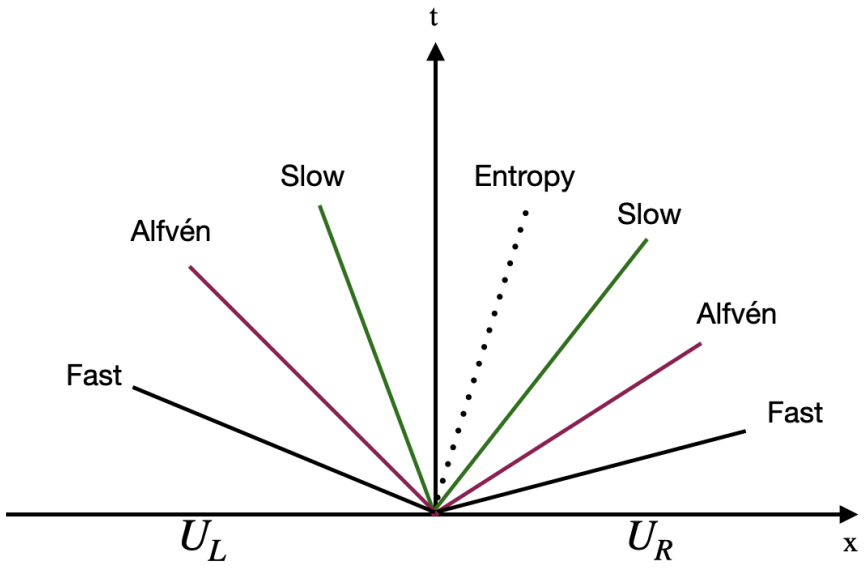

Figure 2.7: Illustration of the MHD waves characteristic velocities which carry information through the system.

solvers can be used. The one used in this thesis is the HLL method, originally proposed by Harten et al. (1983). HLL scheme averages the rightmost and leftmost signal speeds provided they can be estimated. This results in an approximation of the Riemann fan structure, in which all intermediate waves are averaged into a single state bounded by the two outermost waves. In this method, the Riemann problem reduces to three constant states,

$$U = \begin{cases} U_L & V_L \geq 0 \\ U_{HLL} & V_L < 0 < V_R \\ U_R & V_R \leq 0 \end{cases}, \tag{2.77}$$

Here V_L and V_R are the velocities of the leftmost and rightmost signal. In this case, U_{HLL} is constructed using the left and right states such that it would be defined as,

$$U_{HLL} = \frac{V_R U_R - V_L U_L + F_L - F_R}{V_R - V_L}. \tag{2.78}$$

F_L and F_R are the fluxes at a cell interface and are defined the same way as U_L and U_R in Eq.2.77. Eq.2.78 is the integrated average of the Riemann problem, and by imposing consistent jump conditions across the bounding waves, one can derive the numerical flux at the interface,

$$F_{HLL} = \frac{V_R F_L - V_L F_R + V_L V_R (U_R - U_L)}{V_R - V_L}. \tag{2.79}$$

The HLL solver gives an exact solution in the supersonic case as it selects the correct upwind flux. This method is robust and fast while ensuring pressure and density stay

positive. Nonetheless, it is diffusive compared to other solvers. For instance, the HLLD solver, developed by Miyoshi and Kusano (2005), is less diffusive and allows stronger discontinuities. This is achieved by including three more waves than HLL, namely, two rotational discontinuity waves corresponding to Alfvén waves, and a contact wave. Although more accurate, this solver needs more resources and can be numerically demanding. This being said, both HLL and HLLD resolve shocks and so we choose the faster more diffusive scheme.

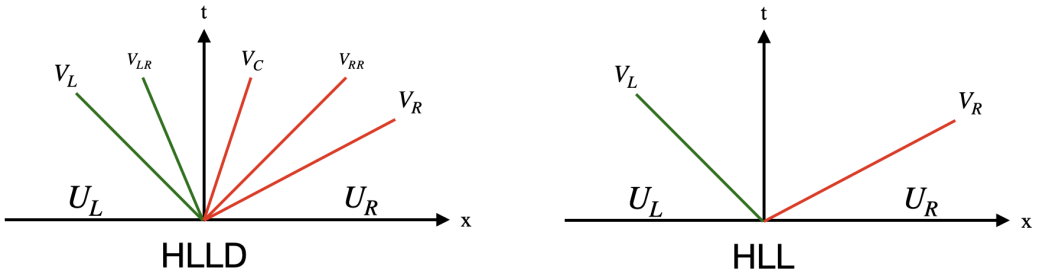

Figure 2.8: the Riemann fan in the case of the HLLD and HLL solvers. V_C is the contact wave velocity, while V_{RR} and V_{LR} are Alfvén waves speeds.

2.5.4 Divergence-free condition

Imposed by Maxwell-Flux equation, magnetic monopoles are forbidden. It is expressed by writing, $\nabla \cdot B = 0$. This states that the magnetic flux across all boundaries of any control volume is zero. Nonetheless, from the numerical point of view, $\nabla \cdot B \neq 0$ can develop during the evolution. This results in a unphysical acceleration along the magnetic fields. For all discretization types, numerical schemes cannot maintain the divergence-free condition. Consequently, alternative methods may be employed to identify the most effective solution, and the relative robustness of one strategy over another can be established through extensive numerical testing. In what follows we give a short description of two approaches. The first uses the cell-centered formalism which has the advantage of being easy to implement and adapt for unstructured grids. In the second approach, the magnetic fields have a cell-centered component in addition to being defined on the face normal to the magnetic field component. This provides a framework by which the induction equation is updated using Stoke's theorem and the divergence-free condition is fulfilled to machine accuracy, if the system is divergence free initially.

2.5.4.1 8-Wave formulation

The idea behind this method is to write MHD equations while allowing magnetic monopoles. This results in the source term transforming into,

$$\sigma = -\nabla \cdot B \, (0, \ \mathbf{B} - \rho \nabla \Phi, \ \mathbf{B} \cdot \mathbf{v}, v)^T \, . \tag{2.80}$$

This method is highly effective and has been successfully applied in many contexts, remaining widely used in astrophysics today. Its success lies in its ability to eliminate $\nabla \cdot B$ errors by advecting them with the flow. However, there are two significant issues. First, at stagnation points (i.e., where the flow velocity is zero), divergence errors accumulate because the flow trajectories converge. Second, the scheme is not strictly conservative, leading to shock wave solutions that generate large conservation errors (Teyssier and Commerçon, 2019).

2.5.4.2 Constrained transport

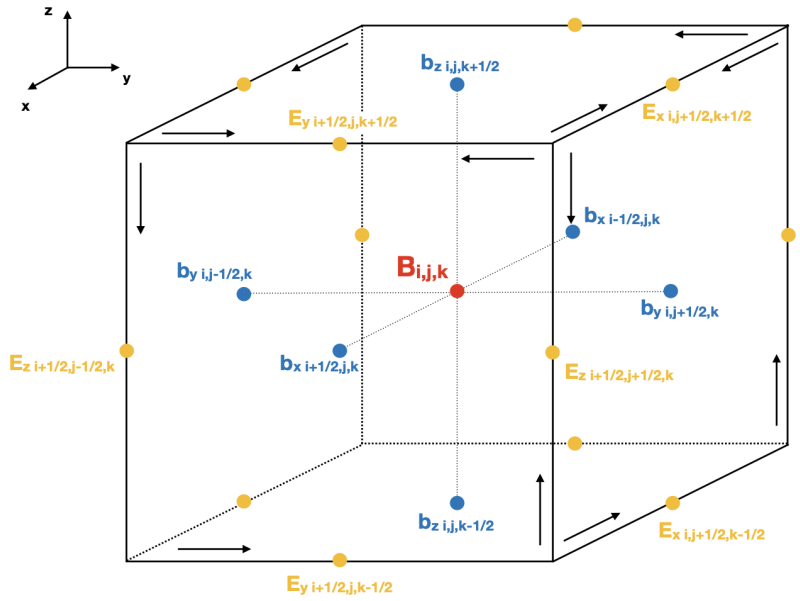

Figure 2.9: Representation of the magnetic field and electromotive forces in a computational cell using the constrained transport method. The quantity in red represents the magnetic field vector defined at the center of the cell. The quantities in blue represent the component of the magnetic field normal to the face, defined at the center of the face. The quantities in orange represent the electromotive forces along the edges, where they are defined. The arrows indicate the direction of the integral on each contour. Taken from Nicolas Scepi thesis manuscript (https://theses.hal.science/tel-02444294).

Designed by Evans and Hawley (1988), this method uses the staggered magnetic and electric fields, shown as blue and yellow dots in Fig. 2.9, to evolve the induction equation with time. The useful nature of such an approach becomes clear when looking at the Stokes's theorem,

$$\frac{\partial}{\partial t}\int_S \mathbf{B}\cdot d\mathbf{S} = \int_S \nabla\times\mathbf{E}\cdot d\mathbf{S} = \int_L \mathbf{E}\cdot d\mathbf{l}. \tag{2.81}$$

S is the closed surface of cell face, and L the contour of the surface S. Summing over all cell faces and contours Eq.2.81 equals zero since field contributions cancel out

in pairs. Consequently, as long as the magnetic field is initially divergence-free, it should stay that way at machine precision. The PLUTO code also uses the constrained transport method to calculate the parabolic flux due to Ohmic diffusion. It computes the currents J on the edges. Similarly, the resistivity, η, is also computed at cell edges. The Ohmic current, ηJ, is then added to the electromotive force on each edge to update the magnetic field on the faces. The energy equation also includes an Ohmic heating term. In the case of ideal-MHD, η is zero, then no ohmic contribution is added.

In this thesis, we use the 8-Wave formulation. A simple reason warrents its use. Since we proceed to mix semi-analytical stellar and disk solutions with non-linear mixing functions (chapter 4), divergence-free conditions are not expected to be fulfilled anymore in the mixing region. Although, we analytically ensure $\nabla \cdot B = 0$ at the boundary condition, the 8-Wave method evacuates any regions that presents magnetic sinks or sources. We have verified this point in the simulations.

2.5.5 Limiters

The classical Godunov method (Godunov and Bohachevsky, 1959) involves using the averages of U as initial conditions for the Riemann problem. This method is first-order in both time and space and is no longer used in practice. Van Leer (1979) proposed an improvement to the classic Godunov method by reconstructing the variables within the cells using piecewise linear functions. This second-order method in both time and space remains stable as long as a limiter, which takes into account the values of neighboring cells, is used to set the slope of the linear reconstruction. We use the default limiters in PLUTO. The Monotonized Center limiter (Van Leer, 1977) for density, the van Leer limiter (Van Leer, 1977) for velocity vectors and magnetic fields, and the Minmod limiter (Roe, 1986) for pressure.

To evolve a Riemann problem with time, Godunov methods integrate cell-centered variables U over time with an increment $\Delta T = t_2 - t_1$, we can rewrite Eq.2.70,

$$U(t_2) = U(t_1) + \int_{t_1}^{t_2} \left(\sigma(t) - \sum_{i=1}^{n} F_i(t) S_i \right) dt, \tag{2.82}$$

$$U(t_2) = U(t_1) + \frac{\Delta T}{x_2 - x_1} \left(\mathbf{F}_{i-\frac{1}{2}} - \mathbf{F}_{i+\frac{1}{2}} \right). \tag{2.83}$$

Here $\mathbf{F}$ is the integrated flux and source term over time at the cell interface $i-1/2$ and $i+1/2$. To ensure the stability of the scheme, it is necessary to choose a time such that no information from the discontinuity at $i-1/2$ disturbs the discontinuity at $i+1/2$ and vice versa. This means that the flux at the interface $i-1/2$ depends only on the initial conditions at $i-1/2$. This amounts to choosing ΔT appropriately, such that

$$\Delta T \leq \frac{x_2 - x_1}{V_{max}}, \tag{2.84}$$

with V_{max} the maximum velocity of the signal.

2.5.6 Heating/cooling module

A time dependant cooling module is included in PLUTO. Its purpose is to update flow variables by solving the energy equation using a fractional step formalism. This means the dynamic evolution - density, pressure, velocity, and magnetic field - is decoupled from energy equation computation. Once the energy equation is solved, its contribution is added to the pressure. Schematically, the fractional step formalism is as follows,

$$\frac{\partial P}{\partial t} = \left(\frac{\partial P}{\partial t}\right)_{MHD} + \left(\frac{\partial P}{\partial t}\right)_{heating} \tag{2.85}$$

The first term on the right hand of the equation is,

$$\left(\frac{\partial P}{\partial t}\right)_{MHD} = -\mathbf{v}\cdot\nabla P - \Gamma_p P \nabla\cdot\mathbf{v}, \tag{2.86}$$

Γ_p is the adiabatic index, which is equal to 5/3 for a monoatomic gas. The code also computes pressure variation from heating,

$$\left(\frac{\partial P}{\partial t}\right)_{Heating} = \Gamma - \Lambda. \tag{2.87}$$

For more details on the module and how it operates, see sections 6.2 and 9.1 of PLUTO userguide.

Using velocity and pressure we can construct a heating rate that will affect the flow. The additional benefit from this strategy is to make the heating exchange rate parametrizable. Originally, the module computes the cooling resulting from a simple power-law. The loss term in the energy equations is,

$$\Lambda = \mathcal{K}\rho^2 T^\alpha. \tag{2.88}$$

We replace the cooling term by other expressions that represent a gain/loss exchange rate (see Sec.4.3.1 for the explicit expressions used).

Chapter 3

Heating sources in the environment of a CTTS

Contents

3.1 Elementary ionization processes 73
3.1.1 Photoionization 74
3.1.2 Collisional ionization 76
3.2 Measure of ionization 77
3.2.1 Ionization in jets 77
3.2.2 Ionization in disks 80
3.3 Ionization sources 83
3.3.1 Stellar photoionization 83
3.3.2 Galactic cosmic rays 85
3.3.3 Local production of energetic particles 88
3.4 Heating and cooling 93
3.4.1 Radiative heating and cooling 94
3.4.2 Photoionization and recombination 95
3.4.3 High energy heating 96
3.4.4 Viscous heating 97
3.4.5 MHD processes 98

3.1 Elementary ionization processes

To ionize the circumstellar environment of T Tauri stars, different physical paths are available. With the central star radiation, photoionization is one of the main physical

processes leading to free electrons in the medium. An other possible path is the collisional ionization. We rely in this section on the works of Rybicki and Lightman (1991), Güdel (2015), and Woitke (2015). The purpose of this short section is to outlay the basic fundamental processes at play in hot classical plasma.

3.1.1 Photoionization

Fundamentally photoelectric absorption and photoionization are treated using quantum mechanics. In this paradigm, the electron is represented as a wave function $\Psi(\mathbf{x}, t)$, which is the probability amplitude. This function follows Schrödinger's equation,

$$i\hbar\frac{\partial\Psi}{\partial t} = \hat{H}\Psi. \tag{3.1}$$

$\hat{H}$ is the Hamiltonian describing the energy of the system. Now by introducing a photon, the quantum state of the system changes. This process is described by the operation $\langle f| H |i\rangle$, where H is the Hamiltonian perturbed by an external radiation field. Here, $|i\rangle$ is the initial state, and $|f\rangle$, the final one.

Let us determine the explicit expression of the Hamiltonian as it is the first step to get to the cross section. The Lagrangian of an electron in an electromagnetic field yields,

$$L = \frac{1}{2}m\dot{\mathbf{x}}^2 + e\varphi(\mathbf{x}, t) - \frac{e\dot{\mathbf{x}}}{c}\mathbf{A}(\mathbf{x}, t). \tag{3.2}$$

The first term is of the kinetic energy, while the second and third terms express the potential energy. ϕ and $\mathbf{A}$ are the scalar and vector potentials, respectively. The Hamiltonian itself derives from the Lagrangian,

$$H = \dot{\mathbf{x}}\frac{\partial L}{\partial\dot{\mathbf{x}}} - L, \tag{3.3}$$

after plugin in Eq.3.2, the Hamiltonian reads as three different contributions,

$$\begin{aligned} H_0 &= \frac{1}{2m_e}\left(\frac{\partial L}{\partial\dot{\mathbf{x}}}\right)^2 - e\varphi(\mathbf{x}), \\ H_1 &= \frac{e}{m_e c}\left(\mathbf{A}\cdot\frac{\partial L}{\partial\dot{\mathbf{x}}}\right), \\ H_2 &= \frac{e^2}{2m_e c^2}\mathbf{A}\cdot\mathbf{A}. \end{aligned} \tag{3.4}$$

The first Hamiltonian, H_0, describes the state of the atom at equilibrium, which is a static term. The second, H_1, is due to one-photon interactions. The final term, H_2, is of the two-photon interactions. The last term will be dropped as its contribution is negligible compared to H_0. This approximation is supported by the ratio $H_2/H_0 \sim a_0^4\mathcal{E}^2/e^2 << 1$ (Güdel, 2015; Shu, 1991). Before reaching the final form of the

Hamiltonian, we have to make an assumption on the vector potential. By considering a monochromatic plane wave, $\mathbf{A}$ can be written as,

$$\mathbf{A}(\mathbf{x},t) = \frac{1}{2}\,|A_0|\,(\hat{\epsilon}e^{i(\mathbf{kx}-\omega t)} + \hat{\epsilon}^* e^{-i(\mathbf{kx}-\omega t)}). \tag{3.5}$$

Going back to the wave function, it can be expressed as the sum of all eigenfunctions which define the complete basis such that,

$$\Psi(\mathbf{x},t) = \sum_j c_j \varphi_j(x) e^{-iE_j t/\hbar}, \tag{3.6}$$

with c_j time-dependent coefficients, E_j the eigenvalue of a state j, and $\hbar$ Planck constant. By substituting the equation above in the time-dependent Schrödinger equation in addition to some mathematical development one can compute the transition rate. This rate translates the probability a system is in its final state at time t. The rate is expressed as,

$$R = \lim_{t\to\infty} \frac{|c_f(t)|^2}{t}. \tag{3.7}$$

In quantum mechanics $|c_f(t)|^2$ is equivalent to the square of the wave function. Subsequently by integrating the transition rate over all energies of the final states and dividing the result by the Poynting energy flux - expressed in terms of the discrete-photon flux through an area F - the ratio yields the differential cross section $d\sigma/d\Omega$. Without going into further mathematical details we can get a concrete meaning of the photoionization by looking at the ionization cross section of the nth shell in a hydrogen-like atom (Güdel, 2015),

$$\sigma_n(\omega) = K\frac{Z^4}{n^5\omega^3}. \tag{3.8}$$

First, K is a constant, Z is the charge of a nucleus, and ω is the frequency of a photon. Eq.3.8 demonstrates that for $n = 1$, i.e. at the inner shell, the cross section is the largest. Moreover, this result is highly dependent on the atomic number, and peaks at the ionization edge then decreases proportionally to ω^{-3}, as shown in Fig.3.1.

For atomic elements in the circumstellar medium the ionization edges are located between 13.6 eV for hydrogen and 7.1 eV for iron. Radiation with energies lower than ~ 7 eV the photons are absorbed more efficiently. On the other hand, photoionization looses its ionization efficiency as the photon frequency increases, which is demonstrated in Eq.3.8. Softer X-rays are more effective ionizers than harder photons, but with great optical depth, ionization occurs closer to the surface of structures such as protoplanetary disks. Harder X-ray photons penetrate deeper into the cooler layers, with the hardest photons passing through the entire disk without being absorbed. Therefore, photoionization is dominated by the lowest energy photons that have not been attenuated, especially those near the energy where the optical depth of photoelectric absorption is unity, making higher energy photons less significant for shallow layers.

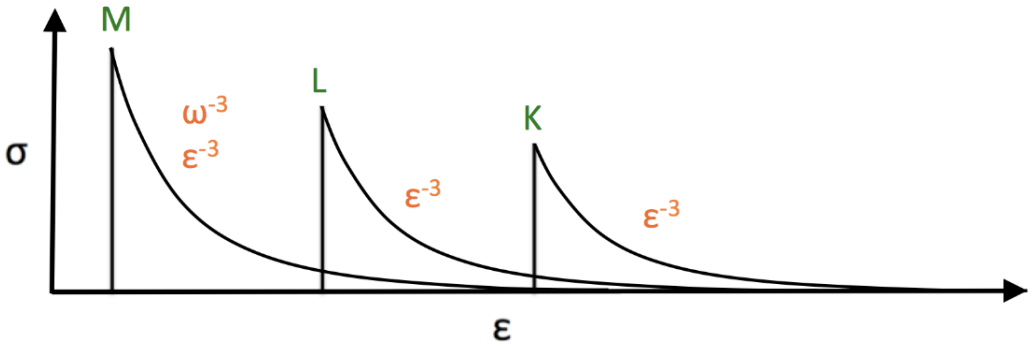

Figure 3.1: Schematic illustrating the absorption cross sections as a function of photon energy for ionization at M,L, and K electronic shells. From Güdel (2015).

3.1.2 Collisional ionization

In the case of collisional ionization, a valence electron at rest is collisionally excited. Here an energetic electron or cosmic ray particle transfers its energy to the electron at rest. Although, similarly to photoionization we can treat this phenomenon with quantum mechanics. Here, we outline the simple classical approach of Kahn et al. (2005).

When two electrons collide with an impact parameter b, one at rest the other having an amount of kinetic energy E, the transfer energy writes,

$$\Delta E = \frac{e^4 E}{e^4 + E^2 b^2}, \tag{3.9}$$

for ionization to occur the energy transfer needs to exceed the ionization potential, ϑ. A direct implication is that the impact parameter has to be less than,

$$b_l = \frac{e^2}{E}\sqrt{\frac{E}{\vartheta} - 1}. \tag{3.10}$$

From the impact parameter we get the geometric cross section, $\sigma = \pi b_l^2$. The classical approximation needs to be summed over all electrons with their associated ionization potentials, and as long as $E >> \vartheta$, this classical treatment holds. A simple expression of the collisional ionization cross section was given by Thompson in the case where ionization occurs by electron impact,

$$\sigma_{CI}^{max} = \pi a_0^2 \left(\frac{E_i^H}{E_i}\right)^2. \tag{3.11}$$

Here, E_i is the ionization energy of a target particle at the nth state. In this expression, the maximum cross section has a dependence on the ionization energy. Eq.3.11 is obtained when the electron has two times the ionization energy of the target particle. For more refined collisional cross sections refer to Mitchner and Kruger Jr (1973).

3.2 Measure of ionization

3.2.1 Ionization in jets

As has been established now, jets are launched along magnetic field lines. Hence, an important physical parameter of the plasma is its ionization fraction,

$$\chi_e = \frac{n_e}{n_H}. \tag{3.12}$$

Here, n_e and n_H are the electronic and hydrogen densities, respectively. This key parameter informs on the coupling strength between the gas and the magnetic field. With such critical information, fundamental parameters can be deduced, such as the total mass loss in jets where the neutral and ionized populations are considered (Fedriani et al., 2019). In jets, the ionization fraction is determined to be between 0.1 and 0.6 (Podio et al., 2006). To observationally determine the ionization fraction, information is extracted from optical and NIR lines emitted from the abundant molecular and atomic species (Reipurth and Bally, 2001). Among the first to study line ratios to examen jet properties, Böhm et al. (1980) and Brugel et al. (1981) used low spatial resolution spectra to estimate these ratios in the shock cooling region. Subsequently coupled with shock models, observed lines enable inferring the ionization fraction, and intensity of the magnetic field (e.g., Raga and Bohm 1986; Hartigan et al. 1987, 1994). Bacciotti et al. (1995) were the first to develop a model which does not depend on the heating, and this in the pre-shock region otherwise the assumption where the emitting gas is at a single temperature does not hold (Podio et al., 2006). The method presented in Bacciotti et al. (1995) was later refined in Bacciotti and Eislöffel (1999). In essence, they use the fact that gas emitting forbidden line is excited through collisions.

Bacciotti and Eislöffel (1999) estimated the ionization fraction in a sample of low-mass stellar jets and found that the ionization fraction generally decreases monotonically along the jet. They derived typical values of ionization ranging from 0.02 to 0.4. In an analysis of Hubble Space Telescope arc-second images of the DG Tau jet, Maurri et al. (2014), observed a low ionization fraction ($\sim$ 0.02) at the base of the jet, i.e. at 0.1″, increasing to a plateau value of $\sim$ 0.7 at a distance of 3″ from the central source, before decreasing again (see Fig.3.2). Converted to a physical distance 0.1″ corresponds to 15 au from the star. This puts into perspective how accurate a measurement of ionization can be made close to the star. As pointed by Bacciotti et al. (2000) line quenching becomes too important below 0.1″.

Hartigan et al. (2004), by modeling the optical [OII]/[OI] line ratio in shocks at the base of the HN Tau jet, found $\chi \sim 0.7$. Teşileanu et al. (2012) developed an MHD model for low-mass stellar jets, which they applied to the source RW Aur. Their model accurately fits the surface brightness fluxes in several forbidden lines, with a value of ionization fraction from 10% to 20% in the central jet. The ionization fraction was attributed to irradiation by X-rays from the stellar magnetic corona for shocks happening at 100 au and above.

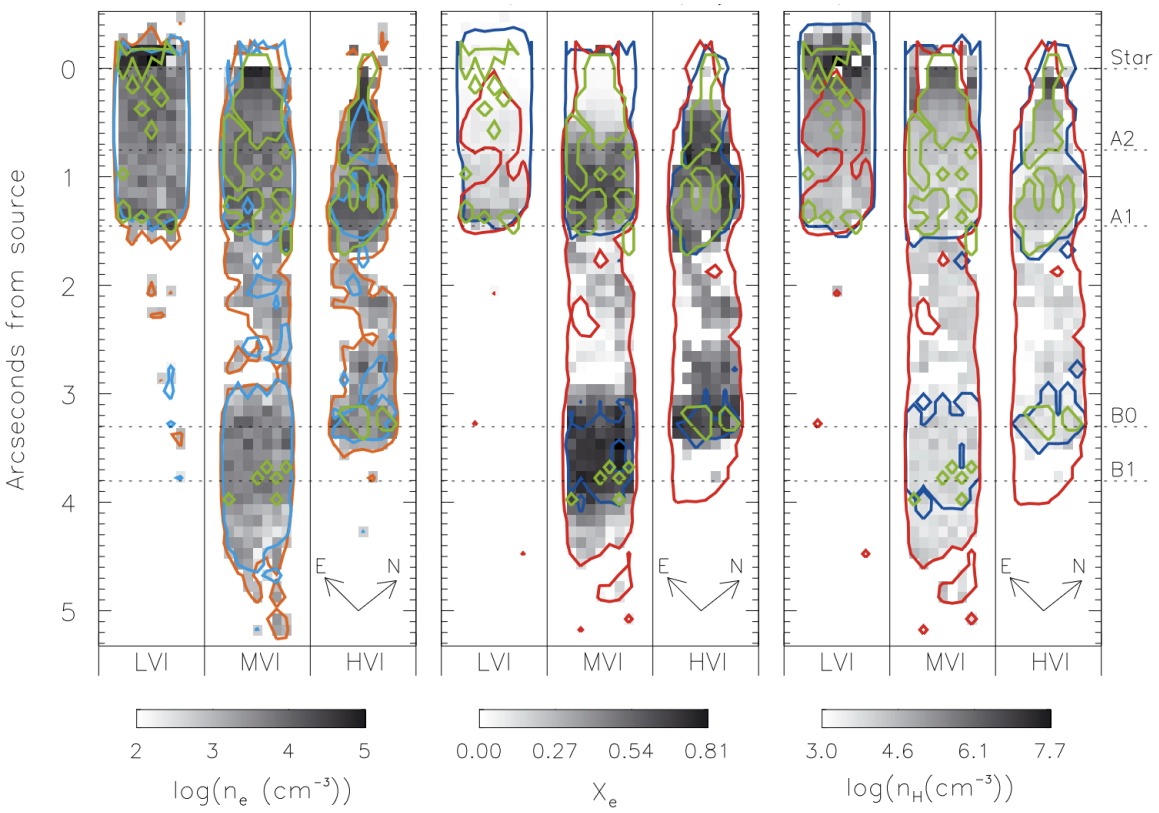

Figure 3.2: This plot groups the electronic density, ionization fraction, and hydrogen density as inferred from DG Tau. Low velocity interval (LVI) is defined as -120 to 25 $km\,s^{-1}$, medium velocity interval (MVI) is defined as -270 to -120 $km\,s^{-1}$ and high velocity interval (HVI) is defined as -420 to -270 $km\,s^{-1}$. The different contours point at [OI] λ6363 at 3σ in blue, [NII] λ6583 in red, the high density limit for [SII] in green, in cyan [SII] λ6716, orange [SII] λ6731. Taken from Maurri et al. (2014)

The weak dependence of brightness and line ratios on the temperature of unshocked jet medium makes it challenging to constrain temperature. In their investigation of low-mass MHD jets launched from accretion disks, Garcia et al. (2001) considered ambipolar diffusion heating and various ionization sources (X-rays, UV radiation, and collisions). Typical jet temperature are found to reach a plateau at $T \sim 10^4 K$ as soon as 0.1 au from the star. Although, as noted by the authors, the dominant heating contributor when $\varpi \leq 0.1$ au is not the ambipolar diffusion, given the high ion density. In high-mass protostars, both ionization and temperature are poorly known. Based on the work done by Garcia et al. (2001), for instance, we expect jets from high-mass protostars to be denser and cooler and have higher mass loss rates than jets from low-mass protostars. Ionization as small as 10^{-4} are found for jets with $T \sim 10^4 K$. Nonetheless, heating sources like turbulence, MHD wave dissipation, magnetic reconnection, or weak shock heating were not considered. Overall, studies of jet ionization are scarce compared to the work done on its counterpart, i.e. the protostellar and protoplanetary disk. A

takeaway message can be that hotter jets have higher ionization fractions, and inversely for colder jets.

A newer study constrains the ionization fraction of disk winds under 5 au (Nisini et al., 2024). To get to the physical properties of warm atomic gas they study the spectra of CTTS. Then, the optical forbidden lines uncovered in these spectra are analysed in terms of luminosity profile. Their region of interest is the low-velocity component where observation of [OI] 557 nm and [OI] 630 nm help infer the kinematics of the wind (Fig.3.3). They find that the LVC has ionization fraction lower than 10%. Although, in the high-velocity component has a higher ionization fraction as they present with [NII] 658 nm (Nisini et al., 2024; Giannini et al., 2019).

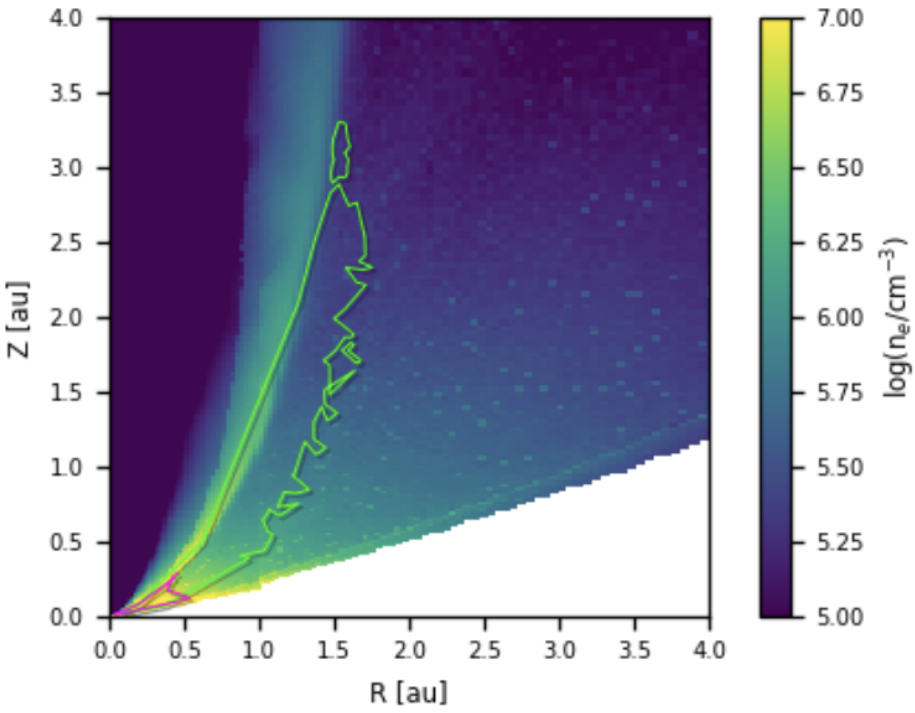

Figure 3.3: Plot of density map to which optical forbidden lines are superimposed in the region they are observed in. the green contour is of [OI] 630 nm, while the red is the contour for [OI] 557 nm. Both these lines show an anti-correlation, which means the green contour is expanding with the flow. Plot taken from Nisini et al. (2024).

To summarize what has been said about the ionization fraction in jets, we look how its value along with temperature and density vary with the jet velocity. In Tab.3.1, we reproduce the results presented in Giannini et al. (2019) where fractional ionization smoothly varies with the jet speeds. This indicates that the different jet components, having either high, medium or low velocities, likely originate from regions with the same material. Although, they vary in temperature and ionization, which can be explained by linking ejection radius and proximity to the central engine. Since high velocity jets are

closer the central axis, their ejection medium must be much more heated than further disk rings. If in addition we add the shock heating along the jet, a clearer picture of ionization fraction begins to emerge.

Velocity interval (km s^{-1})	T_e (10^3 K)	**log(n_e)** (cm^{-3})	x_e	**log(n_H)** (cm^{-3})
DG Tau				
0 to −80	5.9–6.3	4.09–5.15	0.03–0.10	5.91–6.15
−100 to −140	8.9–10.0	4.90–5.10	0.11–0.30	5.61–5.83
−160 to −180	10.3–15.9	4.70–5.10	0.41–0.52	4.98–5.48
HN Tau				
+40 to 0	9.8–14.2	4.40–4.45	0.04–0.06	5.65–5.85
−20 to −80	6.7–9.5	4.70–4.95	0.06–0.20	5.65–5.95
−100 to −180	8.0–13.9	4.95–5.10	0.41–0.83	5.03–5.49
DO Tau				
0 to −40	8.1–11.9	6.50	0.055	7.75
−80 to −160	7.0–8.1	4.70–5.85	0.004–0.008	7.00–7.05
RW Aur				
+150 to +50	9.0–12.9	4.10–4.25	0.008–0.03	5.75–6.20
0 to −100	9.0–11.9	4.50–4.70	0.005–0.009	6.75–7.00
−150 to −250	8.7–16.3	4.75–5.10	0.007–0.04	6.45–6.95

Table 3.1: Physical parameters of the velocity components. Except for DO Tau all the 6 sources present in Giannini et al. (2019) show that high velocity jets are more ionized than the lower velocity ones in the same source. Reproduced from Giannini et al. (2019).

3.2.2 Ionization in disks

Ionization varies greatly within the disk, and with the distance to the central star. Disks are immersed in high energy particle fluxes and radiation (Güdel, 2015). These processes play a crucial role in shaping the disk, as ionization facilitates complex chemistry and interactions, influencing its structure (Béthune et al., 2017). An understanding of the mechanisms of ionization is of great importance for the prediction of the synthesis and distribution of organic molecules, which may be of significance in the context of prebiotic chemistry in the formation of planetary systems. Furthermore, ionization-induced heating affects the thermal equilibrium in T Tauri accretion disks, influencing their vertical structure and the behavior of both dust and gas. This heating source may also serve as a candidate for the launching of winds and jets.

In general two aspects are critical to quantify and understand ionization in the disk. The first aspect is determining the ionization degree. While the second is identifying ionization sources that explain observations. Ionization and recombination rates determine the ionization degree, which is heavily influenced by the propagation of radiation

and chemical composition of the disk (see e.g., Semenov et al. 2004; Woitke et al. 2009; Xu et al. 2019). Given that the screening ionizing radiation goes through the disk, its structures are layered with varying temperatures and chemical species at each layer (van Dishoeck, 2014). A sketch of the disk structures as a function of their chemical composition can be seen in Fig.3.4.

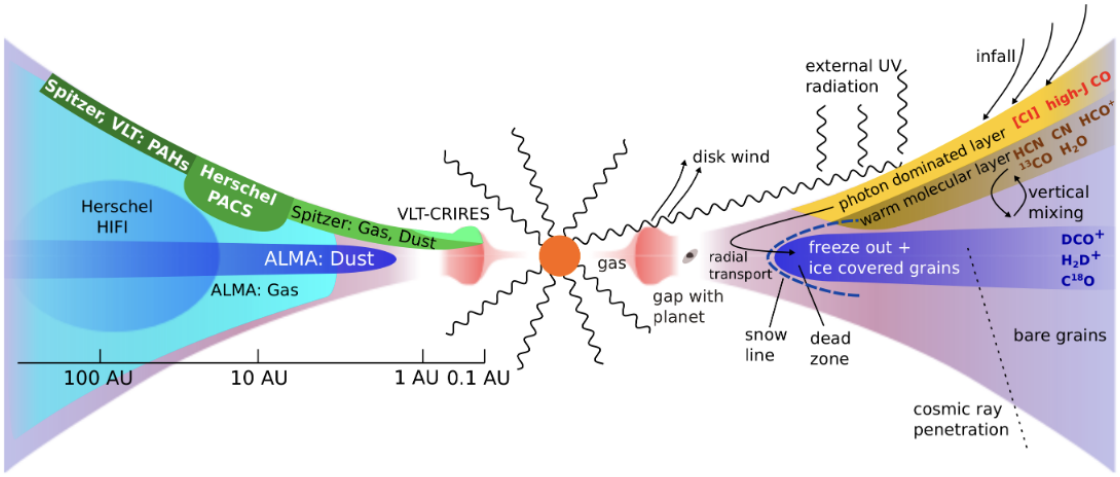

Figure 3.4: Overview of the different chemical and physical processes and the associated measure instruments. Taken from van Dishoeck (2014).

A multitude of chemical components offer information on the disk ionization. Key tracers such as H_3^+, HCO^+, and N_2H^+ are shown by theoretical models to be the dominant molecular ions tracers (e.g., Aikawa et al. 2015, 2021). Atomic ions such as C^+ and S^+ are also observed in the disk (Kama et al., 2016). In the case of molecular ions, their signatures are seen in the millimeter and submillimeter range (Williams and Best, 2014). Atomic ions are observed in submillimeter and far-IR (Thi et al., 2010). The abundance of each type of ions is associated with the presence of dust, gas density, and ionization rate.

The layer at the disk surface is photon dominated unless a substantial number of non-thermal processes are present, such as particles produced by flaring episodes (Brunn et al., 2023, 2024). The gas in this region is extremely hot, $T_{gas} > 10000$K. Ionization is driven by X-rays and cools through O III and Ly α line emissions (Woitke, 2015). This region of the disk is tenuous, hence it produces few signatures, among them [OI]λ6300, and [NeII]12.81μm (Güdel et al., 2010). The primary charge carriers are H^+, C^+ and S^+. The main process for their appearance is photoionization. Not able to penetrate farther than the disk surface, X-rays deposit their energy early in the disk and are not able to reach the midplane. For soft X-rays (below 5 keV), the attenuation length is the smallest since softer photons are absorbed faster, given their higher energy deposition rate. To illustrate this, Aikawa et al. (2021) argue that the attenuation column density of a 1 keV X-ray is $N \sim 10^{21}$ cm^{-2}, while the disk column density is $\sim 10^{23} - 10^{25}$ cm^{-2}.

This being said, even for the high energy X-rays the ionization rate at the disk midplane is expected to be lower than $10^{-18}s^{-1}$ (Rab et al., 2018; Aikawa et al., 2021).

Deeper in the disk, HCO^+ dominates, this behavior is accompanied by an increase of the ratio of CO to electronic number density (Aikawa et al., 2015). Even deeper where temperatures fall below 20 K, an increase of N_2H^+ population occurs as CO molecules attache to grains as they freeze (Aikawa et al., 2021). As temperature decreases in the disk, theoretical models predict a predominance of H_3^+ in addition to N_2H^+. Although, H_3^+ has not been observed as of yet, thus ionization rate is uncertain. An alternative probe to ionization in the disk midplane is N_2D^+ (Cleeves et al., 2014).

To get an idea of the ionization fraction at different disk column densities we select work studying ionization at different disk regions (Öberg et al., 2011; Teague et al., 2015; Cleeves et al., 2015; Aikawa et al., 2021). Starting at the shallow layers of the disk, Teague et al. (2015) determine column densities of $\sim 9.8\ 10^{12}$ cm^{-2} and $\sim 1.8\ 10^{12}$ cm^{-2} for HCO^+ and DCO^+, respectively at a distance of 100 au in the disk. This corresponds to the warm molecular layer. Using the abundance ratio DCO^+/HCO^+ they find an ionization fraction of 10^{-7}. Öberg et al. (2011) determine the ionization fraction at three different regions of the disk. The first is the warm molecular region. They used HCO^+ and found $\chi_e \sim 4\times10^{-10}$. Deeper in the cold molecular layer, they found a lower fraction, $\chi_e \sim 3 \times 10^{-11}$ using DCO^+ and N_2H^+. At the coldest regions, no detection of H_2D^+ leads to an ionization fraction upper limit of $\sim 10^{-10}$

Cleeves et al. (2015) tackle the problem differently by introducing cosmic rays and X-rays in chemical models, subsequently, comparing the results with observations. Their results indicate that the model aligning best with observations featured a low cosmic ray ionization rate, $< 10^{-19}$ s^{-1}, and moderate X-ray radiation. they estimate the ionization fraction between 10^{-11} and 10^{-10} close to the midplane and beyond 100 au. In contrast, newer work done by Aikawa et al. (2021) reports higher ionization rates in the disk both in the molecular layer and disk midplane. The values of χ_e found in their work match those presented in Cleeves et al. (2015), but the ionization rate is one order of magnitude higher closer to 10^{-18}.

Many studies have focused on the ionization processes occurring farther out in the accretion disk, while fewer have examined regions closer to the central star. This discrepancy is primarily due to the intense luminosity of the star, which significantly complicates the investigation of disk ionization near the star. In other terms, most ionization computations are made for standard accretion disks (SAD) without winds. However, Combet and Ferreira (2008) and Combet et al. (2010) demonstrate that when magnetized winds sustain accretion, the disk is thinner and less dense than SAD for the same accretion rates. This translates into a higher disk ionization level.

3.3 Ionization sources

3.3.1 Stellar photoionization

The environment surrounding a young star is subject to a plethora of high energy radiation, primarily from the star. Mainly, the sources of radiation ensue from the stellar hot corona, and span across a broad range of wavelengths. From far-UV with energies between 6 eV and 13.6 eV, Extreme-UV laying between $13.6 - 100$ eV, and X-rays with $h\nu > 100$ eV, all these have a direct impact on ionization and heating. Even in embedded phases of a young star life, where the core is forming, UV and X-ray radiation from nearby stars and astrophysical sources play a role (Gorti and Hollenbach, 2009) Typically, the UV flux is $\sim 1.6 \times 10^{-3}$ erg cm^{-2} s^{-1}. The interstellar radiation field coming from outside sources, can overtake far-UV effects, but only in the outermost regions of accretion disks (Cleeves et al., 2013).

3.3.1.1 X-ray ionization

Primarily from the magnetized corona, X-ray radiation are significantly higher than the ones observed from the Sun. Their energies coast between 10^{29} and 10^{31} erg s^{-1} (Telleschi et al., 2007). X-ray flares in T Tauri stars can generate plasma temperatures up to 10^8 K (Imanishi et al., 2001; Stelzer et al., 2007). These flares are typically caused by magnetic reconnection events occurring either in the stellar magnetosphere, at the star-disk interface, or above the circumstellar disk (Feigelson and Montmerle, 1999). Accretion shocks also produce X-ray emissions. Since the temperature of the accreted plasma is only around 10^3 K, it cannot account for X-ray radiation. What enables this process is the accretion shocks that generate temperature of the order of $\sim 10^6$ K. X-rays can then be absorbed back into the gas, hence contributing to heating. Compelling evidence supports the existence of accretion-related X-ray production, particularly within the very soft X-ray spectrum. For instance, observations have identified excess flux in the O VII and Ne IX line triplets, as presented by Kastner et al. (2002) and Güdel and Telleschi (2007).

Stellar radiation efficiently ionizes atomic hydrogen, forming a hot, ionized layer at the disk surface where free electron density surpasses that of neutrals (Gorti et al., 2009). This layer is pivotal for the system global dynamics, potentially enhancing accretion efficiency and initiating photoevaporative winds and jets. These processes help transport angular momentum away from the disk (Ercolano and Picogna, 2022).

According to Güdel (2015), we can provide a simple X-ray photoionization estimate by approximating a point-like source spectrum with an exponential, $F_\varepsilon = F_0 \exp(-\varepsilon/kT)$, where ε is the photon energy and T the source temperature. Naturally, X-ray radiation will be absorbed by interacting with the gas medium. This photoelectric effect has the following cross section,

$$\sigma(\varepsilon) = \sigma_0 (\frac{\varepsilon}{kT})^{-3}. \tag{3.13}$$

Here σ_0 is the cross section of photoionization normalized to the source. For photons with energies below 600 eV absorption is mainly due to H and He, and above this energy threshold absorption is due to heavier elements (Wilms et al., 2000). The ionization rate is expressed as,

$$\zeta_X = \int_{\varepsilon_0}^{\infty} \sigma(\varepsilon) \frac{F_\varepsilon}{\varepsilon} e^{-\tau(\varepsilon)} d\varepsilon. \tag{3.14}$$

τ, here, is the optical depth. Its expression with the cross section and column density, is $\tau = \sigma_0 N_H$. This approach corresponds to photoionization caused by the photon flux of neighboring stars. In Eq.3.14, the geometrical dilution was not included. however, X-rays are strongly attenuated as a function of height and radius. And although geometrical dilution should attenuate X-ray ionization, they could stay the dominant midplane ionization source for large regions of the disk due to scattering (Rab et al., 2017).

In the case of the central star X-ray emission, the radiation spectrum can also be approximated by an exponential. In particular, stellar X-rays are absorbed continuously along their pathway from the star. Glassgold et al. (1997) separate the flux spectrum dependance on energy and position at the disk. For a flat thin disk the spectrum is,

$$F(\varepsilon, \varpi) = \frac{z}{\varpi} \frac{1}{8\pi\varpi^2} \frac{L_X}{kT} \times \frac{1}{\varepsilon} e^{-\varepsilon/kT}. \tag{3.15}$$

First and foremost, this expression applies when $\varepsilon > \varepsilon_0$, where ε_0 is the low-energy cutoff due to absorption from the star to the disk. z/ϖ indicates the X-ray angle of attack. The ratio L_X/kT is the normalized total luminosity. And last, the factor $1/\varepsilon$ converts the energy flux to photon flux. As the X-rays reach the disk surface, their flux is further attenuated according to the photoionization cross section. Almost all of the initial X-ray energy is consumed in the ionization process, with about $\Delta\varepsilon \sim 37$ eV required for each ionized pair (Güdel, 2015).

In Fig.3.5, the ionization rate remains constant due to the energy cut off. It, then, quickly decreases with greater column densities. As deeper in the disk, the harder photons are responsible for ionization. Deeper than $N_\perp = 10^{24}$ cm^{-2}, X-rays with energies beyond 10 keV prevail and for which the Compton cross section dominates over absorption. Hence, ionization is lead by Compton scattering.

3.3.1.2 Far-UV ionization

UV rays operate the same as X-rays, although, UV radiation is limited to superficial disk layers as they are attenuated faster, see Fig.3.6 for illustration. The column densities at which UV photons are absorbed lay between $10^{19} - 10^{20}$ cm^{-2}. Ionization rates of UV photons are described as follows (McElroy et al., 2013),

$$\zeta_{UV} = G_0 \alpha \times e^{-\beta A_\nu}, \tag{3.16}$$

where A_ν is the extinction caused by dust, α and β the ionization rate coefficients specific to the species, and last, G_0 is the intensity of the radiation field. This intensity

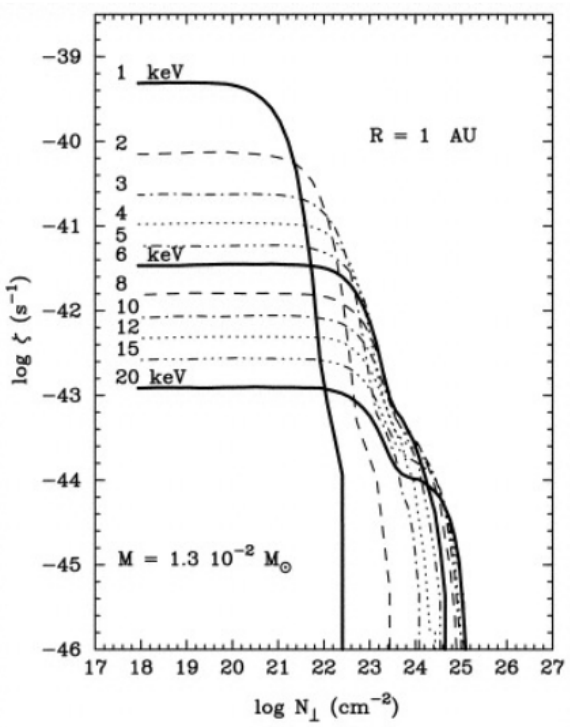

Figure 3.5: Ionization rates for monochromatic X-rays are shown as a function of column density. They are measured vertically in a disk at a radius of 1 au for a gas with a standard interstellar composition. The X-ray luminosity of the source is normalized to 1 erg s^{-1}. The characteristic shoulder at deeper levels is due to Compton scattering. From Igea and Glassgold (1999).

can be explicitly expressed in terms of the Far-UV luminosity and distance from the star,

$$G_0 = \left(\frac{1}{1.6 \times 10^{-3} \text{ erg s}^{-1} \text{ cm}^{-2}}\right)\left(\frac{L_{FUV}}{10^{30} \text{ erg s}^{-1}}\right)\left(\frac{\varpi}{3 \text{ au}}\right)^{-2} \tag{3.17}$$

In the case of carbon, where $\alpha = 2.1 \times 10^{-10}$ s^{-1} and $\beta = 2.6$ (McElroy et al., 2013). If additionally we take the UV luminosity presented in Cleeves et al. (2013), $L_{FUV} = 10^{31}$ erg s^{-1}, one can estimate ionization as seen in Fig.3.6.

3.3.2 Galactic cosmic rays

Galactic cosmic rays (GCRs) are energetic particles originating from galactic sources, for instance supernova remnants (Schlickeiser, 2013). GCRs are mainly composed of electrons and protons, and are linked to fundamental questions related to dust growth, chemical complexity in the disk, and energetic events in it (Padovani et al., 2020). Given their nature, GCRs initiate ionization in disks through collisions with gas molecules. These particles primarily collide with H_2 and He, subsequently creating secondary

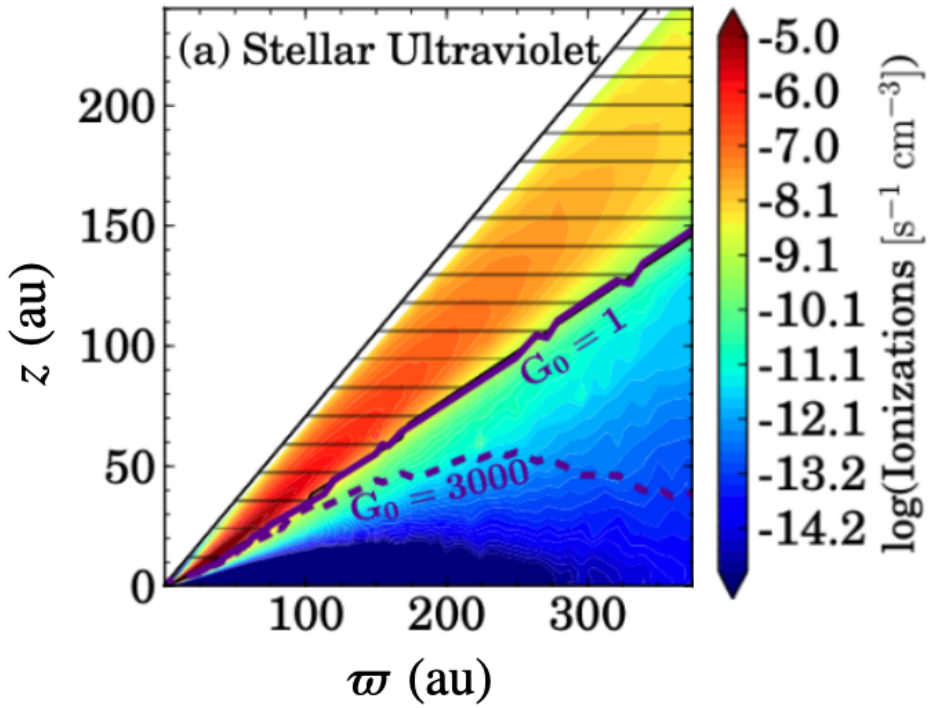

Figure 3.6: Contribution of stellar UV radiation in ionizing the surface layer of accretion disks as estimated by Cleeves et al. (2013). The colors represent the volumetric ionization rate of carbon on a uniform scale ($n_C \zeta_{UV}$). The shaded region indicates where UV contributes over 30% of the total ionizations per unit time and volume within the disk. The volumetric ionization rate serves as an approximate measure of the electron production rate per unit volume. G_0 is a parameter indicating the intensity of the radiation field. Adapted from Cleeves et al. (2013).

particles that further interact with disk material fueling a cascade of ionizing events (Padovani et al., 2009). Contrarily to X-rays, GCRs are efficient in outer disk regions (i.e. beyond 100 au Glassgold et al. 2012). Cosmic rays impact the disk most for low-energies, i.e. below 1 GeV. At these energies CRs have peak cross section, thus efficiently H_2 excitation (Padovani et al., 2018). Although our study does not aim to study regions this far into the disk, we still consider the GCR contribution to the disk, as it might become useful in later bigger scale accretion-ejection simulations.

In recent work considering cosmic ray influence, Padovani et al. (2018) developed an ionization model adapted for dense media such as accretion disks. This model emphasizes the critical importance of accurately selecting the transport regime for CR protons and using robust models for the generation and transport of secondary CRs to ensure precise ionization calculations. The study details how the ionization rate of molecular hydrogen varies with column density, taking into account various parameters of the CR energy spectra (Fig.3.7).

The stellar magnetosphere as well as the winds work to attenuates the galactic cos-

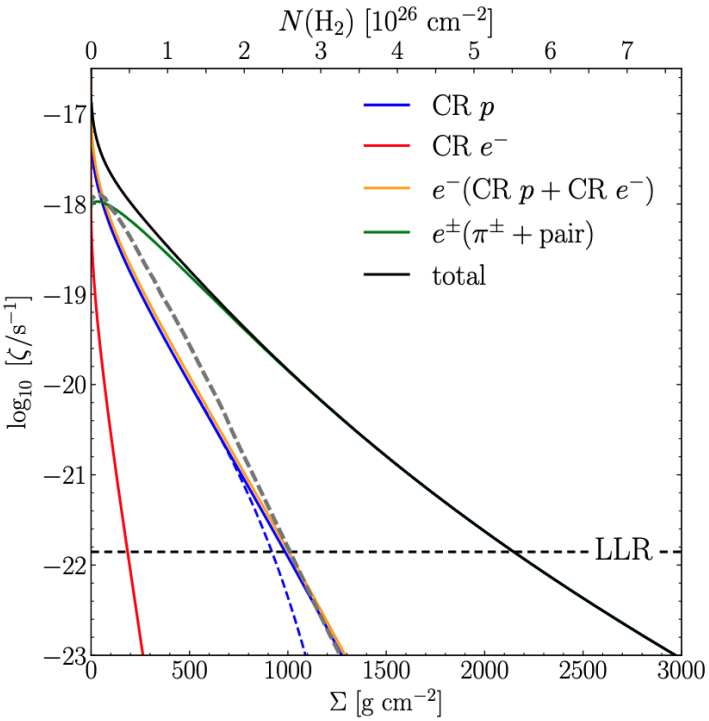

Figure 3.7: This plot shows hydrogen production rate in terms of surface density Σ and column density N for different cosmic ray contributors. The dashed horizontal line delimits the maximum ionization rate of radioactive nuclei. Taken from Padovani et al. (2018).

mic ray flux that reaches the disk (Cleeves et al., 2013; Wurster and Li, 2018; Fujii and Kimura, 2022). Cosmic rays are believed to be a key source of ionization in protoplanetary disks, though their precise role remains unclear. In our solar system, stellar winds can hinder the propagation of cosmic rays in the circumstellar environment, affecting their interaction with the accretion disk. The Sun blocks the low-energy end of the Galactic Cosmic Ray spectrum within the heliosphere. These low-energy CRs play a crucial role in ionizing H_2 in the interstellar medium (Padovani et al., 2009). The solar wind modulates these CRs, especially for energies below 100 MeV, with CR flux at Earth varying by more than one order of magnitude between solar minimum and maximum (Cleeves et al., 2013).

Originating from the hot solar corona, the dense, slow solar wind carries magnetized plasma. The solar wind density and magnetic field strength decrease with distance until the interstellar medium pressure exceeds that of the solar wind, causing a magnetic wall that blocks low-energy CRs (Opher et al., 2011). Young T Tauri stars, with their strong magnetic activity, are expected to exhibit similar stellar winds, forming an equivalent shielding sphere that expels low-energy CRs (Vidotto et al., 2009). Although the mechanisms of magnetic field generation differ between T Tauri stars and main sequence stars like the Sun, the ability to drive stellar winds depends on the presence of a corona, stellar mass, rotation, and magnetic topology.

The extent and shape of the cosmic ray exclusion zone around T Tauri stars are mainly inferred from our understanding of the solar heliosphere. The GCR shielding could potentially span across the entire disk (Cleeves et al., 2013). However, the cosmic ray particles responsible for ionization at column densities above 100 g/cm^2 possess energies above a few GeV. Despite these insights, the impact of stellar wind modulation on cosmic rays at such high energies remains unclear.

3.3.3 Local production of energetic particles

Cosmic rays can reach high column densities, but their impact may be negligible due to stellar shielding. On the other hand, locally generated high energy particles do not suffer the same attenuation process and are able to interact and considerably ionize the stellar environment (Rodgers-Lee et al., 2017; Padovani et al., 2016, 2018; Gaches and Offner, 2018).

3.3.3.1 Radioactive decay

Entrenched deep in the disk, short-lived radionuclides are also able to ionize disk material (e.g.,Umebayashi and Nakano 1981; Finocchi and Gail 1997; Umebayashi and Nakano 2009). Their decay produces energetic particles, such as gamma photons, alpha particles, and subsequently secondary particles (e.g., Dalgarno et al. 1999; Glassgold et al. 2012). The sources of these ionization events are synthesized in massive stars and supernovae, which then dispersed in molecular clouds (Timmes et al., 1995). Hence, radionuclides - such as ^{10}Be, ^{26}Al, ^{36}Cl, ^{41}Ca, and ^{60}Fe - find their way in accretion disks (Lee et al., 1998; Wasserburg et al., 2006).

To compute ionization caused by radionuclide decay, Cleeves et al. (2013) take into account the radiative transfer equations for decay products in the disk, considering energy losses in regions with low surface density. They computed the total ionizing particle flux and ionization rates at various positions in the disk, applying these results to different disk models. They provided a power-law approximation for the ionization rate in the disk midplane as a function of gas surface density and time (Fig.3.8). The ionization rate of short-lived radionuclides is weakly dependent on both time and surface density,

$$\zeta_{\mathrm{H_2}} = 2.5 \times 10^{-19}\,\mathrm{s}^{-1} \left(\frac{1}{2}\right)^{1.04t} \left(\frac{\Sigma}{\mathrm{g\ cm}^{-2}}\right)^{0.27}. \tag{3.18}$$

For a typical disk of age 1 Myr, the ionization rate ranges from $\zeta \sim 10^{-19} - 10^{-20}\mathrm{s}^{-1}$, establishing a minimum ionization rate. In the outer disk and near the midplane, ionization is primarily driven by short-lived radionuclides, with long-lived radionuclides contributing at much lower levels, around a few 10^{-22} s^{-1} (Padovani et al., 2018).

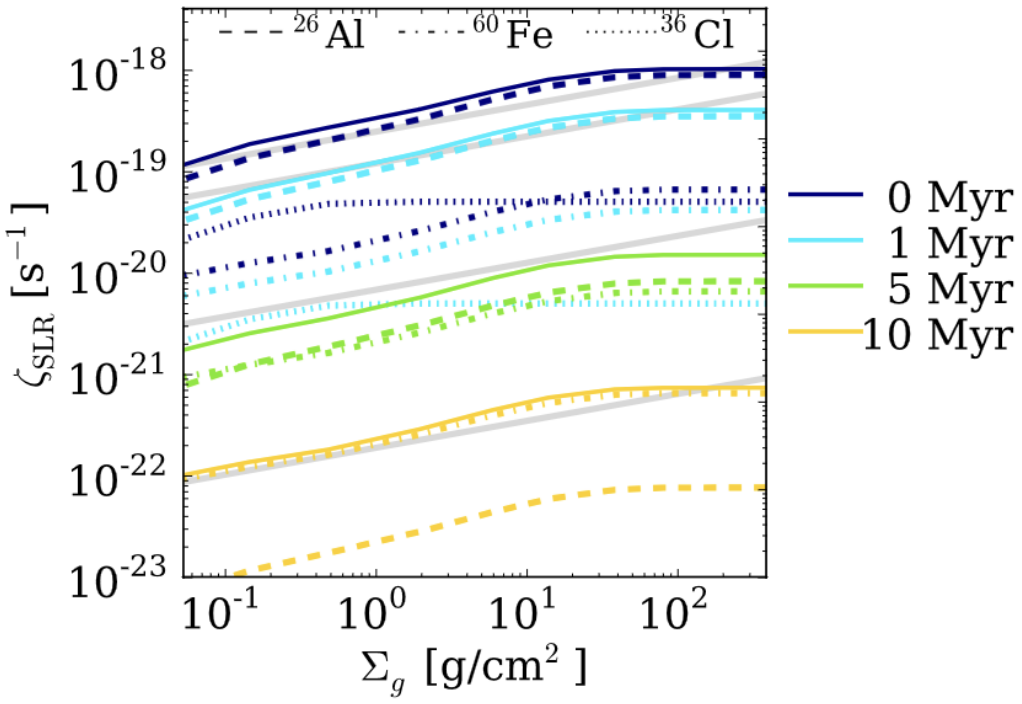

Figure 3.8: Midplane ionization rate as function of surface density at different disk ages. Taken from Cleeves et al. (2013).

3.3.3.2 Shock induced particles

As accretion proceeds, the stellar gravitational potential accelerates disk material which then collides with the stellar surface, creating a shock front (Offner et al., 2019). This shock front mainly produces UV and X-ray photons as gas material is heated and ionized (Güdel and Telleschi, 2007). Moreover, the shock generates energetic particles that contribute to ionizing the surrounding gas (Padovani et al., 2016). The primary process at play is the first-order Fermi process which provides energy to charged particles to ionize gas once a collision occurs with the disk material. The preliminary study conducted by Padovani et al. (2016) quantified shock induced acceleration due to accretion. The process is similar to cosmic ray acceleration in supernova remnants, where propagation in partially ionized and magnetized medium is considered. Later, Gaches and Offner (2018) show that accretion is capable of sustaining a strong local cosmic ray flux.

In their model, Offner et al. (2019) take interest in attenuation of a shock-accelerated CR spectrum generated at the stellar surface. Following the same principale as photons, cosmic rays go through a geometric damping as they propagate outwards. They also interact with gas, thus loose energy as they evolve through the medium. A number of parameters needs to be accounted for to pinpoint the contribution of local CRs in ionization. Such parameters are gas density, turbulence, and magnetic field geometry. In terms of turbulent diffusion, Rodgers-Lee et al. (2017) show that CR spectrum

attenuation varies with turbulence - an attenuation $\propto R^{-2}$ in the case of free streaming, and $\propto R^{-1}$ when the system is most diffusive.

Before thermalizing or leaving the system, stellar CRs can go through three distinct regions with each its damping factor. In accretion funnels, CRs meet upstream totally ionized gas where Coulomb and pion production take place Schlickeiser (2013). The high ionization translates into a strong coupling with the magnetic field. In accretion funnels a typical attenuation by a factor between $10 - 100$ is estimated by the time CRs reach the disk Offner et al. (2019). Above the disk, stellar CR flux suffer marginal energy losses. The main attenuation in this region is geometric, $\propto R^{-2}$, while across the disk surface, the ionization rate is around 10^{-16} s^{-1}, i.e. four orders of magnitude higher than galactic cosmic rays. The three regions CRs travel through are summarized in Fig.3.9.

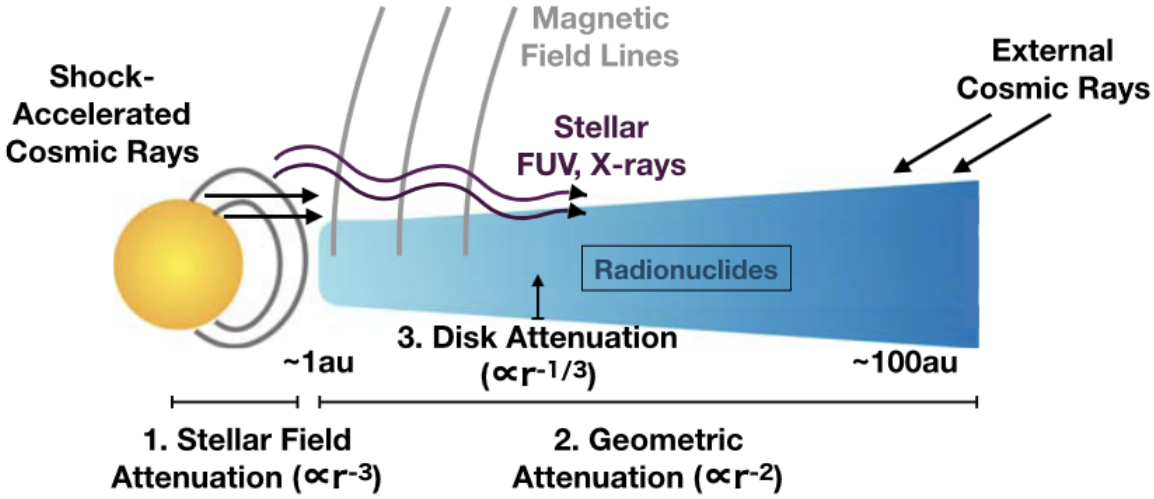

Figure 3.9: A schematic illustrating ionization sources and their respective regions. This focuses exclusively on local ionization sources from the central star, which generally dominate over external sources such as X-rays, stellar cosmic rays, and far-UV backgrounds. Taken from Offner et al. (2019).

3.3.3.3 Flares

Similarly to the Sun, young stars exhibit flaring activity, generating X-ray radiation (Koyama et al., 1996; Getman et al., 2021). Unlike solar flares, YSO flares are significantly more energetic and frequent. These flares can release total X-ray energies ranging from 10^{35} to 10^{37} erg, which likely represent only a small fraction of the total radiative and magnetic energy released (Emslie et al., 2012). Observations suggest that protostellar flares are about 10^4 to 10^6 times more energetic than the largest recorded solar flares (Cliver and Dietrich, 2013). However, the mechanisms triggering these YSO flares, particularly during the T Tauri phase, remain a topic of ongoing debate. Difficulty in constraining flares in YSO arise from the low resolution of the instruments and

the blinding central object. When modeling YSO flares, parameters such as magnetic fields geometry and rapid rotation add complexity.

The efficiency of cosmic ray production in YSO flares remains uncertain. Due to their higher energy compared to solar flares, CR particles in YSO flares are expected to reach much higher energies. CR protons produce gamma rays via nuclear interactions, while CR electrons emit millimeter/submillimeter signals via synchrotron radiation. These signals can penetrate dense, cold media, making them valuable for studying flaring activity and CR production.

Theoretical modeling of non-thermal signatures from YSO, including emissions from jets and magnetospheres, has been explored in several studies (del Valle et al., 2011; Araudo et al., 2021). However, these studies mainly focus on specific T Tauri stars or protostellar jets. The broader detection of non-thermal signatures from YSO flares is a relatively new area of investigation. For example, Waterfall et al. (2019) modeled radio and X-ray emissions from T Tauri flares, while Kimura et al. (2023) modeled gamma-ray emissions.

Since the precise particle spectra and fluxes of young stars are unknown, we must infer this information from the Sun. Stellar energetic particles are likely produced by flares or shock waves driven by coronal mass ejections (CMEs) (Reames, 2015). In particular, particle fluxes are not continuous, but occur in events lasting several hours to days. Feigelson et al. (2002) estimated that solar energetic particle fluxes (SEP) in young stars could be about 10^5 times greater than in the Sun, based on observed X-ray luminosities of solar analogs in the Orion Nebula. T Tauri stars, known for their high activity, experience X-ray flares several times a day, potentially even below detection limits (Getman and Feigelson, 2021). Consequently, these frequent X-ray flares and corresponding SEP emission events can overlap, leading to a continuous and enhanced SEP flux.

Rab et al. (2017) study one particular event presented in Reedy (2012), where, at 1 au, a proton flux with an energy > 10 MeV is observed. In their model, stellar particles propagate straightforward while continuously depositing energy in the medium without scattering. At hydrogen column densities $N_H > 10^{25}$ cm^{-2}, even the most energetic particles are stopped, leading to a decrease in the SEP ionization rate. Since the radial hydrogen column densities in complete T Tauri disks typically exceed 10^{25} cm^{-2}, the SEP ionization rate in the midplane at 1 AU from the star is $\zeta_{SP} << 10^{-20}$ s^{-1}. Under the assumed SEP flux, SEPs become the dominant source of H_2 ionization in the warm molecular layer of the disk beyond the CO ice line, assuming they are not shielded by magnetic fields.

More recently, Brunn et al. (2023) and Brunn et al. (2024) extended the stellar particle range by considering flaring episodes above the disk. These events would ionize the disk farther than what has been achieved in the models of Rab et al. (2017), Rodgers-Lee et al. (2017), and Fraschetti et al. (2018). In the first article, Brunn et al. (2023) find that energetic particles following reconnection events present ionization rates which exceed X-ray, radioactive decay, and stellar energetic particles. The reference case is a flare entering the disk at 0.1 au with a temperature of 1 MK. The particle follows a

vertical magnetic field and produce an ionization rate of 10^{-9} s^{-1} at $N \sim 10^{25}$cm^{-2}. These ionization values are overestimated since temporal effects are not taken into account. Another reason is that ionization is considered as local, while it is actuality spread over the area of the magnetic field line footpoints.

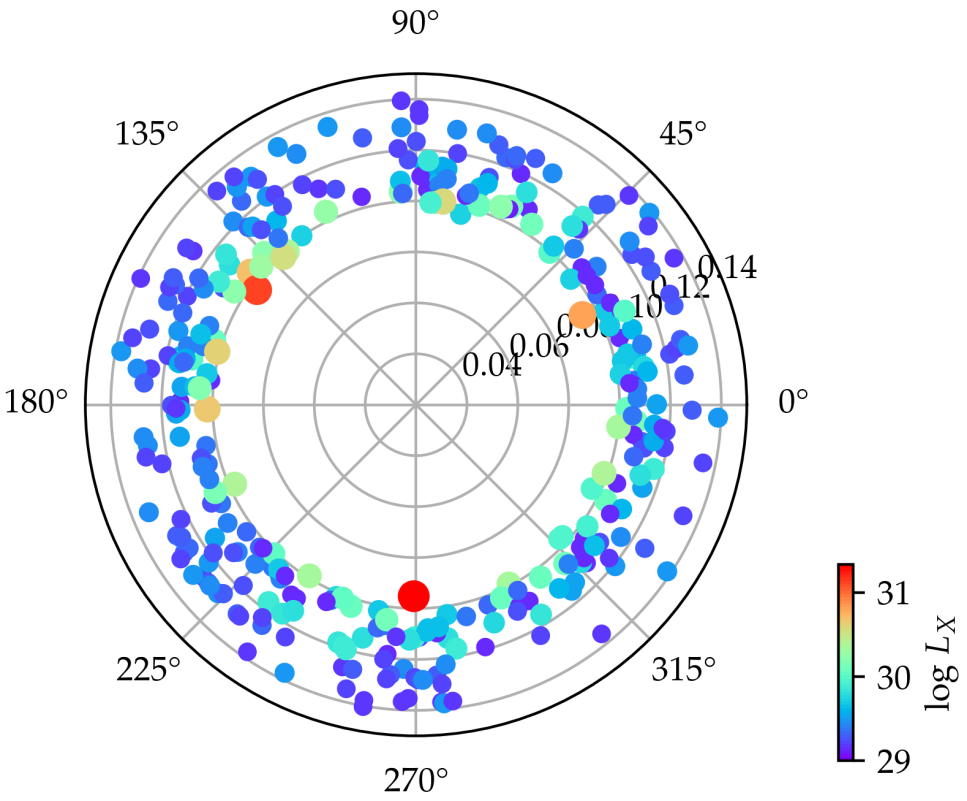

Figure 3.10: Impact positions of charged particles created from flares above the accretion disk. The colors correspond to the luminosity of the flare, and the dots different sizes show the real size of these events on the disk.

Extending this work, Brunn et al. (2024) incorporate a time-dependent model where flare frequency and luminosity are considered (Fig.3.10). By examining the average ionization rate of a single flare and comparing it to X-rays, they find that at low column densities, $N < 10^{22}$ cm^{-2}, both sources, X-ray photons and energetic particles, yield comparable average ionization rates. However, at high column densities $N > 10^{22}$ cm^{-2}, particles emitted by flares generate ionization rates 1 to 3 orders of magnitude greater than those induced by X-rays. These flares are very promising as they can ionize the disk up to 0.2 au. Hence, heating up the disk and enabling turbulence to proceed reduce the dead zone extension in the midplane. By reducing the dead zone, a higher accretion rate is possible in the disk.

The size of the flares is still subject of debate. Especially when studying the existence of large flares connecting the star and the disk surface. Favata et al. (2005) examine

large flares observed in the Orion cloud using the continuous Chandra Orion Ultradeep Project (COUP) data. They conclude that 10 of these flares occurs between 3 and 5 stellar radii. Such large eruptive structures are not observed in older stars. They suggest that the magnetic loops possibly connect the star and the disk at the corotation radius. The reasoning behind their conclusion is that loops anchored at the stellar surface would face major instabilities due to young stars being fast rotators. Therefore, loops anchored at the star and the disk are good candidates to explain observations.

3.4 Heating and cooling

Understanding ionization processes is important not only to determine the chemical composition of YSO environment, but also to the heating contribution that results from it. All the aforementioned ionization processes deposit energy as they interact with the material of the disk and the jet material. It heats up the gas and the dust changing the disk thermal equilibrium (Igea and Glassgold, 1999; Ercolano et al., 2008, 2009; Rab et al., 2017). Ionization-induced heating is especially significant in the upper layers of the disk, where ionization rates are higher due to the penetration of external radiation (Glassgold et al., 2004). For example, when X-ray photons ionize an electron, the electron loses its remaining kinetic energy through inelastic collisions with the atoms and molecules in the disk, depositing heat. Approximately half of the energy from X-rays and cosmic rays is converted into heat (Glassgold et al., 2012). Additionally, other sources such as viscosity, molecular emission, thermal Bremsstrahlung contribute to the total heating and cooling processes.

Dalgarno et al. (1999) were the first to estimate heat deposition by ionization in a hydrogen-helium gas mixture. They studied the heat produced by elastic scattering and collisional de-excitation of rotationally excited hydrogen molecules. Building on this, Glassgold et al. (2012) studied the heating resulting from all ionization and excitation processes, focusing on the interactions between ions generated by cosmic rays and X-rays and heavy neutral species, known as chemical heating. In molecular regions such as dense cores or protoplanetary disks, chemical heating is the dominant factor, contributing to 50% of the energy used to produce ion pairs. The heating per ion pair ranges from about 4.3 eV in diffuse atomic gas to about 13 eV, in moderately dense molecular clouds, and up to 18 eV, in highly dense accretion disk regions. Cosmic ray and X-ray heating depends on the physical properties of the medium, including molecular and electron fractions, total hydrogen nucleus density, and temperature. In addition, chemical heating, the primary mechanism for cosmic ray and X-ray heating, also plays a role in UV-irradiated molecular gas. In this section, we heavily rely on the review made by Woitke (2015). Sources of cooling and heating are numerous. Fig.3.11 describes a global picture of heating and cooling distribution in the disk of various physical processes studied.

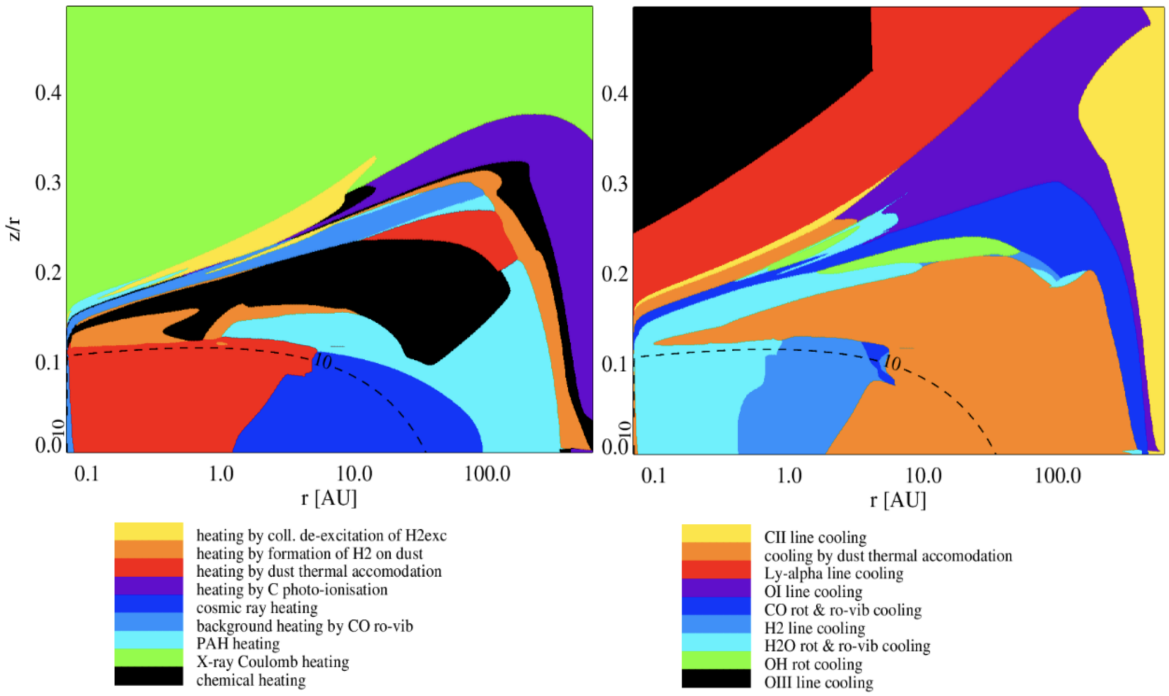

Figure 3.11: A global view of heating and cooling distribution in the disk. On the left we have heating processes, while the right panel presents cooling. At each point on the disk, ProDiMo solves the gas heating and cooling balance, resulting in the gas temperature structure T_g(r,z). The standard setup includes 102 heating processes and 95 cooling processes. From ProDiMo official website (https://prodimo.iwf.oeaw.ac.at/heating-and-cooling).

3.4.1 Radiative heating and cooling

In the LTE approximation, all paths of storing energy in the gas are included in the internal energy term. Such paths are ionization potential, chemical binding energy, electronic excitation, etc. Interactions between internal processes mentioned before are assumed to rapidly redistribute the available energy among all the internal energy sources. By balancing photon energy losses and gains, the radiative heating rate is expressed as follows,

$$Q = 4\pi \int \kappa_\nu \left(J_\nu - B_\nu\right) d\nu, \tag{3.19}$$

where κ_ν is the frequency dependent absorption coefficient, J_ν is the mean spectral intensity, and B_ν the Planck function which depends on the temperature.

Gas exposed to external radiation with a higher temperature than the local gas and dust is the typical scenario of astrophysical material. Generally speaking, a small amount of external radiation penetrates deep in the disk. In addition, given the local characteristics of gas around YSOs and using Eq.3.19, radiative heating occurs thanks to high energy absorption processes where κ_ν is large (Woitke, 2015). On the other hand, cooling is due to emission lines at large wavelengths (see Fig.3.12).

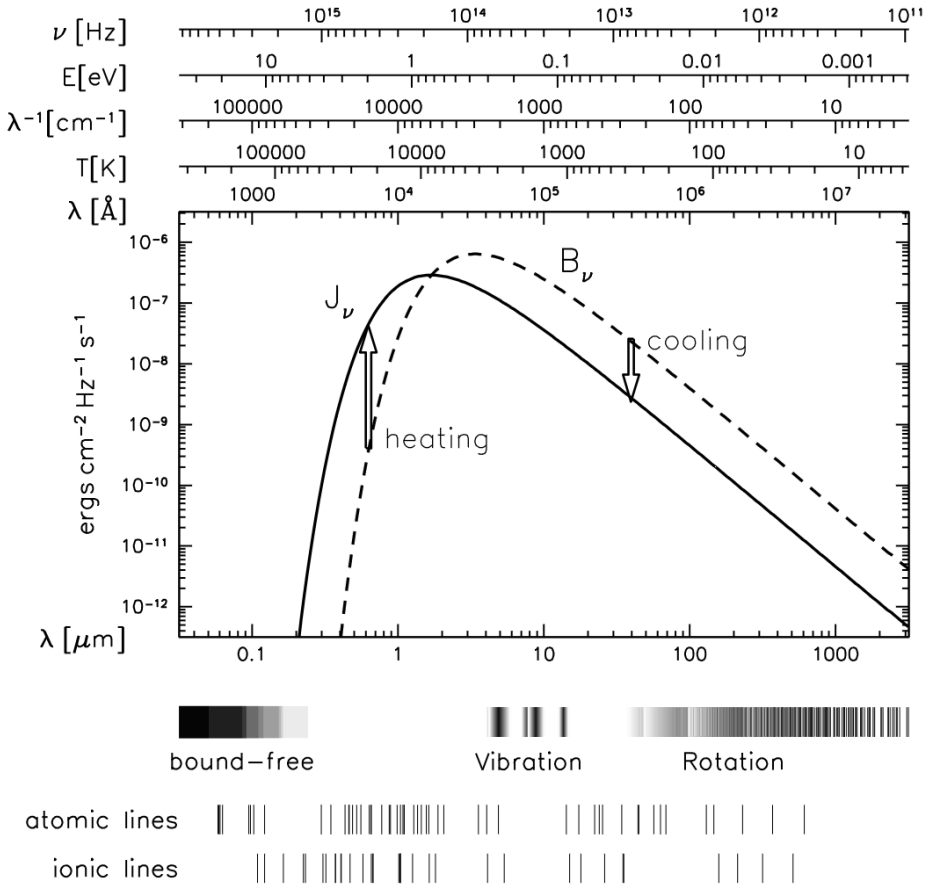

Figure 3.12: Radiative heating and cooling in LTE. The arrows illustrate the energy exchange between matter and radiation. The lower most panel indicates the wavelengths of some radiative processes. Taken from Woitke (2015).

3.4.2 Photoionization and recombination

Photoionization and recombination are responsible for heating and cooling, respectively. One can express the general form of photo-dissociation and recombination by taking photo-processes of type,

$$AB + h\nu \rightleftharpoons A + B, \tag{3.20}$$

A, B can be replaced by H^+ and e^-, hence AB would be H. Instead of hydrogen, carbon or any other chemical component can be considered. The forward production rate is,

$$k_f = 4\pi \int_{\nu_{thr}}^{\infty} \frac{J_\nu}{h\nu} \sigma(\nu) d\nu. \tag{3.21}$$

Here, ν_{thr} is the threshold frequency, and $\sigma(\nu)$ is the cross section of the bound-free forward reaction (Woitke, 2015). Since energy is conserved, $h\nu = h\nu_{thr} + 1/2mv^2$ with $1/2mv^2$ the excess thermal energy produced by the reaction. A possible way is for

A and B to be in an excited state. An other way, in the case of molecules, is for rotational and vibro-rotational energies to be carried away by products. All in all, these products should also thermalize as they interact with the medium. Considering the photoionization heating rate of an electron from the bound to the free composition we get,

$$\Gamma = 4\pi N_{AB} \int_{\nu_{thr}}^{\infty} J_\nu \frac{\nu - \nu_{thr}}{\nu} \sigma(\nu) d\nu, \tag{3.22}$$

N_{AB} is the number density of population AB.

To obtain the cooling rate, one can follow the same process. In this case, a direct recombination reduces the number of particles. Contrary to photoionization, the cooling rate uses the recombination coefficient, k_b. It writes,

$$\Lambda = N_A N_B k_b \langle E_{th} \rangle. \tag{3.23}$$

Here, $N_A N_B k_b$ is the number of recombination events per volume and time, it is in units of $cm^{-3}\ s^{-1}$. $\langle E_{th} \rangle$ is the mean energy lost after a recombination process (for the detailed expression of $\langle E_{th} \rangle$ see, Eq.32 of Woitke (2015)).

3.4.3 High energy heating

As presented in Sec.3.3, when X-rays and cosmic rays interact with the matter of the disk a series of collisions occur, which induces ionization, radiative and chemical processes that reduce incrementally the kinetic energy of the original ionizing particle. X-rays and cosmic rays begin to interact with the gas via primary ionization, e.g. by knocking out K-shell electrons from surrounding atoms and molecules (see Sec.3.1). The resulting electrons travel through the gas, ionizing other particles along the way, generating more ionization. The ionized particles can produce secondary X-rays, and the recombination of the ionized atoms can emit secondary UV photons, leading to further ionization. Coulomb heating is the most effective process in heat generation (Dalgarno et al., 1999), where super-heated electrons undergo elastic collisions with thermal electrons, thereby accelerating and heating them. The general form of heating for these processes is,

$$\Gamma_{X,CR} = \zeta_{X,CR} \left(N_H q_H + N_{H_2} q_{H_2} + ... \right), \tag{3.24}$$

where q is the amount of energy produced along the ionization cascade, and is in units of erg. Values of q range between a fraction to a few eV per ion-pair (Dalgarno et al., 1999).

Solving the radiative transfer equations of these processes is crucial to understand the heating. Ionization rates and UV radiation field are all subject to absorption and scattering, which greatly affects the heating distribution. The ionization distribution can drastically change if instead of absorption only, one also considers scattering (Fig.3.13).

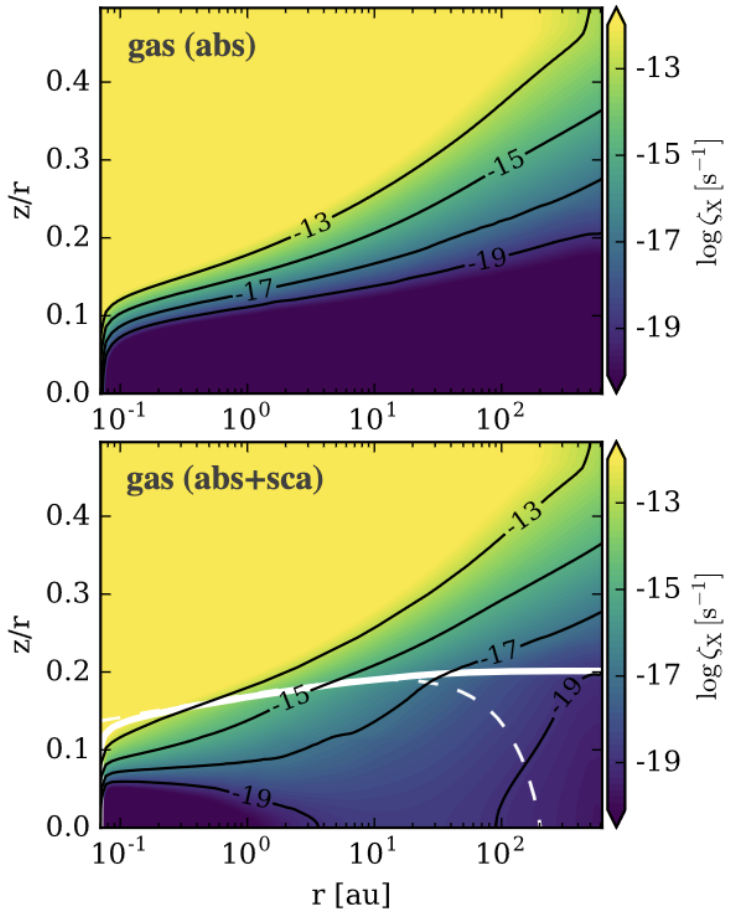

Figure 3.13: The top panel of the 2D disk structure model displays the X-ray ionization rate considering only gas absorption, while the bottom panel includes both gas absorption and scattering. The white solid contour line represents $N_H = 2 \times 10^{24}$ cm^{-2}, roughly indicating the X-ray scattering surface. Below this surface, ζ_X becomes predominantly influenced by scattered X-ray photons. Taken from Rab et al. (2018).

Flaring episodes produce high energy particle that participate in heating. Out of all the processes presented before, these events produce heating rates that match what was injected in chapter 4. They additionally increase the viscosity in the disk, which in turn increases the viscous heating in the disk. The heating rate distribution computed for flaring episodes that originate from star disk magnetic interaction can be seen in Fig.3.14.

3.4.4 Viscous heating

Viscosity accounts for a part of the heating in the disk, as it slows down the disk making it accreting towards the central mass. When considering a disk isolated from

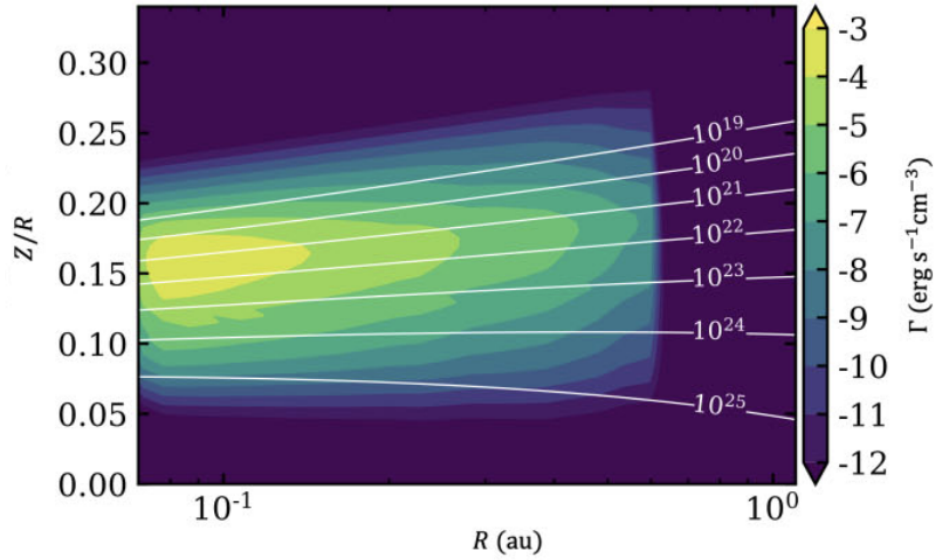

Figure 3.14: The distribution of the heating rate in the disk, produced by flares generated from star-disk magnetic reconnection. Taken from Brunn et al. (2024).

its environment, we can assume the following,

$$\frac{d}{dt}\left(E_{\text{potential}} + E_{\text{kinetic}} + E_{\text{thermal}}\right) = 0. \tag{3.25}$$

Computing the variation of potential and kinetic energies during a small time interval dt at a position ϖ bears $\frac{d}{dt}(E_{\text{potential}} + E_{\text{kinetic}}) < 0$. It follows that the sum of potential and kinetic energies must decrease for accretion to proceed. Given the conservation of energy, Eq.3.25, the net decrease of $E_{\text{potential}} + E_{\text{kinetic}}$ must be compensated by an increase of the gas internal energy.

Viscous heating in the disk is strongly dependent on the α parameter as it hides the microphysics of the disk viscosity. For a geometrically thin disk, the heating can be expressed as (Pringle, 1981),

$$\Gamma = \frac{9}{4}\alpha\rho c_s^2. \tag{3.26}$$

As shown in Brunn et al. (2024) the flaring activity can change the disk structure by increasing the area where MRI is active and where viscosity is non-negligible (Fig.3.15). Essentially, flares should also create favorable conditions for turbulence and disk dynamo to take place. Referring to this work, viscous heating encompasses a bigger region with the help of energetic particles.

3.4.5 MHD processes

Alfvén waves are good candidates for heating the close vicinity of the stellar and disk atmospheres. The damping of these waves imparts energy onto the medium heating

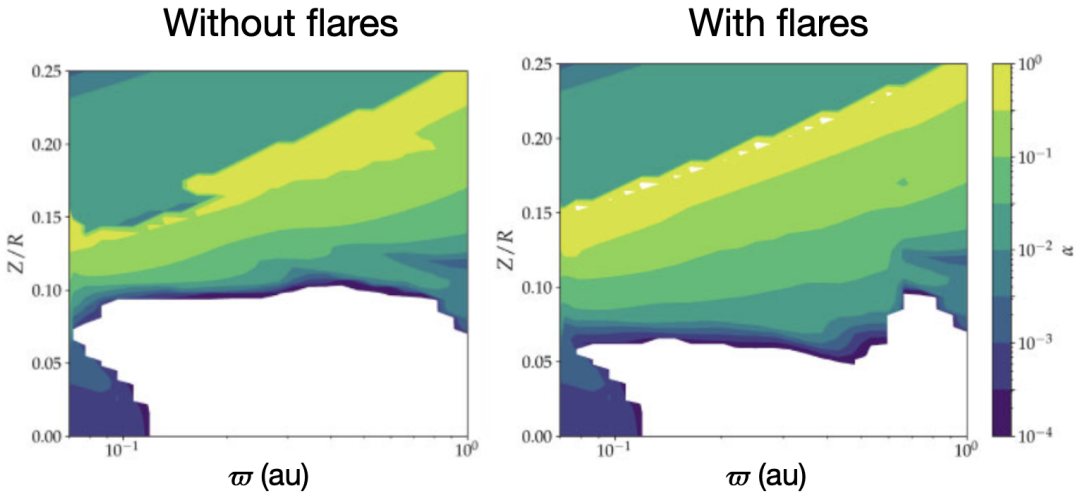

Figure 3.15: Plots of the 2D maps of the viscous parameter α expressed by (Thi et al., 2019) and adapted for MRI-driven disks. The explicit formulation of α can be found in Eq.17 of Brunn et al. (2024). The figure is adapted from Brunn et al. (2024).

it up. Vasconcelos et al. (2000) proposed that turbulence in the disk generate Alfvén waves that propagate in the ionized regions of the disk towards the disk, heating up the gas material. Although, as mentioned before, for heating to occur, the Alfvén waves need to drop part of their energy. The authors study two damping processes, nonlinear and turbulent mechanisms. For the turbulent damping, a turbulent cascade channels the energy of the waves from large-scale regions to smaller ones along a damping length proportional to the magnetic field and velocity (Eq.22 in Vasconcelos et al. 2000). The dissipation of this energy through turbulence is governed by a small-scale linear absorption mechanism. More than what the viscosity can provide, Alfvén wave damping modes can partially ionize the disk starting around ~ 0.5 au, with a frequency about 10% the cyclotron frequency of an ion and a wave amplitude 0.2% of the Alfvén velocity. The difference between the two mechanisms is where Alfvénic heating dominates over the viscous one. In the turbulent case, Alfvén heating dominates over all the disk, while in the nonlinear case, that is true for $\varpi > 0.2$ au. This path of heating can also increase the temperature of the stellar magnetosphere. In short, although nonlinear and turbulent damping have been treated as different mechanisms, they only differ in their profile and could be connected to the same physical processes.

Measures of the solar magnetic field show turbulent fluctuations of this field in the plasma (Goldstein et al., 1995; Bruno and Carbone, 2013). Upon reaching the smallest scales, the turbulent energy dissipates heating up the plasma (Schekochihin et al., 2009). Also in the case of the Sun, the cascading energy to smaller scales is thought to occur through opposite propagating Alfvén waves (Chandran and Hollweg, 2009). To generate inward-propagating waves, studies parameterize the instabilities (e.g., Viñas and Goldstein 1991; Del Zanna et al. 2001). Other studies invoke velocity shear instabilities (Roberts et al., 1992; Breech et al., 2008). A third possible mechanism could

be where outward and inward propagating Alfvén waves couple (Hollweg and Isenberg, 2007). Although, mostly studied in the context of solar physics, this mechanism can also exist in the stellar corona of young stars. Once the plasma is heated, cooling occurs through line emissions. The bulk of the heating is at the base of the jet. Supplementary heating in the jet is added through shocks, which are limited to the shock front.

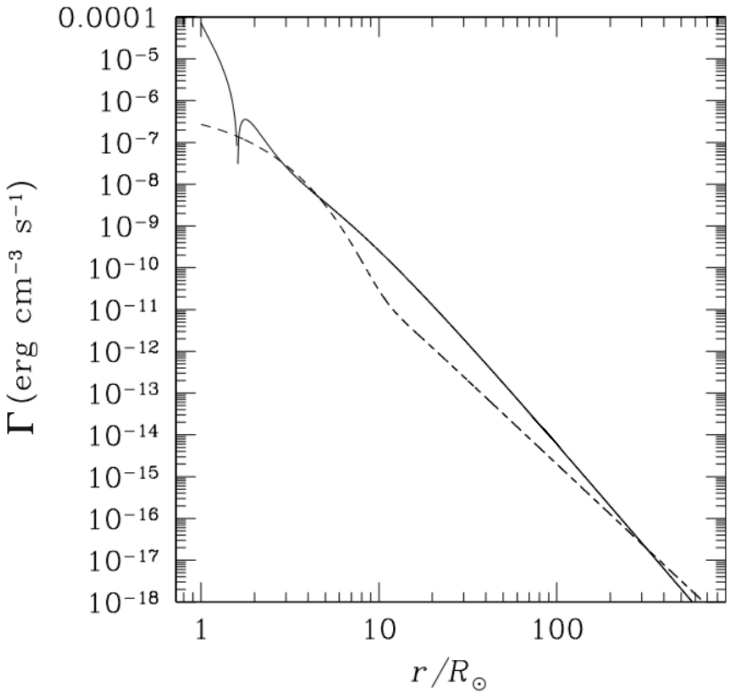

Figure 3.16: The solid thin line is the heating resulting from Alfvén wave reflection as computed in Chandran and Hollweg (2009). The dashed line is the proton and electron heating is Allen et al. (1998). The heating source in the dashed line comes from the collision between protons and neutrals and the resulting wave motions. Modified from Chandran and Hollweg (2009).

As can be seen in Fig.3.16, Alfvén waves could, when outward and backward propagating waves are coupled, produce enough heating near the Sun. This mechanism alone can match the heating we have between the stellar surface and the first few solar radii. The studies cited above are based on observation of the Sun, but the same physical ingredients are all gathered around young stars.

Other MHD heating processes are possible, such mechanisms are related to Ohmic and ambipolar diffusions. Both contributions depend heavily on the medium conditions and are subject to large uncertainties. A measure of these processes through observations is hard to evaluate. Even in numerical simulations, most works studying disk and jet evolution remove the Ohmic and the ambipolar contributions as heating terms (Sheikhnezami et al., 2012; Stepanovs and Fendt, 2014; Mattia and Fendt, 2020a,b, 2022).

Chapter 4

Effects of heating on the jet launching and collimation

Contents

4.1 Summary of the publication 102
4.2 Introduction 102
4.3 MHD equations and analytical solutions 106
4.3.1 Physical framework and MHD equations 106
4.3.2 Analytical solutions 108
4.3.3 Mixing analytical solutions 111
4.4 From analytical solutions to numerical simulations 111
4.4.1 Grid and initial conditions 111
4.4.2 Parameters and normalization 113
4.4.3 The mixing function 114
4.4.4 The heating function 115
4.4.5 Boundary conditions 118
4.5 Results 119
4.5.1 Parameter space 119
4.5.2 Varying the disk wind density 123
4.5.3 Effect of heating 126
4.5.4 Electric circuit 131
4.5.5 Increasing accretion rate 132
4.5.6 Standing recollimation 134
4.6 Discussion 137
4.6.1 Comparison to other simulations 137

4.6.2 Comparison to observations 140
4.6.3 Possible heating sources 142
4.7 Conclusions 142

This chapter is based on the article published in Astronomy and Astrophysics: Meskini, C., Sauty, C., Marcowith, A., Vlahakis, N., and Brunn, V. (2024). A&A, 686:A287. Minimal changes have been applied.

4.1 Summary of the publication

Theoretical arguments as well as observations of young stellar objects (YSOs) support the presence of a diversified circum-stellar environment. A stellar jet is thought to account for most of the stellar spin down and disk wind outflow for the observed high mass-loss rate, thus playing a major role in the launching of powerful jets. RY Tau, for instance, is an extensively studied intermediate mass pre-main sequence star. Observational data reveal a small-scale jet called micro-jet. Nevertheless, it is not clear how the micro-jet shapes the jet observed at a large scale. The goal is to investigate the spatial stability and structure of the central jet at a large scale by mixing the stellar and disk components. Two existing analytical self-similar models for the disk and the stellar winds are used to build the initial setups. Instead of using a polytropic equation of state, we mapped the heating and cooling sources from the analytical solutions. The heating exchange rate was controlled by two parameters, its spatial extent and its intensity. The central jet and the surrounding disk are strongly affected by these two parameters. We separate the results into three categories, which show different emissivity, temperature, and velocity maps. We reached this categorization by looking at the opening angle of the stellar solution. For cylindrically, well-collimated jets, we have opening angles as low as 10 degrees between 8 and 10 au, and for the wider jets, we can reach 30 degrees with a morphology closer to radial solar winds. Our parametric study shows that the less heated the outflow is, the more collimated it appears. We also show thatrecollimation shocks appear consistently with UV observations in terms of temperature but not density.

4.2 Introduction

Pre-main sequence stars, particularly Class II classical T Tauri stars (CTTSs), are in an active evolutionary stage with ongoing accretion and ejection processes (Ray et al., 2007; Bally et al., 2007; Garufi et al., 2019; Sauty, 2019; Ray and Ferreira, 2021). A substantial fraction of CTTSs present observational signatures of outflows, and more than 60% exhibit stellar winds (Kwan et al., 2007). CTTSs show a wide interval of rotation rates. However, the trend for the rotation speed of these stars stay way below the break-up velocity (Bouvier et al., 1986; Bertout, 1989; Bouvier et al., 1993; Rebull et al., 2004; Herbst et al., 2007). Although CTTSs are actively accreting mass from the

disk with mass accretion rates around $\sim 10^{-10} - 10^{-8}\ M_{\odot}\,\mathrm{yr}^{-1}$, observations indicate that the rotational velocities of CTTSs stay constant over a few million years.

The resulting jets are supersonic, collimated outflows that are closely linked to accretion. Observations establish a correlation between accretion and ejection, which clearly shows that the disk is an essential ingredient in jet formation (Cabrit et al., 1990; Hartigan et al., 1995; Mirabel et al., 1998; Manara et al., 2016). It was found that at early stages of a young star life, the strength of the winds and the jets are more powerful. Such an observation is explained by the vigorous matter infall phase early in the evolutionary stage of the star (Andre et al., 1992).

The presence of a jet is determined by the existence of a surrounding accretion disk. No disk or no disk-star interaction implies no observable jet. This is confirmed by the absence of detectable jets in weak-lined T Tauri stars (WTTS). Nonetheless, the opposite is not necessarily true (Ray and Ferreira, 2021). A jet may originate from different sources – the star, the circumstellar accretion disk, or from the star-disk interaction (hereafter SDI) region where the stellar magnetosphere connects to the disk. Some jets appear in the form of sporadic non-collimated ejections. Overall, arguments on the jet nature support the idea that there must be more than one mechanism to explain the outflows. Although, the outflows can extend from a few hundred au to the parsec scale, the main region of jet collimation and acceleration is below ~ 100 au (Bally et al., 2007; Petrov et al., 2019; Takami et al., 2022).

To explain the observed low rotational velocities, angular momentum must be removed from the star and its surrounding accretion disk. Many models have been developed to explain the mechanism responsible for angular momentum transport. Hydrodynamical models alone fail to explain young stellar object (YSO) jets. Adding a magnetic field is a promising mechanism that matches the observed jet collimation and ejection efficiency (Cabrit, 2007).

As for the solar wind (Pantellini et al., 1988), pure thermal coronal wind models fail to explain jets with high enough mass-loss rates because they would require higher temperatures than is observed (DeCampli, 1981). In fact, if we consider the high temperatures coupled with the high densities necessary for jets, the resulting X-ray emissions would be in excess with respect to the data. Bisnovatyi-Kogan and Lamzin (1977) estimated X-ray luminosities on the order of 10^{34} erg s^{-1} for a spherical model of thermally driven coronal wind. On the other hand, observed luminosities emanating from T Tauri stars are $L_X \leq 10^{30}$ erg s^{-1} (Feigelson and Montmerle, 1999; Imanishi et al., 2003). Invoking Alfvén waves, so as to support coronal heating, would alleviate the X-ray luminosity excess. Alone, Alfvén waves would require a strong luminosity. Although good candidates for energy transport, the non-dissipative nature of these waves makes it difficult to extract the embedded mechanical energy in the form of heat. X-ray emission plus Alfvén waves can support ejections close to $10^{-9} M_{\odot}\,\mathrm{yr}^{-1}$, and for temperatures around one million degrees the jets can reach velocities up to 300 $km\,\mathrm{s}^{-1}$ (DeCampli, 1981). Another source of heating could be turbulent ram or magnetic pressure. Thus turbulent pressure (Hartmann and MacGregor, 1982) or accretion-powered stellar wind (APSW) scenarios (Matt and Pudritz, 2005) have the potential

to produce sufficient mass-loss rates. For some parameters in accretion-powered wind, the model also results in magnetic braking spinning the star down. The decrease in rotational velocity occurs in the lifetime of the star (Matt et al., 2012).

Nonetheless, thermal winds can be invoked to launch micro-jets with low mass-loss rates of a few $10^{-9} M_{\odot}\,\mathrm{yr}^{-1}$, such as the RY Tau micro-jet observed by St-Onge and Bastien (2008) with $H\alpha$ tracers (Sauty et al., 2011; Sauty et al., 2022). The stellar wind is strong enough to brake the star in its lifetime.

Magnetocetrifugal driving, for instance, has the advantage of keeping the outflows corotating with the star using magnetic torque to carry off a substantial fraction of the angular momentum. Yet this model lacks efficient ways of launching plasma out of the star.

The most efficient mechanism to explain collimated outflows is the presence of large-scale magnetic fields combined with a rotating disk (Casse and Ferreira, 2000). Large-scale magnetic fields can be created during the contraction of the primordial envelope, thus advecting the magnetic field, or by the dynamo effect (Mouschovias, 1976; Rekowski et al., 2000). Since the work by Blandford and Payne (1982) (hereafter BP82), it has been known that a disk threaded by a magnetic field can accelerate material if the latter crosses all critical surfaces. The model presented in BP82, based on the work of Bardeen and Berger (1978), uses a self-similar approximation to solve the magnetohydrodynamical (MHD) equations. Nevertheless, self-similarity could impact the jet dynamics given that the axis of rotation as well as the interaction with the ambient medium are not taken into account. However, self-similarity is a good proxy for objects where the rotational axis and the jet are almost parallel. It also shortens the list of free parameters, and thus helps for the exploration of more space parameters in regards to the magnetic field distribution (e.g., Contopoulos and Lovelace 1994; Ferreira 1997) and the thermal effects (e.g., Vlahakis et al. 2000; Casse and Keppens 2004; Jannaud et al. 2023).

A numerical study of a jet launching and collimation can be tackled in two main ways: either one can consider the disk as a boundary condition (Ustyugova et al. 1995, 1999; Koldoba et al. 1995; Ouyed and Pudritz 1997a; Pudritz et al. 2006; Porth and Fendt 2010; Jannaud et al. 2023; and references therein) or one can include the complete physics of the disk to investigate the feedback of the disk structure on the jet launching (e.g., Casse and Keppens 2002, 2004; Zanni et al. 2007; Tzeferacos et al. 2009, 2013; Fendt and Sheikhnezami 2013; Jacquemin-Ide et al. 2021; Takasao et al. 2022). These simulations used a turbulent diffusivity due to the development and saturation of magnetorotational instability in the disk. Thus the authors used an α-disk prescription for the viscosity and magnetic diffusivity following Shakura-Sunyaev. Mattia and Fendt (2020a,b, 2022) have explored more realistic diffusion coefficients including a full study of the dynamo development and saturation in the disk. In Mattia and Fendt (2022), the authors show how the diffusive quenching of the dynamo, taking the feedback of the large dynamo magnetic field, stabilizes the system. A stronger quenching of the dynamo leads to lower magnetization.

Each of these methods has its drawbacks. While platform simulations (using the

disk as a boundary) enable the study of jets at very large scales, they have extensive degrees of freedom. Several distributions have to be specified at the wind injection boundary. Consequently, inferring a set of generic results on collimation has proven difficult. On the other hand, including the disk substantially increases the computation time. To mitigate a long computation time, we had to use a lower resolution. In turn, smaller domains of parameters were studied.

Before including the disk physics in a future work, for the present publication, we used platform simulations to investigate jet launching and collimation by choosing computational domains bigger than the ones used in Zanni and Ferreira (2013), Ireland et al. (2021), and Ireland et al. (2022a), but smaller than the ones in Matsakos et al. (2009), Stute et al. (2014), and Jannaud et al. (2023). We used semi-analytical models for the disk (Vlahakis et al., 2000) (ADO), and the model from Sauty et al. (2011) for the stellar component (ASO). We followed the procedure of Sauty et al. (2022) to include a dead zone, which is a static stellar atmosphere, and an accretion zone. Both structures are not present in the original stellar model and have been tested in regards to the stability in Sauty et al. (2022).

The presence of a hot corona above the disk surface heats the base of the disk wind, significantly increasing the outflow mass (Casse and Ferreira, 2000; Ferreira and Casse, 2004; Bai et al., 2016). Casse and Ferreira (2000) showed that adding a similar heating source to what is emitted by an embedded source (i.e., a star) counterbalances the magnetic compression, enabling smaller mass loading. This illustrates the importance of heating in jet formation. We follow here this framework by including a heating rate in the stellar and disk wind components to infer the jet properties, that is, the degree of collimation, velocities, mass-loss rates, temperatures, etc. Further more, Ferreira and Casse (2004) showed that to recover the solutions presented by Vlahakis et al. (2000) from accretion disk solutions where winds are consistently added, the disk corona needs a non-negligible heating amount. This has possibles consequences on UV emission lines (Gómez de Castro and Verdugo, 2001).

This work is the first of a series aiming to explore the effects of extra sources of heating, besides magnetocentrifugal driving, for jet launching and the production of stable collimated jets. Our approach uses a parameterized heating to quantitatively determine the amount of heating rate needed to launch and maintain a jet.

The paper is organized as follows. Sec.4.3 describes the ideal MHD equations and the analytical solutions used at initialization. The stellar analytical solution surrounded by the disk wind solution were used to map the initial conditions. In Sec.4.4, the normalization factors as well as the mixing and heating functions are introduced. We show, in Sec.4.5, the effect of heating on the jet dynamics, that is, the degree of collimation, speed, velocities, etc. Namely, as we heated up the disk atmosphere, the jet became wider. On the other hand, if we decreased the heating available, we got a propeller regime (Romanova et al., 2009, 2011), where magnetospheric ejections affect the jet. In Sec.4.6, we discuss which configurations are closest to the observations. We then explore possible heating processes.

4.3 MHD equations and analytical solutions

4.3.1 Physical framework and MHD equations

We intend to study properties and stability of magnetically driven disk outflows which will be referred to as " disk jet" hereafter. We call "spine" jet the plasma ejected from the star, as well as the plasma from the magnetosphere heated by the stellar corona up to the SDI zone. We use the same nomenclature that was used in Jannaud et al. (2023) to clearly differentiate between the contribution of each component. To keep track of the separation, we use a passive tracer C_{Tr} that canvas the evolution of each component, for which an example is given in Appendix A,

$$\frac{\partial(\rho C_{Tr})}{\partial t} + \nabla \cdot (\rho C_{Tr} \mathbf{V}) = 0. \tag{4.1}$$

We use MHD equations, following the evolution of the heaviest species which dominate in the plasma. The plasma of interest is partially ionized, but still can be described by a one fluid approximation. Ionization has to be high enough for the magnetic field to play a role in the plasma evolution.

The disk itself is set as a boundary condition with a Keplerian profile. Both the central object and the disk are assumed to be threaded by a large scale magnetic field. This is not the case of Zanni and Ferreira (2009); Romanova et al. (2009); Zanni and Ferreira (2013), where they use a stellar dipolar field that thread the accretion disk. In order to describe such a flow we use the ideal MHD equations that express the conservation of macroscopic fluid quantities,

$$\frac{\partial \rho}{\partial t} + \nabla \cdot (\rho \mathbf{V}) = 0, \tag{4.2}$$

$$\rho \left[\frac{\partial \mathbf{V}}{\partial t} + (\mathbf{V} \cdot \nabla)\mathbf{V} \right] = -\nabla P + \frac{c}{4\pi}(\nabla \times \mathbf{B}) \times \mathbf{B} - \rho \frac{\mathcal{GM}}{r^2}\hat{\mathbf{r}}, \tag{4.3}$$

$$\frac{\partial \mathbf{B}}{\partial t} - \nabla \times (\mathbf{V} \times \mathbf{B}) = 0, \tag{4.4}$$

$$\frac{\partial P}{\partial t} + \mathbf{V} \cdot \nabla P + \Gamma P \nabla \cdot \mathbf{V} = Q, \tag{4.5}$$

where ρ, P, and $\mathbf{V}$ are the plasma density, pressure and velocity, respectively. Finally, $\mathbf{B}$ refers to the magnetic field. Hereafter, for clarity, we have adopted the following notations. Subscripts d and s are for the Disk and Stellar solutions, respectively, and the $\star$ indicates quantities at the Alfvén location along a given fieldline for a given model. We also note that $(r,\ \theta,\ \phi)$ and $(\varpi,\ \phi,\ z)$ are spherical and cylindrical coordinates, respectively. θ in spherical coordinates is the colatitude. We solve the MHD equations using spherical coordinates. A detailed description of the computational grid is found in Sec.4.4.1.

Since axisymmetry is assumed, mass conservation (Eq.4.2) is solved using the poloidal components of the velocity, V_r and V_θ, respectively. The left hand side of Eq.4.3 describes acceleration, while the right hand side is the sum of hydrostatic effects, Lorentz force expressed as $(\nabla\times\mathbf{B})\times\mathbf{B}$, and the gravitational force, with $\mathcal{G}$ the gravitational constant, and $\mathcal{M}$ the stellar mass. The induction equation (Eq.4.4) describes the temporal evolution of the magnetic field where magnetic resistivity is neglected since we assume ideal MHD. Finally, Eq.4.5 describes the time dependent energy equation. Q is the volumetric heating rate accounting for energy gains and losses. We use $Q = (\Gamma - 1)q$, with q the volumetric energy source term, and Γ the adiabatic index, which has the value of 5/3 for a monoatomic gas.

Different source terms are used for each component, keeping in mind the initial pressures and velocities that we use are computed from the analytical solutions. The disk wind can be described by an adiabatic or isothermal evolution through the polytropic index γ. To implement such a behavior we will use the source term presented in Matsakos et al. (2008, 2009),

$$Q = (\Gamma - \gamma)P(\nabla \cdot \mathbf{V}), \tag{4.6}$$

with γ the effective polytropic index. In the case of adiabatic evolution, $\gamma = \Gamma = 5/3$. The entropy, which is proportional to P/ρ^Γ is conserved along each streamline. This equation ensures that the pressure does not take negative values. When the system is not adiabatic, $\gamma \neq \Gamma$ and the heating rate is not zero. We calculate it with Eq. 4.6 in the disk wind solution, using $\gamma = 1.05$. In that case, Eq.4.6 is equivalent to writing $P \propto \rho^\gamma$.

As for the stellar jet, the analytical solution describes dense jet with an underpressured structure as in Sauty et al. (2002). The stellar jet has a lower density along the axis than at its edges. Conversely, in the works mentioned above, the stellar contribution is either very weak compared to the disk wind or is completely neglected. The main physical variables have been constrained from observations (Sauty et al., 2011). For the jet to maintain physical mass loss rates we have to use a higher energy source term than the polytropic equation offers. One could play on polytropic index γ to toggle heat exchange in the stellar component. If not enough heating is present in the stellar component then simulations show a collapse of the jet. An adiabatic evolution results in the jet turning into a static atmosphere, while isothermal conditions produce a weak turbulent jet (e.g., Matsakos et al. 2009; Stute et al. 2014). The stellar analytical solution is computed given a heat rate along the flow. This rate is given by,

$$Q = \rho\mathbf{V} \cdot \left[\Gamma\nabla\left(\frac{P}{\rho}\right) - (\Gamma - 1)\frac{\nabla P}{\rho}\right]. \tag{4.7}$$

First, Eq.4.7 is equivalent to Eq.4.5 in the steady case. Eq.4.7 characterizes the heat rate deposit in a comoving frame with the fluid. The energy equation has to be proportional to the velocity. However, changes in direction and magnitude are not considered outside the accretion region. As a consequence, the spine jet solution no

longer starts at an equilibrium state. Nevertheless, since we use a relaxation method from a heat map that does not vary from its initial structure, we do not account for velocity changes in the time dependent energy equation. The poloidal velocity sign is reversed in the accretion funnel, and observed accretion mass flux is reproduced by multiplying velocity and density by constant factors. Subsequently, modifying velocity has to be reflected onto the heating rate by introducing the same constant to the quantity. This keeps a self-consistent description of the accretion region. The inflow is sub-Alfvénic in the accretion region, which means the solution starts close to an equilibrium state. For an in depth explanation refer to Sec.2.2 of Sauty et al. (2022).

4.3.2 Analytical solutions

4.3.2.1 Spine jet solution, ASO

In order to model the RY Tau micro-jet, Sauty et al. (2011) applied a semi-analytical solution (analytical stellar outflow: ASO) derived from the self-similar approach introduced by Sauty and Tsinganos (1994). Crafted for jets originating from low-mass accreting T Tauri stars (TTS) they constitute an exact solution to the steady ideal MHD equations. This solution describes density (ρ), pressure (P), velocity field (V), and magnetic field (B) of a mono-fluid. These equations govern the behavior of a fully ionized plasma composed of protons and electrons only around a TTS.

We use the solution presented in Sauty et al. (2011), the stellar parameters of RY Tau for mass and radius, respectively, $M = 1.6 M_\odot$, $R = 2.4 R_\odot$ (Hartigan et al., 1995). For the mass-loss rate, we use $\dot{M} = 10^{-8.5} M_\odot \, \mathrm{yr}^{-1}$ (Gómez de Castro and Verdugo, 2001). More recent observations propose higher masses and radii (e.g., Calvet et al. 2004; Dotter et al. 2008; Bressan et al. 2012; Dotter 2016), with a mass centered around $2 M_\odot$, and a radius varying between 2.37 and $3.7 R_\odot$ for RY Tau (Davies et al., 2020). While $1.6 M_\odot$ is certainly below the lower limit, a change in mass from $1.6 M_\odot$ to $2 M_\odot$ does not affect the solution. A scaling of the velocity, magnetic field, and mass flux to match higher masses would increase these quantities by 10%. At the stellar surface, the equatorial rotational velocity given by the solution is 8.6 km s^{-1} (Sauty et al., 2011), corresponding to a period of 14 days, which is the value present in the simulations. RY Tau is a faster rotator with a period closer to 3 days, if an inclination of 66° is taken into account in the projected velocity. The difference in rotational velocity between observations and our simulations can be overlooked for now as the stellar outflow is mainly pressure driven which lessens the importance of the rotational output of the analytical solution on the dynamics of the jet.

Overall, the stellar component is within the constraints set by Gómez de Castro and Verdugo (2001, 2007), St-Onge and Bastien (2008), and Agra-Amboage et al. (2009). The specific stellar solution we used is tailored for the large scales and small scales of RY Tau jet. To study other objects we can either compute new stellar solutions with different stellar parameters or scale the solution presented above to a star with a different mass. However, Albuquerque (2020) showed that a simple rescaling of the

solution is usually not sufficient to be in agreement with all physical parameters. To make simulations of a jet from another CTTS, we would need to produce new self-similar solutions as initial conditions.

Further modifications have been applied to the spine jet solution in order to take into account physical features not contained in the initial model. In addition to a micro-jet, a second region between 0.03 and 0.09 *au* on the equatorial plane was adapted to describe an accretion region. To obtain such a region, density, and velocity were multiplied by constant factors as to inverse the flow of material and increase accretion mass flux. Physically, the accretion speed is close to 290 km s^{-1}, and accretion rate is in the order of $10^{-8} M_{\odot}\,\mathrm{yr}^{-1}$. A static corona was added between the star and the accretion zone, where the poloidal velocity is set to zero. Thus no angular momentum is transported in this region. For more details about the consequences of varying the size and density of the accretion regions, see Sauty et al. (2022). We use the same densities and velocities in the accretion region as testC and testD from the above paper to compare the evolution of the stellar solution with a more realistic disk wind.

4.3.2.2 Disk wind solution, ADO

In the analytical disk outflow (ADO), disk winds originate from streamlines that reach the surface of the disk. From that point on they follow the magnetic field and cannot cross them. Faraday's induction law dictates that an electromotive force across the disk creates a differential electric potential, and by closing the electric circuit (see lecture notes from chapter on MHD disk winds in Ferreira et al. 2007), a radial Lorentz force appears. This force induces, at the same time, a slowing down of the disk as expected from Lenz's law. To collimate the jet the azimuthal component of the magnetic field is crucial. By coiling along the jet, the magnetic field creates an inward force that collimates the jet. If a horizontal cut is made at some distance, z, and if the current is non-vanishing, then the Laplace force is directed toward the jet axis. Blandford and Payne (1982) originally proposed the first MHD radial self-similar solutions describing a cold disk wind.

Their work was, later, extended to fill in for some of the models short comings. Ferreira (1997) (referred to as F97 hereafter) consistently connect disk and disk wind. Vlahakis et al. (2000) (referred to as VTST00 hereafter) on the other hand present a model, with a thermal component, crossing all critical surfaces causally disassociating the outflow from its origin. As we do not implement the physics of the accretion disk and use it as a boundary condition, we will rather use the VTST00 self-similar solution, because it crosses all three critical surfaces. In order to match the MHD wind solution with the resistive accretion disk in a consistent way, one has to avoid discontinuities, which put extra constraints on the wind. Such an investigation is postponed to future work.

To describe the disk wind solution we have to specify eight physical quantities (P, ρ, $\mathbf{V}$, $\mathbf{B}$) at the disk surface. The self-similar ansatz to determine these quantities is presented in the Appendix B. VTST00 built a model with a finite temperature and a

solution that starts at a subslow magnetosonic velocity. The solution then crosses the slow magnetosonic, Alfvén, and fast magnetosonic critical surfaces. The authors discuss the implication of a slightly higher magnetic field distribution on crossing critical points, and point out the minimal effect it may have on the resulting solution. The magnetic scaling parameter, x, which controls the magnetic field distribution, can be directly linked to the ejection index, ξ, as expressed in Ferreira (1997) ($\xi = 2(x - 3/4)$). This parameter defines the disk accretion rate as $\dot{M} \propto r^{\xi}$ (Ferreira and Pelletier, 1995) and mass flux in the wind for a disk with a radially self-similar structure. We choose a value from BP82, $x = 3/4$, which corresponds to $\xi = 0$. In that case $\dot{M}$ varies logarithmically with ϖ.

Ferreira (1997) demonstrates that for ejection to happen ξ has to be higher than 0, and as ξ grows larger, so does the ejection efficiency. We argue that since VTST00 show almost identical behavior for a solution with a higher ejection index, the solution should not go against the theoretical arguments put forward by Ferreira (1997) (see discussion below). The constraint present in F97 arises from linking disk and wind, a condition absent in the chosen disk model. Having a consistent disk seems to come at a price, as solutions crossing the fast surface are hard to find.

Although, we have chosen $\xi \approx 0$, this does not mean we do not have mass losses from the disk. The model adds a thermal component that helps material travel outside the disk. To further understand the effect due to this parameter, we vary its value close to 3/4 and notice no quantitative difference. Testing with $x = 0.7575$, above what was probed by VTST00, we obtain small differences on scales not yet achieved by the current instruments. A higher ejection efficiency does not change the external equilibrium. Thus, linking the accretion disk and its wind is not a fundamental issue in this paper. This being said, other solutions with different ξ are going to be chosen in a future work.

We focus here on the physical implications of using the solution presented in VTST00. The ratio of the Alfvén poloidal speed to the Keplerian velocity at the disk boundary level results in a value of ~ 0.014. Such a value means that at the disk surface the energy density of the magnetic field is less than the kinetic energy from rotation, implying the magnetic field follows the plasma.

Then, looking at the ratio of the sound speed and the initial velocity we deduce that the ejection velocity at the base of the flow is negligible compared to the sound speed. The disk wind solution of VTST00 is magnetically driven but there is a heating source above the disk. It helps the initial acceleration of the flow. The Keplerian velocity is around two times larger than the thermal speed ($C_s = \sqrt{\partial P/\partial \rho}$). Consequently, the disk rotation cannot be suppressed by thermal effects. The terminal velocity of the solution is ~ 400 km s^{-1} which is well within the observational range of YSOs. VTST00 estimated the mass-loss rate for a field anchored at 0.6 au with a magnetic field of 8 G. They estimate mass loss at $10^{-8}\ M_{\odot}\,\mathrm{yr}^{-1}$ with a temperature of $8 \times 10^3\ K$. Finally, the specific angular momentum carried by the wind to the angular momentum needed for accretion ratio is $\leq 1.5\%$. Since the outflowing plasma is at most 1% the value of accreted materiel, this implies all the angular momentum is carried by the wind.

4.3.3 Mixing analytical solutions

In Sauty et al. (2022), the authors show that the inner analytical solution of Sauty et al. (2011) is quite stable in the inner spine jet region. Even with the introduction of an accretion region, simulations and analytical work give similar stellar spin-downs. Both angular momentum and mass-loss rates extracted by the stellar jet match values given by the analytical work (Sauty et al., 2011). The stellar braking time was computed to be approximately 0.6 million years. The convergence of these results between the analytical solution and the numerical simulations can be attributed to two primary factors. First, as described in Sauty et al. (2011), only the open field-line region of the stellar jet is responsible for the stellar braking. Second, reversing the sign of the toroidal magnetic field ($B_\phi = -B_{\phi,analytic}$) and the poloidal velocity ($V_p = -1.5V_{p,analytic}$) inside the magnetospheric accretion zone guaranties the azimuthal velocity stays unchanged on the star and consistent with isorotation law. Moreover the density was multiplied by a factor 5 to increase the accretion rate to $\sim 10^{-8} M_\odot\,\mathrm{yr}^{-1}$ (Sauty et al., 2022). See Fig.1 in this publication where we kept the initial conditions in domains 1 (the stellar jet component), 2 (the magnetospheric accretion columns), 3 (the magnetostatic dead zone), and changed them in region 4 (the disk wind domain). In essence, the disk effectively exerts magnetic braking on the star as the magnetospheric field lines efficiently lock the star to the disk. This way of treating the accretion zone is kept in our study. Consequently, the simulations demonstrate that the stellar jet and magnetospheric accretion collectively contribute to the star spin-down in a manner resembling of Sauty et al. (2011), resulting in a spin-down period of less than one million years for the star − a timescale well within the lifetime of the CTTS phase.

We extend the work simulating RY Tau environment (Sauty et al., 2022) by adding a more realistic disk wind. The one used in their study is not dense enough, resulting in a low mass loss from the disk. Furthermore, we go beyond studying the jet dynamics above the fast magnetosonic surface as in (Matsakos et al., 2009; Stute et al., 2008), by including the launching region. This, in turn, will enable us to build consistently the launching region in the disk and its interaction with the stellar component.

4.4 From analytical solutions to numerical simulations

4.4.1 Grid and initial conditions

To solve our system of equations we use *PLUTO*, a code based on finite volume methods (Mignone et al., 2007). Spatial reconstruction of primitive quantities is achieved with linear interpolation (Mignone, 2014). For flux computation we choose a robust solver, HLL (for Hartan Lax, Van Leer approximate Riemann). Finally, to ensure the divergence-free condition $\nabla \cdot \mathbf{B} = 0$ we use the eight-wave structure (Powell, 1997).

The simulations presented below are 2.5D. We consider a 3D grid while assuming

axisymmetry around the stellar axis of rotation. The grid is spherical with (R, θ) as coordinate components.

The equatorial plane has a planar symmetry, and the colatitude θ is discretized into 128 points starting from $\theta \sim 0$, at the polar axis, to $\theta = 1.552$. This limit arises when *PLUTO* creates a ghost zone that reaches the equatorial plane. At the equator, the analytical equations used to initialize the disk wind diverge. Hence, the system is not solved beyond $\theta_{lim} = 1.552$, unless we increase the number of points in colatitude to decrease the size of the ghost zones. But this increase in turn decreases the time step of a simulation. The right compromise between resolution and time convergence is obtained by using 128 discretization points. Adding more points does not affect the global evolution or the steady state solutions if reached.

The radial coordinate runs between $r = 0.02$ au and $r = 10$ au, and has three zones. For $[r_0, r_1] = [0.02, 0.18]$ au we set a uniform grid of 512 points, then from $r = 0.18$ au to $r = 3$ au we use a less accurate grid resolution of 1024 points. Finally, between $r = 3$ au to $r = 10$ au we adopt a stretched grid spanning 512 points where the mesh size increases with the radial component (Fig.4.1). We also run simulations that extend to 30 au that show the existence of a standing recollimation point in Sec. 4.5.6.

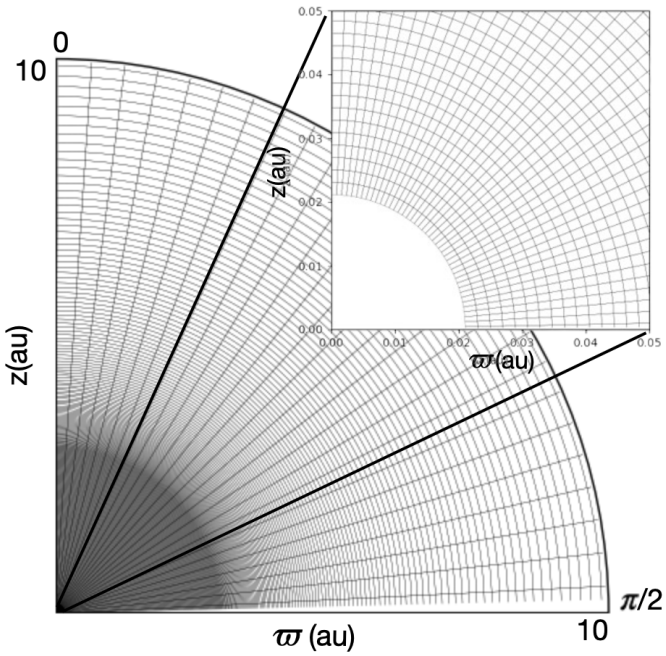

Figure 4.1: Rarefied computational grid. Proportionality of cells with the original grid is respected. We make sure the grid cells form a square close to the stellar boundary.

The fine grid in the radial direction results in a slightly compressed grid along r (Fig.4.1). Other less compressed grids were tested, namely by increasing theta to 256 points or decreasing the number of points in the radial direction, but no differences were noted. We obtained higher or lower resolution plots and no change in the dynamics.

The run time drastically increased on the other hand. A coarser grid in R smoothes the density resulting in the disappearance of shocks. Overall, changing the grid did not change the steady state reached.

4.4.2 Parameters and normalization

The ASO solution is determined by four parameters. The ADO solution, on the other hand, has five free parameters. These parameters describe the dynamics of the self-similar models, as well as allow us to normalize all the components to the same stellar object. The parameter set used in this work are all presented in Tab. 4.1. The parameters λ_d and λ_s are related to the rotational velocity of the disk wind and stellar solutions, respectively. They provide a measure of the lever arm. Therefore, they also give an indication of the braking efficiency of each solution. The parameters δ and κ control the longitudinal profile of the pressure and density of the ASO solution. The parameters $\mathcal{K}$ and ν impose the gravitational potential for each solution. μ is related to the relative magnitudes of magnetic and thermal pressure. The parameter γ is the polytropic index. Another parameter is needed to match the two solutions together. It is labeled α_m, and defines the isocontour which encloses a constant magnetic flux. More details on its position and role in mixing ASO and ADO solutions are given in Sec. 4.4.3. $\mathcal{K}$ and ν are both expressed in Eq.4.9, as they are directly used to normalize the solutions. The explicit expressions of the other parameters are introduced in Appendix C when applicable.

ADO parameters

λ_d	μ	γ	$\mathcal{K}$	x
11.7	2.99	1.05	2.0	0.75

ASO parameters

λ_S	δ	κ	ν
0.775	0.0778	0.021	1.5

Table 4.1: Parameters used in the ADO and ASO solutions.

To normalize the solutions, three scaling ratios have been chosen at the Alfvénic surface. They are nondimensional and denote by a $\star$. Values from the ASO solution are taken as a reference to scale the ADO solution. The scale length, velocity, and density ratios are, respectively,

$$l_r = \frac{r_{\star d}}{r_{\star s}}, \quad l_v = \frac{V_{\star d}}{V_{\star s}}, \quad l_\rho = \frac{\rho_{\star d}}{\rho_{\star s}}, \tag{4.8}$$

$r_{\star s}$, $V_{\star s}$, and $\rho_{\star s}$ are all set to unity hereafter. The length factor is set by choosing where the two solutions are mixed together. The position of ADO and ASO reference field lines ($\alpha_d = \alpha_s = 1$, Appendix C) on the equator gives the normalization factor for

length. The meeting points of the two solutions are not unique, but the normalization factor is. We obtain $r_{\star s} = 1$ and $r_{\star d} = 6.25$. The reference field line is located at ~ 0.1 au. Observations indicate that the launching region of disk winds is between $0.2 - 3$ au (Coffey et al., 2004). By setting up the disk wind closer to the star than 0.2 au, we ensured the right physics was in the launching region. From $\mathcal{K}$ and ν we can determine $V_{\star d}$ and $V_{\star s}$ as both describe the gravitational potential as shown here,

$$\mathcal{K} = \sqrt{\frac{\mathcal{GM}}{\varpi_{\star d}\, V_{\star d}^2}} \quad \text{and} \quad \nu = \sqrt{\frac{2\mathcal{GM}}{r_{\star s}\, V_{\star s}^2}}. \tag{4.9}$$

$\mathcal{GM}$ depends only on the star mass. Using this information we get l_V from Eq.4.9, and determine that $V_{\star s} = 1$, and $V_{\star d} = 0.212$. The last parameter, l_ρ, can be chosen freely. We construct this ratio so as to make the density of the ASO and ADO solutions equal at the equator. The effect of this free parameter will be discussed in Sec.4.5.2. With the density ratio, we impose the magnetic field normalization factor as the two are bound by $V_a = B/\sqrt{4\pi\rho}$.

In order to return to physical units, we set the velocity, length, and density units from Sauty et al. (2011). Radius and velocity are normalized at the Alfvén radius. Then, the factor for the radius and velocity are $r_0 = r_{alf} = 0.104$ au and $V_0 = 106.84$ km s^{-1}, respectively. The density is $\rho_0 = 2.48 \times 10^{-15}$ g cm^{-3}. With these units we can subsequently determine pressure density, $P_0 = \rho_0 V_0^2 = 0.28$ dyne cm^{-2}. The magnetic field factor is defined as follows, $B_0 = \sqrt{4\pi P_0} = 1.87$ G. Finally, the time scale is, $t_0 = r_0/V_0 = 1.67$ days.

4.4.3 The mixing function

The semi-analytical solutions that are used in this work have different symmetries and values. This difference introduces discontinuities we want to avoid by smoothly transitioning from one solution to the other in the numerical grid. Using a mixing function to link two objects consistently is not new (Matsakos et al., 2009, 2012) and is still currently used. For instance, Jannaud et al. (2023) have used a spline function that depends on θ to go from a nonrotating central object to a Keplerian disk at the boundary. In (Matsakos et al., 2009, 2012), the mixing function is in terms of the magnetic flux, and used on all physical quantities that describe the evolution of the plasma.

The mixing procedure in this work is inspired from Matsakos et al. (2009). We adapt their mixing procedure but we keep the launching region close to the star close to the initial setup presented in Sauty et al. (2022). It ensures a better treatment of the inner accretion zone and makes it easier to compare the various simulation results. Additionally, by refining the mixing function presented in Matsakos et al. (2009) we chose to reduce the mixing parameters from two free parameters to only one, which controls the mixing width.

We use the magnetic flux as the main mixing parameter. The purpose of which is to avoid introducing regions where $\nabla \cdot \mathbf{B} \neq 0$ at the initial step. $\mathbf{B}$ depends on the

magnetic flux $A(\alpha)$ as shown in Eq.4.10. Given $A(\alpha)$ has a different slope for each component, special care has to be considered to ensure a divergence-free magnetic field at the boundary conditions,

$$B_p = \frac{\nabla A \times \hat{\phi}}{\varpi}. \tag{4.10}$$

We define the mixing function as follows,

$$U = w_s U_s + w_d U_d \tag{4.11}$$

with

$$w_s = exp\left[-\left(\frac{\alpha_s}{\alpha_m} - 1\right)^d\right] \text{andw}_\text{d} = 1 - \text{w}_\text{s}, \tag{4.12}$$

α_s is the nondimensional magnetic flux of the stellar solution and α_m is a constant defining the last open field. Along the polar axis, w_s is equal to one until the last open fieldline. Then, starting the last open field, it decreases exponentially to zero as the cylindrical radius increases.

The last open magnetic field, associated in the stellar solution to the iso-contour $\alpha_m \sim 1$, sets the strip along which the mixing occurs (gray region in Fig.4.2). The width of the mixing, that is, the speed at which we transition from the stellar solution to the disk solution, is controlled by the parameter d_m in Eq.4.12. We can see in Fig.4.2 that the higher d_m is chosen, the steeper the transition becomes. Another consequence of increasing d_m is expanding the region where w_s is equal to one. In fact, this has the same effect as pushing the ASO component further into the disk wind by increasing α_m. Given this behavior, we fix $d_m = 2$ to insure w_s starts decreasing soon after entering the ADO region. The wind disk should have a higher density than the ASO solution can provide in the transition region.

The physical quantities ρ, P, V_r, V_ϕ, B_ϕ, and A, are all blended using the mixing function presented above. The exception to this rule are $\mathbf{B_p}$ and $\mathbf{V_p}$. The poloidal components of the magnetic field are computed with Eq.4.10, which takes into account derivatives of the weights. Then, in ideal MHD, the poloidal velocity is parallel to the poloidal magnetic field. Thus, the velocity can be expressed as,

$$V_\theta = V_r \frac{B_\theta}{B_r}. \tag{4.13}$$

where V_r is computed as shown in Eq.4.11.

4.4.4 The heating function

From photoevaporation to viscous heating, an abundant number of processes can explain how the disk and its environment may be heated, but the details of such processes are still not resolved. We opt to consider two different atmospheres associated to the spine outflow and the disk jet, as there is no reason for the two regions to have the same

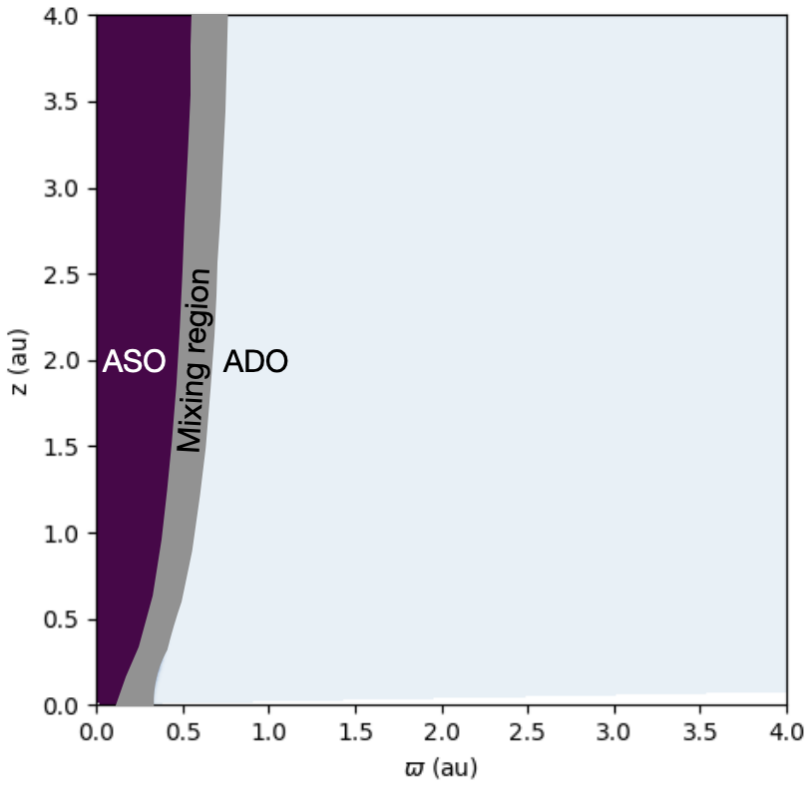

(a)

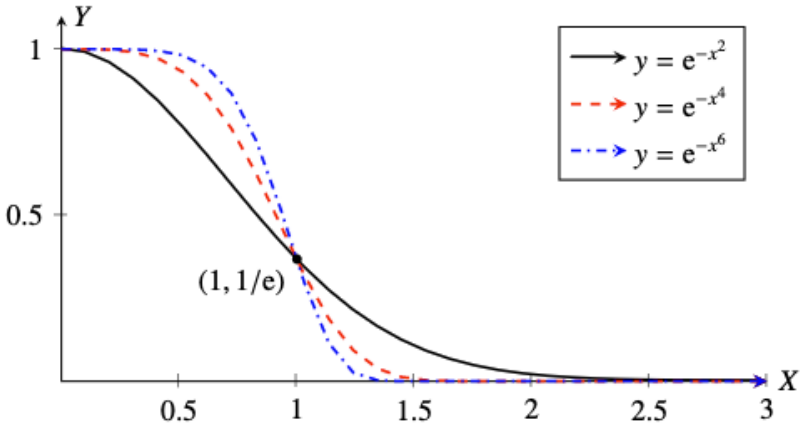

(b)

Figure 4.2: (a) the 2D map of the mixing function that goes from zero (Blueish region) to one (purple region). ϖ is the cylindrical radius and z the rotational axis. The jet propagates along the z axis and ϖ is the cylindrical radius in the equatorial plane. A gray mask was added to better denote the mixing region. The speed of transition inside this region can be controlled through d_m, as shown in (b). (b) illustration of the extension of the ASO component over the selected region. The functions are of qualitative value. This shows the dependence of the parameter d on the mixing speed. We also shift the center of the function in this plot to zero. This allows for a better presentation of the mixing parameters.

physical origin, order of magnitude in terms of heating, or even the same geometry. As a first approach to the problem, we use the analytical heating provided by the analytical solutions, and introduce parameters that will help us control the heating input by parametrizing it.

The disk wind uses the values of Eq.4.6 (ADO heating) mixed with Eq.4.7 (ASO heating) as decribed in the mixing procedure. Heating above the disk is contained in a smaller region of the disk component. The reason is that velocities are too high, which leads Eq.4.6 to produce non physical heating rates. Given the physical limitations linked to this equation, we restrain the disk atmosphere from the equator to around 20° above the disk. We use the stellar heating equation (Eq.4.7) for the rest of the domain, that is, part of the disk and spine jet components (orange part of Fig.4.3).

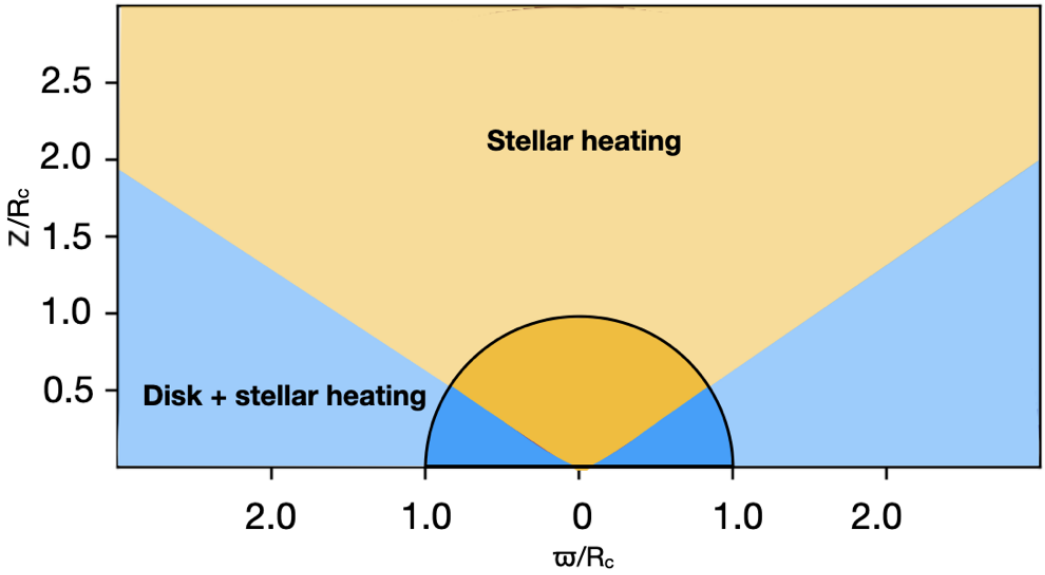

Figure 4.3: Scheme of heating allocation to the stellar and disk wind components. The black half circle indicates the spherical nature of the parameter R_c. The fading colors refer to where the heating is suppressed slowly using the method presented in Eq.4.14. The heating profiles along the polar and equatorial axes are given in Fig. 4.10.

We further introduce a decreasing function to force the heating rate of both the disk and the spine outflow to go toward zero beyond a radius we call R_c. This radius is a free parameter that controls where the heating starts to smoothly dip. We also introduce a second free parameter, I_h, which in turn controls the heating in the disk atmosphere. Eq.4.14 describes the final form of the total heating the whole simulation box,

$$Q(r) = \begin{cases} Q_{an} \times \arctan\left(\frac{1}{(r-R_c)^4}\right) & \text{orange region} \\ I_h \times Q_{an} \times \arctan\left(\frac{1}{(r-R_c)^4}\right) & \text{blue region} \end{cases}, \tag{4.14}$$

where Q_{an} is the analytical heating computed with the solutions pressures and velocities

dispatched as shown in Fig.4.3. Q_{an} is computed using Eq.4.7 in the stellar atmosphere (orange region in Fig.4.3). In the disk atmosphere (blue region in Fig.4.3), Q_{an} is computed as follows:

$$Q_{an} = w_s \times \rho_{ASO} \mathbf{V_{ASO}} \cdot \left[\Gamma \nabla \left(\frac{P_{ASO}}{\rho_{ASO}} \right) - (\Gamma - 1) \frac{\nabla P_{ASO}}{\rho_{ASO}} \right] + w_d \times (\Gamma - \gamma) P_{ADO} (\nabla \cdot \mathbf{V_{ADO}}). \tag{4.15}$$

In Sec.4.5.1 we present the behavior of the outflow over the parameter space.

4.4.5 Boundary conditions

At the outer radial boundary, the quantities that describe the plasma are fixed to the analytical solutions values. If on the contrary we set the gradient, on every physical quantity, to be zero at the boundary by imposing outflow conditions, we note that the system develop over-density waves created below the Alfvén surface which bounce back toward the jet. These waves artificially modify the jet collimation radius making it narrower. Choosing to impose the analytical solution for all quantities on the boundary does not change the evolution in the super-Alfvénic region. However, it dampens the density that reaches the boundary, which in turn prevents the over-density waves from traveling back toward the axis. Consequently, the jet as a whole does not recollimate. Stute et al. (2008) noticed that imposing an "outflow" condition at the boundary precipitate the collapse of the simulated jets. This collapse is thought to be artificially triggered, since all gradients at the outer radial boundary are equal to zero. The terms that survive are related to the pinching force (i.e., B_ϕ/ϖ) which is directed toward the axis. By damping B_ϕ to zero on the outer boundary, the artificial collimation reportedly disappears, which reinforces the conclusion that such an artifact is solely numerical (see model ER2 in Stute et al. (2008)). Choosing a bigger box only postpones the boundary effect to later times.

To identify the cause of the jet narrowing, we plot the Lorentz force density from grids with analytical boundary conditions and outflow conditions. In Fig.4.4, we have a representative example of what we get. We see a difference between the total force if the radial gradient is included or not. This is the case for all simulations, but no clear behavior emerges. We argue that the radial boundary in our case acts as a wall that partially reflects matter. Since the reflection happens in the sub-Alfénic region, the wave travels back and changes the jet dynamics. To remove the reflection we set the outer radial boundary to always have the values defined by the analytical solution. By doing so, we mitigate any over-density that reach the boundary. Subsequently, artificial boundary effects are suppressed. Stute et al. (2008) on the other hand dampen B_ϕ, only, to zero.

In summary, it is crucial to either minimize the toroidal magnetic field component B_ϕ at the outer radial boundary or make self-consistent modifications to all quantities, ensuring equilibrium in the external region.

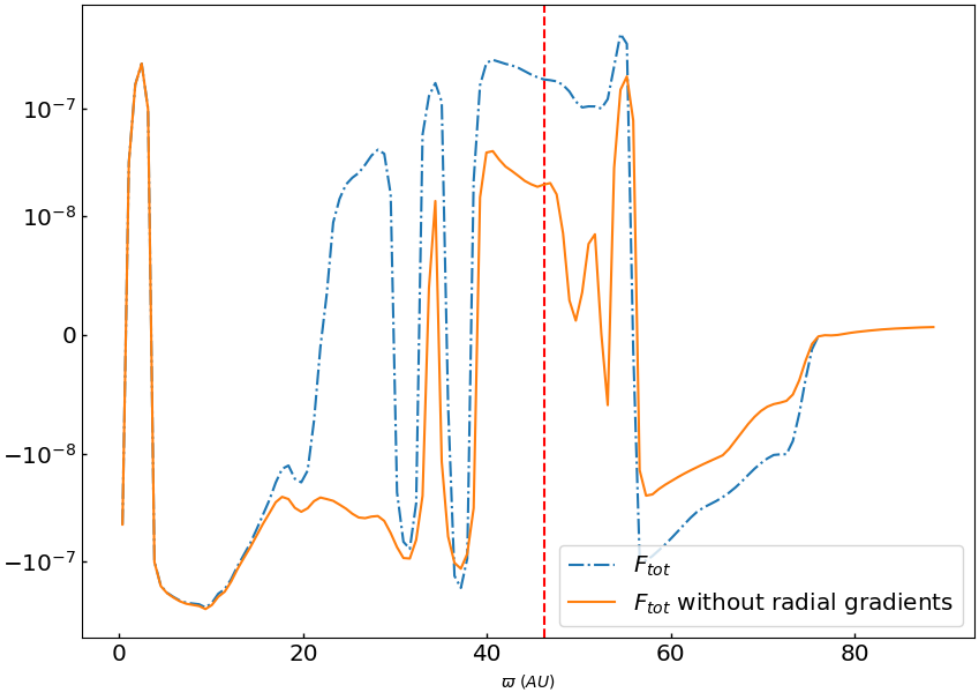

Figure 4.4: Total radial force applied by the pressure gradient, gravity, and Lorentz force on the plasma with the radial gradient (blue curve) and then without it (orange curve). We fix R at the radial boundary and vary the colatitude θ. The vertical line separates the super-Alfvénic and sub-Alfvénic regions. The total Lorentz force density is computed using $\mathbf{J} \times \mathbf{B}$ adapted to a spherical grid.

4.5 Results

4.5.1 Parameter space

Our study concentrates on the effect of our two main controlling parameters. The first parameter I_h controls the intensity of the heating computed from the disk. As shown in Eq.4.14, the heating is computed from the disk, then multiplied by I_h to lower the heating rate input. The second parameter R_c sets the radius at which heating is smoothly dropped in the computational grid. The first parameter is a simple constant we append to the disk heating rate. The purpose of changing the heating intensity is to gauge how the heating affects the magnetic collimation of the jet, given the intensity of heating of the disk wind. The second parameter allows one to evaluate how small the heating area around the YSO can be for the jet to be maintained.

Fig.4.5 presents the results produced by the parameter variations. We obtain three basic morphologies with a smooth transition between the different cases. We distinguish each case using tracers that follow the spine jet, and part of the disk material emanating from radii $\sim 0.9-3$ au. The semi-opening angle of the spine jet is then determined close to the radial boundary condition (10 au). For the narrowest spine jet (cylindrical solu-

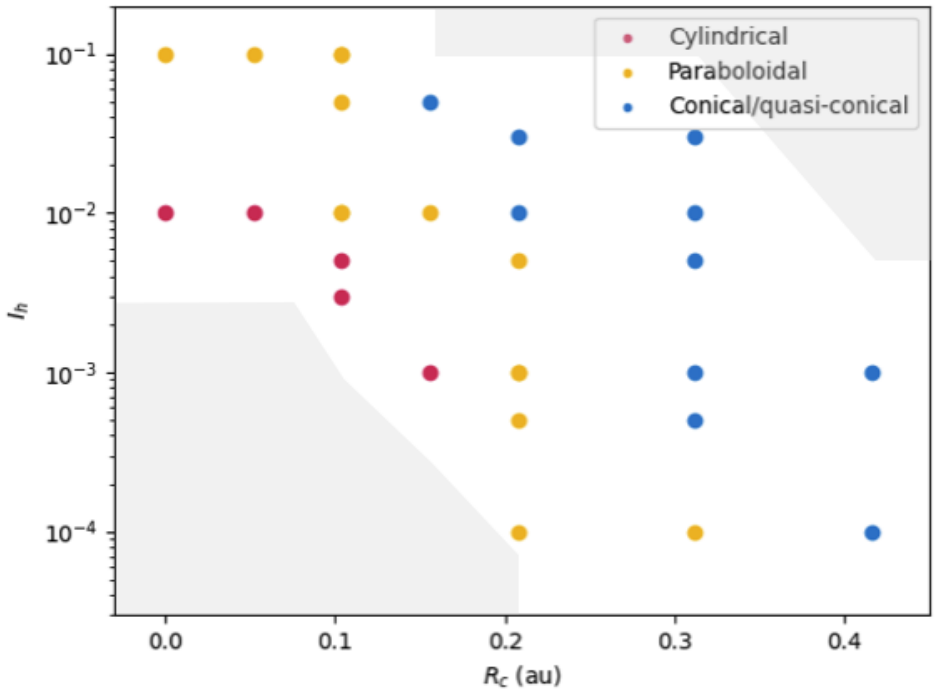

Figure 4.5: Parameter space mapping the simulations performed. Each dot is a set of parameters. Red dots are cylindrical jets, yellow is for paraboloidal jets, finally the blue dots represent wide paraboloidal or conical solutions. The gray areas are parameter space zones not covered by MHD simulations because the code crashes systematically.

tion), the semi-opening angle is $< 10°$, the widest configurations (quasi-conical/conical solutions) have semi-opening angles $> 20°$, and in between lays the paraboloidal solutions. An additional way of distinguishing cylindrical and paraboloidal solutions is by looking at the density along the axis. All the narrow cylindrical morphologies have a dense spine outflow with most of the density concentrated around the polar axis, as can be seen in Fig.4.6. The close-up to the central engine is displayed in Fig.4.7. This eases the distinction between cylindrical and paraboloidal solutions regardless if the opening angles overlap. Finally, while for lower I_h the jet slowly transitions from one morphology to the other, this change is faster for $I_h \sim 10^{-2}$ then becomes slow again for higher I_h. The gray regions in Fig.4.5 represent where simulations crash.

Our simulations do not contain a lower density threshold as it is common to implement in MHD simulations. Because of this choice, the space parameter is void of points in the top right corner in Fig.4.5. As we heat up matter, the density in regions close to the equator drops drastically. Since MHD codes have a weakness treating matter-poor environments, this leads to a lack of points. The lower left corner, on the other hand, does not contain points, because without sufficient heating, matter accretes and creates a strong gradient against the inner region close to the star. The code time increment

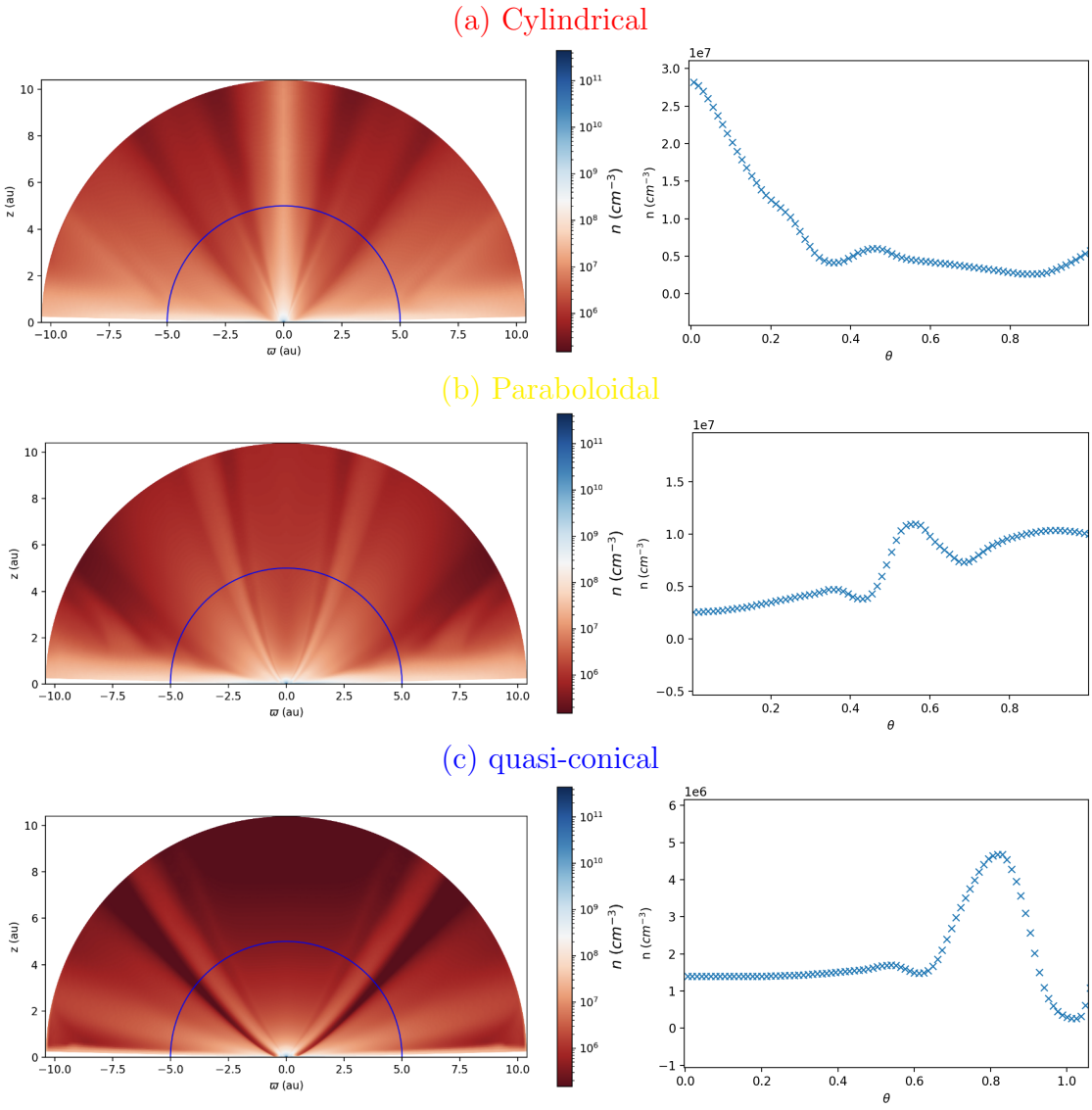

Figure 4.6: Plots of jet shapes found in the parameter space. The 2D maps of density show the collimation up to 10 au. What differs between cylindrical and paraboloidal, in this case, is the density at the axis. Generally, the opening angle is sufficient to distinguish cylindrical from paraboloidal solutions. The numerical diffusion is so low that the density isocontours coincide with the magnetic flux tubes and the poloidal velocity line (as in Fig. 4.9). The more collimated the flow is, the lower the acceleration efficiency. When this does not apply we look at the density distribution on the polar axis. For (a), $R_c = 0$ au and $I_h = 10^{-1}$ (R0_I1). Next, for (b), $R_c = 0.2$ au and $I_h = 10^{-3}$ (R2_I3). Finally, for (c), $R_c = 0.4$ au and $I_h = 10^{-3}$ (R4_I3). The blues half circle on all the cases indicates the radius along which the number density is plotted. We plot the density along θ starting at the axis and stop before reaching the disk wind region.

decreases drastically as a consequence, making it impossible to explore these areas. Both gray regions in Fig.4.5 are of no major interest to us since the jets produced are either too wide (upper right region) or too narrow (lower left region). Thus, we choose to not add a density threshold to keep artificial effects to a minimum, and maintain coherence between simulations.

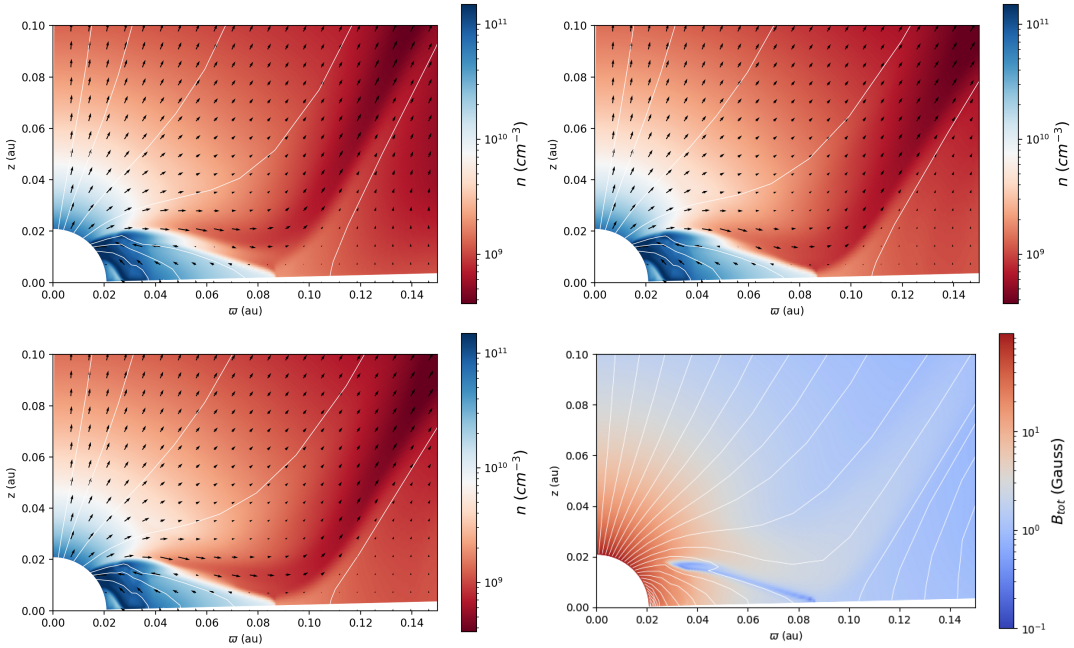

Figure 4.7: Close-up to the star for the three cases shown in Fig.4.6. Although the envelope changes dramatically between morphologies, the central component is similar through out the cases. The denser region with magnetic fields connecting the star and the disk boundary is the accretion region. The last plot is of the total magnetic field 2D profile close to the star. We see a current sheet in the right lower panel. Even though this region is favorable for numerical instabilities, it does not introduce time dependent features in completely steady cases.

Since for all the simulations presented here the magnetic field distribution is constant, adding more heating is equivalent to enhancing the pressure gradient. The additional pressure is located outside the spine jet and above the disk. As we heat up this region, the pressure gradient steepens and forces the jet to open up more.

In Tab.B.2 we show a mean value of the heating rate taken from the disk atmosphere. We average the heating until 1 au. the disk jet mass loss is determined once we exit the spine jet, between two minima that contain a local maximum in density, as shown in fig.4.6. As for the radius in which ejection from the disk occurs, reported in the last column of the table, we obtain its value by equating the mass loss in the disk jet and at the base of the jet. Following MHD arguments, plasma is not free to cross magnetic flux tubes. Thus, by tracking the flux tube containing the totality of the disk jet mass loss to the base, we deduce the radius of ejection.

4.5.2 Varying the disk wind density

First and foremost, we have to quantify the effect the disk density has on the dynamics of the jet. To do so, we vary l_ρ and adapt the normalization of the magnetic field to be consistent with the MHD formalism. Tab.B.1 displays the chosen values for l_ρ, l_B, and d_m. When the disk wind has a lower density than the magnetosphere the disk is not magnetically strong enough to maintain a jet. On the other hand too large densities need a high heating to produce a jet. To constrain the normalization, we use $ProDIMo$, PROtostellar DIsk MOdel, (Woitke et al., 2009; Kamp et al., 2010; Woitke et al., 2016; Rab et al., 2018) to determine the surface density of the accretion disk at the jet launching region in the disk. $ProDIMo$ is a thermo-chemical radiation code, where wavelength-dependent radiative transfer calculation are conducted. $ProDIMo$ computes gas and dust temperatures, in addition to the local radiation field. The code, then, computes the chemical abundances and determine the thermo-chemical disk structure taking into account the radiative transfer of an external X-ray flux. The temperature is dictated by the heating and cooling processes based on chemical abundances. This involves a network of 235 different species and 3143 reactions (Kamp et al., 2017; Rab et al., 2017). Due to the uncertainty of the chemical composition and physical surface of such a disk, we find values for disk density between $10^9 - 10^{10}$ cm^{-3} at $R = 0.5$ au and for $z/r = [0.1, 0.2]$. We choose to fix l_ρ at 0.014 which lays in the density limits inferred from $ProDIMo$. This density is consistent with MHD winds extracted from a standard disk. We will discuss how changing the density modifies our results in this section.

The solutions for the parameter set (R_c, I_h) displayed in Fig.4.5 is not unique and depends on the disk density. As for the evolution of the space taken by each case in the space parameter, we would have to run another set of simulations changing density. We choose to fix heating and vary density between the maximum and minimum values given by $ProDIMo$. We have run three types of simulations. The first one uses the maximum value of the density. The second is performed with an intermediary density. The third one is conducted with the minimum density as shown in Tab.B.1.

We find that raising the density shifts the parameter space of the jet solutions to the right, while lower density simulations produce higher velocities than what is observed for these objects. We discard the latter configuration, because the space parameter becomes difficult to pave. We describe in the next section the normalization chosen for our parametric study. Hereafter, however we will not further study the effect of density on the parameter space as we reserve it for future work where an other type of disk solutions will be used, such as the solutions presented in Ferreira (1997). These solutions have a higher mass loss rate and have been upgraded to include a magnetic pressure component that does not hide its contribution behind an effective heating.

However, we stress that the present study is, nonetheless, robust. The points associated to each class of solution may shift but the position of the colors stay fixed in relation to each other. The cylindrical jets, then the parabolic, and finally the quasi-conical jets all appear in this sequence. The more we heat up the disk wind, the shorter

the cross over between colors. We give each dot a name as presented in Tab.B.2 to facilitate the transition between the parameter space and the jet dynamic.

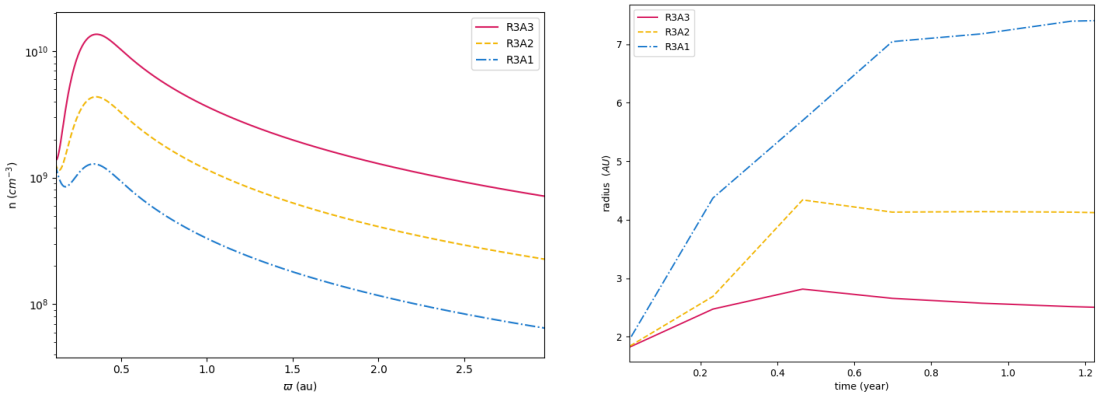

Figure 4.8: (a) The effect of different normalizations on the disk density. (b) Evolution of the radius with respect to time. Lowest values of the radius are from R3A3, the highest jet radii are given by R3A1. And in between the jet radii from R3A2. the radii are extracted at the radial boundary, close to 10 au on the axis.

In Fig.4.8, we plot the jet radii as function of time. We find that the simulations reach their final jet radius only after a few stellar rotations, between 8 and 9 stellar revolutions for all simulations. The number of stellar rotations needed to achieve jet stability depends on the size of the computational box. From Fig.4.8, we see that the lowest density normalization almost matches the slope of the stellar solution at the equator. In this case, looking at the forces profiles near the star, we see that the pressure gradient takes over the Lorentz force. Conversely, for the smallest jet, the Lorentz force is dominant. Doing the same analysis on the forces at a higher z shows an overall agreement between the three cases. This implies that the steady state reached mainly depends on the force balance at the boundary condition on the equator. The reason we notice a predominant pressure gradient as we decrease density is due to the fact that by decreasing density the magnetic field strength also decreases.

We observe that as we increase density, the heating tank available for a volume is smaller. It effectively reduces the energy delivered to the plasma. As a result, outflow regions narrow and plasma material returns to the disk. This bends the magnetic field lines above the disk and increases the magnetic tension. In this configuration, we see the formation of periodic magnetospheric ejections (MEs) happen whenever the magnetic tension is high. The opening and closing of the field lines expel matter outwards with a timescale of around 7 years. These episodic outflows cross the fast magnetosonic surface, which makes them decoupled from the base of the outflow. In short, the observed MEs are not entirely ballistic outflows and constitute a part of the low velocity component of the jet. Fig.4.9 shows the kind of episodic outflows in our simulations, this case corresponds to $R_c = 0$ and $I_h = 10^{-2}$ (R0_I2). Consequently, after MEs are launched, they travel and affect the jet itself. As magnetic density grows near the polar axis the

jet collimates more. Then, when matter is released, a wobbling structure can be seen along the jet in accordance with observations (López-Martín et al., 2003; Pyo et al., 2003; Takami et al., 2020).

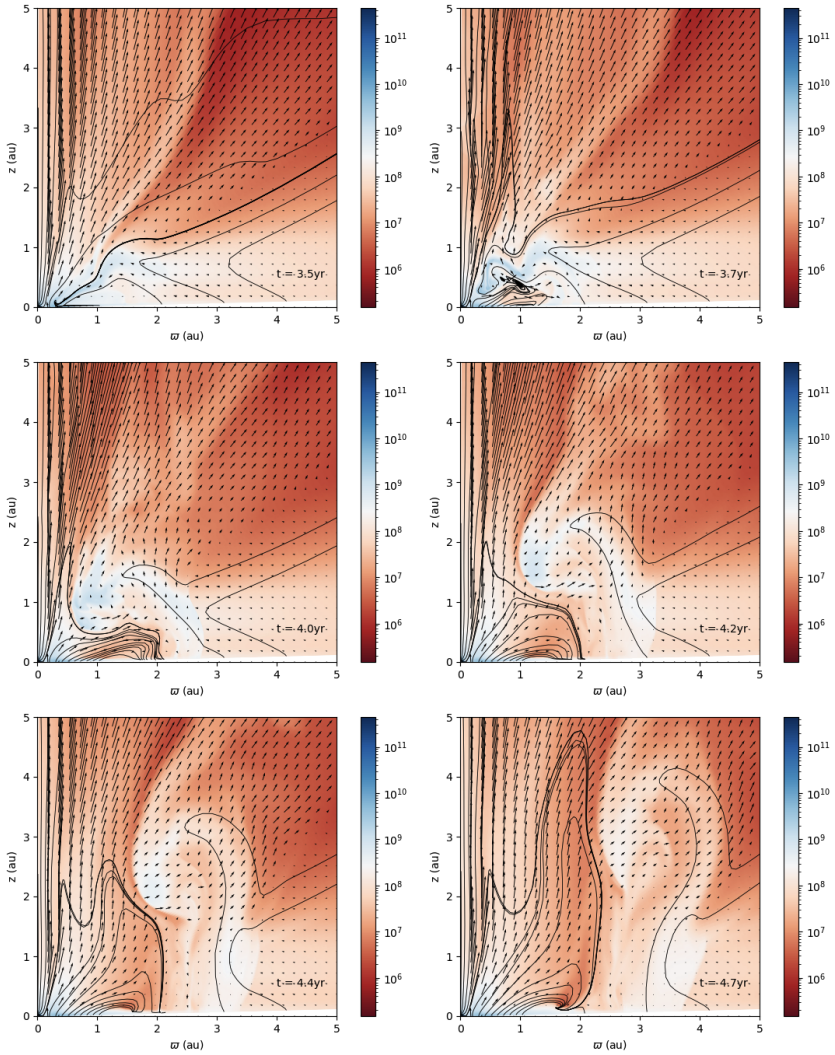

Figure 4.9: Appearance and evolution of a magnetospheric ejection (hereafter ME). The ME creation and ejection processes span over a year. At t=0, we have the initial state. In all plots, the black lines trace the magnetic field, the black arrows trace the velocity field, and the color map traces the density. At $t = 4$ years, we see the formation of two shocks on the axis, which propagates along the jet. For this simulation, $R_c = 0$ and $I_h = 10^{-2}$.

Observed knots coming from young stars jets are attributed to mass and velocity variations during ejection (Purser et al., 2018), which is the case here. This configuration does not reach a steady state, and has more abrupt periodic ejections than what can be seen in Zanni and Ferreira (2013), and Ireland et al. (2022a). Like in Zanni and Ferreira (2013), MEs mostly include disk material and only a very small percentage of

stellar material mixes in the MEs in a stable non-irruptive way. The more energetic part of the ME spans over years and is constituted of disk material only. If compared to Ireland et al. (2022a), models where strong MEs are presents are accompanied by a pause in accretion. In our case, even with strong MEs, material keeps accreting. Without fail, accretion and outflow close to the star stay close to the initial condition and matches the final steady state reached in Sauty et al. (2022) for case C. We discuss the effect of increasing accretion in Sec.4.5.5.

Since the magnetic field lines at the disk protect the central engine, the accretion rate and pressure balance are not modified. Thus, the close up is very similar to those found in Sauty et al. (2022). We can notice a small difference due to a denser and stronger magnetic field at the star vicinity. Compared to simulations from Sauty et al. (2022), the stellar jet is more collimated. Fig.4.7, contains a close up of the inner region with the same color scale and box size.

4.5.3 Effect of heating

To gauge what effect heating has on the jets dynamics, we can look at the radius, force balance, electric currents, and integrals of motion. Still we choose to show physical tracers that can help the set of parameters that better fit observations to be determined. We will try to address the following:

- The evolution of the jet radius with heating.
- The size of the jet emitting disk.
- The mass-loss evolution with the heating.
- The range of temperatures obtained.

4.5.3.1 Radius evolution with heating

Referring to Fig.4.5, we have two ways of controlling the jet width. We can either fix R_c and vary I_h, or conversely fix I_h and vary R_c. We first look at how the radius evolves in Fig.4.10 where R_c is fixed. We put the cut off of the analytical heating at 0.3 au and vary I_h (in Tab.B.2 this concerns all the simulations starting with R3_#). We follow the spine evolution through the passive tracer introduced previously. The larger and slower disk jet is hard to probe with the tracers. The reason is that the launching region at the base varies from one solution to another. The launching region of the jet is not the same for all cases, and depends heavily on the heating intensity. If we want to understand the evolution of the jet and disk wind ,we need to use the density maps directly. These maps show the gap between the disk and the jet. They show as well the standing collimation shocks that appear inside the computational domain for some of the parameters. Fig.4.10 shows the values the heating rate takes and, consequently, the jet radii. The stellar heating is common to the three cases, and only the wind heating varies by changing I_h. We note that as we increase the wind heating, the jet radius also

increases. We can explain such a behavior by the additional radial pressure introduced by the heating process. This pressure pushes the disk wind at a higher angle out of the disk, which results in a less collimated jet.

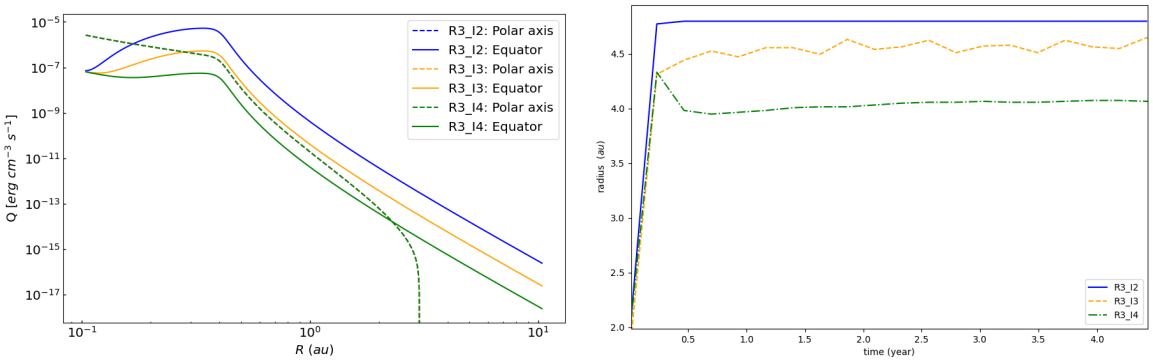

Figure 4.10: Heating rates (left plot) and the corresponding jet radius (right plot) extracted from the simulations for a fixed R_c and a variable I_h. For all the cases, the stellar component is unchanged and matches the green dotted curve. In the upper plot, the dotted lines express the heating extracted at $\theta \sim 0$, and the solid lines are for values of the heating on the equator ($\theta \sim \pi/2$).

In Fig.4.11, we see that by selecting a fixed value for I_h and varying R_c, the wind also acquires extra heating. This is expected as we extend the heating farther away from the star for both components. If we only increase the heating of the stellar component, this leads to a lower increase in the jet radius. It means that only varying R_c does not isolate the contribution of the stellar heating. When we isolate it we, once again, see that the farther we heat up the stellar atmosphere, the larger the jet radius is. It is in concordance with our conclusions so far.

Same as for the spine jet, the disk jet opens up as more heating is added. Its opening angle is larger by definition. For the wider disk jet, it is difficult to define a formal characterization of its radius. For that reason, we rely mainly on the spine component to extract information on the radius. We nonetheless notice a number of generic behaviors common to all cases. The disk jet has the same topology as the spine jet no matter the heating, for example, if the spine is paraboloidal, the disk jet is as well. This holds for the two other cases. By extracting the mean heating rate from $R = 0.085$ au (outside the accretion region) to $R = 1$ au and above the disk up to $\theta = 1.3$ rad, we see that above $Q = 3 \cdot 10^{-6}$ erg cm^{-3} s^{-1} the low density corridors separating jet and disk are more pronounced. The outflow separation region is lower than 10^{-5} cm^{-3} in density. The lower the heating, the narrower and denser the medium.

Overall, we can fit the evolution of the disk jet radius emitted at the base using a power-law of the average heating rate. We exclude in Fig.4.12 all the cases that have a surface accretion as they do not reach a steady state. To fit the data we keep 18 simulations out of 26. All nonsteady jets are found on the upper left corner of the parameter space (Fig.4.5). We argue it is due to the weaker contribution of the stellar

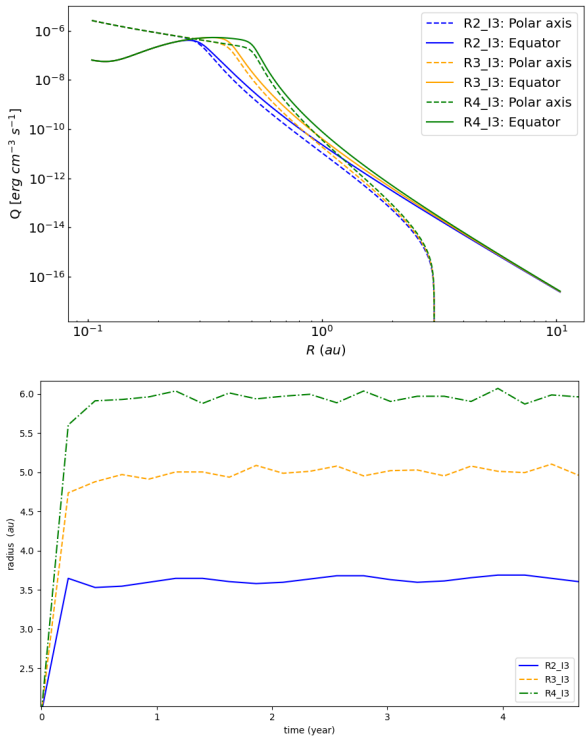

Figure 4.11: Same plot as in Fig. 4.10 but for a fixed I_h and a variable R_c.

heating. Even if they overlap with stationary cases when looking at the average heating rate. Having a stronger stellar heating component expels more matter at initial steps, which in turn lightens the wind in terms of mass. If enough material is expelled in the launching region it becomes easier for the centrifugal and Lorentz forces to keep plasma from migrating closer to the disk. It is worthwhile noting that the values of the average heating rate depend heavily on the area of the grid we extract the information from. As can be seen from the upper plots of Fig.(4.10,4.11), most of the heating is close to the star. The value of heating presented in these plots is sensitive to the size of the region over which we take the heating average. This being said, even if the value of the heating rate changes the scaling law does not, following $\varpi_{JED} \propto Q^{-0.25}$. This power law of $-1/4$ can be explained by looking at the thermal pressure added by the heating. The plasma is accelerated more. Given the disk is a boundary that refills the wind at a constant rate, the region, which has enough matter to form a disk jet, also decreases in size.

We assume that no matter how small the heating, the flow does not fall back onto the disk but goes out. Under this assumtion, we can infer from Fig.4.12 that below $2.56 \cdot 10^{-8}$ erg cm^{-3} s^{-1} the radius of the jet emitted by the disk is larger than 0.7 au. For a jet to form, MHD requires the gas to support an electrical current, which in turn needs charge carriers. We need processes that can sufficiently ionize the gas outwards. Typically, a Class II star can thermally ionize up to ~ 0.1 au, above the disk, which only represents a small fraction of the disk. In accreting systems, the magneto-rotational

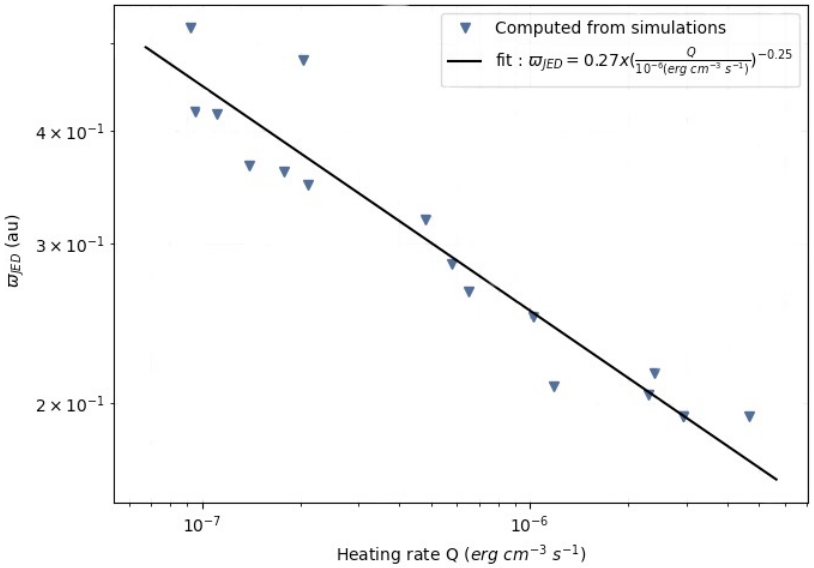

Figure 4.12: Fitting the disk jet radius at the base of the launching. All cases with surface accretion were excluded.

instability (MRI) also needs ionization further outward in the disk. Otherwise a dead zone appears in the mid-plane of the disk lowering accretion. The degree of ionization is uncertain and varies with the strength of each ionization process. For RY Tau, we assume the ionized part of the disk that can produce a jet between $0.1 - 0.7$ au. This makes $2.56 \cdot 10^{-8}$ erg cm^{-3} s^{-1} a lower limit for heating.

The ionization level needed to initiate MRI and to create a medium with enough charge carriers to facilitate ejection is easily modeled up to ~ 0.3 au through energetic particles produced during reconnection events of the stellar magnetic field with the disk. Brunn et al. (2023) estimate the ionization generated by protons, electrons, and secondary electrons accelerated from solar flares. They find ionization rates 6 times higher than what is proposed by other sources such as stellar X-rays, and galactic cosmic rays (Rab et al., 2017). This extra energy contributed by flaring is sufficient to maintain MRI on secular scales, and generates heating rates that match what we have parameterized in our model (Brunn et al., 2024). Above 0.3 au we need other injection sources and/or sources of ionization.

4.5.3.2 Disk wind mass loss

The mass loss rates follow the same trend as the radius as the heating increases (Fig.4.13). This is expected, since by reducing the launching region, the jet mass loss rate should also decrease. We can extend the analysis on the upper limit of the disk ejection radius. We can infer an upper boundary for the mass loss rate as well. We obtain that the disk jet should not expel more than $2.8 \cdot 10^{-8} M_{\odot}\,\mathrm{yr}^{-1}$. We infer that result from Fig.4.13. The mass loss scales as $\dot{M}_{JED} \propto Q^{-0.7}$. Anderson et al. (2005)

investigate how the wind structure is influenced by the mass loading. They measure the cylindrical radius (called in their paper, ϖ_j) along the field containing %50 of the mass flux, which originates from the same disk region in all their simulations. The increase in collimation is found to be slow, and they fit ϖ_j using a power-law in $\dot{M}_{\varpi_j}$ bearing a rough relation that goes as follows $\varpi_j \propto \dot{M}_{\varpi_j}^{0.1}$. We obtain by fitting ϖ_{JED} and $\dot{M}_{JED}$, the following rule, $\varpi_{JED} \propto \dot{M}_{JED}^{0.33} \propto (\dot{M}_{tot} - \dot{M}_{spine})^{0.33}$. Contrarily to Anderson et al. (2005), we do not fix the ejection radius to where the magnetic field line accounts for half the mass flux, but we instead measure the whole mass flux coming from the region of the disk that produces the jet.

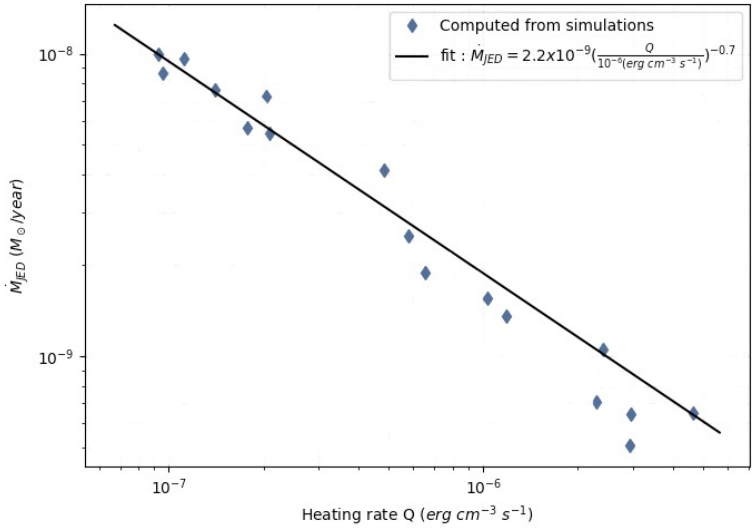

Figure 4.13: Plot of the mass loss with the heating rate. The mass loss as function of the heating can be fitted by a power law.

4.5.3.3 Magnetospheric outflows

Magnetospheric winds and jets expelled by a larger portion of the disk are both observed in the parameter space. They depend on the amount of heating introduced. To obtain jets with launching regions above 0.2 au, we need heating rates lower than $\sim 3{\cdot}10^{-6}$ erg cm^{-3} s^{-1}. Cases with launching regions below $\sim 0.2au$ have a morphology similar to that of X-type winds modeled by Shu et al. (1994).

An important result from this study is that the more the heating we input in the disk wind, the wider the jet is. If too much heating is implemented, the outflows are too wide to be called jets. This is the case for the quasi-conical solutions. The outflows become radial in the form of a wind. The eventual velocities from the disk outflows are too high ($\sim$ 1000km s^{-1}).

The X-type winds observed in this work emanate from the corotation radius (r_c). The funnel stream starts at a truncation radius (r_t) close to r_c ($r_t \approx r_c$). This means the system is in a configuration that does not add angular momentum to the star through

the closed magnetic lines in the accretion zone. Since r_c and r_t are imposed by the boundary conditions, the angular momentum is not affected by the changes that may occur in the disk. The exception would be if enough matter migrates closer to the star and interferes with accretion. However, we do not get such configurations, because they lead to a steeper time increment and make these scenarios difficult to obtain and study. Similar to Romanova et al. (2009) we get conical winds with wide opening angles. Unlike their work, we have a fast inner jet component on the axis. Additionally, the outflows are steady with no inflation of the magnetic field lines. Although, the extraction region of these conical outflows are constrained to a small spatial range, the mass loss rate is on the order of $\sim 10^{-9}$. As a comparison, the mass loss rate of the stellar engine is $3.0 \cdot 10^{-9} M_\odot\,\mathrm{yr}^{-1}$. In the upper plot of Fig.4.14, the mass loss from the conical wind only is $1.3 \cdot 10^{-9} M_\odot\,\mathrm{yr}^{-1}$. The middle plot produces $2.3 \cdot 10^{-9} M_\odot\,\mathrm{yr}^{-1}$. The last one gives $5.5 \cdot 10^{-9} M_\odot\,\mathrm{yr}^{-1}$. These values were obtained by computing the mass loss rate between two colatitudes that contain the conical component, namely,

$$\dot{M} = 2\pi R^2 \int_{\theta 1}^{\theta 2} \rho V_R \sin\theta d\theta. \tag{4.16}$$

We hence determine what constitutes the global mass loss of the disk jet by looking at the mass flux passing through two density minimums.

These solutions have a shortcoming due to the regions below $10^{-5}\ cm^{-3}$ that separate the jet and the disk wind. They appear because the heating rate is strong enough to expel matter faster than the disk can repopulate the region. The resulting temperature is on the order of one million degrees. Density decreases faster than pressure, which leads to these high temperatures. The temperature we derive from the simulations are effective values that contain extra terms that do not describe the gas pressure only. Thus, because the pressure has extra terms, we argue that our temperatures are overestimated when density is below 10^{-5} cm^{-3}.

4.5.4 Electric circuit

The poloidal electric current responsible for the collimation leaves the disk to enter again at closer radii. The current direction has to change in the jet as a whole. The current density J_p is outwards in the outer disk and inwards in the jet. Anchored field lines have, consequently, two regions, one where the field lines close on the axis, the other where the magnetic field lines decollimate. Since the initial bow shock leaves the simulation domain, the global electric circuit is maintained by the boundary conditions.

Near the axis ϖB_ϕ is necessarily zero. Its value decreases as we get farther from the axis, and reaches a minimum at the end of the jet. This pattern is similar for all the cases we studied. We begin to see differences outside the jet. For winds with the highest heating rates, very low density regions appear, which disconnect the disk electric circuit from the jet. ϖB_ϕ profile increases after leaving the jet to reach approximately zero in all the low density region.

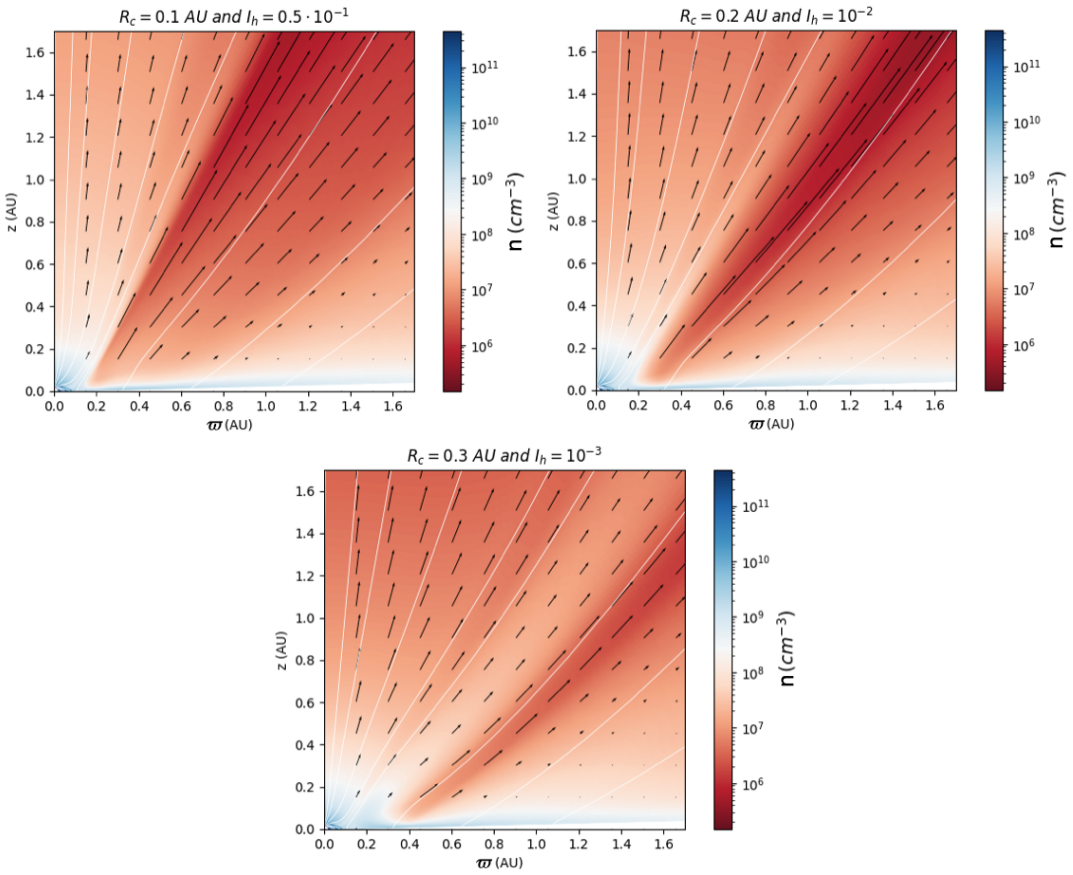

Figure 4.14: Width of the conical winds given the chosen parameters. The simulations are steady.

The paraboloidal and conical jets present the expected butterfly shape. The overall circuit is well behaved, and without any particular feature that would help identify the morphology of the jet. Heyvaerts and Norman (1989) focused on the electric poloidal current present at infinity. Their results indicated that any stationary axisymmetric magnetized jet will eventually converge into either paraboloids or cylinders, asymptotically from the source. The outcome depends on whether the asymptotic electric current vanishes or takes finite values. This fundamental theorem was later extended by Heyvaerts and Norman (2003) to incorporate considerations of current closure and its influence on the solution geometry. The actual amount of current left is not known since linking current value to the source is not simple to make in numerical works.

4.5.5 Increasing accretion rate

Two accretion rates were chosen to quantify the effect of changing accretion rate on the global jet. Observed accretion rates of intermediate mass young stars ($1.5 - 3\ M_\odot$) are between $10^{-8} - 10^{-7} M_\odot\,\mathrm{yr}^{-1}$ (Garufi et al., 2019). All the simulations shown so

far have an accretion rate of $1.3 \cdot 10^{-8}$ $M_{\odot}\,\mathrm{yr}^{-1}$. Increasing the accretion rate by a factor of three creates a wave pattern on the spine jet (Fig.4.15). This wavy stellar jet evolution is the consequence of magnetospheric ejections. Similarly to cases D, D.1, and D.2 from Sauty et al. (2022), increasing the mass accretion rate in the magnetospheric columns introduces quasi-periodic stable magnetospheric ejections that remove angular momentum from the star and the disk. It would prove highly challenging to differentiate observationally between the two accretion rates due to the substantially greater uncertainties in the measurements compared to the variation identified in our simulations. Nonetheless, they serve as proof for magnetospheric ejections in the case of an increased accretion rate, where up to 25% of accretion mass loss feeds the spine outflow.

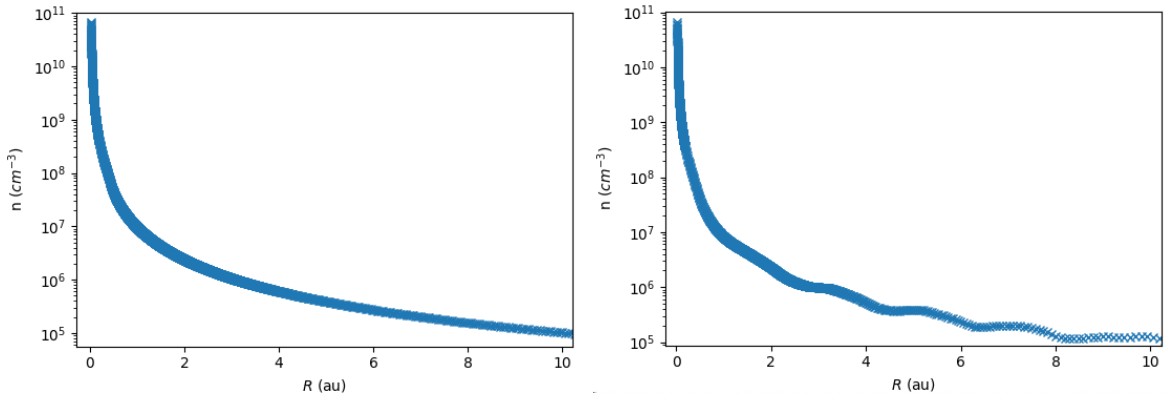

Figure 4.15: Number density of the R3_I4 with an accretion rate of $1.3 \cdot 10^{-8}$ in the left plot and $3.1 \cdot 10^{-8}$ in the right one. We fix θ at ~ 0 to follow the evolution of density along the polar axis.

Grinin (1992) proposed that RY Tau exhibits irregular eclipse-like dips in brightness, attributed to fluctuations in obscuration resulting from circumstellar dust. In the same spirit, Petrov et al. (2019) suggest a bimodal behavior of RY Tau. One where the brightness of the star increases, and so does the variability of ejection. The other mode is called quiescent, and is characterized by a fainter source. the authors explain the change in luminosity by a changing dust structure around the star. With more activity, the geometry of the dust changes and clears the star line of sight.

We suggest that in addition to the steady variability introduced by increasing accretion onto the star (Sauty et al., 2022), an increase in matter infall farther in the disk also contributes. This episode in the early life of the star would let dust migrate closer to the star. Then with the eruptive ejection that occurs after, dust is evacuated. In the simulations where we see this scenario, the period for the cycle to complete is between 1 and 2 years (Fig.4.9), followed then by a calmer phase, where plasma that has not been evacuated in the jet fall back and repopulates the disk farther outward.

4.5.6 Standing recollimation

We note the presence of a standing shock structure in R3_I4. This happens when the flow hits the axis at a velocity greater than the fast magnetosonic velocity, resulting in a jump in the flow quantities. After the shock, the magnetic fields are refracted outwards. We can better see the collimation and appearance of a shock in the temperature plots (Fig.4.16). The outflow is collimated through inwards Lorentz force that become larger as the jet widens. The flow reaches the axis at $R \sim 15$ au, resulting in a shock surface that has the shape of a cone along the polar axis. In Fig.4.17 we show that a jump in the flow occurs after at the shock. The compression ratio χ, defined as the density post- and pre-shock, is around 2. Given the uncertainty on when the shock front starts, we obtain a compression factor in the interval $[2, 3]$.The maximum compression rate possible for an adiabatic hydrodynamical 1D flow is $\chi_0 = \Gamma + 1/\Gamma - 1 = 4$.

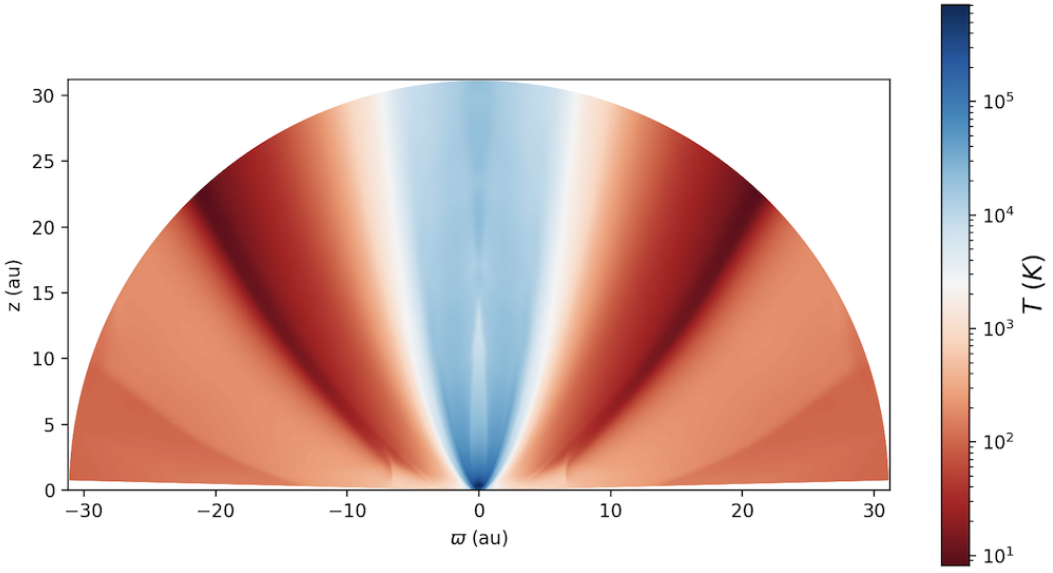

Figure 4.16: Temperature plot of R3_I4. We extended the computational grid for this simulation to 30 au to capture the standing shock. the maximum temperature is around 10^6 K and can be found below 1 au, near the star.

As can be seen in Fig.4.16, the shock is not normal to the flow. In this case, the shock is an oblique one. To determine its properties we have to look at the normal components to the shock surface.

The outflow is supersonic and super-Alfvénic, and the sound speed is computed in the jet using $C_s = \sqrt{\partial P/\partial \rho}$, along the polar axis. The toroidal component of the field is the dominant one ($B_\phi/B_p >> 1$). To best capture the nature of the shock, we compute the fast magnetosonic Mach number using the velocity perpendicular to the shock $M_{mf} = V_{p,\perp}/V_{fast,\perp}$. We call it the modified fast Mach number. If, on the other hand, we look at the poloidal fast magnetosonic Mach number, $M_f = V_p/V_{fast}$, we see that the flow remains super-fast even where the shock lays. The two quantities

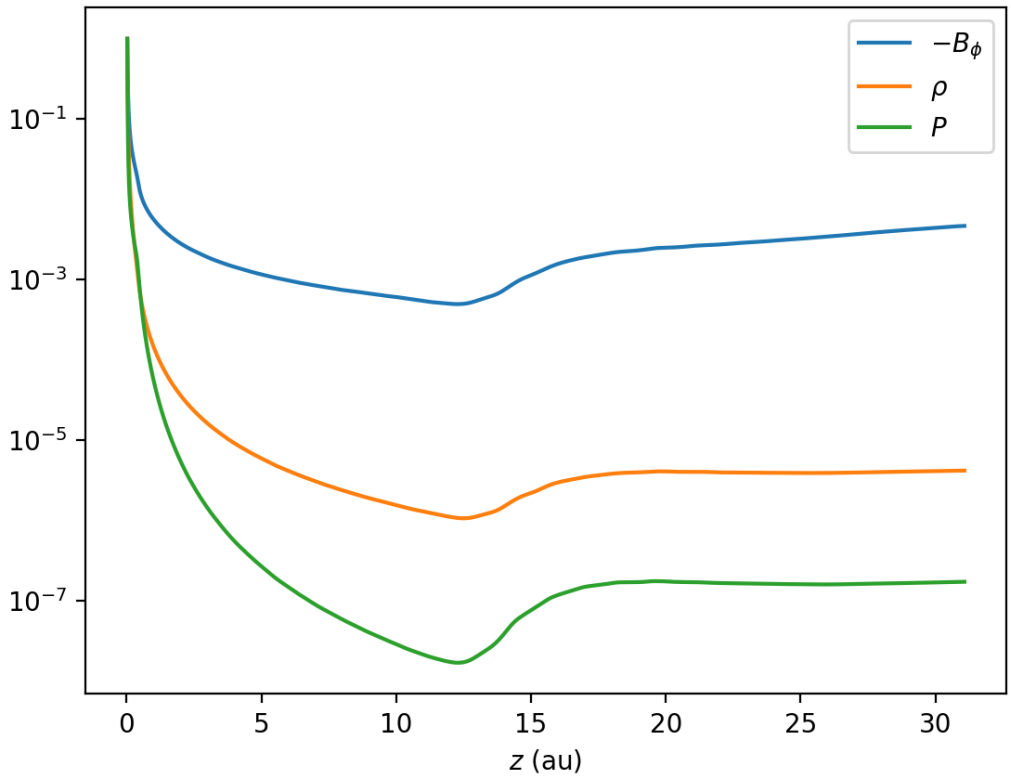

Figure 4.17: Plot of the toroidal magnetic field, density, and pressure, along the jet axis. All quantities are normalized such as to fit in the same plot.

are computed along $\theta \sim 0.3$ deg as there is no perpendicular velocities on the axis by construction. Fig.4.18 shows a clear jump of the velocity from the super fast regime before the shock to a sub-fast velocity after. The shock wave angle (i) is difficult to determine precisely given the grid resolution. We find i between 0.5 and 2.6 degrees. Consequently, the shock occurs when the M_{mf} is between $1 - 1.7$. In Fig. 4.18, we plot the modified fast Mach number, using the perpendicular velocities, for a cone of 0.5 deg.

Using an angle of 0.5 deg, we find that, at the shock location, the modified fast Mach number is equal to one. This coincides with the results of Matsakos et al. (2008) where the shock converges to the fast critical surface. The fact that the poloidal fast Mach number remains above one, shows that the real critical surface is on the modified fast critical surface, which was demonstrated by Bogovalov (1994) as a singularity. Yet we extend here the conclusion of Tsinganos et al. (1996) for axi-symmetric and self-similar solutions. The real critical surface is only the modified critical surface. For the critical surfaces, the component of the flow velocity perpendicular to the directions of axi-symmetry and self-similarity equals the slow/fast MHD wave speed in that direction. The modified fast surface coincides with the real MHD horizon, while the poloidal fast surface is the MHD ergosphere, analogously to black holes, see Carter (1968).

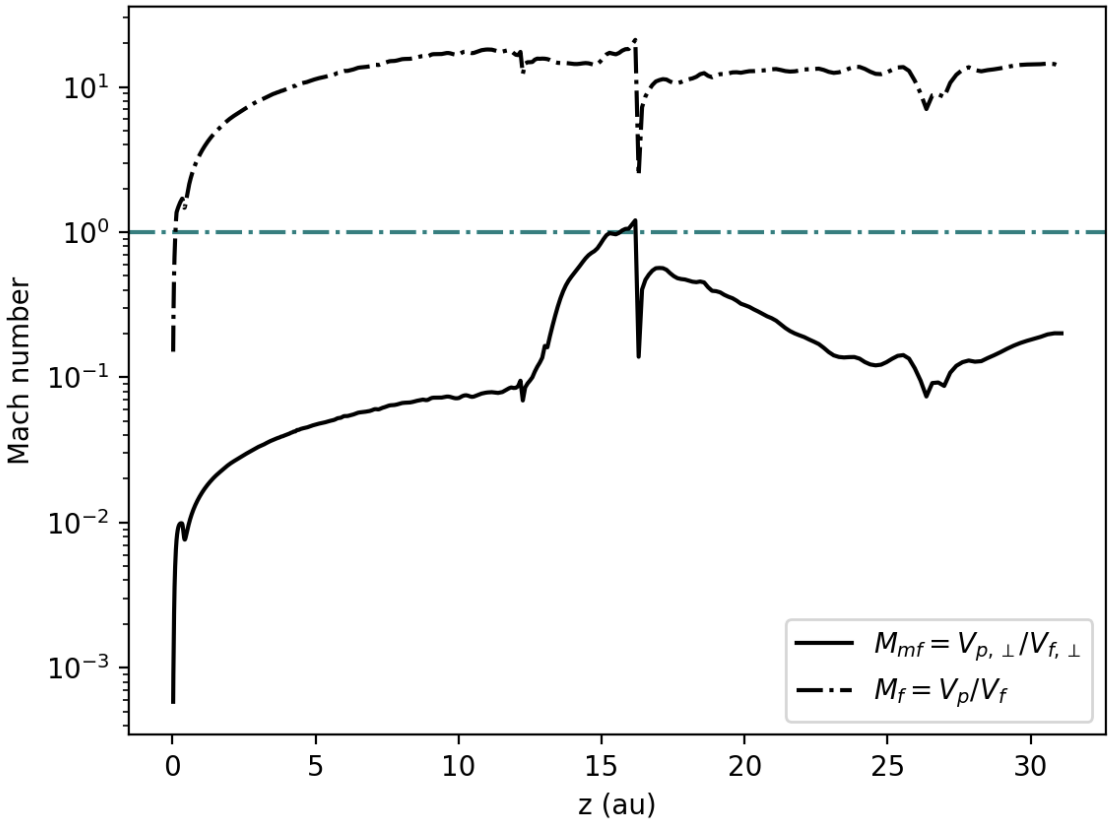

Figure 4.18: Plot of the perpendicular fast magnetosonic Mach number M_{mf} (same terminology as VTST00) and with M_f describing the Mach number parallel to the flow. The blue dash-dotted line corresponds to the fast magnetosonic limiting characteristic where the perpendicular fast Mach number equals to 1. The M_{mf} and M_f shown are computed along $\theta \sim 0.3$.

Recollimated plasma is systematically seen in R3_I# (all simulations starting with R3). The characteristic flow toward the axis happens inside the computational grid, but the shock itself can occur outside. For the closest shocks, they happen between 5 and 15 au. By lowering the heating rate in the disk wind, the shock appear closer to the star.

4.6 Discussion

4.6.1 Comparison to other simulations

We compare our work to other platform and global 2.5D simulations of nonrelativistic jets. Three-dimensional simulations would allow us to explore a larger range of possible instabilities and phenomenological behaviors but at the cost that they would limit the spatial and temporal grids. This extension is postponed to future work. Other 2D studies also include a disk in an idealized manner by introducing a resistive term which controls any excess in turbulence. Despite the decrease in the time step by the shorter interaction time scales in the disk (e.g., Casse and Keppens 2002; Zanni et al. 2007; Suriano et al. 2017; Ireland et al. 2021; Ireland et al. 2022a), the disk is treated more realistically. Computations on the largest domains were performed by Anderson et al. (2005) with a jet followed up to 100 au and Stepanovs and Fendt (2014); Stepanovs et al. (2014) with a jet propagating to 140 au. These studies lack a stellar driven component, but include a resistive ingredient which is an important step toward more realistic disks.

4.6.1.1 Small scales

For the inner part of the simulations, we reached a steady state in three stellar rotations only, equivalent to 42.6 days for the star of our simulations. This is not different from the results of Sauty et al. (2022), despite the more consistent treatment of the disk wind. The outer part, which contains the disk wind, takes longer to stabilize. Indeed, the initial perturbations due to the mixing of the spine jet and the disk wind need to relax. This takes time as the perturbations must exit from the outer boundary. In contrast, Zanni and Ferreira (2013) required over 50 stellar rotations, which amounts to more than 250 days, due to their faster rotating star. Romanova et al. (2009, 2011) reached an equilibrium after 500 days, approximately 100 stellar rotations in their case. Consequently, our approach significantly shortens the relaxation timescale in the inner part even if the outer region has not yet stabilized. In more recent simulations by Ireland et al. (2021); Ireland et al. (2022a), steady state was achieved after only 2 to 3 rotations of the central star, possibly because they included a high-velocity, low-density stellar jet component. It is worth noting that these simulations used smaller grids and/or lower resolutions. Another factor contributing to our shorter simulation time could be our initial conditions, which are closer to an equilibrium state, since we use analytical solutions for the inner spine jet and the outer disk wind.

4.6.1.2 Large scales

According to BP82, cold disk models with $\kappa = 0.1$ should have $\lambda \sim 10 - 30$ for $\xi_0^{'} = B_r/B_z \sim 1.2 - 1.5$ (see their Fig.2). We, on the other hand, obtain lever arms that depend on the heating used in the disk. For this reason, even though the magnetic profiles, mass loads and magnetization of the disk are imposed as boundary conditions, the heating modifies the outflow dynamics. It provides extra pressure to accelerate plasma above the disk. By doing so, the outflow does not need to have high lever arms as cold winds. It does not need such high lever arms to efficiently extract a significant part of the angular momentum.

The shock structures observed in our simulations seem to be a general by product of MHD collimation. They have been proposed as an outcome to self similar models of jet launching for nonrelativistic jets (Gomez de Castro and Pudritz, 1993; Ferreira, 1997) and for relativistic jets (Polko et al., 2010). The recollimation process is induced hoop-stress by the magnetic field. This is shown in Ferreira (1997) with self-similar cold models. It has been confirmed by 2D time-dependent simulations of Hervet et al. (2017) for the relativistic case and Jannaud et al. (2023) for nonrelativistic jets (shocks between $z \sim 70 - 250$ au). This force makes cold jets move toward the axis, creating standing recollimation shocks. This mechanism should work around different astrophysical objects, no matter the external environment. The authors of Jannaud et al. (2023) propose that such collimation shocks have not been seen before due to, either, lower physical scales or smaller times scales. Same as for analytical studies, they find that the recollimation position depends on the mass loading. the higher the mass loading, the closer the shocks are to the source. The key quantity that shapes the asymptotic of the jet is $B_z \propto r^{x-2}$. We also observe in our simulations standing recollimation shocks closer to the central engine, around $z \sim 15$ au (see Sec.4.5.6). Yet, there are three main differences in the present work. (i) First, the nature of the spine jet is different. Jannaud et al. (2023) minimize the contribution of the spine jet to isolate the collimation dynamic of the jet emitting disk. We, on the other hand, choose a spine jet solution that reproduces the key features of RY Tau micro-jet. (ii) Second, the disk wind of our simulations is not cold as we map the local heating rate. (iii) Third, we take into account the launching region and the disk produces a jet below 0.6 au. We directly attribute the close occurrence of shocks near the star to one fact: shocks are not produced due to magnetic recollimation of disk magnetic field lines. In our simulations, it is actually stellar magnetic field lines that focus towards the shock surface.

However, despite the differences, the shocks that appear in Matsakos et al. (2008, 2009); Stute et al. (2008, 2014); Jannaud et al. (2023) and in this work are all of the same nature. They are weak, oblique and with low compression factors between $\sim 1.5 - 2.5$, even if the launching at the base differs. In the case of Matsakos et al. (2008, 2009) the flow is already super fast at launching, and the magnetic field lines are being focused on the axis. For Matsakos et al. (2008, 2009) and Stute et al. (2008), the collimation is partly caused by outer radial boundary condition effects, and partly because the internal jet region is not strong enough to withstand the outer jet. In Jannaud et al.

(2023) the shocks are related to the disk jet physics, where their choice of supersonic outflows at the base of the disk grants control over mass loading of the disk wind.

Let us consider the parameters that we did not vary in this study, namely, x, $\mathcal{K}$ and μ, which corresponds to the Blandford and Payne (1982) (BP82) parameters. This helps the comparison with results presented in other publications. We modified the outflow conditions through heating, but other methods are possible as will be discussed below. The parameter $x = 3/4$ is the same as what was used by BP82 for the magnetic field distribution. $\mathcal{K}$ is the mass-loading parameter and μ, the ratio of thermal to magnetic pressures. The normalization is somewhat different from VTST00. In terms of BP82 formulation, we have $\kappa = 0.1$ and $\mu = 0.07$. These parameters are constant along the disk surface.

First, the parameter x, which controls the magnetic profile, controls the collimation degree of the jet. Naively, the more we increase x, the wider the jet. Fendt (2006) performed 40 simulations to study the influence of the magnetic field profile on the collimation. They chose $\kappa \propto r^{3/2-2x}$, using the same boundary condition as Ouyed and Pudritz (1997a,b). μ was varied between science runs, as the inverse of κ. It has a increasing profile as ϖ increases. They also explored the evolution of collimation given different density profiles. The grid they used to perform simulations is $[z, \varpi] = [300, 150]$ in units of $10R_\odot$ equivalent to $z \times \varpi = 13.3 \times 6.7$ au. No spine component was considered in their work. Fendt (2006) confirmed the role of the parameter x on collimation. A decrease in the magnetic profile results in a decrease in collimation, irrespective of the density profile. Above $x > 1.6$, they obtain no steady jet, and a wave shape is seen to propagate along the outflow. This observation is confirmed by more recent work, where for $x \geq 1$ time scales become too large to reach a steady state in a realistic computation time (Jannaud et al., 2023). In the same spirit, Pudritz et al. (2006) showed by varying $x = 1, 3/4, 1/2, 1/4$, with a similar κ profile as before, that a smaller x leads to a less collimated jets. Although, they attribute the collimation property of the jet in their simulation to the current distribution, it is controlled by the mass load. The expression of the azimuthal magnetic field is as follows, $B_\phi \propto r^{-1/2-x}$. For cases with $x = 1$ and $x = 3/4$, the jet collimates, since B_ϕ is larger by decreasing κ. Conversely, the jet decollimates when κ is increased.

Anderson et al. (2005) explore the jet evolution by changing the mass load from the disk for a cold jet model with $x = 3/4$. They choose a constant κ along the disk boundary. Its value goes from $6.3 \cdot 10^{-4}$ to 19, and outflow occurs in a distance of 1au in the inner part of the disk. In this region B_z is reduced to minimize its role in shaping the poloidal field. They use a cylindrical grid $[z, \varpi] = [100, 100]$ au with 256×256 cells. They report a wider jet as κ decreases. For a κ larger than unity, they do not reach a steady state, and the magnetic field oscillates. This trend is in agreement with work done on steady jet theory (e.g., Pelletier and Pudritz (1992); Ferreira (1997)). When a jet is heavily mass loaded, it affects its ability to produce a super Alfvénic outflow. Magnetic driven winds are possible up to $\kappa \sim 1$ producing a lever arm of 2 (Blandford and Payne, 1982). Higher mass loadings bring the Alfvén surface closer to the disk, which in turn means the magnetic field has to have more inclination.

4.6.1.3 Disk interior

It is clear that platform simulations can only describe the accretion disk as a mere boundary condition for the wind. This in turn overlooks disk physics - not only pertaining to diffusivity and viscosity, but also the origin of the magnetic field. Simulations including the disk physics, Zanni et al. (2007), find that increasing the resistivity reduces the ejection efficiency. The energy generated from the accretion is released in the jet and produces more powerful jets the less dissipation there is. In other words, the magnetic field applies a torque on the disk which will modify the efficiency of accretion. The evolution of the magnetic field leads to the readjustment of the jet itself. Zanni et al. (2007) characterize the effect of Ohmic heating on the ejection efficiency and find that an increase in the thermal energy inside the disk allows more mass loading in the jet. Our simulations are in agreement in that regard but for the outer part of the disk.

An important question to consider when studying an accretion disk is the origin of the magnetic field. Disk dynamos have been suggested to account for the large scale magnetic field having a direct effect on the evolution of the system. Mattia and Fendt (2020a) for instance consider the effect of a non-scalar dynamo tensor which was later extended to include analytical turbulent dynamo model with both magnetic diffusivity and a turbulent dynamo term (Mattia and Fendt, 2020b). They succeed at connecting both terms with the Coriolis number Ω^*, related to the rotation frequency and the turbulence correlation time. As the Coriolis number increases so does the accretion rate. In other terms, accretion increases with the strength of the mean-field dynamo (refer to Mattia and Fendt 2020b for more details). Even if we do not include diffusivity in our simulations, the magnetic field inversion in the nonstationary state depicted in Fig.4.9 is similar to those present in their simulations. When the Coriolis number is low the disk is more turbulent and magnetic loops form. We argue in our case that without sufficient heating the diffusivity is not enough to amplify the magnetic field and have collimated ejections. In Mattia and Fendt (2022), the same authors studied the various quenching of the dynamo and the diffusivity. In particular, they show that for high Coriolis numbers, the higher the magnetic field, the lower the acceleration and the higher the collimation. This is somehow similar to our simulations. Decreasing the total heating enhances the influence of the magnetic field and the collimation while reducing the terminal jet speed.

4.6.2 Comparison to observations

Class II stars are studied using spectro-imaging, as well as forbidden emission lines and optical lines like H_α to trace the wind and jet behavior. From these lines, mass loss rates can be estimated. They, nonetheless, greatly depend on the geometry of the wind and its temperature (Fang et al., 2018). Through optical tracers the ratio of mass loss rates to accretion rates is $\dot{M}_{wind}/\dot{M}_{acc} \sim 0.1$ (Bouvier et al., 2002). This ratio stays constant throughout all evolutionary stages of young stars. This highlights the strong link between accretion and ejection (Königl et al., 2000). In Tab. B.2, we list the wind

mass loss rates, the accretion rates and the ratio of mass loss to mass accretion rates of our simulations. All these quantities are calculated once a steady state is reached. As we increase the mass loss rate from the disk wind, the ratio of the stellar to the disk wind mass loss rates decreases. The stellar value remains nonetheless significant.

Differentiating disk wind or stellar-driven material through observations is not possible for the jet itself, as it is not spatially resolved at the base. It follows that in the cases where a micro-jet is present, the separation between the stellar and the disk component is rather difficult. For RY Tau, for instance, a small jet confined to the axis is observed and attributed to the inner most part of the jet (St-Onge and Bastien, 2008). Thus, even if the spine jet contribution is not known, it is expected to be important compared to the wind mass loss. In this study, the mass loss of the star is between $\sim 20-80\%$ of the total mass loss. Overall, the micro-jet can be explained by the stellar component while the large scale jet is mainly comprised of disk wind.

Gómez de Castro and Verdugo (2001) used UV semi-forbidden lines as tracers to determine the physical properties of plasma near the base of the jet for RY Tau and RU Lup. They analyzed the high resolution spectra of $C_{III}]_{1908}$ and $Si_{III}]_{1892}$. They noted that the velocities of these lines are comparable to those of optical lines. The luminosity of the optical and semi-forbidden lines are also comparable. Looking at the emission of RY Tau in terms of semi-forbidden lines, the authors concluded they are not associated to the accretion shocks and should be produced farther than 2 stellar radii. Given the semi-forbidden lines are spatially broader than the optical lines, they argued that the observed profiles are due to shock structures close to the base of the jet. Provided the plasma is collisional and originating from the disk, they constrained the temperature of the emission region, $4.7 < \log\ T_e(K) < 5.0$, and the electronic density, $9 < \log\ n_e(\mathrm{cm}^{-3}) < 11$. In a follow up paper, Gómez de Castro and Verdugo (2007) further constrained the physical properties, given by the semi-forbidden lines, and determined that the outflows can not be of disk-origin only. Their argument is that the jet should be produced by the contributions of several outflows from atmospheric open-field structures like those observed in the Sun. The refined temperature for the shocks is $\log\ T_e(K) = 4.8$, and $9.5 < \log\ n_e(\mathrm{cm}^{-3}) < 10.2$. The shocks we obtain in our simulations have temperatures of the same order as they presented. However they lack the density to be linked to UV emissions. The plasma density in the shocks of our simulations is two orders of magnitude lower than what is expected in the UV shocks.

To have the necessary density the shock has to occur between 0.1 and 0.45 au, which is consistent with the conclusion of Gómez de Castro and Verdugo (2001). The shock layer is inferred to occur closer than $\sim 38R_\star$ (~ 0.5 au). Thus, the shocks in our simulations cannot be stricltly related to the UV shocks. However, they clearly show that jets with knots close to the star such as the ones we present in this article are of stellar origin. St-Onge and Bastien (2008) reported for the first time a jet in H_α, which is also expected to be of stellar origin. The knots presence span from ~ 200 au to 4000 au. In our model the knots would be created at the shock layer and start migrating along the jet.

4.6.3 Possible heating sources

In the disk wind regions, the chemical state and thermal energy balance are influenced by stellar UV and X-ray flux. Accurately determining the gas temperature is crucial for calculating pressure gradients, wind flows and interpreting line emissions. Gas temperature is affected by heating and cooling processes, including collisions with dust grains, line emissions from ions, atoms, molecules and molecular abundances shaped by chemical reactions. However, including the microphysics of the heating rate is postponed to a later study. The uncertainty on the physical processes taking place in and above the disk are still not sufficiently well constrained to have a definitive answer.

At the disk surface where the wind originates, factors like Far UV photon-induced grain heating, conversion of binding energy during molecular hydrogen formation and excess electron energy from photo-dissociation and photo-ionization contribute to the gas heating. In addition, there is a promising source which is the energetic particles from flares. They may serve as another important ionizing and heating source (Brunn et al., 2023). Above the disk, magnetized jets and winds experience heating through nonideal MHD processes like Alfvén wave damping, Ohmic heating and ambipolar diffusion, especially at altitudes where photo-heating is less effective (e.g., Wang et al., 2019). This paper, focuses however on winds where the heating does not evolve with the fluid, underestimating the importance of the retro-action of heating sources on jet/wind generation.

4.7 Conclusions

We conducted 2.5D simulations of a jet showing key features from RY Tau, surrounded by a disk wind solution that reproduce outflows coming from a standard accretion disk. The jet is nonrelativistic, and the disk has a Keplerian rotation velocity profile. We mapped and parametrized the heating rate computed using the analytical solution quantities, namely, velocity and pressure. The outflows evolve, taking into account the heating map. To control the map, we added two parameters, with which we show a clear dependence of the jet shape at large distances with the heating rate at the base of the launching region. We find that the higher the heating rate, the less collimated the jet is. We distinguished between three cases using the measured opening angle of the spine at 10 au. While our definition of the jet radius remains ambiguous, it enables a consistent ordering between the different jet morphologies.

We showed, in the case of nonsteady jets, that a periodic behavior is possible. We showed that the jet can have two different states. The first may match the quiescent mode of RY Tau (Petrov et al., 2019), and the second one may match the other phase eruptive. These phases alternate in time. The eruptive phase occurs whenever the jet is perturbed by flares. During the flares, reconnection events occur. Matter is expelled due to the buildup of magnetic pressure. A stable period follows during which the length depends on the heating. Conversely, the quiescent phase takes place in between the mass ejection episodes. For the case we have shown, the simulation runs up to 14

years and we observed two events with this type of nature. Each occurrence is followed by a normal shock that moves outward along the axis. Observationally, the shocks are similar in nature to the H_α optical lines observed by St-Onge and Bastien (2008). Changing the heating map would change the period and strength of magnetospheric ejections, but the extent to which the period varies has not been studied. Even with a static heat map, we observed nonsteady cases with stable variations taking place over long periods (around 1 to 7 years)

Out of the effects heating has, there are two power laws linking the jet-launching radius and the mass-loss rate to the heating rate. The radius from which the disk jet originates follows the power-law $\varpi_{JED} \propto Q^{-0.25}$, and the mass loss has the power-law $\dot{M}_{JED} \propto Q^{-0.7}$. Using these power laws, we further deduced a third link between the launching radius and the mass-loss rate, $\varpi \propto \dot{M}_{JED}^{0.33}$. This result is comparable to what was found by Anderson et al. (2005) ($\varpi_j \propto \dot{M}_{\varpi_j}^{0.1}$). The main difference arises from the fact that Anderson et al. (2005) used a cold wind with no spine jet being considered. Thus, the transverse force equilibrium is different.

Although unexpected, we obtain standing recollimation shocks below 100 au. These shocks may not be linked to the shocks observed in UV semi-forbidden lines (Gómez de Castro and Verdugo, 2001, 2007) because this would require them to occur closer to the source. Such a configuration may exist in a parameter space region we have not explored yet. However, the main takeaway from their study is that the shocks are of stellar origin, which is what we have observed in our simulations. In any case, they match the shock structures found in St-Onge and Bastien (2008), and previous numerical works, for example, Matsakos et al. (2009) and Jannaud et al. (2023). The novelty resides in using a spine jet that matches the observations of the RY Tau micro-jet and extracts enough kinetic energy to maintain a constant rotation rate of the star. We also implemented a heating model that gives three jet shapes that can be compared to observations to identify the most probable heating values around a YSO.

Chapter 5

A complete axi-symmetric system

Contents

5.1 Introduction 145
5.2 Including the physics of the accretion disk 148
5.2.1 Physical framework and resistive MHD equations 148
5.2.2 Self-similar disk solution 150
5.2.3 Disk solution parameters 151
5.2.4 Normalization 152
5.3 Numerical set-up 154
5.3.1 Computational grid 154
5.3.2 Connecting the accretion funnel and the disk 157
5.4 Results of fiducial simulations results 158
5.4.1 General behavior 158
5.4.2 Episodic accretion 159
5.5 Adding heating inside the disk 161
5.5.1 Treatment of the Joule term 161
5.5.2 Energetic particle heating inside the disk 163
5.6 Magnetization and turbulence 163
5.7 Discussion and conclusion 165

This Chapter is a draft for a second article that still has to be submitted.

5.1 Introduction

Most observations of young stars and their environment show that ejection and accretion are closely related (Ray and Ferreira, 2021). Jets emitted from these objects are

magnetized and travel with a high velocity away from the central engine and towards the interstellar medium. The magnetic fields contained in the jets themselves and their surrounding help collimate these outflows. It is now commonly accepted that the source for such outflows is the accretion disk (e.g., Burrows et al. 1996; Dougados et al. 2000; Bally et al. 2007; Hawley et al. 2016). Further highlighting the link between accretion and outflows is the strong correlation between accretion and ejection rates (Cabrit et al., 1990; Hartigan et al., 1995; Ferreira et al., 2006). Accretion disks also present with less collimated, slower and more massive winds (Tabone et al., 2017; De Valon et al., 2020). The dependence of both jets and winds on magnetic fields is clear, nonetheless, jets being produced closer the star should be affected by the stellar component. Whether both events have the same source has yet to be determined.

A number of scenarios have been developed to account for observations of outflows. One of such scenarios is the accretion-powered winds model. This model assumes the disk is threaded with a large scale magnetic field, and to investigate these outflows various solution have been proposed (Blandford and Payne, 1982; Wardle and Königl, 1993; Ferreira and Pelletier, 1995; Vlahakis et al., 2000; Ferreira et al., 2000; Ferreira and Casse, 2004). On the other end of the spectrum, Shu et al. (1994) and Shu et al. (1995) proposed a model where all ejection occurs from a single ring around in the disk. In this model the disk does not contain a large scale field as in extended wind models. Both models refer to jet launching from accretion disks.

Other jet launching sources have been proposed. For instance, strong outflows can originate from the stellar component (Matt and Pudritz, 2005; Cranmer, 2008; Matt et al., 2012). However, as pointed out by Takasao et al. (2022) in their discussion, stellar jets are limited by the amount of material they can eject. A series of 1D MHD simulations were performed by Shoda et al. (2020) where they follow the stellar wind along averaged flux tubes. Based on observation of magnetic geometry of solar-type stars (See et al., 2019, 2020), they find that the ejection rate reaches a maximum at $\sim 3 \times 10^{-14} M_\odot\,\mathrm{yr}^{-1}$. In Meskini et al. (2024) we see jets with a stellar mass loss rate close to $\sim 3 \times 10^{-9}$. We attribute the gap to the difference in energy carriers. Shoda et al. (2020) consider Alfvén waves as the main energy carriers in their models, while we consider a parameterized heating. In the case of the Sun, Wood et al. (2005) and Wood et al. (2021) measure rates around $\sim 10^{-12} M_\odot\,\mathrm{yr}^{-1}$, while other observations of sun-like prominences show rates of $\sim 10^{-11} M_\odot\,\mathrm{yr}^{-1}$ (Waugh et al., 2021). Episodic ejection is also an efficient way of stripping disk material away from the star, and removing excess angular momentum. These events happen in response to star-disk interaction (Zanni and Ferreira, 2013). We show in Meskini et al. (2024) that a stellar wind can be maintained with temperatures no higher than $\sim 10^6$ K close to the stellar surface. The resulting jets are stable and constitute a non-negligible proportion of the total jet, i.e. from the stellar and the disk components.

All the scenarios mentioned above have an important role in extracting angular momentum from the disk which, in turn, allows for accretion to proceed. By applying laminar torque, these processes transport momentum away from the disk. Another mean of momentum transport exists inside the disk. In this case, momentum is redis-

tributed to the outer layers of the accretion disk through a turbulent torque (Shakura and Sunyaev, 1973). Both types of torques are interdependent and ensue from the same basic physical phenomena (Lesur et al., 2013). Balbus and Hawley (1991) showed that a disk threaded with a magnetic field can trigger a magneto-rotational instability. In turn, this leads to turbulence, and subsequently radial transport of angular momentum. 3D Simulations showed that winds can be launched by MRI-generated turbulence (Bai and Stone, 2013; Suzuki and Inutsuka, 2014; Takasao et al., 2018, 2022). Although, Simulations that couple MRI-driven turbulence and magnetically-driven winds show different behavior from 2D simulations with an effective α-prescribed disk.

Numerical results from 2D simulations generally show bulk accretion within the disk (Stepanovs and Fendt, 2016), with some works presenting with surface accretion at $\sim 3h$ (Guilet and Ogilvie, 2013; Jacquemin-Ide et al., 2021), here h is the scale height. On the other hand, 3D simulations such as the ones shown in Zhu and Stone (2018) and Mishra et al. (2020) contain surface accretion, in a much higher region in the disk atmosphere, at $\sim 10h$. Such behavior may come from the accretion instability as presented by Campbell (2009). Stepanovs and Fendt (2014) avoid this instability by choosing that the feedback between the magnetization and magnetic diffusivity to be stronger than $\sqrt{\mu}$, with μ the magnetization (for more details about *standard* and *strong* diffusivity models refer to Stepanovs and Fendt (2014) for strong diffusivity and Jacquemin-Ide et al. (2019) for the standard one).

One of the main questions that models and numerical works try to answer, in a direct or indirect way, is the evolution of the stellar spin. It is a crucial factor in understanding accretion and ejection processes around a star. How much angular momentum and material is accreted and ejected onto and from the star, respectively, controls the braking time of the star. Bouvier et al. (1993) and Edwards et al. (1993) show through observations that most of the angular momentum excess is evacuated before the star reaches the main sequence. Stellar spin is also essential in wind production. A number of numerical works find that when the disk truncation radius is lower than the corotation radius, strong winds emerge from the magnetosphere (Miller and Stone, 1997; Lovelace et al., 1999; Romanova et al., 2009). The resulting outflows reduce or even suppress accretion. Similarly, the simulations in the work also show a strongly inhibited accretion due to the propeller regime. Moreover, stability of the magnetosphere depends on the stellar spin (Spruit et al., 1995; Blinova et al., 2016). In particular, the instability can impact how accretion proceeds onto the star. Depending on the stellar parameters, accretion can occur through multiple columns. Such behavior is a result of the Rayleigh–Taylor instability (Blinova et al., 2016), which are fundamentally 3D phenomena. These instabilities will be addressed in a future work.

Another crucial key parameter of accretion-ejection systems is the magnetic field transport in the disk and its winds. In addition, magnetic fields contribute in the form of a turbulent magnetic pressure gradient, which in turn plays a role in shaping the vertical disk structure (Zhu and Stone, 2018; Jacquemin-Ide et al., 2021; Zimniak et al., 2024). In this chapter, we aim to include, in the same computational domain, a disk with large scale magnetic fields and the stellar magnetosphere. The first results show a

heavily unstable accretion-ejection system, where magnetization determines how long accretion proceeds. In this work, we use semi-analytical solutions to initialize the stellar component and the accretion disk. The disk solution produces disk winds, which means the simulations start with all the outflow ingredients at the initialization step.

In Sec.5.2 we describe the physical framework of accretions disk with resistive MHD. We also describe the analytical solutions and the parameters used to initialize the computational box. In Sec.5.3 we describe the numerical set-up in terms of grid resolution and treatment of the accretion region at the initial step. Sec.5.4 shows the results of including an accretion disk. We see that the accretion is turbulent, with accretion arms that originate from failed jet launching. Accretion cyclically affects the system as a whole. We then test the heating produced by EP in Sec.5.5. The level of magnetization seems to be important in elongating accretion of the disk, a behavior described in Sec.5.6. Last, we discuss the results of the simulations in Sec.5.7.

5.2 Including the physics of the accretion disk

In the previous chapter, we have used a wind disk model that only considers the disk interior as a boundary condition (Vlahakis et al., 2000). In this chapter, we take interest in the evolution of a complete accretion-ejection system. It is thus essential to take into account a new model where both, a turbulent/resistive MHD disk and a jet described by ideal MHD are consistently connected. Ferreira (1997) mathematically connected the two regions by linking the toroidal magnetic strength and where the Alfvén critical point is crossed in the disk. By ensuring a smooth crossing of the slow magnetosonic critical surface, this treatment fixes the disk magnetization in addition to its ejection efficiency. For a detailed explanation refer to Ferreira (1997).

5.2.1 Physical framework and resistive MHD equations

We assume axisymmetry in the accretion-jet models, whether in the ideal MHD domain or in its resistive counterpart. The disk is considered rotating at a sub-Keplerian velocity and its self-gravity is neglected. In the presence of an accretion disk, the equations describing the flow evolution are the same as those of ideal MHD as they obey the same continuity principles. The difference lays in the additional terms that account for non-ideal effects. The equations describing magnetized accretion-ejection are,

$$\frac{\partial \rho}{\partial t} + \nabla \cdot (\rho \mathbf{V}) = 0, \tag{5.1}$$

$$\rho \left[\frac{\partial \mathbf{V}}{\partial t} + (\mathbf{V} \cdot \nabla)\mathbf{V} \right] = -\nabla P + \frac{1}{4\pi}(\nabla \times \mathbf{B}) \times \mathbf{B} - \rho \frac{\mathcal{GM}}{r^2}\hat{\mathbf{r}} + \nabla \cdot \mathcal{T}, \tag{5.2}$$

$$\frac{\partial \mathbf{B}}{\partial t} - \nabla \times (\mathbf{V} \times \mathbf{B} + \eta \cdot (\nabla \times \mathbf{B})) = 0, \tag{5.3}$$

$$\frac{\partial P}{\partial t} + \mathbf{V}\cdot\nabla P + \Gamma P \nabla\cdot\mathbf{V} - \frac{\Gamma-1}{c_s^2}(\eta\cdot\mathbf{J})\cdot\mathbf{J} = Q. \tag{5.4}$$

Here, ρ is the density, P the pressure, $\mathbf{V}$ the velocity and $\mathbf{B}$ the magnetic field. c_s is the sound speed. Q represents the heating rate, which encompasses heating and cooling sources. Compared to the energy equation presented in the previous chapter we have a term that appears which is purely due to the Joule heating. Two terms appear in the resistive-MHD framework. The first is related to the viscous aspect of the disk and is expressed by, $\nabla\cdot\mathcal{T}$, with $\mathcal{T}$ the turbulent viscosity stress tensor. The second, is expressed by magnetic diffusivity, $\eta\cdot(\nabla\times\mathbf{B})$.

The turbulent torque is dominated by its $\varpi\phi$ component, or at least assumed to be, and is expressed as (Balbus, 2003),

$$\mathcal{T}_{\varpi\phi} = \nu_v \varpi \rho \frac{\partial\Omega}{\partial\varpi}\hat{e}_\varpi. \tag{5.5}$$

Here, ν_v is the turbulent viscosity. It is expressed as $\nu_v = \alpha_v c_s h$. In shearing box simulations (Hawley et al., 1995; Salvesen et al., 2016), the value of the Shakura-Sunyaev parameter, α_v, follows a scaling law dependent on the magnetization μ, $\alpha_v \simeq 7\mu^{1/2}$. Although the simulations are consistent with MRI-driven turbulence, this measure of α_v is influenced by the disk aspect ratio. In the solution we use, the viscous torque is negligible compared to the magnetic torque. We shall subsequently neglect the effects of turbulent viscosity in our simulations.

In the same line as turbulent viscosity, Ferreira and Pelletier (1993) propose that the magnetic diffusivity should be written as,

$$\eta = \alpha_m V_A h, \tag{5.6}$$

where α_m is a constant, and V_A is Alfvén velocity. The magnetic diffusivity η acts on the magnetic fields allowing accretion through the magnetic lines. Ferreira and Pelletier (1995) consider a disk with an anisotropic magnetic diffusivity. They do so by imposing a diagonal form to the resistivity tensor, differentiating between the poloidal components which is expressed by η, and the toroidal one, given by η', the tensor is expressed as follows,

$$\overline{\overline{\eta}} = \begin{bmatrix} \eta_R & 0 & 0 \\ 0 & \eta_\theta & 0 \\ 0 & 0 & \eta'_\phi \end{bmatrix}. \tag{5.7}$$

A possible explanation for this anisotropy is the occurrence of magnetic field reconnection at the disk mid plane, adding to its turbulent diffusivity. To measure the degree of anisotropy, Ferreira and Pelletier (1995) introduce the parameter χ_m which is the ratio of the poloidal to the toroidal diffusivity,

$$\chi_m = \frac{\eta}{\eta'}. \tag{5.8}$$

Ferreira and Pelletier (1995) measure a value around ~ 0.3 for χ_m. Later this value has been confirmed by shearing box simulations (Lesur and Longaretti, 2009). They

found that the toroidal diffusion is systematically $2-3$ times larger than the poloidal one. This difference is shown to improve the launching conditions of cold jets (Ferreira and Pelletier, 1995). For a recent parametric study of the effect of anisotropy on the analytical solutions parameter space, refer to Jacquemin-Ide et al. (2019). They find that for $\chi_m << 1$, a magnetization $\mu > 10^{-2}$ becomes unachievable unless the magnetic bending is reduced, which in turn creates an excreting disk at its midplane. The physical relevance of such an anisotropy is still to be studied. For the sake of simplicity we will choose $\chi_m = 1$. Given we perform 2.5D simulations, the value of χ_m does not affect the results.

The disk solution available for this work presents a negligible viscous torque compared to the magnetic torque. This allows us to reduce the complexity of the problem by only including the turbulent magnetic diffusivity in our time dependent simulations. Regardless of the source of turbulence, We assume that the transport coefficients vanish outside the disk. To smoothly transition from the resistive to the ideal regions, we use a Gaussian profile,

$$f(x) = e^{-x^2}. \tag{5.9}$$

In this equation, $x = z/h$. This profile is consistent with magnetized jet emitting disks (Jacquemin-Ide et al., 2021).

The treatment of the energy equation is slightly different than was presented in Sec.4.3.1 as now the energy equation solved by PLUTO includes the Joule heating. Besides, we use a fractional time-step to add heating contribution to the flow (Sauty et al., 2022). For the wind and disk interior, the same energy source is used,

$$Q = (\Gamma - \gamma) P (\nabla \cdot \mathbf{V}). \tag{5.10}$$

Inside the disk, we further impose adiabatic regions ($Q = 0$) when the radial velocity is positive, only considering layers of the disk where $V_r < 0$ as isothermal. This step has an important consequence on the heating profile inside the disk. Including resistivity produces an additional source in form of Joule heating. Furthermore, this contribution is always positive, while, as can be seen in Eq. 5.10, $V_r < 0$ implies that heating is also negative. This in turn, removes the added resistive heating. Regarding the jet heating rate, no modifications to the expression presented was made (rewritten below in Eq.5.11 for the sake of convenience).

$$Q = \rho \mathbf{V} \cdot \left[\Gamma \nabla \left(\frac{P}{\rho} \right) - (\Gamma - 1) \frac{\nabla P}{\rho} \right]. \tag{5.11}$$

5.2.2 Self-similar disk solution

The starting point of the simulations in this work is semi-analytical solutions. As mentioned before, we use the models put forward by Ferreira and Pelletier (1993), Ferreira and Pelletier (1995), and Ferreira (1997). This model links the interior of the disk with its wind component, while in the work of Vlahakis et al. (2000) the disk wind alone is modeled. Underneath both models, the same principle is at play. The

quantities describing the flow evolution are simplified using variable separation. In the disk solution, the self-similar variable is $x = z/h = z/\epsilon\varpi$, where ϵ the disk aspect ratio (geometrical thickness). This variable is analogous to the colatitude, θ. It should be stressed that both the solution in Vlahakis et al. (2000) and Ferreira (1997) are similar as they use power-laws to the retrieve the flow quantities at all points of the domain. The only difference between the two models is to use a formally different self-similar variable, but those variables are equivalent.

At a fixed x, the variable traces a line at a constant angle with respect to the axis. To, then, recover all physical quantities, we use a power-law with radius, following the expression below,

$$u = u_0(\frac{\varpi}{\varpi_0})^{\zeta_u} f_u(x). \tag{5.12}$$

The subscript 0 indicates that the quantity is defined in the midplane, equivalent to $x = 0$. The exponent ζ_u fixes the power-law for each quantity, and is in most of cases function of the ejection index, ξ, as defined by Ferreira (1997). Finally, f_u is a self-similar function of x whose expression varies with the physical quantity of interest.

To initialize the computational domain, we use density, pressure, velocity, magnetic field, and magnetic diffusivity. Their variation with radius is as follows,

$$\begin{aligned} \rho &\propto \varpi^{\xi-3/2} \quad P \propto \varpi^{\xi-5/2}, \\ V &\propto \varpi^{-1/2} \quad B \propto \varpi^{\xi/2-5/4}, \\ &\eta \propto \varpi^{1/2}. \end{aligned} \tag{5.13}$$

If, in addition, the energy equation is taken to be isothermal, the solution is stationary.

5.2.3 Disk solution parameters

A number of parameters need to be specified to fix the disk physical quantities and nature. Starting with the ejection index, ξ, this parameter determines the accretion and ejection efficiency. The accretion rate $\dot{M}$ scales with ξ such that,

$$\dot{M}_{acc} \propto \varpi^{\xi}. \tag{5.14}$$

This parameter lies between 0 and 1, and the higher its values, the more material is ejected. Requiring that both jet launching and disk luminosity to be powered by the energy released within the disk sets an upper limit for ξ (Jacquemin-Ide et al., 2019). A consequence of self-similarity is that all the parameters of a solution are defined by constant quantities. In the case of jet emitting disks (JEDs), there are seven parameters that constrain its nature at the midplane, which are as follows,

$$\begin{aligned} \xi &= \frac{d\ln\dot{M}}{d\ln\varpi}, \quad \alpha_m = \frac{\nu_m}{V_A h}, \quad \chi_m = \frac{\eta}{\eta'}, \\ \mathcal{P}_m &= \frac{\nu_v}{\eta_m}, \qquad \epsilon = \frac{z}{h}, \qquad \mu = \frac{B_z^2}{4\pi P_{gas}}, \quad p = \frac{4\pi h J_\phi}{B_z}. \end{aligned} \tag{5.15}$$

Three parameters are important to describe the level of turbulence which are α_m, χ_m, and $\mathcal{P}_m$. Note that ϵ was not computed using the energy equation, but instead fixed to the common value 0.1 (Jacquemin-Ide et al., 2019). The parameter p controls the toroidal current density in the disk midplane. It quantifies the bending of the magnetic surface at this location resulting from the interaction between advection and turbulent diffusion. In addition, p provides an approximate measure of the bending of the field lines at the disk surface, since $p \sim B_{\varpi}^{+}/B_z$. The parameters and the values chosen for the disk are summerized in Tab.5.1.

Parameter	**value**
Aspect ratio, ϵ	0.1
Magnetic Prandtl number, $\mathcal{P}_m$	1
Magnetic turbulence, α_m	1
Anisotropy, χ_m	1
Ejection index, ξ	0.163
Magnetization, μ	0.0135
Toroidal current, p	2.33

Table 5.1: Table of parameters with their respective values.

With the used parameters, the disk outflows obtained from the solution at hand cross two critical surfaces, namely, the slow and the Alfvén points, the blue and yellow lines in Fig.5.1, respectively. One can obtain solutions that cross the fast critical surface, but this demands to further adjusting the adiabatic index, which in turn does not provide more constraints on the disk physics. This being said, even if the fast surface is not crossed in the semi-analytical solution, it is the case in numerical simulations. The flow almost always exceeds the fast magnetosonic speed at the fast surface.

5.2.4 Normalization

The normalization step is necessary, as we use two solutions that have not been normalized the same way. It should be noted that the mixing procedure of the stellar wind and this new disk solution follows the one presented in Meskini et al. (2024). Additionally, this step is important to fix both solutions to describe the same central object, and accretion rates. Given the universality of the models used, one can easily adapt the solutions to match objects with different masses, and disk accretion rates. This is done

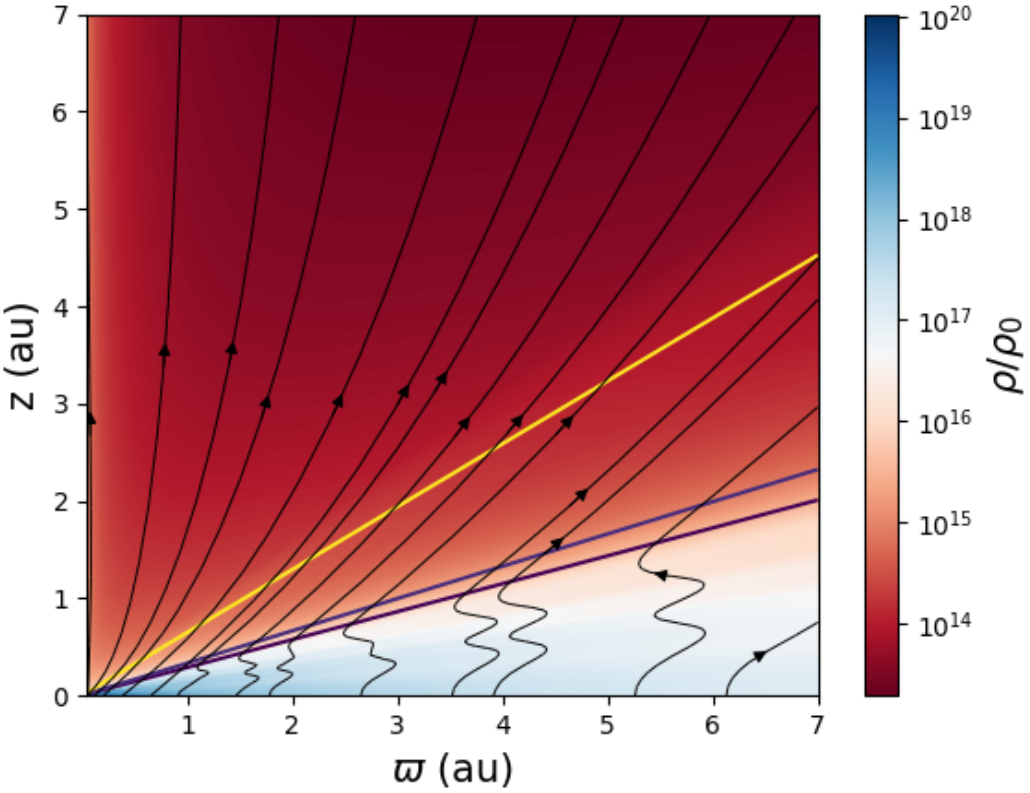

Figure 5.1: Density plot of the disk semi-analytical solution provided by J. Ferreira and N. Zimniak. The black lines are the magnetic fields. The diagonal purple line shows where the disk transition from the resistive MHD region to the ideal-MHD one. The blue line represents the slow magnetosonic surface while the yellow line is the Alfvén surface. The density is in normalized units.

as follows,

$$\begin{aligned}
\rho_0 &= \left(\frac{\dot{M}}{1M_\odot\,\mathrm{yr}^{-1}}\right)\left(\frac{M}{1M_\odot}\right)^{-1/2}, \\
P_0 &= \left(\frac{\dot{M}}{1M_\odot\,\mathrm{yr}^{-1}}\right)\left(\frac{M}{1M_\odot}\right)^{1/2}, \\
V_0 &= \left(\frac{\dot{M}}{1M_\odot\,\mathrm{yr}^{-1}}\right)^{1/2}, \\
B_0 &= \left(\frac{\dot{M}}{1M_\odot\,\mathrm{yr}^{-1}}\right)^{1/2}\left(\frac{M}{1M_\odot}\right)^{1/4}.
\end{aligned} \tag{5.16}$$

To adapt the solutions, we need to replace the reference mass M and accretion rate $\dot{M}$ by 2 and $10^{-8} M_{\odot}\,\mathrm{yr}^{-1}$, respectively. This way the solutions match typical values of intermediate YSOs. Subsequently, in order to be ready for simulations, we use the normalization of the stellar component, which can be found in chapter 4. In that solution, the star had a mass of $1.5 M_{\odot}$. We increase the stellar mass to $2 M_{\odot}$ to better match the measurements inferred for RY Tau (Garufi et al., 2019).

In order to express the quantities computed from simulations into physical units, we set the reference length unit from Sauty et al. (2011) and adapt the velocity, and density units for a star with 2 solar masses. Radius and velocity are normalized at the Alfvén radius, which gives the factors $r_{alf} = 0.104$ au and $V_{\star} = 123.13$ km s^{-1}, respectively. The density is $\rho_{\star} = 2.08 \times 10^{-15}$ g cm^{-3}. With these units, we can subsequently determine the pressure, $P_{\star} = \rho_{\star} V_{\star}^2 = 0.31$ dyne cm^{-2}. The magnetic field factor is defined as follows, $B_{\star} = \sqrt{4\pi P_{\star}} = 1.99\ G$. Finally, the time scale is, $t_{\star} = r_{\star}/V_{\star} = 1.46$ days. It is worth noting that the duration of a single stellar rotation is approximately 8.2 days. At a distance of 1 au one disk rotation takes 218 days. For a 8 years of numerical evolution the disk at 1 au has time to revolve 13 times around the stellar engine.

5.3 Numerical set-up

5.3.1 Computational grid

The system of equations (Eq.5.1-5.4) are solved using PLUTO (Mignone et al., 2007). We use a shock capturing HLL solver, although more diffusive than other solvers such as HLLD. The HLL scheme is robust. Spatial reconstruction is performed using linear interpolation (Mignone, 2014), and the limiters chosen are the ones set by default in PLUTO (see, Sec.2.5.5). To ensure the divergence-free condition ($\nabla \cdot \mathbf{B} = 0$), we use the 8-wave Powell method (Powell, 1997). The reason we do not use the more accurate constrained transport (CT) is because the mixing between the stellar and the disk solutions introduces non-linear regions. Since CT needs the divergence-free to be insured from the start we avoid this method as some regions do not fill this condition at the initial step.

The computational grid is 2.5D described by (R, θ) coordinates. In the radial direction the grid was decomposed into three zones. The first contains 256 points uniformly distributed in the range $[0.02, 0.18]$ au. The second zone has also a uniform spacing between cells. The grid here is chosen to be coarser and spans from 0.18 to 3 au. The last computational region uses a stretched grid between 3 and 5 au, with 64 points. In terms of the second component, θ, three zones were also used, all with uniform spacing from 0 to π. In the disk wind where ideal-MHD dominates, i,e, $[0, 1.29]$ and $[1.85, \pi]$, we choose 64 points to match the simulation grid used in chapter 4. In the region between [1.29, 1.85], we choose 128 points. The boundary conditions are only specified at the outer radial boundary. On the polar axis, axisymmetry is assumed. Every other region

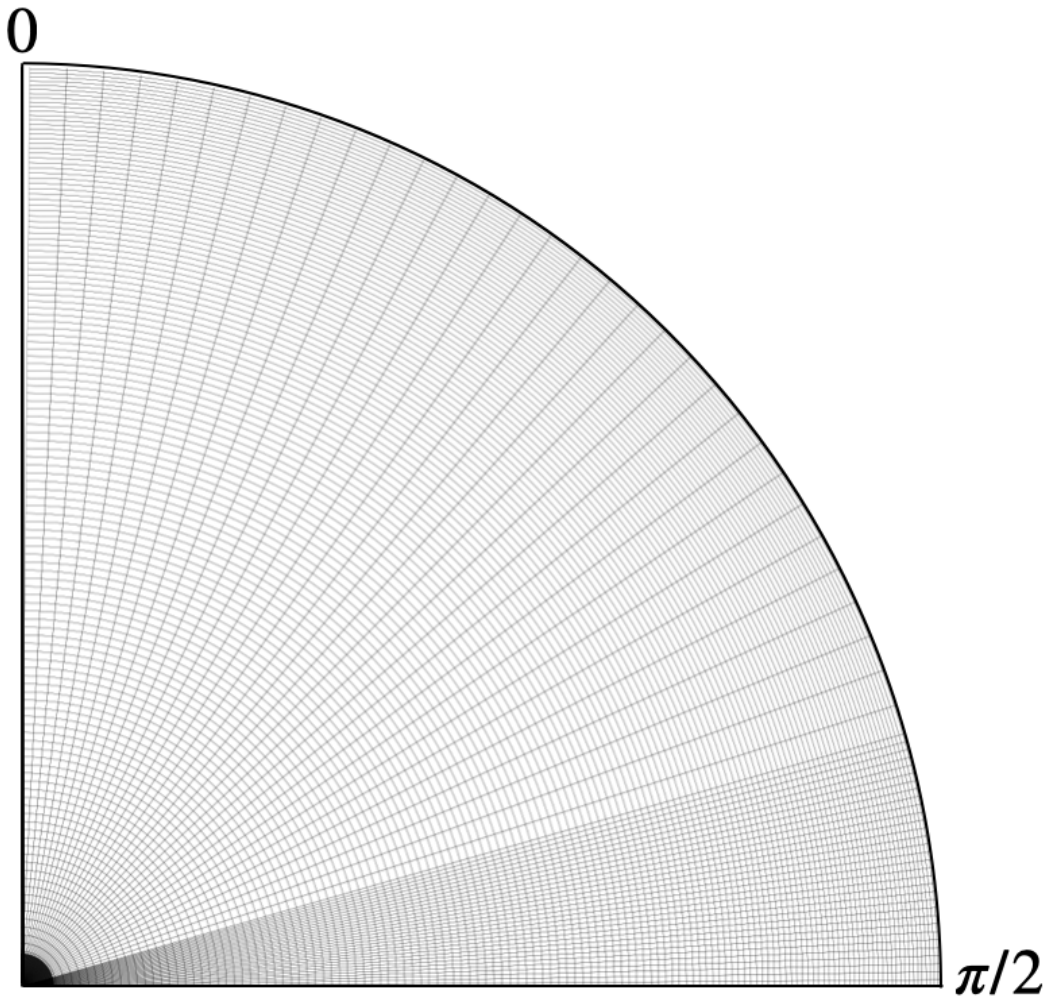

Figure 5.2: The grid used in the runs cover half a circle, from 0 to π. This plot stops at $\pi/2$ for the sake of convenience.

of the simulations are left free to evolve with time. A floor value for density was set to avoid low density regions and to minimize the integration time, but this threshold density is not absolutely necessary.

Although the grid is fixed for the science runs, testing for variation due to the grid should be performed. We reduce the resolution near the star and added a fourth zone right after to gradually transition between grid resolutions without generating a steep change in cell ratios. Same as the grid above, the θ component is divided in three regions, although with 80 points each in the second set-up. The radial component is configured as follows, $[0.02, 0.15]$ au is divided into 128 points, then between $[0.15, 0.5]$ au, 100 points are fixed. From 0.5 to 3 au, 128 points are chosen. Finally, the last region lies between 3 and 5 au with a stretched grid over 64 points.

The fundamental difference between the two grids is that there is a steep jump

between the first and the second zone in the science grid, coupled with the growth of a magnetic island in these regions. We devised a second grid (test grid) that verifies $\Delta R \sim R\Delta\theta$ inside and outside the disk. The purpose of the new grid is to see whether the turbulence retrieved in the simulations is grid dependant. We shall describe the differences in what follows.

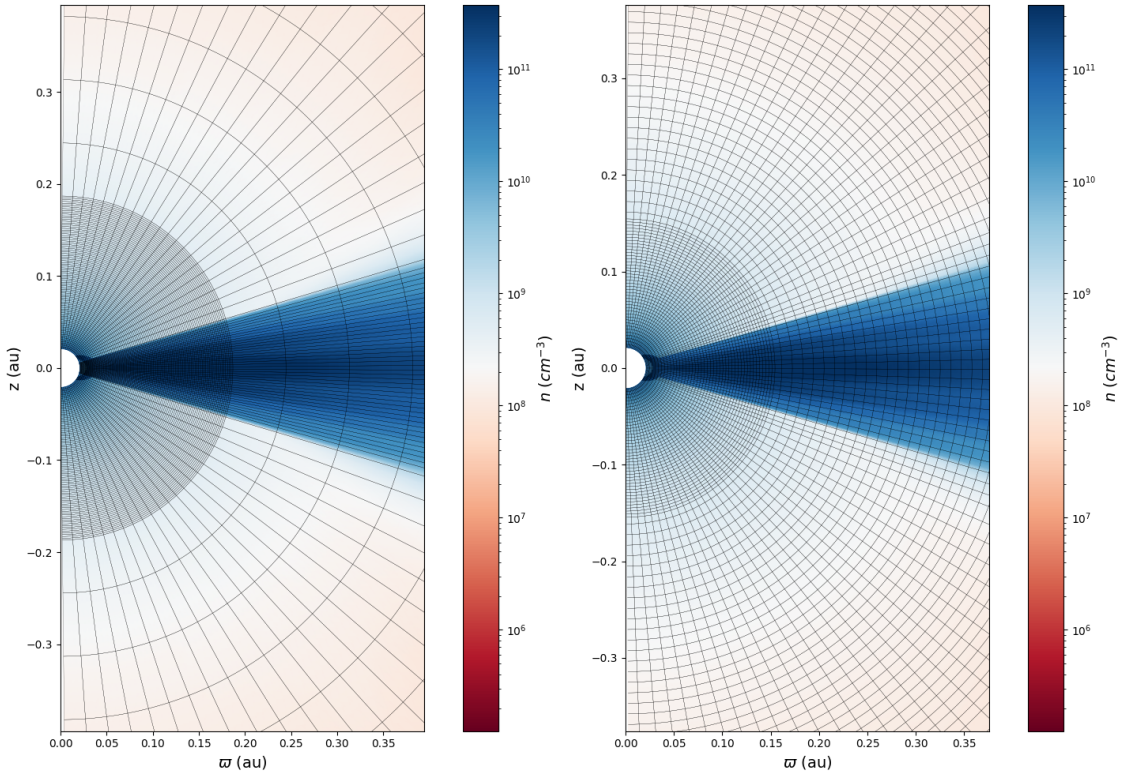

Figure 5.3: Left plot shows the grid used in science runs while the right plot is the test grid. In the test grid we reduce the resolution of the region [0.02, 0.15], and increase the number of cells between [0.15, 0.5] au. We test in this case the effect of choosing a squarer grid, in addition to smoothing the transition between the first two zones.

Noticeable changes are observed below 0.18 au between the science and the test grid. Fig.5.4, illustrates these changes. We see that already at the very first steps of the evolution turbulence appears more pronounced in the disk with a steep resolution transition between the first and second zone. Overall, the test grid is better than the science grid. Nonetheless, given the time constraints, we cannot run all the simulations twice with both grids. We selected a few and except for the turbulent behavior of the disk below 0.18au, the subsequent temporal evolution is the same, as both grids reproduce the same events, namely, the episodic accretion (Sec.5.4.2).

The direct impact of the grid choice is clear here as no boundary effects would be able to travel back fast enough to perturb the inner disk. Furthermore, by prescribing the analytical initial conditions as is done in chapter 4, any waves produced as a result of perturbations from the initial conditions are absorbed. The analytical solution is

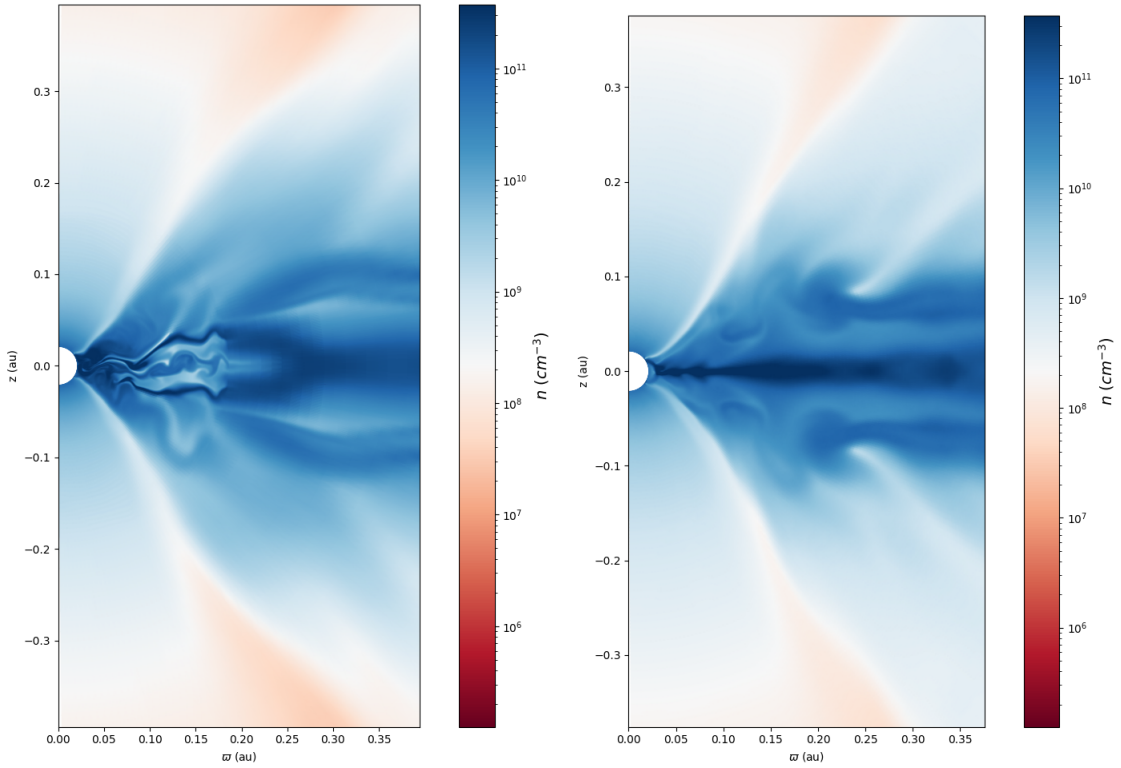

Figure 5.4: Differences in the density map due to the grid choice. In both panels the snapshot is taken at $t = 7.3$ days which is slightly below one stellar rotation.

prescribed on the outer radial boundary, while the equatorial boundary is not present as the grid varies between 0 and π along the colatitude. Subsequently, wave reflection is damped. So if any reflection occurs, it is of minimal impact on the inner parts of the simulations.

5.3.2 Connecting the accretion funnel and the disk

To reduce the relaxation time, we introduce a smooth function to go from the stellar analytical solution to the analytical disk solution. This function is simpler than what is presented in Sec.4.11. The purpose is to keep the stellar solution inside the accretion region, and reduces the density of the disk in a small region adjacent to the accretion zone. The function is as follows,

$$f_m = \exp\{-(R - 0.2)^2\}. \tag{5.17}$$

f_m starts at the inner radial boundary and is only applied in the resistive region of the disk. This treatment reduces the shock occurring at the stellar boundary condition during the first steps of the evolution. The excess density in the cases where the analytical solutions are not modified, is eventually evacuated through sporadic ejections.

When most of the initial disk material is launched, the runs become comparable in behavior to the density damped cases.

5.4 Results of fiducial simulations results

5.4.1 General behavior

We give a general description of the global behavior of the simulation where the disk is initialized with the parameters summarized in Tab.5.1 and is further connected to the stellar surface as described in Sec.5.3.2. The stellar solution has been described in chapter 4 (see also the mixing procedure), and was adapted to the gravitational potential to a 2 $M_\odot$ star. The parameters presented for the stellar solution stay unchanged (see Tab.4.1). We present in Fig.5.5 the behavior of the system. The first observation is that this simulation does not reach a steady state. Two main factors contribute to the lack of stability. The primary one stems from failed launch of disk material. Part of the disk wind accretes again at higher altitudes. The second reason is the instability generated by the episodic accretion.

The bulk density lies at the midplane with a turbulent flow. In Fig.5.5, surface accretion episodes alternate between the northern and the southern hemispheres. The process itself is chaotic. Disk jets close to the star reduce the amount of accreted material. The consequence of these episodes is an increase of the chaotic disk configuration. The turbulence originating at the midplane close to the star (below 0.5 au) slowly grows with time. Subsequently, a magnetic island develops, which can be seen in the midplane between 0.5 and 1au in Fig.5.5. In terms of the magnetic field lines once the initial conditions are evacuated, the magnetic configuration inside the disk simplifies. Compared to the initial state where the chosen magnetization induces vertical oscillations in the field lines (refer to Jacquemin-Ide et al. (2019) for a detailed discussion).

In Fig.5.6, the snapshot of the system after two years of evolution is plotted. The magnetic field in the disk is almost vertical, while at higher altitudes the disk arms bend the field lines. These accreting arms are assumed to force advection, which in turn transfers part of the angular momentum to the disk. Above the arms, we find the usual ideal-MHD behavior where the magnetic and velocity fields are parallel. In a general manner, the jet emitting region is complex. The disk jet does not simply follow the magnetic lines as they are turbulent and reconnect frequently. Contrary to the X-wind model, the reconnection occurs above the disk, in its atmosphere, in addition to a large scale magnetic field present in the disk. In this process, the open field lines, carried in by the surface accretion, reconnect with the closed stellar field lines. This scenario is compatible with the reconnection X-winds (ReX-winds) (Ferreira et al., 2006). Even though the magnetic field in the star-disk interaction region depicts a ReX-wind scenario, we can still see laminar disk jets. Measurements of the jet mass loss show variations in the ejection rate through out the run time (Fig.5.7).

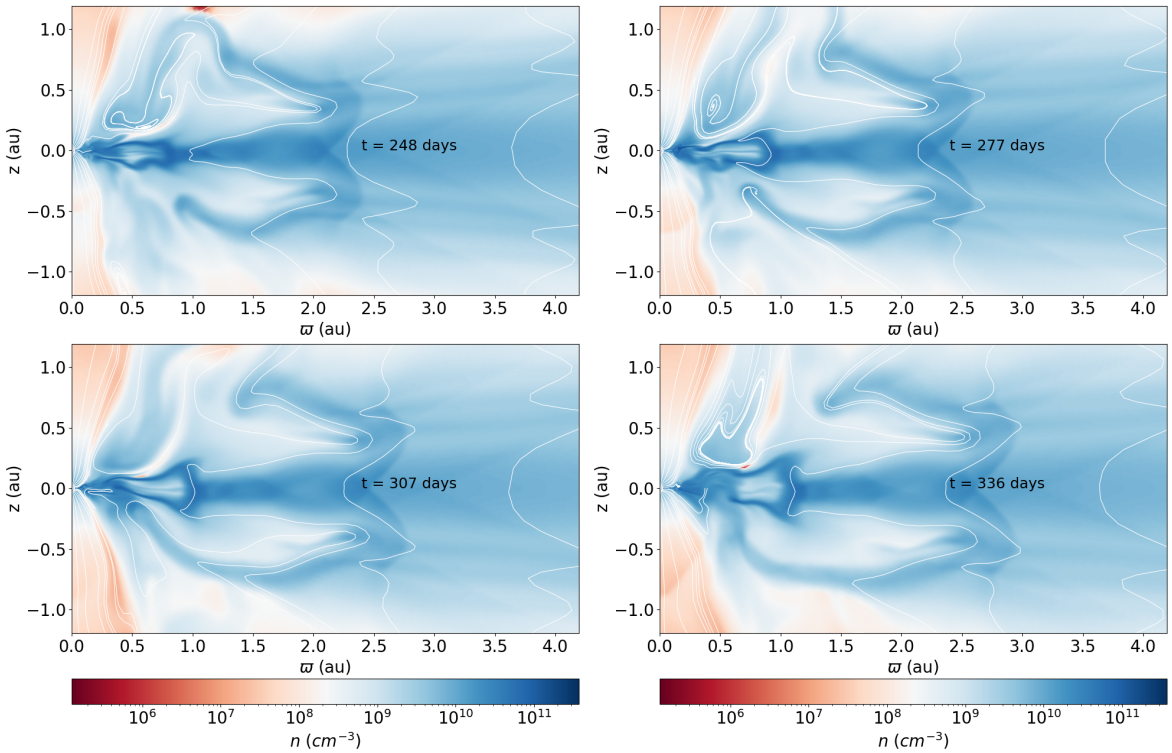

Figure 5.5: Numerical density map showing the disk up to 4 au. The four sequential snapshots aim to show how superficial accretion perturbs the disk structure. The white lines represent the magnetic field lines. This simulation lasts for 8 years of evolution. The perturbations that arise in the disk below 0.5 au create a magnetic island. No accretion occurs in the midplane. These dead zones naturally form with accretion proceeding on the surface Lesur (2021).

5.4.2 Episodic accretion

Measuring accretion and ejection clearly shows the chaotic behavior of the system (see Fig.5.7). Accretion in this simulation is of episodic nature. Material from the disk stops funneling to the star 8 times during the entire time evolution of the simulation, which last more than 8 years. We cover long time scale compared to Ireland et al. (2022b) and Takasao et al. (2022). Since the work shown in Takasao et al. (2022) is in 3D they are limited by the computational wall. Ireland et al. (2022b) assume an axisymmetric grid, as we do, and cover 20 stellar periods which is equivalent to a period of the order of months. In our simulation, each time accretion resumes, a symmetry is seen between the northern and southern hemisphere. After the 8th occurrence the disk completely disconnects from the star, and a magnetic wall develops which definitively ensures the disk and stellar component stay apart. The toroidal contribution in the magnetic wall is very small, making the poloidal components dominant. The disk becomes also super-Keplerian. This event happens at $t \sim 6.5$ years, when the disk has lost most of its mass. Accretion at $r \sim 1$ au shows rates varying around $3 \times 10^{-8}\ M_{\odot}\ \mathrm{yr}^{-1}$ without going below

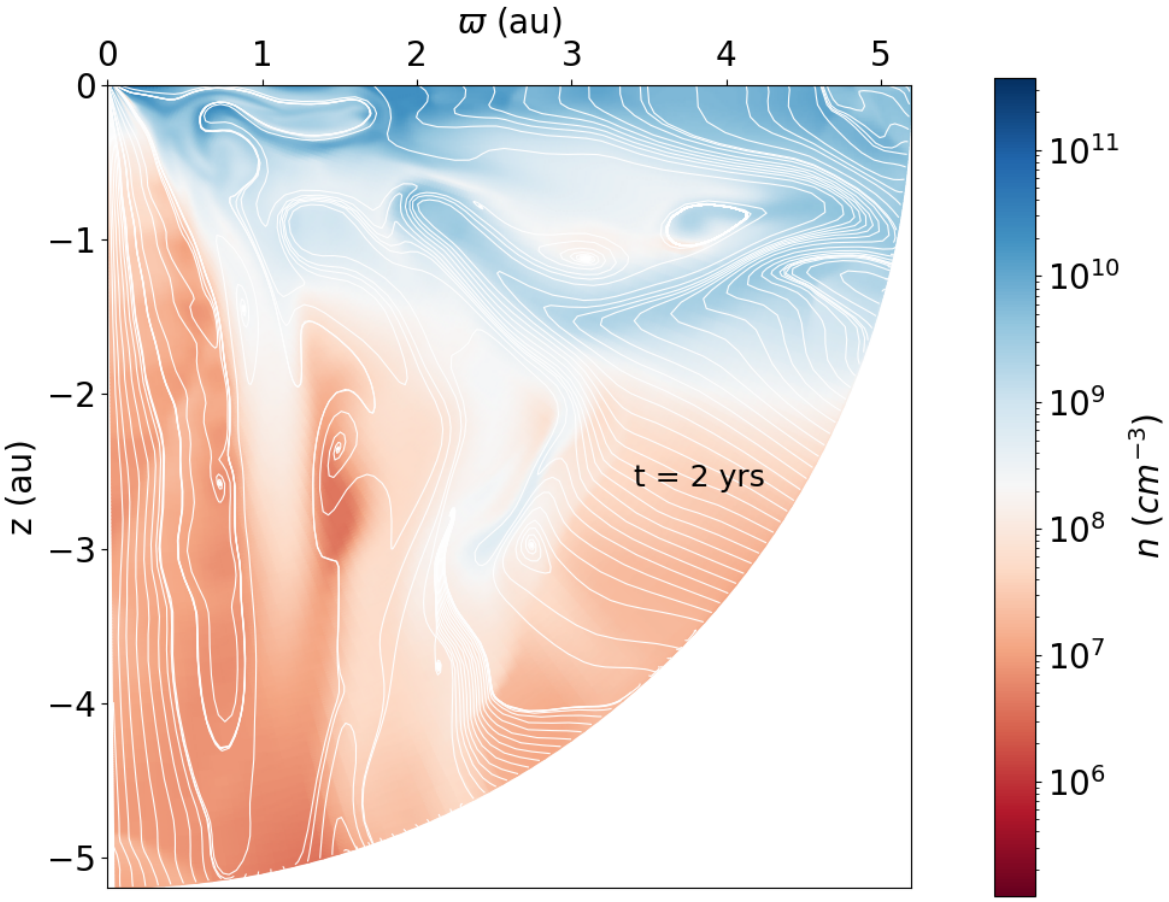

Figure 5.6: A map of density with superimposed magnetic field lines. The disk is thinner than initially, and the magnetic structure does not contain the oscillations that ensue from a magnetization between 10^{-3} and 10^{-2}. Here, we show the lower half as it contains a clear depiction of magnetic behavior in the stellar and disk components as well as where they interact. The northern hemisphere is similar to the southern, but given the field plotting technique we see less lines.

$2 \times 10^{-8}\ M_{\odot}\,\mathrm{yr}^{-1}$. This would mean that most of the disk material is ejected. Given the stellar ejection rate is fixed at $3 \times 10^{-9}\ M_{\odot}\,\mathrm{yr}^{-1}$ by the boundary conditions, it is straightforward to deduce the outflow rate from the disk. Overall, Fig. 5.6 shows accretion rates well within the domain of observations (de Albuquerque, 2020).

When the disk becomes less massive, any event such as surface accretion (see Fig.5.5), drastically changes the disk configuration. The flow becomes more disorganized, and subsequently magnetic fields spin-up the disk. This added angular momentum help the disk become super-Keplerian, thus making accretion impossible. A transition like the one seen after the last disconnection may be related to what happens during the transition from class II to the class III objects. However, we need to be cautious and this needs further investigations. A better comparison for our simulations is

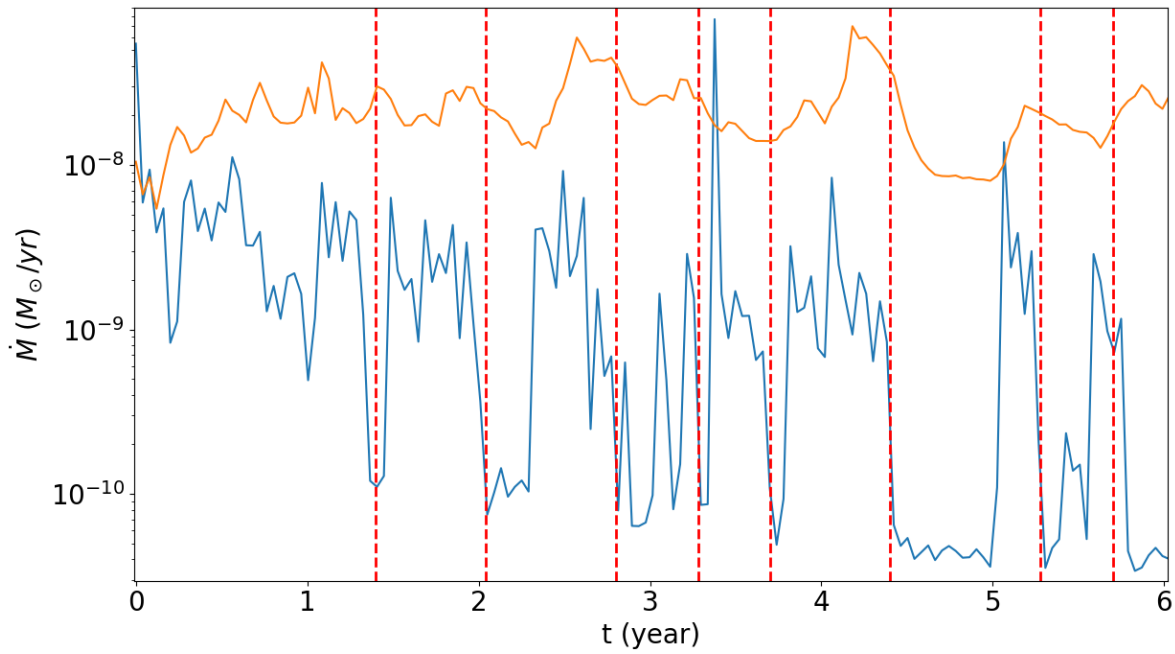

Figure 5.7: This plot shows the evolution with time of the mass accretion rate, in orange, and the ejection mass loss rate, in blue, for the fiducial case. The red dashed vertical lines delineate times at which accretion ceases. These periods where no accretion happen vary in duration. The interruption can be a few days to a few months long.

the transition between the active and quiescent phases observed by Petrov et al. (1999). Later Petrov et al. (2021) find an anti-phase correlation between accretion and outflow. Whenever the accretion increases the outflow decreases. This back and forth has a period of 22 days, which is closer to the period accretion arms take to form towards the star, and finally disperse as outflows. In Fig.5.5 we can see that accretion arms need around 30 to 40 days to go through the processes as described. This flip-flop is observed in both the northern and the southern hemispheres. In their study, Petrov et al. (2021) also consider the presence of a planet at 0.2 au as a possible cause for the observed variation.

In the simulation presented here, after the disk disconnects, the stellar outflow become radial similar to the solar wind. Note that the time it takes to transition to the class III phase is not known, since it has never been observed before. Such a transition may take years, which makes continuous observations the only way to see it.

5.5 Adding heating inside the disk

5.5.1 Treatment of the Joule term

As already presented in Sec.5.2.1, the heating within the disk has been modified to allow for an adiabatic evolution of the disk. We suppress the Joule heating term in

the energy equation using the heating rate produced by the analytical solution (noted Q in Eq.5.4). The heating map in Fig.5.8 does not separate from the initial heating rate configuration as time evolves. In Fig.5.8, three regions can be distinguished. The region numbered one, contains the stellar atmosphere. The heating in this zone is determined by using velocity, density, and pressure produced by the stellar analytical solution in Eq.5.11 (refer to the ASO heating in chapter 4). The disk atmosphere is represented in region two, and the disk interior lies in region three. In region two, both stellar and disk are mixed so that Eq.5.11 sets the heating rate near the star, while further in the disk atmosphere, Eq.5.10 dominates the heating expression (as shown in Eq.4.14). In the third region, only negatives values of the heating rate are kept. The fact that the heating rate is negative in this region does not mean cooling processes are dominant. On the contrary, since the flow is itself accreting, the negative value coupled with accretion are consistent with a net heating of the disk.. In different terms, the heating rate follows the flow, so if the velocity is negative the heating rate is negative, see (Sauty et al., 2022).

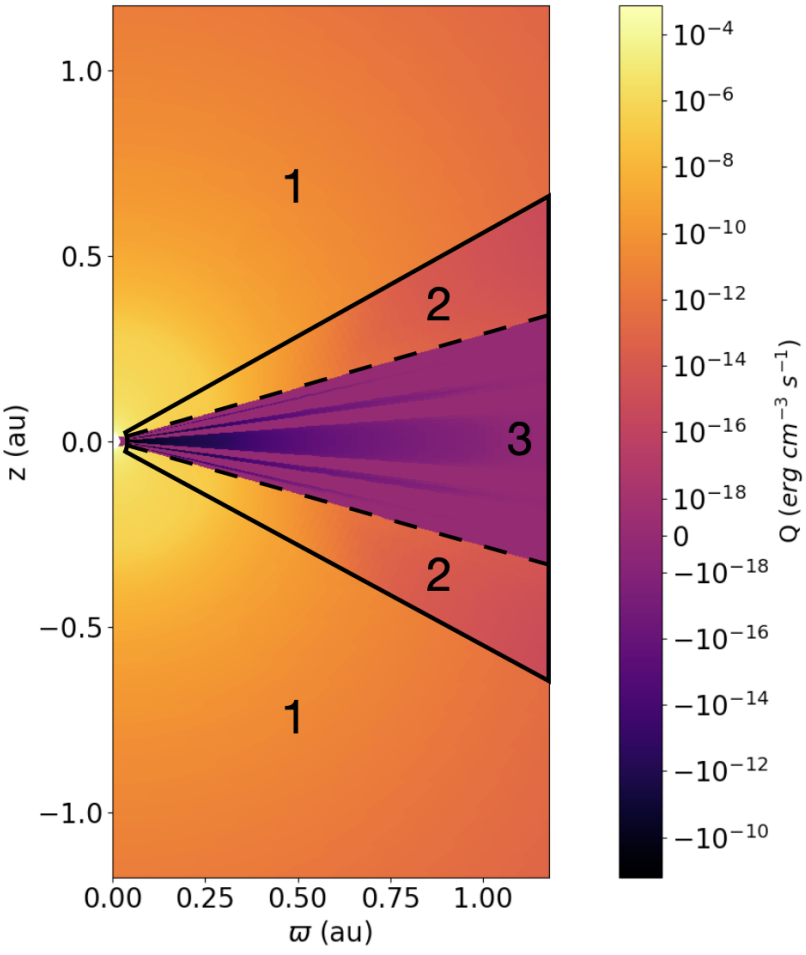

Figure 5.8: 2D map of the heating rate. This plot shows the three regions that compose the system in terms of heating. Region 1 represents the heating from a purely stellar atmosphere. Regions two and three represent the heating rate in the disk and its atmosphere. Note that only $Q < 0$ are kept and reduced to oppose the heating added by diffusivity.

In practice, the negative heating rate within the disk counteracts the positive heating

introduced by diffusivity. The maximum amount of diffusivity-induced heating is at the midplane. Note that $\Gamma_{diff} = \eta \cdot \mathbf{J}$. This means that most of the heating occurs when η and the electric current $\mathbf{J}$ are at their maximum. By construction accretion disk are most diffusive at the midplane, while $\mathbf{J}$ reaches the maximum at magnetic reconnection sites. Both these conditions are met at the disk midplane near the accretion funnel where most advecting disk field lines reconnect with stellar field lines. Overall, the disk stays adiabatic during the run time with minimal heating added. We can thus neglect the effect of any heating contribution inside the disk.

5.5.2 Energetic particle heating inside the disk

We also study the change of behavior introduced by including a heating source of physical nature inside the disk. We choose to match the heating map over the heating produced by reconnection events and ionization that results from the energetic particles. We refer to Brunn et al. (2023, 2024) for details on the models that produce ionization in the disk. The top panel of Fig.5.9 shows the heating map used to mimic heating from energetic particles, while the bottom panel is the analytical heating computed from the model presented by Brunn et al. (2024). The top panel roughly reproduces the values expected from the model (bottom panel of Fig.5.9). Above $z/\varpi \sim 0.25$ in the lower panel of Fig.5.9, we can see that the heating rate is extremely low while in the upper panel, the heating rate is non-negligible. This is due to the fact that we also consider processes that deposit energy above the disk. The model presented in Brunn et al. (2024), note that only the heat deposit inside the disk has been considered.

This added heating source inside the disk is expected to increase the mass loss rate in the outflow. One of the purposes for its use is to see whether added thermal pressure would suppress or reduce the accretion arms that develop in the fiducial simulation, thus, making the system more stable. As we can see in Fig.5.10, this added thermal pressure does not inhibit the formation of the disk arms. As they develop above the disk and far from the central object, the effect of the added heating source is low. Once the arms are formed and in motion towards the star, their kinetic energy is too high to be halted before reaching regions below 0.5 au. On the other hand, between 0.1 and 0.5 au we see an enhanced jet mass loss rate. The jet extracts all the accreted disk material. The resulting simulation does not present accretion features. This being said, we infer that the solution at hand is more adapted to produce outflows and less prone to facilitate accretion. The resulting behavior in no means eliminates energetic particles as a physical source of heating and should still be considered as viable source of heating in the disk.

5.6 Magnetization and turbulence

In an attempt to reduce the amount of turbulence in the disk and hence stabilize accretion, we reduce the disk density by one order of magnitude and increase the analytical

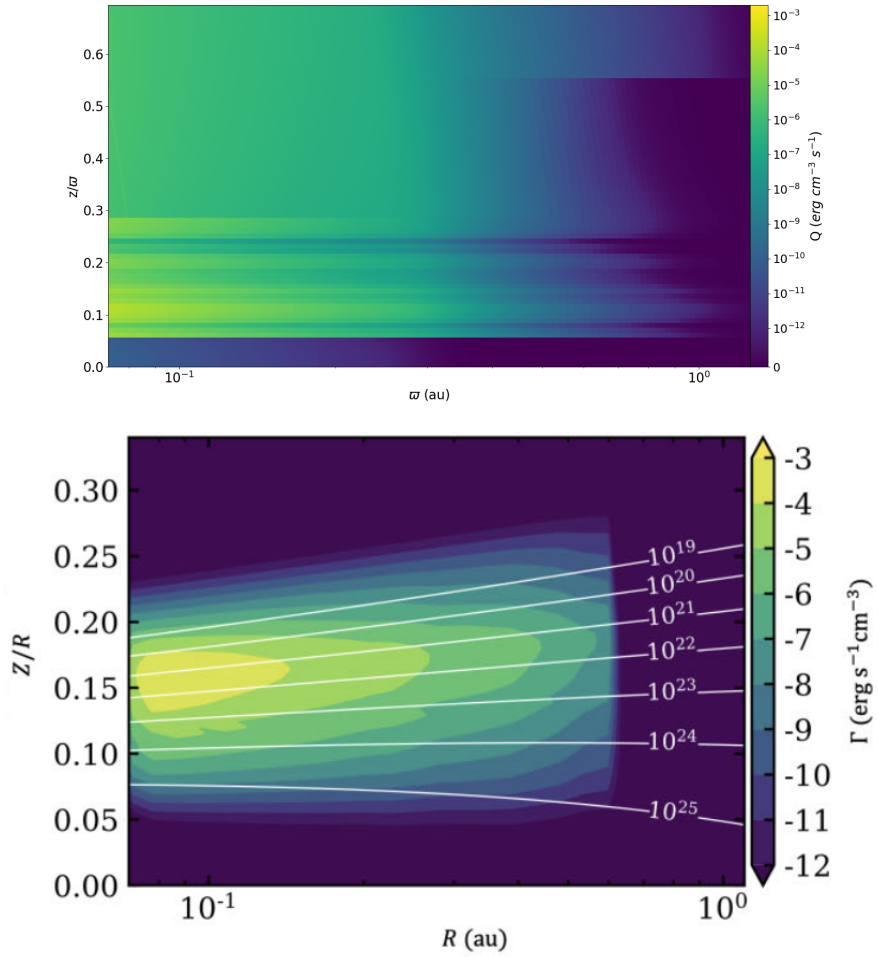

Figure 5.9: Plot of the heating rate maps produced by EP. The top panel is what is used in the simulation. The bottom one is what is produced in Brunn et al. (2024). We use the bottom panel as a reference heat map.

magnetic field by 50%. Fig.5.11 shows the evolution of such a system. We tested three values for the field strength, and noticed that with stronger disk fields we are able to postpone the moment accretion stops. The total simulation time is 2 years in these simulations and compared to the case presented in Sec.5.4.1 the disk disconnection occurs approximately $\sim$ 5 years earlier. We list the information on the magnetic field strengths and the corresponding accretion life time in Tab.5.2. In more massive disks, such as the one presented in Fig.5.5, accretion continues after the initial disconnection because farther disk material has time to agglomerate and feed the star again.

On the other hand, the thinner disk obtained here is easily disrupted once the accretion stops, and the poloidal magnetic field component dominates over the toroidal component.

Indeed, this configuration indeed reduces the amount of turbulence inside the disk and stops the excess surface accretion observed in more massive disks. The accretion

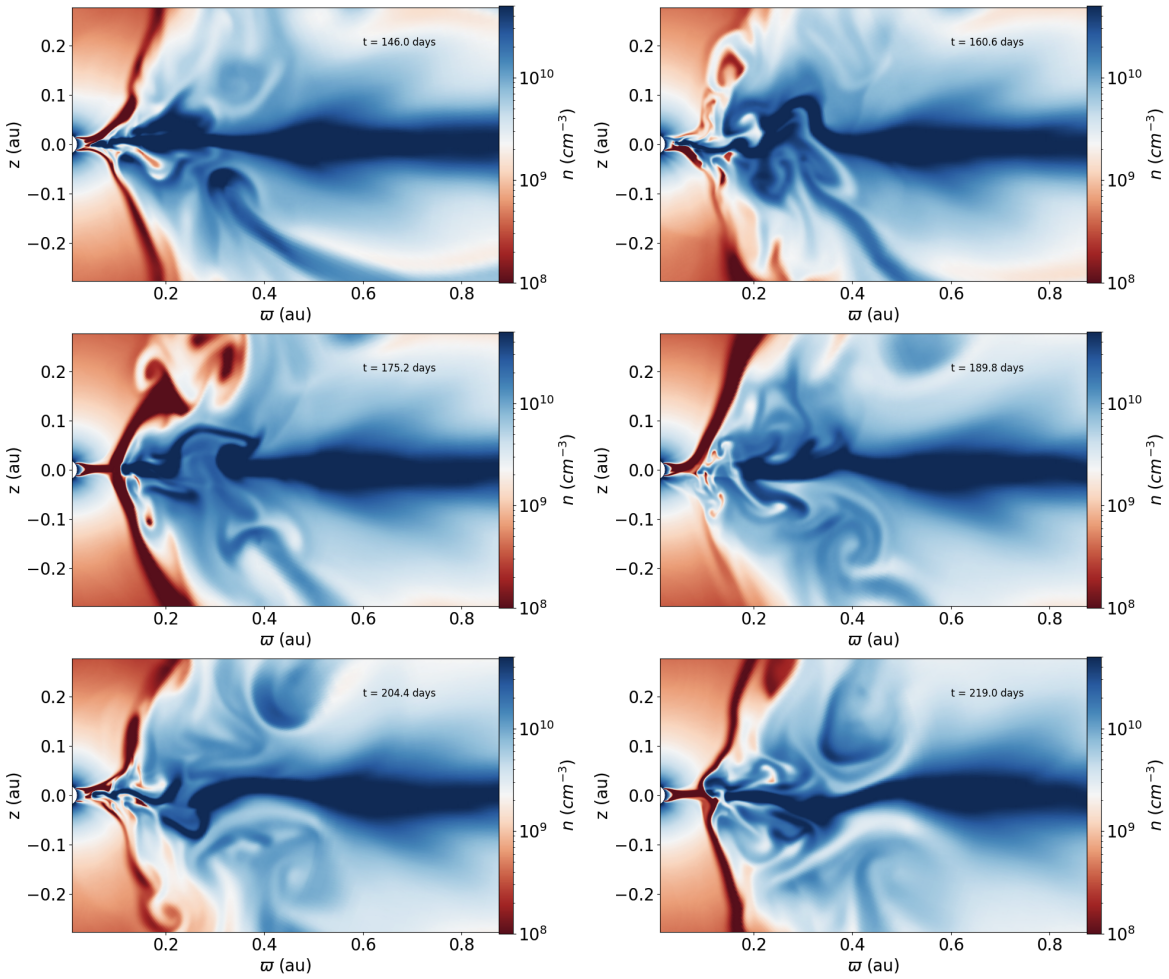

Figure 5.10: Evolution of the density using the heating map resulting from heating produced by energetic particles. The accretion never stabilizes to form an funnels of disk material to the star in these simulations.

seems more laminar and advects magnetic field lines, as it does move towards the central star. It is clearer here that part of the ejection is due to reconnection (ReX-winds). Although, it is difficult to separate the magnetospheric ejection from the disk wind contribution in the jet. The outflows resulting from this disk recollimate.

5.7 Discussion and conclusion

We shall start by comparing our simulations to other 2.5D axisymmetric models. Ustyugova et al. (2006), for instance, show that in the propeller regime occurs when the disk truncation radius is larger than the corotation radius. In this regime accretion is heavily reduced, and winds launch as a consequence of stellar-disk interaction (Ustyugova et al., 2006; Lii et al., 2014). The fiducial simulation also falls under the label propeller

Accretion duration	Magnetic field strength
530 days	$1.5 \times \mathbf{B}_{analytic}$
430 days	$1 \times \mathbf{B}_{analytic}$
58 days	$0.316 \times \mathbf{B}_{analytic}$

Table 5.2: Table of the accretion duration as function of the magnetic field strength of the disk.

regime as the corotation radius lies at $\sim 2R_\star$ while disk truncation is at $\sim 3R_\star$. Even increasing the diffusivity, such that magnetic coupling decreases, does not induce more sustained accretion. Ustyugova et al. (2006) find that when diffusivity is high enough accretion intensifies and the winds become weaker. In comparison the turbulent diffusive parameter in our model is set to unity at the midplane.

The 2.5D simulations of Zanni and Ferreira (2013) or Ireland et al. (2021) and Ireland et al. (2022b) present with strong intermittent magnetospheric ejection episodes. These events happen where magnetic fields anchored on the disk and on the star inflate and subsequently open. Our model shows the same trend for strong magnetospheric ejection. Ejection like these are generally followed by accretion stopping. Ireland et al. (2021) and Ireland et al. (2022b) studied the stellar spin evolution. In the first paper no spin-down configurations were found. The authors suggested that for stellar braking to happen, the central engine needs to expel a sizable amount of the accreted material, around 10% of accretion. Subsequently, in the second paper, they found that stellar spin-down occurs only if their system is in the propeller phase. In our case, given the long propeller periods and since stellar outflow is fixed as a boundary condition, the star should be in a spin-down regime as was found in Sauty et al. (2011) and Sauty et al. (2022). The variation in the mass accretion rate should shift the computed braking time from $\sim 10^6$ years to lower values.

Takasao et al. (2022) conducted 3D simulations on accretion and winds near the star. Compared to our 2.5D simulations, their run time is much smaller (~ 300 days). Besides, they have an active diffusivity only in the reconnection regions, outside the disk in the close vicinity of the magnetosphere. They find that independently of the stellar rotation and the fastness parameter, the magnetospheric ejections are weaker than in 2D models, since accretion proceeds towards the star as a fragmented flow. The fastness parameter is $\omega_s = \Omega_\star/\Omega_K(\varpi_{tr})$, where ϖ_{tr} is the disk truncation radius. Thus, it makes it difficult for the inflow to efficiently twist the stellar magnetosphere. One of the reasons given by the authors is that for violent reconnection flares to happen, the plasma β needs to be below unity. We argue that the twist of magnetospheric magnetic fields also needs to be supported by a build up of the magnetic force, which is instigated by disk material ramming against the magnetosphere.

Two scenarios for flare production are presented by Brunn et al. (2024). In the first one, the magnetic lines are anchored in the star and the disk generate energetic particles. In the second model, flares are generated by magnetic loops where both foot points are anchored into the stellar surface. In the first case, the ionization power covers a larger

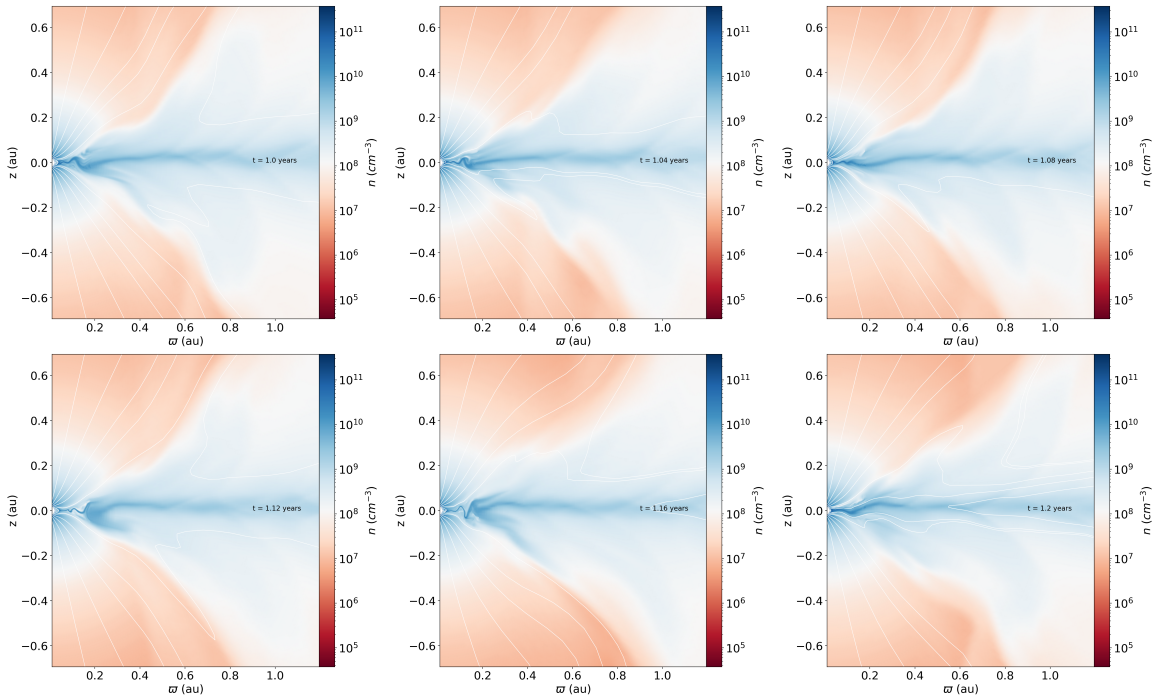

Figure 5.11: Logarithmic plot of the density showing the evolution of a disk with a 50% stronger magnetic fields. The white lines represent the magnetic field. The disk magnetic field lines are advected as time evolves. Eventually, they connect with the star once they reach the magnetosphere.

disk region and this due to the larger loops. For the coronal magnetic loops the spatial coverage is smaller, nonetheless, the ionization power one order of magnitude higher. Moreover, coronal loops should be able to heat up the accreting gas and thus produce the observed X-ray signature. Since the plasma β in all the simulations performed here are below unity, the magnetic diffusion may also partly explain heating processes in the star vicinity. When both processes are combined they match the surface heating needed for realistic jets as described in chapter 4. Nonetheless, it seems premature to implement a realistic heating in the simulations performed in this chapter as there are still steps to be done to obtain a stable accretion-jet system.

Overall, simulations that include the inside of the disk are extremely turbulent. Two main mechanism feed the system instability. The first is the accretion arms which ensue from massive disks. Unlike surface accretion as seen in Jacquemin-Ide et al. (2021) or Mishra et al. (2020), for instance, the accretion arms have cycles and do not produce a continuous flow towards the star. The second instability mechanism lies closer to the magnetosphere, where star-disk interaction plays a large role in the evolution. We were able to suppress surface accretion through lowering the disk mass, but is not sufficient to ensure a long term accretion without intermittence. The key to achieve this is to better understand how to choose the stellar parameters and properties of the magnetosphere. These simulations being performed in 2.5D hide 3D generated instabilities

that might shed light on a different accretion-ejection behavior with our chosen configuration. Especially the Rayleigh-Taylor instability might show that the disconnection episodes seen in our simulations do not translate into a complete disconnection of the accretion disk from the star.

An entirely new result found in these simulations is the symmetric accretion on the stellar surface. Other works, whether in 2.5D or 3D (all the studies mentioned here), show a preferential accretion hemisphere. Takasao et al. (2022) do obtain an initially symmetric accretion, but as the system evolves the symmetry breaks. We argue that since the flow is turbulent and accretion is cyclical, the instability responsible for the Northern-Southern asymmetry does not have time develop or is completely suppressed.

Chapter 6

Conclusion and prospects

Contents

6.1 Concluding summary and remarks 169

6.1.1 Platform simulations 170

6.1.2 Resistive MHD simulations 171

6.2 Prospects 171

6.2.1 Physical origin of heating 171

6.2.2 MHD-PIC codes 172

6.2.3 3D Simulations 172

6.2.4 Observations in the era of JWST 173

6.1 Concluding summary and remarks

The environment of a young star, as shown by observations and theory, is a rich and complex system. As the system evolves so does its morphology, composition, ionization, temperature, etc. Initially in this thesis, We started by creating a multicomponent canvas, with both the stellar and disk winds in the picture. To do so, we connected semi-analytical solutions of the stellar and disk components, where the spine jet is realistic and matches observations. Once a stable system was found, we distinguished between the stellar and disk atmospheres that were additionally parameterized for better input control. Subsequently, these MHD simulations were used to constrain heating rate values in the vicinity of YSOs by values that better reproduce observations. In a sense, we concealed the issue of the actual physical sources of heating by relying on parametrization. To cover a large parameter space, we rely on semi-analytical solutions as well as platform simulations (i.e., when the disk is a boundary condition). We also extended these platform simulations by including the disk interior. The advantage of platform simulations is that by considering the disk as a boundary condition, we can

neglect non-ideal MHD effects which considerably increase the simulation run time. On the other hand, starting with semi-analytical solutions instead of *ad hoc* configurations, reduces the relaxation time needed for the system to reach a steady or stable state.

In chapter 1, we described the process by which YSO are formed from molecular clouds, and the different stages of a young stars evolution. We further look at the accretion and ejection paradigm as the key to understanding the structures observationally seen. In chapter 2, we introduced the reasons that justify the use of the fluid approximation to describe astrophysical plasma. Since the plasma around YSOs are threaded by magnetic fields, one can further use the MHD approach to describe the flow evolution. Many numerical codes and schemes exist to study such a flow. We present in chapter 2 the PLUTO code and discuss the setup used in this work. The chapter 3, presented the physical processes responsible for ionizing jets, winds, and accretion disk. It is an important step to understand how the magnetic field is coupled to the plasma as well as what heating and cooling options are available to the system. These three chapters constitute an introduction that paint a global picture of YSO, their evolution, and how to study them observationally as well as theoretically.

6.1.1 Platform simulations

Chapter 4 is based on published results (Meskini et al., 2024). We quantified in it the effects of heating on the jet. We found simple power laws between the disk ejection radius and the heating rate, same for the jet mass loss rate and heating rate. In brief, the more heating we input the less the magnetic lines are mass loaded and the narrower the jet emitting region. The parameter space survey shows two main behaviors. One where the jets and winds achieve a steady state evolution, the second shows an ejection that varies periodically which produces shock structures in the inner jet.

In the non-steady runs two phases co-exist, quiescent and eruptive, respectively, compatible with RY Tau observations (Petrov et al., 2019). Shocks also appear in steady simulations and are consistent with recollimation shocks as presented by Ferreira (1997) and observations in particular the UV shocks presented in Gómez de Castro and Verdugo (2001) and Gómez de Castro and Verdugo (2007). We argue that these standing recollimation shocks must be present in all the steady cases, and occur at different altitudes, depending on the heating rate at the base of the outflow. the lowest observed shocks occur at ~ 5 au and the highest at ~ 20 au. Too much heating pushes the height above 30 au. Thus why we do not observe such shocks in the parameter space with the highest heating rates. These shocks collapse on the fast separatrix, which ensures the flow is not disrupted by shocks happening above the fast critical point on the axis. Jannaud et al. (2023) were the first to show standing shocks are possible with platform simulations. However, our simulations are the first to show standing collimation shock as close as 5 au to the source, which we attribute to the presence of a physical spine jet. Last, it should be pointed out that these simulations simultaneously address the star-disk interaction as well as collimation in jets.

Jets consistent with observations need a reduced heating compared to what is pro-

vided by analytical solutions. Hence, the temperatures implied to produce jets close to observations do not need to exceed $\sim 10^6$ K even though the stellar wind is pressure driven (see introduction of chapter 4). Moreover, Brunn et al. (2024) predict heating rates from EPs that are compatible with our parametric study.

6.1.2 Resistive MHD simulations

By adding the physical description of the accretion disck in chapter 5 we completed the system since we included in the same simulation box the stellar component and the disk interior. The aim was to study the efficiency of jet emission and the feedback of the jet on the accretion disk. Given we are still in the 2.5D paradigm, we include a turbulent magnetic diffusivity through the effective α parameter. Overall, the system is turbulent and we retrieve a cyclical accretion. The cycles can take months to years. RY Tau may also have a cyclical behavior, since observations show an alternation between quiescent and active phases. However, the period of this phenomenon is not known. To confirm if the cycles seen in our simulations match the period of quiescent to active stage in RY Tau, we need longer surveys. Cycles with precise periods are, on the other hand, observed in other accretion/ejection systems such as microquasars, which is on the scale of months. Thus, such cycles may be a natural non linear evolution of all accreting systems with outflows.

Similar to jet launching simulations, we consider a disk with a standard diffusivity model (Jacquemin-Ide et al., 2019). Other works exist where the dynamo generates and maintains a large magnetic field (Mattia and Fendt, 2020a,b, 2022). These simulations avoid accretion instability from occurring by increasing magnetic diffusivity. An interesting feature in our work including the disk interior is the symmetric North-South accretion columns. Studies with accretion structures all show accretion funnels evolve to choose one of the hemispheres as the preferred path to fall onto the star.

6.2 Prospects

6.2.1 Physical origin of heating

Since in chapter 5 the disk interior is present we can use the full power of the flaring models by testing the 2D maps of heating produced by energetic particles. It seems the heating rate considered is too large for accretion to proceed. Due to the large pressure introduced by the heating, most of the accreting material is ejected as an outflow, either from too much heating, or lack of viscosity. A turbulent viscosity might remove the excess angular momentum. It is important to keep in mind that the flare effects may be overestimated. The models need to be adapted to the rate of reconnection events, the shape of the topology of the magnetic fields and their ability to produce strong energetic particles.

Other sources are available in magnetically confined plasma in the form of Alfvén waves. They are ideal for energy transport as well as play a role in stability and

heating of plasma. Charged particles can exchange energy and momentum with the Alfvén waves because they carry electromagnetic perturbations. Compared to other slow magnetosonic MHD modes they do not reflect at discontinuities, which makes them a good energy carrier. Nevertheless, in order for these waves to heat the plasma, we still need a dissipation mechanism. Heyvaerts and Priest (1983) and Bogdan et al. (2003) propose dissipation processes for the Sun, but these ones mostly act on scales too small for our objects. Little we know about Alfvén waves around young stars. Nonetheless, they could be a non-negligible heating sources as they dissipate through the disk atmosphere and the stellar corona.

6.2.2 MHD-PIC codes

As we already shown in this thesis, we can use MHD codes to include heating. The heating in question can stem from various phenomena, for instance, the interaction of non-thermal particles with the plasma fluid. In this case, however, the temperature obtained from the simulations shows a value that does not discern between the gas and particle temperature.

An other alternative to pure MHD simulations is the use of hybrid codes. Codes such as MHD-Particle-In-Cell (MHD-PIC) which would explicitly include particles on top of an MHD fluid layer. If the right feedback is found between the fluid itself and the particles, then we would be moving closer to simulations with finer details. This treatment would need that the plasma and particles interact and act on each other. Recent works, such as the one presented by Sun and Bai (2023) implement a PIC module in ATHENA++ where energetic particle are treated as usual in PIC codes. The MHD counterpart on the other hand describes a background fluid. As they note, the primary target in this framework is kinetic physics. They used test-particle, which implies no feedback of EPs over MHD. They essentially focused on the transport of particles in MRI-driven turbulence. Since flare production originates from dynamic processes, namely, reconnection of magnetic lines, the MHD component needs to be actively updated at each step.

For now this project is still in the discussion phase. We need to determine which code would be more suited for treating MHD and kinetic processes at the same time. Subsequently, a preliminary study of feedback processes between energetic particles and plasma fluid is essential. Different models of particle transport and heat deposit are expected to produce noticeable variations.

6.2.3 3D Simulations

The advantage of 2.5D grids compared to purely 2D ones is that when axisymmetry is toggled on, the flow takes into account the toroidal velocity and magnetic fields. Switching to 3D would allow all the scalar and vectorial quantities to evolve in the toroidal direction. In general, 3D allows to test for jet stability as 2D flows are blind to several instability mechanisms (e.g., the kink instability). Further more, collimation

shocks occurs when the flow converges towards a single points on the axis. It might prove difficult to meet this condition in 3D grids, another reason as to why shocks might not be detected is the grid size. Although, we were able to obtain standing recollimation shocks at 5 au, adding the ϕ component will force us to drastically reduce the grid size. Only then would we be able to run the 3D simulations as long as the 2.5D ones.

The grids used for the platform simulations contain $\sim 2 \times 10^2$ cells. If we were to move to 3D grids, we would need to add the ϕ component. By adding 32 points between 0 and 2π in the ϕ-direction, we reduce the size of the smallest cells at the jet axis to $r \sin\theta d\phi \sim 3 \times 10^{-5}$ while $dr \sim 3 \times 10^{-3}$, $rd\theta \sim 10^{-2}$. In turn this reduces the timestep by a factor ~ 100.

6.2.4 Observations in the era of JWST

The infrared detection instruments integrated in the JWST enable probing the atomic, hot, and ionized spine jet. Such instruments are able to see beyond the layer of dust that can surround YSO jets. The resolution of these instruments could further uncover the knotty features observed in jets. The exact source of periodicity is not as of yet resolved. If such cycles exist, we would need observational surveys over a long time scale, since we predict one cycle per year. One way to monitor the cycle is to measure the evolution of accretion rates over a period of three years using spectroscopic instruments in the near-IR (SPIRou, NIRCam). These cycles could stem from ejection periodicity of the star itself or from the interaction between the disk jet and stellar jet. Additionally, these types of instruments can reconstruct the magnetic topology better constraining the disk funneling onto the star (Donati et al., 2024).

Ionization rates, line ratios, and emission properties of the jets are not readily available from numerical simulations. Extracting these information requires an additional layer of modeling to create synthetic maps. These maps produce spectra of observable tracers based on the flow dynamics. One way to create such synthetic maps is to use radiative transfer codes.

Résumé

L'environnement d'une jeune étoile, tel qu'il est révélé par les observations et la théorie, est un système riche et complexe. Au fur et à mesure que ce système évolue, sa morphologie, sa composition, son ionisation, sa température, etc., se transforment également. Dans cette thèse, nous avons commencé par créer une toile multicomposantes, intégrant à la fois les vents stellaires et les vents du disque. Pour ce faire, nous avons connecté des solutions semi-analytiques pour les composantes stellaires et du disque, où le jet central est réaliste et conforme aux observations. Une fois un système stable établi, nous avons différencié les atmosphères stellaires et du disque, qui ont été paramétrées pour permettre un meilleur contrôle des conditions initiales.

Par la suite, ces simulations MHD ont été utilisées pour contraindre les taux de chauffage dans la région entourant les jeunes étoiles (YSO), en ajustant les paramètres afin de mieux reproduire les observations. En quelque sorte, nous avons éludé la question des sources physiques réelles du chauffage en nous appuyant sur une paramétrisation. Afin d'explorer un large espace de paramètres, nous nous sommes appuyés sur des solutions semi-analytiques ainsi que sur des simulations dites "de plateforme" (c'est-à-dire lorsque le disque est traité comme une condition aux limites). Nous avons également étendu ces simulations en incluant l'intérieur du disque. L'avantage des simulations de plateforme réside dans le fait que, en considérant le disque comme une condition aux limites, nous pouvons négliger les effets MHD non idéaux, qui augmentent considérablement le temps de calcul des simulations. Par ailleurs, en partant de solutions semi-analytiques plutôt que de configurations ad hoc, nous réduisons le temps de relaxation nécessaire pour que le système atteigne un état stable ou stationnaire.

Dans le chapitre 1, nous avons décrit le processus de formation des YSO à partir des nuages moléculaires, ainsi que les différentes étapes de l'évolution des jeunes étoiles. Nous avons également exploré le paradigme accrétion-éjection comme clé pour comprendre les structures observées. Dans le chapitre 2, nous avons introduit les raisons justifiant l'utilisation de l'approximation fluide pour décrire les plasmas astrophysiques. Puisque le plasma autour des YSO est traversé par des champs magnétiques, il est possible d'utiliser l'approche MHD pour décrire l'évolution des flux. De nombreux codes numériques et schémas existent pour étudier de tels flux. Nous présentons dans ce même chapitre le code PLUTO et discutons des configurations utilisées dans ce travail.

Dans le chapitre 3 figure des processus physiques responsables de l'ionisation des jets, des vents et des disques d'accrétion. Cela constitue une étape importante pour com-

prendre comment le champ magnétique est couplé au plasma ainsi que les mécanismes de chauffage et de refroidissement disponibles pour le système. Ces trois chapitres constituent une introduction qui dresse un tableau global des YSO, de leur évolution, et de la manière dont ils peuvent être étudiés à la fois par des observations et des approches théoriques.

Le chapitre 4 est basé sur des résultats publiés (Meskini et al., 2024). Nous y avons quantifié les effets du chauffage sur le jet. Nous avons trouvé des lois de puissance simples entre le rayon d'éjection du disque et le taux de chauffage, ainsi qu'entre le taux de perte de masse du jet et le taux de chauffage. En résumé, plus le chauffage est important, moins les lignes magnétiques sont chargées en masse, et plus la région émettrice du jet est étroite. L'exploration de l'espace des paramètres montre deux comportements principaux : dans le premier, les jets et les vents atteignent un état d'évolution stationnaire, tandis que dans le second, l'éjection varie de manière périodique, produisant des structures de chocs dans la région interne du jet.

Dans les simulations non stationnaires, deux phases coexistent : une phase quiescente et une phase éruptive, respectivement compatibles avec les observations de RY Tau (Petrov et al., 2019). Des chocs apparaissent également dans les simulations stationnaires, et ils sont cohérents avec les chocs de recolimation présentés par Ferreira (1997), ainsi qu'avec des observations, en particulier les chocs UV décrits par Gómez de Castro and Verdugo (2001, 2007). Nous soutenons que ces chocs de recolimation fixes doivent être présents dans tous les cas stationnaires, et qu'ils se produisent à différentes altitudes selon le taux de chauffage à la base de l'écoulement. Les chocs les plus bas observés se produisent à environ 5 ua, et les plus hauts à environ 20 ua. Un chauffage trop important pousse la hauteur au-delà de 30 ua, ce qui explique pourquoi ces chocs ne sont pas observés dans les simulations avec les taux de chauffage les plus élevés. Ces chocs se concentrent sur la séparatrice rapide, ce qui garantit que le flux n'est pas perturbé par des chocs se produisant au-dessus du point critique rapide sur l'axe.

Jannaud et al. (2023) ont été les premiers à montrer que des chocs fixes sont possibles avec des simulations de plateforme. Cependant, nos simulations sont les premières à montrer des chocs de collimation fixes aussi proches que 5 ua de la source, ce que nous attribuons à la présence d'un jet axial physique. Enfin, il convient de souligner que ces simulations abordent simultanément l'interaction étoile-disque et la collimation dans les jets.

Pour que les jets soient cohérents avec les observations, le chauffage doit être réduit par rapport aux valeurs fournies par les solutions analytiques. Ainsi, les températures nécessaires pour produire des jets proches des observations n'ont pas besoin d'excéder $\sim 10^6$K, bien que le vent stellaire soit entraîné par la pression (voir l'introduction du chapitre 4). De plus, Brunn et al. (2024) prédisent des taux de chauffage liés aux particules énergétiques qui sont compatibles avec notre étude paramétrique.

En ajoutant la description physique de l'intérieur du disque d'accrétion dans le chapitre 5, nous avons complété le système en incluant, dans une même boîte de simulation, la composante stellaire et l'intérieur du disque. L'objectif était d'étudier l'efficacité de l'émission du jet ainsi que le rétroaction du jet sur le disque d'accrétion. Étant tou-

jours dans un cadre 2.5D, nous avons introduit une diffusivité magnétique turbulente via le paramètre effectif α. Globalement, le système est turbulent, et nous retrouvons un cycle d'accrétion périodique. Ces cycles peuvent durer de quelques mois à plusieurs années. RY Tau pourrait également présenter un comportement cyclique, car les observations montrent une alternance entre des phases quiescentes et actives. Cependant, la période de ce phénomène reste inconnue.

Pour confirmer si les cycles observés dans nos simulations correspondent à la période de transition entre phases quiescentes et actives dans RY Tau, des observations sur des périodes plus longues seraient nécessaires. En revanche, des cycles avec des périodes précises sont observés dans d'autres systèmes d'accrétion/éjection, comme les microquasars, où ces cycles se déroulent sur des échelles de temps de l'ordre de quelques mois. Ainsi, de tels cycles pourraient être une évolution non linéaire naturelle de tous les systèmes d'accrétion avec écoulements.

Comme dans les simulations de lancement de jets, nous considérons un disque avec un modèle de diffusivité standard (Jacquemin-Ide et al., 2019). D'autres travaux montrent que le dynamo peut générer et maintenir un champ magnétique important (Mattia and Fendt, 2020a,b, 2022). Ces simulations évitent l'apparition de l'instabilité d'accrétion en augmentant la diffusivité magnétique. Une caractéristique intéressante de notre travail, qui inclut l'intérieur du disque, est l'apparition de colonnes d'accrétion symétriques Nord-Sud. Les études sur les structures d'accrétion montrent généralement que les entonnoirs d'accrétion évoluent pour privilégier l'un des hémisphères comme chemin préféré pour chuter vers l'étoile.

Étant donné que l'intérieur du disque est inclus dans le chapitre 5, nous pouvons exploiter pleinement les modèles de flambée en testant les cartes 2D de chauffage produites par les particules énergétiques. Il semble que le taux de chauffage considéré soit trop élevé pour permettre la progression de l'accrétion. En raison de la forte pression introduite par ce chauffage, la majeure partie du matériau accrété est éjectée sous forme d'écoulement, que ce soit à cause d'un chauffage excessif ou d'un manque de viscosité. Une viscosité turbulente pourrait éliminer l'excès de moment cinétique. Il est important de noter que les effets des flambées peuvent être surestimés. Les modèles doivent être adaptés pour tenir compte du taux des événements de reconnexion, de la forme de la topologie des champs magnétiques, et de leur capacité à produire des particules énergétiques intenses.

D'autres sources de chauffage existent dans les plasmas confinés magnétiquement, notamment sous la forme d'ondes d'Alfvén. Ces ondes sont idéales pour le transport d'énergie et jouent également un rôle dans la stabilité et le chauffage du plasma. Les particules chargées peuvent échanger de l'énergie et du moment avec les ondes d'Alfvén, car celles-ci transportent des perturbations électromagnétiques. Comparées à d'autres modes MHD magnéto-soniques lents, les ondes d'Alfvén ne se réfléchissent pas aux discontinuités, ce qui en fait de bons vecteurs d'énergie. Cependant, pour que ces ondes chauffent le plasma, un mécanisme de dissipation est nécessaire. Heyvaerts and Priest (1983) et Bogdan et al. (2003) proposent des processus de dissipation pour le Soleil, mais ceux-ci agissent principalement à des échelles trop petites pour nos objets.

Nous savons encore peu de choses sur les ondes d'Alfvén autour des jeunes étoiles. Néanmoins, elles pourraient constituer une source de chauffage non négligeable en se dissipant à travers l'atmosphère du disque et la couronne stellaire.

Comme nous l'avons déjà montré dans cette thèse, les codes MHD peuvent être utilisés pour inclure des effets de chauffage. Ce chauffage peut provenir de divers phénomènes, tels que l'interaction de particules non thermiques avec le fluide plasma. Cependant, dans ce cas, la température obtenue à partir des simulations ne permet pas de distinguer entre la température du gaz et celle des particules.

Une alternative aux simulations purement MHD est l'utilisation de codes hybrides, comme les codes MHD-Particle-In-Cell (MHD-PIC), qui intègrent explicitement les particules en plus d'une couche fluide MHD. Si un retour d'information adéquat est établi entre le fluide et les particules, nous pourrions obtenir des simulations avec des détails plus fins. Ce traitement exige que le plasma et les particules interagissent et exercent une influence réciproque.

Des travaux récents, tels que celui présenté par Sun and Bai (2023), implémentent un module PIC dans le code ATHENA++, où les particules énergétiques sont traitées comme dans les codes PIC classiques. La composante MHD, quant à elle, décrit un fluide de fond. Comme les auteurs le soulignent, l'objectif principal de ce cadre est d'explorer la physique cinétique. Ils ont utilisé des particules tests, ce qui signifie qu'il n'y a pas de rétroaction des particules énergétiques sur le MHD. Leur étude s'est essentiellement concentrée sur le transport des particules dans une turbulence entraînée par l'instabilité magnétorotationnelle (MRI). Étant donné que la production de flambées découle de processus dynamiques, tels que la reconnexion des lignes magnétiques, la composante MHD doit être mise à jour activement à chaque étape.

Pour l'instant, ce projet est encore en phase de discussion. Il est nécessaire de déterminer quel code serait le plus adapté pour traiter simultanément les processus MHD et cinétiques. Par la suite, une étude préliminaire des processus de rétroaction entre les particules énergétiques et le fluide plasma est essentielle. Différents modèles de transport des particules et de dépôt de chaleur devraient produire des variations significatives.

L'avantage des grilles 2.5D par rapport aux grilles purement 2D réside dans le fait que, lorsque l'axisymétrie est activée, l'écoulement prend en compte la vitesse et les champs magnétiques toroïdaux. Passer à la 3D permettrait à toutes les grandeurs scalaires et vectorielles d'évoluer dans la direction toroïdale. En général, la 3D permet de tester la stabilité des jets, car les écoulements 2D ne sont pas sensibles à plusieurs mécanismes d'instabilité (par exemple, l'instabilité de kink). De plus, les chocs de collimation se produisent lorsque l'écoulement converge vers un point unique sur l'axe. Il pourrait s'avérer difficile de satisfaire cette condition dans les grilles 3D. Une autre raison pour laquelle ces chocs pourraient ne pas être détectés est la résolution de la grille. Bien que nous ayons réussi à obtenir des chocs de recollimation stationnaires à 5 au en 2.5D, l'ajout de la composante ϕ nous obligerait à réduire drastiquement la taille des cellules de la grille. Ce n'est qu'à cette condition que nous pourrions exécuter des simulations 3D aussi longues que celles en 2.5D.

Les grilles utilisées pour les simulations de type plateforme contiennent environ $2\times1022\times102$ cellules. Si nous devions passer à des grilles 3D, il faudrait inclure la composante ϕ. En ajoutant 32 points entre 0 et 2π dans la direction ϕ, la taille des plus petites cellules près de l'axe du jet serait réduite à $r\sin\theta d\phi \sim 3\times10^{-5}$, tandis que $dr \sim 3\times10^{-3}$ et $rd\theta \sim 10^{-2}$. Cela réduirait à son tour le pas de temps d'un facteur d'environ 100.

Les instruments de détection infrarouge intégrés dans le JWST permettent de sonder le jet axial atomique, chaud et ionisé. Ces instruments sont capables de voir au-delà de la couche de poussière qui peut entourer les jets des jeunes étoiles. La résolution de ces instruments pourrait également révéler les structures de chocs observées dans les jets. Cependant, la source exacte de la périodicité reste à déterminer. Si de tels cycles existent, des relevés d'observation sur une longue période seraient nécessaires, puisque nous prédisons un cycle par an. Une façon de surveiller ces cycles serait de mesurer l'évolution des taux d'accrétion sur une période de trois ans à l'aide d'instruments spectroscopiques dans le proche infrarouge (SPIRou, NIRCam). Ces cycles pourraient provenir de la périodicité des éjections de l'étoile elle-même ou de l'interaction entre le jet du disque et celui de l'étoile. De plus, ce type d'instruments peut reconstruire la topologie magnétique, ce qui permettrait de mieux contraindre le canal d'accrétion entre le disque et l'étoile (Donati et al., 2024).

Les taux d'ionisation, les rapports de raies et les propriétés d'émission des jets ne sont pas directement accessibles à partir des simulations numériques. Extraire ces informations nécessite une couche supplémentaire de modélisation pour créer des cartes synthétiques. Ces cartes permettent de produire des spectres d'indicateurs observables basés sur la dynamique de l'écoulement. Une méthode pour créer ces cartes synthétiques consiste à utiliser des codes de transfert radiatif.

Bibliography

Agra-Amboage, V., Cabrit, S., Dougados, C., Kristensen, L., Ibgui, L., and Reunanen, J. (2014). Origin of the wide-angle hot h2 in dg tauri-new insight from sinfoni spectro-imaging. *Astronomy & Astrophysics*, 564:A11.

Agra-Amboage, V., Dougados, C., Cabrit, S., Garcia, P. J. V., and Ferruit, P. (2009). [O I] sub-arcsecond study of a microjet from an intermediate mass young star: RY Tauri. *A&A*, 493:1029–1041.

Agra-Amboage, V., Dougados, C., Cabrit, S., and Reunanen, J. (2011). Sub-arcsecond [fe ii] spectro-imaging of the dg tauri jet-periodic bubbles and a dusty disk wind? *Astronomy & Astrophysics*, 532:A59.

Aikawa, Y., Cataldi, G., Yamato, Y., Zhang, K., Booth, A. S., Furuya, K., Andrews, S. M., Bae, J., Bergin, E. A., Bergner, J. B., et al. (2021). Molecules with alma at planet-forming scales (maps). xiii. hco+ and disk ionization structure. *The Astrophysical Journal Supplement Series*, 257(1):13.

Aikawa, Y., Furuya, K., Nomura, H., and Qi, C. (2015). Analytical formulae of molecular ion abundances and the n2h+ ring in protoplanetary disks. *The Astrophysical Journal*, 807(2):120.

Albuquerque, R. (2020). *Accretion versus outflow regions around Young Stellar Objects*. PhD thesis, Université Paris sciences et lettres; Universidade do Porto.

Alcalá, J., Manara, C., Natta, A., Frasca, A., Testi, L., Nisini, B., Stelzer, B., Williams, J., Antoniucci, S., Biazzo, K., et al. (2017). X-shooter spectroscopy of young stellar objects in lupus-accretion properties of class ii and transitional objects. *Astronomy & Astrophysics*, 600:A20.

Alencar, S., Bouvier, J., Walter, F., Dougados, C., Donati, J.-F., Kurosawa, R., Romanova, M., Bonfils, X., Lima, G., Massaro, S., et al. (2012). Accretion dynamics in the classical t tauri star v2129 ophiuchi. *Astronomy & Astrophysics*, 541:A116.

Allen, L. A., Habbal, S. R., and Hu, Y. Q. (1998). Thermal coupling of protons and neutral hydrogen in the fast solar wind. *Journal of Geophysical Research: Space Physics*, 103(A4):6551–6569.

Anderson, J. M., Li, Z.-Y., Krasnopolsky, R., and Blandford, R. D. (2003). Locating the launching region of t tauri winds: the case of dg tauri. *The Astrophysical Journal*, 590(2):L107.

Anderson, J. M., Li, Z.-Y., Krasnopolsky, R., and Blandford, R. D. (2005). The structure of magnetocentrifugal winds. i. steady mass loading. *ApJ*, 630(2):945.

Andre, P., Deeney, B. D., Phillips, R. B., and Lestrade, J.-F. (1992). Vlbi survey of rho ophiuchi-a population of magnetized, diskless young stellar objects. *ApJ*, 401:667–677.

André, P., Di Francesco, J., Ward-Thompson, D., Inutsuka, S.-i., Pudritz, R. E., and Pineda, J. (2014). From filamentary networks to dense cores in molecular clouds: toward a new paradigm for star formation. *Protostars and Planets VI*, 27.

Andre, P., Ward-Thompson, D., and Barsony, M. (1993). Submillimeter continuum observations of rho ophiuchi a-the candidate protostar vla 1623 and prestellar clumps. *ApJ*, 406:122–141.

Antoniucci, S., Nisini, B., Giannini, T., and Lorenzetti, D. (2008). Accretion and ejection properties of embedded protostars: the case of hh26, hh34, and hh46 irs. *Astronomy & Astrophysics*, 479(2):503–514.

Araudo, A. T., Padovani, M., and Marcowith, A. (2021). Particle acceleration and magnetic field amplification in massive young stellar object jets. *Monthly Notices of the RAS*, 504(2):2405–2419.

Armitage, P. J. (2011). Dynamics of protoplanetary disks. *Annual Review of Astronomy and Astrophysics*, 49:195–236.

Bacciotti, F., Chiuderi, C., and Oliva, E. (1995). The structure of optical stellar jets: a phenomenological analysis. *Astronomy and Astrophysics, v. 296, p. 185*, 296:185.

Bacciotti, F. and Eislöffel, J. (1999). Ionization and density along the beams of herbig-haro jets. *Astronomy and Astrophysics, v. 342, p. 717-735 (1999)*, 342:717–735.

Bacciotti, F., Mundt, R., Ray, T. P., Eislöffel, J., Solf, J., and Camezind, M. (2000). Hubble space telescope stis spectroscopy of the optical outflow from dg tauri: Structure and kinematics on subarcsecond scales. *The Astrophysical Journal*, 537(1):L49.

Bacciotti, F., Ray, T. P., Mundt, R., Eislöffel, J., and Solf, J. (2002). Hubble space telescope/stis spectroscopy of the optical outflow from dg tauri: Indications for rotation in the initial jet channel. *The Astrophysical Journal*, 576(1):222.

Bai, X.-N. (2017). Global simulations of the inner regions of protoplanetary disks with comprehensive disk microphysics. *The Astrophysical Journal*, 845(1):75.

Bai, X.-N. and Stone, J. M. (2011). Effect of ambipolar diffusion on the nonlinear evolution of magnetorotational instability in weakly ionized disks. *The Astrophysical Journal*, 736(2):144.

Bai, X.-N. and Stone, J. M. (2013). Wind-driven accretion in protoplanetary disks. i. suppression of the magnetorotational instability and launching of the magnetocentrifugal wind. *The Astrophysical Journal*, 769(1):76.

Bai, X.-N., Ye, J., Goodman, J., and Yuan, F. (2016). Magneto-thermal disk winds from protoplanetary disks. *ApJ*, 818(2):152.

Balbus, S. A. (2003). Enhanced Angular Momentum Transport in Accretion Disks. *Annual Review of Astron and Astrophys*, 41:555–597.

Balbus, S. A. and Hawley, J. F. (1991). A Powerful Local Shear Instability in Weakly Magnetized Disks. I. Linear Analysis. *Astrophysical Journal*, 376:214.

Ballesteros-Paredes, J., André, P., Hennebelle, P., Klessen, R. S., Kruijssen, J. D., Chevance, M., Nakamura, F., Adamo, A., and Vazquez-Semadeni, E. (2020). From diffuse gas to dense molecular cloud cores. *Space Science Reviews*, 216:1–58.

Bally, J. (2016). Protostellar outflows. *Annual Review of Astronomy and Astrophysics*, 54:491–528.

Bally, J., Reipurth, B., and Davis, C. J. (2007). Observations of jets and outflows from young stars. *Protostars and Planets V*, pages 215–230.

Bally, J. and Scoville, N. (1982). Structure and evolution of molecular clouds near h ii regions. ii-the disk constrained h ii region, s106. *Astrophysical Journal, Part 1, vol. 255, Apr. 15, 1982, p. 497-509.*, 255:497–509.

Baraffe, I., Homeier, D., Allard, F., and Chabrier, G. (2015). New evolutionary models for pre-main sequence and main sequence low-mass stars down to the hydrogen-burning limit. *Astronomy & Astrophysics*, 577:A42.

Bardeen, J. M. and Berger, B. K. (1978). A model for winds from galactic disks. *ApJ*, 221:105–113.

Barral, J. and Canto, J. (1981). A stellar wind model for bipolar nebulae. *Revista Mexicana de Astronomia y Astrofisica, Vol. 5, P. 101, 1981*, 5:101.

Benisty, M., Perraut, K., Mourard, D., Stee, P., Lima, G., Le Bouquin, J., Fernandes, M. B., Chesneau, O., Nardetto, N., Tallon-Bosc, I., et al. (2013). Enhanced hα activity at periastron in the young and massive spectroscopic binary hd 200775. *Astronomy & Astrophysics*, 555:A113.

Bergin, E. A. and Tafalla, M. (2007). Cold dark clouds: the initial conditions for star formation. *Annu. Rev. Astron. Astrophys.*, 45:339–396.

Bertout, C. (1989). T tauri stars: Wild as dust. *ARA&A*, 27(1):351–395.

Béthune, W., Lesur, G., and Ferreira, J. (2016). Self-organisation in protoplanetary discs-global, non-stratified hall-mhd simulations. *Astronomy & Astrophysics*, 589:A87.

Béthune, W., Lesur, G., and Ferreira, J. (2017). Global simulations of protoplanetary disks with net magnetic flux-i. non-ideal mhd case. *Astronomy & Astrophysics*, 600:A75.

Birnstiel, T., Klahr, H., and Ercolano, B. (2012). A simple model for the evolution of the dust population in protoplanetary disks. *Astronomy & Astrophysics*, 539:A148.

Bisnovatyi-Kogan, G. and Lamzin, S. (1977). Models of the outflowing envelopes of t tau stars. *Soviet Ast.*, 21:720–727.

Bjerkeli, P., Ramsey, J. P., Harsono, D., Calcutt, H., Kristensen, L. E., van der Wiel, M. H., Jørgensen, J. K., Muller, S., and Persson, M. V. (2019). Kinematics around the b335 protostar down to au scales. *Astronomy & Astrophysics*, 631:A64.

Blandford, R. and Payne, D. (1982). Hydromagnetic flows from accretion discs and the production of radio jets. *MNRAS*, 199(4):883–903.

Blinova, A., Romanova, M., and Lovelace, R. (2016). Boundary between stable and unstable regimes of accretion. ordered and chaotic unstable regimes. *Monthly Notices of the Royal Astronomical Society*, 459(3):2354–2369.

Bogdan, T., Hansteen, M. C. V., McMurry, A., Rosenthal, C., Johnson, M., Petty-Powell, S., Zita, E., Stein, R., McIntosh, S., and Nordlund, Å. (2003). Waves in the magnetized solar atmosphere. ii. waves from localized sources in magnetic flux concentrations. *The Astrophysical Journal*, 599(1):626.

Bogovalov, S. V. (1994). On the Theory of Magnetohydrodynamic Winds from a Magnetosphere of Axisymmetric Rotators. *MNRAS*, 270:721.

Böhm, K., Mannery, E., and Brugel, E. (1980). Very low-excitation herbig-haro objects. *Astrophysical Journal, Part 2-Letters to the Editor, vol. 235, Feb. 1, 1980, p. L137-L141.*, 235:L137–L141.

Bontemps, S., Andre, P., Terebey, S., and Cabrit, S. (1996). Evolution of outflow activity around low-mass embedded young stellar objects. *Astronomy and Astrophysics*, 311:858–872.

Bouvier, J., Bertout, C., Benz, W., and Mayor, M. (1986). Rotation in t tauri stars. i-observations and immediate analysis. *A&A*, 165:110–119.

Bouvier, J., Cabrit, S., Fernandez, M., Martin, E. L., and Matthews, J. M. (1993). COYOTES - Part One - Multisite UBVRI Photometry of 24 Pre Main Sequence Stars of the Taurus-Auriga Cloud. *A&AS*, 101:485.

Bouvier, J., Zahn, J.-P., and Cabrit, S. (2002). Constraints on accretion-ejection structures in young stars. *EAS Publ. Ser.*, 3:147–182.

Braun, T. A., Yen, H.-W., Koch, P. M., Manara, C. F., Miotello, A., and Testi, L. (2021). Dynamical stellar masses of pre-main-sequence stars in lupus and taurus obtained with alma surveys in comparison with stellar evolutionary models. *The Astrophysical Journal*, 908(1):46.

Breech, B., Matthaeus, W. H., Minnie, J., Bieber, J., Oughton, S., Smith, C. W., and Isenberg, P. (2008). Turbulence transport throughout the heliosphere. *Journal of Geophysical Research: Space Physics*, 113(A8).

Bressan, A., Marigo, P., Girardi, L., Salasnich, B., Dal Cero, C., Rubele, S., and Nanni, A. (2012). Parsec: stellar tracks and isochrones with the padova and trieste stellar evolution code. *MNRAS*, 427(1):127–145.

Brugel, E., Böhm, K., and Mannery, E. (1981). Emission line spectra of herbig-haro objects. *Astrophysical Journal Supplement Series, vol. 47, Oct. 1981, p. 117-138.*, 47:117–138.

Brunn, V., Marcowith, A., Sauty, C., Padovani, M., Rab, C., and Meskini, C. (2023). Ionization of inner t tauri star discs: effects of in situ energetic particles produced by strong magnetic reconnection events. *MNRAS*, 519(4):5673–5688.

Brunn, V., Rab, C., Marcowith, A., Sauty, C., Padovani, M., and Meskini, C. (2024). Impacts of energetic particles from t tauri flares on inner protoplanetary discs. *Monthly Notices of the Royal Astronomical Society*, 530(4):3669–3687.

Bruno, R. and Carbone, V. (2013). The solar wind as a turbulence laboratory. *Living Reviews in Solar Physics*, 10(1):2.

Burrows, C. J., Stapelfeldt, K. R., Watson, A. M., Krist, J. E., Ballester, G. E., Clarke, J. T., Crisp, D., Gallagher III, J. S., Griffiths, R. E., Hester, J. J., et al. (1996). Hubble space telescope observations of the disk and jet of hh 30. *The Astrophysical Journal*, 473(1):437.

Cabrit, S. (2007). Jets from young stars: The need for mhd collimation and acceleration processes. In *Jets from Young Stars: Models and Constraints*, pages 21–53. Springer.

Cabrit, S., Edwards, S., Strom, S. E., and Strom, K. M. (1990). Forbidden-line emission and infrared excesses in t tauri stars-evidence for accretion-driven mass loss? *ApJ*, 354:687–700.

Calvet, N., Basri, G., and Kuhi, L. V. (1984). The chromospheric hypothesis for the t tauri phenomenon. *Astrophysical Journal, Part 1 (ISSN 0004-637X), vol. 277, Feb. 15, 1984, p. 725-737. Research supported by the Alexander von Humboldt Stiftung.*, 277:725–737.

Calvet, N., Muzerolle, J., Briceño, C., Hernández, J., Hartmann, L., Saucedo, J. L., and Gordon, K. D. (2004). The Mass Accretion Rates of Intermediate-Mass T Tauri Stars. *AJ*, 128:1294–1318.

Cameron, A. (1978). Physics of the primitive solar accretion disk. *The moon and the planets*, 18(1):5–40.

Campbell, C. (2009). The stability of accretion discs with inflow driven purely by magnetic winds. *Monthly Notices of the Royal Astronomical Society*, 392(1):271–280.

Carter, B. (1968). Global Structure of the Kerr Family of Gravitational Fields. *Physical Review*, 174(5):1559–1571.

Casse, F. and Ferreira, J. (2000). Magnetized accretion-ejection structures v. effects of entropy generation inside the disc. *A&A*, 361:1178–1190.

Casse, F. and Keppens, R. (2002). Magnetized accretion-ejection structures: 2.5-dimensional magnetohydrodynamic simulations of continuous ideal jet launching from resistive accretion disks. *ApJ*, 581(2):988.

Casse, F. and Keppens, R. (2004). Radiatively inefficient magnetohydrodynamic accretion-ejection structures. *ApJ*, 601(1):90.

Chandran, B. D. and Hollweg, J. V. (2009). Alfvén wave reflection and turbulent heating in the solar wind from 1 solar radius to 1 au: an analytical treatment. *The Astrophysical Journal*, 707(2):1659.

Chen, C.-Y. and Ostriker, E. C. (2014). Formation of magnetized prestellar cores with ambipolar diffusion and turbulence. *The Astrophysical Journal*, 785(1):69.

Chevance, M., Kruijssen, J. D., Vazquez-Semadeni, E., Nakamura, F., Klessen, R., Ballesteros-Paredes, J., Inutsuka, S.-i., Adamo, A., and Hennebelle, P. (2020). The molecular cloud lifecycle. *Space Science Reviews*, 216:1–42.

Chou, M.-Y., Takami, M., Manset, N., Beck, T., Pyo, T.-S., Chen, W.-P., Panwar, N., Karr, J. L., Shang, H., and Liu, H. B. (2013). Time variability of emission lines for four active t tauri stars. i. october- december in 2010. *The Astronomical Journal*, 145(4):108.

Cleeves, L. I., Adams, F. C., and Bergin, E. A. (2013). Exclusion of Cosmic Rays in Protoplanetary Disks: Stellar and Magnetic Effects. *Astrophysical Journal*, 772(1):5.

Cleeves, L. I., Bergin, E. A., Alexander, C. M. O., Du, F., Graninger, D., Öberg, K. I., and Harries, T. J. (2014). The ancient heritage of water ice in the solar system. *Science*, 345(6204):1590–1593.

Cleeves, L. I., Bergin, E. A., Qi, C., Adams, F. C., and Öberg, K. I. (2015). Constraining the x-ray and cosmic-ray ionization chemistry of the tw hya protoplanetary disk: evidence for a sub-interstellar cosmic-ray rate. *The Astrophysical Journal*, 799(2):204.

Cliver, E. W. and Dietrich, W. F. (2013). The 1859 space weather event revisited: limits of extreme activity. *Journal of Space Weather and Space Climate*, 3:A31.

Coffey, D., Bacciotti, F., Ray, T. P., Eislöffel, J., and Woitas, J. (2007). Further indications of jet rotation in new ultraviolet and optical hubble space telescope stis spectra. *The Astrophysical Journal*, 663(1):350.

Coffey, D., Bacciotti, F., Woitas, J., Ray, T. P., and Eislöffel, J. (2004). Rotation of jets from young stars: New clues from the hubble space telescope imaging spectrograph. *ApJ*, 604(2):758.

Coffey, D., Rigliaco, E., Bacciotti, F., Ray, T. P., and Eislöffel, J. (2012). Jet rotation investigated in the near-ultraviolet with hst/stis. *arXiv preprint arXiv:1202.3250*.

Combet, C. and Ferreira, J. (2008). The radial structure of protostellar accretion disks: influence of jets. *Astronomy & Astrophysics*, 479(2):481–491.

Combet, C., Ferreira, J., and Casse, F. (2010). Dead zones in protostellar discs: the case of jet emitting discs. *Astronomy & Astrophysics*, 519:A108.

Contopoulos, I. and Sauty, C. (2001). The origin of molecular protostellar outflows. *Astronomy and Astrophysics*, 365:165–173.

Contopoulos, J. and Lovelace, R. (1994). Magnetically driven jets and winds: Exact solutions. *ApJ*, 429(1).

Cranmer, S. R. (2008). Turbulence-driven polar winds from t tauri stars energized by magnetospheric accretion. *The Astrophysical Journal*, 689(1):316.

Cranmer, S. R. (2009). Testing models of accretion-driven coronal heating and stellar wind acceleration for t tauri stars. *The Astrophysical Journal*, 706(1):824.

Dalgarno, A., Yan, M., and Liu, W. (1999). Electron energy deposition in a gas mixture of atomic and molecular hydrogen and helium. *The Astrophysical Journal Supplement Series*, 125(1):237.

Davies, C. L., Kraus, S., Harries, T. J., Monnier, J. D., Kloppenborg, B., Aarnio, A., Baron, F., Lopez, R. G., Millan-Gabet, R., Parks, R., et al. (2020). The inner disk of ry tau: evidence of stellar occultation by the disk atmosphere at the sublimation rim from k-band continuum interferometry. *ApJ*, 897(1):31.

de Albuquerque, R. M. G. (2020). *Accretion versus outflow regions around Young Stellar Objects*. PhD thesis, university of Porto and Observatoire de Paris.

De Valon, A., Dougados, C., Cabrit, S., Louvet, F., Zapata, L., and Mardones, D. (2020). Alma reveals a large structured disk and nested rotating outflows in dg tauri b. *Astronomy & Astrophysics*, 634:L12.

DeCampli, W. M. (1981). T tauri winds. *ApJ*, 244:124–146.

del Valle, M. V., Romero, G. E., Luque-Escamilla, P. L., Martí, J., and Ramón Sánchez-Sutil, J. (2011). Are T Tauri Stars Gamma-Ray Emitters? *Astrophysical Journal*, 738(1):115.

Del Zanna, L., Velli, M., and Londrillo, P. (2001). Parametric decay of circularly polarized alfvén waves: Multidimensional simulations in periodic and open domains. *Astronomy & Astrophysics*, 367(2):705–718.

di Francesco, J., Evans, N., Caselli, P., Myers, P., Shirley, Y., Aikawa, Y., and Tafalla, M. (2007). An observational perspective of low-mass dense cores i: Internal physical and chemical properties. *Protostars and Planets V*, page 17.

Dobbs, C. (2013). Giant molecular clouds: star factories of the galaxy. *Astronomy and Geophysics*, 54(5):5–24.

Dodin, A. (2015). Non-lte modeling of the structure and spectra of hot accretion spots on the surface of young stars. *Astronomy Letters*, 41:196–210.

Donati, J.-F., Finociety, B., Cristofari, P., Alencar, S., Moutou, C., Delfosse, X., Fouqué, P., Arnold, L., Baruteau, C., Kóspál, Á., et al. (2024). The classical t tauri star ci tau observed with spirou: magnetospheric accretion and planetary formation. *Monthly Notices of the Royal Astronomical Society*, 530(1):264–286.

Donati, J. F. and Landstreet, J. D. (2009). Magnetic Fields of Nondegenerate Stars. *Annual Review of Astron and Astrophys*, 47(1):333–370.

Donati, J.-F., Morin, J., Petit, P., Delfosse, X., Forveille, T., Aurière, M., Cabanac, R., Dintrans, B., Fares, R., Gastine, T., et al. (2008). Large-scale magnetic topologies of early m dwarfs. *Monthly Notices of the Royal Astronomical Society*, 390(2):545–560.

Dotter, A. (2016). Mesa isochrones and stellar tracks (mist) 0: methods for the construction of stellar isochrones. *ApJS*, 222(1):8.

Dotter, A., Chaboyer, B., Jevremović, D., Kostov, V., Baron, E., and Ferguson, J. W. (2008). The dartmouth stellar evolution database. *ApJS*, 178(1):89.

Dougados, C., Cabrit, S., Lavalley, C., and Ménard, F. (2000). T tauri stars microjets resolved by adaptive optics. *Astronomy and Astrophysics, v. 357, p. L61-L64 (2000)*, 357:L61–L64.

Dullemond, C. and Monnier, J. (2010). The inner regions of protoplanetary disks. *Annual Review of Astronomy and Astrophysics*, 48:205–239.

Edwards, S., Strom, S. E., Hartigan, P., Strom, K. M., Hillenbrand, L. A., Herbst, W., Attridge, J., Merrill, K. M., Probst, R., and Gatley, I. (1993). Angular momentum regulation in low-mass young stars surrounded by accretion disks. *Astronomical Journal (ISSN 0004-6256), vol. 106, no. 1, p. 372-382.*, 106:372–382.

Emslie, A., Dennis, B., Shih, A., Chamberlin, P., Mewaldt, R., Moore, C., Share, G., Vourlidas, A., and Welsch, B. (2012). Global energetics of thirty-eight large solar eruptive events. *The Astrophysical Journal*, 759(1):71.

Ercolano, B., Clarke, C. J., and Drake, J. J. (2009). X-Ray Irradiated Protoplanetary Disk Atmospheres. II. Predictions from Models in Hydrostatic Equilibrium. *Astrophysical Journal*, 699(2):1639–1649.

Ercolano, B., Drake, J. J., Raymond, J. C., and Clarke, C. C. (2008). X-Ray-Irradiated Protoplanetary Disk Atmospheres. I. Predicted Emission-Line Spectrum and Photoevaporation. *Astrophysical Journal*, 688(1):398–407.

Ercolano, B. and Picogna, G. (2022). Modelling photoevaporation in planet forming discs. *European Physical Journal Plus*, 137(12):1357.

Esplin, T. and Luhman, K. (2022). A census of stars and disks in corona australis. *The Astronomical Journal*, 163(2):64.

Evans, C. R. and Hawley, J. F. (1988). Simulation of magnetohydrodynamic flows-a constrained transport method. *Astrophysical Journal, Part 1 (ISSN 0004-637X), vol. 332, Sept. 15, 1988, p. 659-677.*, 332:659–677.

Fang, M., Pascucci, I., Edwards, S., Gorti, U., Banzatti, A., Flock, M., Hartigan, P., Herczeg, G. J., and Dupree, A. K. (2018). A new look at t tauri star forbidden lines: Mhd-driven winds from the inner disk. *ApJ*, 868(1):28.

Favata, F., Flaccomio, E., Reale, F., Micela, G., Sciortino, S., Shang, H., Stassun, K. G., and Feigelson, E. D. (2005). Bright X-Ray Flares in Orion Young Stars from COUP: Evidence for Star-Disk Magnetic Fields? *Astrophysical Journals*, 160(2):469–502.

Fedriani, R., Caratti o Garatti, A., Purser, S., Sanna, A., Tan, J., Garcia-Lopez, R., Ray, T., Coffey, D., Stecklum, B., and Hoare, M. (2019). Measuring the ionisation fraction in a jet from a massive protostar. *Nature communications*, 10(1):3630.

Feiden, G. A. (2016). Magnetic inhibition of convection and the fundamental properties of low-mass stars-iii. a consistent 10 myr age for the upper scorpius ob association. *Astronomy & Astrophysics*, 593:A99.

Feigelson, E. D., Broos, P., Gaffney, James A., I., Garmire, G., Hillenbrand, L. A., Pravdo, S. H., Townsley, L., and Tsuboi, Y. (2002). X-Ray-emitting Young Stars in the Orion Nebula. *Astrophysical Journal*, 574(1):258–292.

Feigelson, E. D. and Montmerle, T. (1999). High-energy processes in young stellar objects. *ARA&A*, 37(1):363–408.

Fendt, C. (2006). Collimation of astrophysical jets: The role of the accretion disk magnetic field distribution. *ApJ*, 651(1):272.

Fendt, C. and Sheikhnezami, S. (2013). Bipolar jets launched from accretion disks. ii. the formation of asymmetric jets and counter jets. *ApJ*, 774(1):12.

Ferreira, J. (1994). *Structures magnétiques d'accrétion-éjection*. PhD thesis, Université Paris-Diderot-Paris VII.

Ferreira, J. (1997). Magnetically-driven jets from keplerian accretion discs. *A&A*, 319:340–359.

Ferreira, J. and Casse, F. (2004). Stationary accretion disks launching super-fast-magnetosonic magnetohydrodynamic jets. *The Astrophysical Journal*, 601(2):L139.

Ferreira, J. and Casse, F. (2013). On fan-shaped cold mhd winds from keplerian accretion discs. *Monthly Notices of the Royal Astronomical Society*, 428(1):307–320.

Ferreira, J., Dougados, C., and Cabrit, S. (2006). Which jet launching mechanism (s) in t tauri stars? *A&A*, 453(3):785–796.

Ferreira, J., Dougados, C., and Whelan, E. (2007). *Jets from young stars: models and constraints*, volume 723. Springer.

Ferreira, J. and Pelletier, G. (1993). Magnetized accretion-ejection structures. 1. General statements. *Astronomy and Astrophysics*, 276:625.

Ferreira, J. and Pelletier, G. (1995). Magnetized accretion-ejection structures. iii. stellar and extragalactic jets as weakly dissipative disk outflows. *A&A*, 295:807.

Ferreira, J., Pelletier, G., and Appl, S. (2000). Reconnection x-winds: spin-down of low-mass protostars. *Monthly Notices of the Royal Astronomical Society*, 312(2):387–397.

Finocchi, F. and Gail, H.-P. (1997). Chemical reactions in protoplanetary accretion disks. iii. the role of ionisation processes. *Astronomy and Astrophysics, v. 327, p. 825-844*, 327:825–844.

Fischer, W. J., Hillenbrand, L. A., Herczeg, G. J., Johnstone, D., Kospal, A., and Dunham, M. M. (2023). Accretion Variability as a Guide to Stellar Mass Assembly. In Inutsuka, S., Aikawa, Y., Muto, T., Tomida, K., and Tamura, M., editors, *Astronomical Society of the Pacific Conference Series*, volume 534 of *Astronomical Society of the Pacific Conference Series*, page 355.

Flock, M., Turner, N. J., Nelson, R. P., Lyra, W., Manger, N., and Klahr, H. (2020). Gas and dust dynamics in starlight-heated protoplanetary disks. *The Astrophysical Journal*, 897(2):155.

Font, A. S., McCarthy, I. G., Johnstone, D., and Ballantyne, D. R. (2004). Photoevaporation of circumstellar disks around young stars. *The Astrophysical Journal*, 607(2):890.

Frank, A., Ray, T., Cabrit, S., Hartigan, P., Arce, H., Bacciotti, F., Bally, J., Benisty, M., Eislöffel, J., Güdel, M., et al. (2014). Jets and outflows from star to cloud: observations confront theory. *Protostars and planets VI*, 451(1402.3553).

Fraschetti, F., Drake, J. J., Cohen, O., and Garraffo, C. (2018). Mottled Protoplanetary Disk Ionization by Magnetically Channeled T Tauri Star Energetic Particles. *Astrophysical Journal*, 853(2):112.

Fromang, S., Latter, H., Lesur, G., and Ogilvie, G. I. (2013). Local outflows from turbulent accretion disks. *Astronomy & Astrophysics*, 552:A71.

Fujii, Y. I. and Kimura, S. S. (2022). Cosmic-Ray Ionization Rate in Protoplanetary Disks with Sheared Magnetic Fields. *Astrophysical Journal, Letters*, 937(2):L37.

Gaches, B. A. L. and Offner, S. S. R. (2018). Exploration of Cosmic-ray Acceleration in Protostellar Accretion Shocks and a Model for Ionization Rates in Embedded Protoclusters. *Astrophysical Journal*, 861(2):87.

Gammie, C. F. (1996). Layered accretion in t tauri disks. *Astrophysical Journal v. 457, p. 355*, 457:355.

Garcia, P. J., Ferreira, J., Cabrit, S., and Binette, L. (2001). Atomic t tauri disk winds heated by ambipolar diffusion-i. thermal structure. *Astronomy & Astrophysics*, 377(2):589–608.

Garufi, A., Podio, L., Bacciotti, F., Antoniucci, S., Boccaletti, A., Codella, C., Dougados, C., Ménard, F., Mesa, D., Meyer, M., et al. (2019). Sphere view of the jet and the envelope of ry tauri. *A&A*, 628:A68.

Getman, K. V. and Feigelson, E. D. (2021). X-ray superflares from pre-main-sequence stars: Flare energetics and frequency. *The Astrophysical Journal*, 916(1):32.

Getman, K. V., Feigelson, E. D., Broos, P. S., Micela, G., and Garmire, G. P. (2008). X-ray flares in orion young stars. i. flare characteristics. *The Astrophysical Journal*, 688(1):418.

Getman, K. V., Feigelson, E. D., and Garmire, G. P. (2021). X-ray superflares from pre-main-sequence stars: Flare modeling. *The Astrophysical Journal*, 920(2):154.

Giannini, T., Nisini, B., Antoniucci, S., Biazzo, K., Alcalá, J., Bacciotti, F., Fedele, D., Frasca, A., Harutyunyan, A., Munari, U., et al. (2019). Giarps high-resolution observations of t tauri stars (ghost)-i. jet line emission. *Astronomy & Astrophysics*, 631:A44.

Glassgold, A., Najita, J., and Igea, J. (1997). X-ray ionization of protoplanetary disks. *The Astrophysical Journal*, 480(1):344.

Glassgold, A. E., Galli, D., and Padovani, M. (2012). Cosmic-ray and x-ray heating of interstellar clouds and protoplanetary disks. *The Astrophysical Journal*, 756(2):157.

Glassgold, A. E., Najita, J., and Igea, J. (2004). Heating Protoplanetary Disk Atmospheres. *Astrophysical Journal*, 615(2):972–990.

Godunov, S. K. and Bohachevsky, I. (1959). Finite difference method for numerical computation of discontinuous solutions of the equations of fluid dynamics. *Matematičeskij sbornik*, 47(3):271–306.

Goldstein, M., Roberts, D., and Matthaeus, W. (1995). Turbulence in the solar wind1. *Annu. Rev. Amen. Astmphys*, 33:283–325.

Gomez de Castro, A. I. and Pudritz, R. E. (1993). The origin of forbidden line emission from young stellar objects. *The Astrophysical Journal*, 409:748–761.

Gómez de Castro, A. I. and Verdugo, E. (2001). New Constraints on Protostellar Jet Collimation from High-Density Gas UV Tracers. *ApJ*, 548:976–989.

Gómez de Castro, A. I. and Verdugo, E. (2007). Evidence of Stellar-driven Outflows from the Classical T Tauri Star RY Tau. *ApJ*, 654:L91–L94.

Goodson, A. P., Winglee, R. M., and Böhm, K.-H. (1997). Time-dependent accretion by magnetic young stellar objects as a launching mechanism for stellar jets. *The Astrophysical Journal*, 489(1):199.

Gorti, U., Dullemond, C., and Hollenbach, D. (2009). Time evolution of viscous circumstellar disks due to photoevaporation by far-ultraviolet, extreme-ultraviolet, and x-ray radiation from the central star. *The Astrophysical Journal*, 705(2):1237.

Gorti, U. and Hollenbach, D. (2009). Photoevaporation of Circumstellar Disks By Far-Ultraviolet, Extreme-Ultraviolet and X-Ray Radiation from the Central Star. *Astrophysical Journal*, 690(2):1539–1552.

Greene, T. P., Wilking, B. A., Andre, P., Young, E. T., and Lada, C. J. (1994). Further mid-infrared study of the rho ophiuchi cloud young stellar population: Luminosities and masses of pre-main-sequence stars. *Astrophysical Journal, Part 1 (ISSN 0004-637X), vol. 434, no. 2, p. 614-626*, 434:614–626.

Grinin, V. (1992). Young stars with non-periodic algol-type minima. *Astron. Astrophys. Trans.*, 3(1):17–32.

Großschedl, J. E., Alves, J., Teixeira, P. S., Bouy, H., Forbrich, J., Lada, C. J., Meingast, S., Hacar, Á., Ascenso, J., Ackerl, C., et al. (2019). Vision–vienna survey in orion-iii. young stellar objects in orion a. *Astronomy & Astrophysics*, 622:A149.

Güdel, M. (2015). Ionization and heating by x-rays and cosmic rays. In *EPJ Web of Conferences*, volume 102, page 00015. EDP Sciences.

Güdel, M., Lahuis, F., Briggs, K. R., Carr, J., Glassgold, A. E., Henning, T., Najita, J. R., van Boekel, R., and van Dishoeck, E. F. (2010). On the origin of [neii] 12.81 μm emission from pre-main sequence stars: Disks, jets, and accretion. *Astronomy & Astrophysics*, 519:A113.

Güdel, M. and Telleschi, A. (2007). The X-ray soft excess in classical T Tauri stars. *Astronomy and Astrophysics*, 474(2):L25–L28.

Gueth, F. and Guilloteau, S. (1999). The jet-driven molecular outflow of hh 211. *Astronomy and Astrophysics, v. 343, p. 571-584 (1999)*, 343:571–584.

Guilet, J. and Ogilvie, G. I. (2013). Transport of magnetic flux and the vertical structure of accretion discs–ii. vertical profile of the diffusion coefficients. *Monthly Notices of the Royal Astronomical Society*, 430(2):822–835.

Harsono, D., Bjerkeli, P., Ramsey, J., Pontoppidan, K., Kristensen, L., Jørgensen, J., Calcutt, H., Li, Z.-Y., and Plunkett, A. (2023). Jwst peers into the class i protostar tmc1a: Atomic jet and spatially resolved dissociative shock region. *The Astrophysical Journal Letters*, 951(2):L32.

Harten, A., Lax, P. D., and Leer, B. v. (1983). On upstream differencing and godunov-type schemes for hyperbolic conservation laws. *SIAM review*, 25(1):35–61.

Hartigan, P., Edwards, S., and Ghandour, L. (1995). Disk accretion and mass loss from young stars. *The Astrophysical Journal*, 452:736.

Hartigan, P., Frank, A., Foster, J., Wilde, B., Douglas, M., Rosen, P., Coker, R., Blue, B., and Hansen, J. (2011). Fluid dynamics of stellar jets in real time: Third epoch hubble space telescope images of hh 1, hh 34, and hh 47. *The Astrophysical Journal*, 736(1):29.

Hartigan, P., Morse, J. A., and Raymond, J. (1994). Mass-loss rates, ionization fractions, shock velocities, and magnetic fields of stellar jets. *Astrophysical Journal, Part 1 (ISSN 0004-367X), vol. 436, no. 1, p. 125-143*, 436:125–143.

Hartigan, P., Raymond, J., and Hartmann, L. (1987). Radiative bow shock models of herbig-haro objects. *Astrophysical Journal, Part 1 (ISSN 0004-637X), vol. 316, May 1, 1987, p. 323-348.*, 316:323–348.

Hartigan, P., Raymond, J., and Pierson, R. (2004). Infrared emission lines of [fe ii] as diagnostics of shocked gas in stellar jets. *The Astrophysical Journal*, 614(1):L69.

Hartmann, L., Calvet, N., Gullbring, E., and D'Alessio, P. (1998). Accretion and the evolution of t tauri disks. *The Astrophysical Journal*, 495(1):385.

Hartmann, L., Herczeg, G., and Calvet, N. (2016). Accretion onto pre-main-sequence stars. *Annual Review of Astronomy and Astrophysics*, 54:135–180.

Hartmann, L. and MacGregor, K. (1982). Wave-driven winds from cool stars. i-some effects of magnetic field geometry. *ApJ*, 257:264–268.

Hawley, J. F., Fendt, C., Hardcastle, M., Nokhrina, E., and Tchekhovskoy, A. (2016). Disks and jets: gravity, rotation and magnetic fields. *The strongest magnetic fields in the universe*, pages 449–477.

Hawley, J. F., Gammie, C. F., and Balbus, S. A. (1995). Local three-dimensional magnetohydrodynamic simulations of accretion disks. *Astrophysical Journal v. 440, p. 742*, 440:742.

Hennebelle, P. and Chabrier, G. (2008). Analytical Theory for the Initial Mass Function: CO Clumps and Prestellar Cores. *Astrophysical Journal*, 684(1):395–410.

Hennebelle, P., Commerçon, B., Joos, M., Klessen, R. S., Krumholz, M., Tan, J. C., and Teyssier, R. (2011). Collapse, outflows and fragmentation of massive, turbulent and magnetized prestellar barotropic cores. *Astronomy & Astrophysics*, 528:A72.

Herbig, G. H. (1962). The properties and problems of t tauri stars and related objects. In *Advances in Astronomy and Astrophysics*, volume 1, pages 47–103. Elsevier.

Herbst, W., Eislöffel, J., Mundt, R., Scholz, A., Reipurth, B., Jewitt, D., and Keil, K. (2007). Protostars and planets v: The rotation of young low-mass stars and brown dwarfs.

Herbst, W., Herbst, D. K., Grossman, E. J., and Weinstein, D. (1994). Catalogue of ubvri photometry of t tauri stars and analysis of the causes of their variability. *The Astronomical Journal (ISSN 0004-6256), vol. 108, no. 5, p. 1906-1923*, 108:1906–1923.

Herczeg, G. J. and Hillenbrand, L. A. (2015). Empirical isochrones for low mass stars in nearby young associations. *The Astrophysical Journal*, 808(1):23.

Hersant, F., Dubrulle, B., and Huré, J.-M. (2005). Turbulence in circumstellar disks. *Astronomy & Astrophysics*, 429(2):531–542.

Hervet, O., Meliani, Z., Zech, A., Boisson, C., Cayatte, V., Sauty, C., and Sol, H. (2017). Shocks in relativistic transverse stratified jets-a new paradigm for radio-loud agn. *Astronomy & Astrophysics*, 606:A103.

Heyvaerts, J. and Norman, C. (1989). The collimation of magnetized winds. *ApJ*, 347:1055–1081.

Heyvaerts, J. and Norman, C. (2003). Global asymptotic solutions for nonrelativistic magnetohydrodynamic jets and winds. *ApJ*, 596(2):1270.

Heyvaerts, J. and Priest, E. R. (1983). Coronal heating by phase-mixed shear alfven waves. *Astronomy and Astrophysics, vol. 117, no. 2, Jan. 1983, p. 220-234.*, 117:220–234.

Hind, J. R. (1852). List of variable stars discovered. *Monthly Notices of the RAS*, 13:33.

Hirai, K., Katoh, Y., Terada, N., and Kawai, S. (2018). Study of the transition from mri to magnetic turbulence via parasitic instability by a high-order mhd simulation code. *The Astrophysical Journal*, 853(2):174.

Hirano, N., Ho, P. P., Liu, S.-Y., Shang, H., Lee, C.-F., and Bourke, T. L. (2010). Extreme active molecular jets in l1448c. *The Astrophysical Journal*, 717(1):58.

Hollenbach, D., Johnstone, D., Lizano, S., and Shu, F. (1994). Photoevaporation of disks around massive stars and application to ultracompact h ii regions. *The Astrophysical Journal, vol. 428, no. 2, pt. 1, p. 654-669*, 428:654–669.

Hollweg, J. V. and Isenberg, P. (2007). Reflection of alfvén waves in the corona and solar wind: An impulse function approach. *Journal of Geophysical Research: Space Physics*, 112(A8).

Hugoniot, H. (1887). Mémoire sur la propagation du mouvement dans un fluide indéfini (première partie). *Journal de Mathématiques Pures et Appliquées*, 3:477–492.

Igea, J. and Glassgold, A. (1999). X-ray ionization of the disks of young stellar objects. *The Astrophysical Journal*, 518(2):848.

Imanishi, K., Koyama, K., and Tsuboi, Y. (2001). Chandra observation of the ρ ophiuchi cloud. *The Astrophysical Journal*, 557(2):747.

Imanishi, K., Nakajima, H., Tsujimoto, M., Koyama, K., and Tsuboi, Y. (2003). A systematic study of x-ray flares from low-mass young stellar objects in the ophiuchi star-forming region with chandra. *PASJ*, 55(3):653–681.

Ireland, L. G., Matt, S. P., Davey, C. R., Harris, O. L., Slade-Harajda, T. W., Finley, A. J., and Zanni, C. (2022a). Effect of differential rotation on the magnetic braking of low-mass and solar-like stars: A proof-of-concept study. *ApJ*, 925(1):100.

Ireland, L. G., Matt, S. P., and Zanni, C. (2022b). Magnetic braking of accreting t tauri stars ii: Torque formulation spanning spin-up and spin-down regimes. *The Astrophysical Journal*, 929(1):65.

Ireland, L. G., Zanni, C., Matt, S. P., and Pantolmos, G. (2021). Magnetic Braking of Accreting T Tauri Stars: Effects of Mass Accretion Rate, Rotation, and Dipolar Field Strength. *ApJ*, 906(1):4.

Jacquemin-Ide, J., Ferreira, J., and Lesur, G. (2019). Magnetically driven jets and winds from weakly magnetized accretion discs. *Monthly Notices of the RAS*, 490(3):3112–3133.

Jacquemin-Ide, J., Lesur, G., and Ferreira, J. (2021). Magnetic outflows from turbulent accretion disks. I. Vertical structure and secular evolution. *Astronomy and Astrophysics*, 647:A192.

Jannaud, T., Zanni, C., and Ferreira, J. (2023). Numerical simulations of mhd jets from keplerian accretion disks. i. recollimation shocks. *A&A*, 669:A159.

Jeffreys, H. (1924). *The Earth: its origin, history and physical constitution.* University Press.

Johns-Krull, C. M. (2007). The magnetic fields of classical t tauri stars. *The Astrophysical Journal*, 664(2):975.

Johnstone, C., Jardine, M., Gregory, S., Donati, J.-F., and Hussain, G. (2014). Classical t tauri stars: magnetic fields, coronae and star–disc interactions. *Monthly Notices of the Royal Astronomical Society*, 437(4):3202–3220.

Joy, A. H. (1945). T tauri variable stars. *ApJ*, 102:168.

Kahn, S. M., Ballmoos, P., and Sunyaev, R. A. (2005). *High-Energy Spectroscopic Astrophysics: Saas Fee Advanced Course 30. Lecture Notes 2000. Swiss Society for Astrophysics and Astronomy*, volume 30. Springer.

Kama, M., Bruderer, S., Van Dishoeck, E., Hogerheijde, M., Folsom, C., Miotello, A., Fedele, D., Belloche, A., Güsten, R., and Wyrowski, F. (2016). Volatile-carbon locking and release in protoplanetary disks-a study of tw hya and hd 100546. *Astronomy & Astrophysics*, 592:A83.

Kamp, I., Thi, W.-F., Woitke, P., Rab, C., Bouma, S., and Menard, F. (2017). Consistent dust and gas models for protoplanetary disks-ii. chemical networks and rates. *A&A*, 607:A41.

Kamp, I., Tilling, I., Woitke, P., Thi, W.-F., and Hogerheijde, M. (2010). Radiation thermo-chemical models of protoplanetary disks-ii. line diagnostics. *A&A*, 510:A18.

Kang, S.-J., Kerton, C., Choi, M., and Kang, M. (2017). A comparative observational study of yso classification in four small star-forming h ii regions. *The Astrophysical Journal*, 845(1):21.

Kant, I. (2012). *Universal natural history and theory of the heavens or essay on the constitution and the mechanical origin of the whole universe according to Newtonian principles (1755).* Cambridge University Press.

Kastner, J. H., Huenemoerder, D. P., Schulz, N. S., Canizares, C. R., and Weintraub, D. A. (2002). Evidence for accretion: High-resolution x-ray spectroscopy of the classical t tauri star tw hydrae. *The Astrophysical Journal*, 567(1):434.

Kennel, C. F., Blandford, R. D., and Coppi, P. (1989). Mhd intermediate shock discontinuities. part 1. rankine—hugoniot conditions. *Journal of Plasma Physics*, 42(2):299–319.

Keto, E., Caselli, P., and Rawlings, J. (2015). The dynamics of collapsing cores and star formation. *Monthly Notices of the Royal Astronomical Society*, 446(4):3731–3740.

Kimura, S. S., Takasao, S., and Tomida, K. (2023). Modeling Hadronic Gamma-Ray Emissions from Solar Flares and Prospects for Detecting Nonthermal Signatures from Protostars. *Astrophysical Journal*, 944(2):192.

Koldoba, A., Ustyugova, G., Romanova, M., Chechetkin, V., and Lovelace, R. (1995). Simulations of jet formation from a magnetized accretion disk. *Astrophysics and Space Science*, 232:241–261.

Königl, A., Pudritz, R., Mannings, V., Boss, A., and Russell, S. (2000). Protostars and planets iv. *(Tucson: Univ. Arizona Press).*

Koyama, K., Hamaguchi, K., Ueno, S., Kobayashi, N., and Feigelson, E. D. (1996). Discovery of Hard X-Rays from a Cluster of Protostars. *Publications of the ASJ*, 48:L87–L92.

Kratter, K. and Lodato, G. (2016). Gravitational instabilities in circumstellar disks. *Annual Review of Astronomy and Astrophysics*, 54:271–311.

Kunz, M. W. and Balbus, S. A. (2004). Ambipolar diffusion in the magnetorotational instability. *Monthly Notices of the Royal Astronomical Society*, 348(1):355–360.

Kurosawa, R. and Romanova, M. M. (2013). Spectral variability of classical t tauri stars accreting in an unstable regime. *Monthly Notices of the Royal Astronomical Society*, 431(3):2673–2689.

Kwan, J., Edwards, S., and Fischer, W. (2007). Modeling T Tauri Winds from He I λ10830 Profiles. *ApJ*, 657(2):897–915.

Lada, C. J. (1987). Star formation: from ob associations to protostars. In *Symposium-International astronomical union*, volume 115, pages 1–18. Cambridge University Press.

Lada, C. J. and Fich, M. (1996). The structure and energetics of a highly collimated bipolar outflow: Ngc 2264g. *Astrophysical Journal v. 459, p. 638*, 459:638.

Lada, C. J. and Lada, E. A. (2003). Embedded clusters in molecular clouds. *Annual Review of Astronomy and Astrophysics*, 41(1):57–115.

Lada, C. J. and Wilking, B. (1984). The nature of the embedded population in the rho ophiuchi dark cloud-mid-infrared observations. *ApJ*, 287:610–621.

Landau, L. and Lifschitz, E. (1989). Mécanique des fluides, collection physique théorique, vol. 6, editions mir 2eme édn.

Larson, R. B. (1969). Numerical calculations of the dynamics of a collapsing proto-star. *Monthly Notices of the Royal Astronomical Society*, 145(3):271–295.

Larson, R. B. (1981). Turbulence and star formation in molecular clouds. *Monthly Notices of the Royal Astronomical Society*, 194(4):809–826.

Lee, C.-F. (2020). Molecular jets from low-mass young protostellar objects. *The Astronomy and Astrophysics Review*, 28(1):1.

Lee, C.-F., Hasegawa, T. I., Hirano, N., Palau, A., Shang, H., Ho, P. T., and Zhang, Q. (2010). The reflection-symmetric wiggle of the young protostellar jet hh 211. *The Astrophysical Journal*, 713(2):731.

Lee, C.-F., Hirano, N., Zhang, Q., Shang, H., Ho, P. T., and Mizuno, Y. (2015). Jet motion, internal working surfaces, and nested shells in the protostellar system hh 212. *The Astrophysical Journal*, 805(2):186.

Lee, C.-F., Ho, P. T., Bourke, T. L., Hirano, N., Shang, H., and Zhang, Q. (2008). Sio shocks of the protostellar jet hh 212: a search for jet rotation. *The Astrophysical Journal*, 685(2):1026.

Lee, C.-F., Ho, P. T. P., Li, Z.-Y., Hirano, N., Zhang, Q., and Shang, H. (2017a). A rotating protostellar jet launched from the innermost disk of hh 212. *Nature Astronomy*, 1(7):0152.

Lee, J. W., Hull, C. L., and Offner, S. S. (2017b). Synthetic observations of magnetic fields in protostellar cores. *The Astrophysical Journal*, 834(2):201.

Lee, T., Shu, F. H., Shang, H., Glassgold, A. E., and Rehm, K. (1998). Protostellar cosmic rays and extinct radioactivities in meteorites. *The Astrophysical Journal*, 506(2):898.

Lehmann, A., Federrath, C., and Wardle, M. (2016). Shockfind-an algorithm to identify magnetohydrodynamic shock waves in turbulent clouds. *Monthly Notices of the Royal Astronomical Society*, 463(1):1026–1039.

Lesur, G., Ferreira, J., and Ogilvie, G. I. (2013). The magnetorotational instability as a jet launching mechanism. *Astronomy & Astrophysics*, 550:A61.

Lesur, G., Flock, M., Ercolano, B., Lin, M., Yang, C., Barranco, J. A., Benitez-Llambay, P., Goodman, J., Johansen, A., Klahr, H., Laibe, G., Lyra, W., Marcus, P. S., Nelson, R. P., Squire, J., Simon, J. B., Turner, N. J., Umurhan, O. M., and Youdin, A. N. (2023). Hydro-, Magnetohydro-, and Dust-Gas Dynamics of Protoplanetary Disks. In Inutsuka, S., Aikawa, Y., Muto, T., Tomida, K., and Tamura, M., editors, *Astronomical Society of the Pacific Conference Series*, volume 534 of *Astronomical Society of the Pacific Conference Series*, page 465.

Lesur, G., Hennebelle, P., and Fromang, S. (2015). Spiral-driven accretion in protoplanetary discs-i. 2d models. *Astronomy & Astrophysics*, 582:L9.

Lesur, G. and Longaretti, P.-Y. (2009). Turbulent resistivity evaluation in magnetorotational instability generated turbulence. *Astronomy & Astrophysics*, 504(2):309–320.

Lesur, G. R. (2021). Magnetohydrodynamics of protoplanetary discs. *Journal of Plasma Physics*, 87(1):205870101.

Leung, P. K. and Ogilvie, G. I. (2019). Local semi-analytic models of magnetic flux transport in protoplanetary discs. *Monthly Notices of the Royal Astronomical Society*, 487(4):5155–5174.

Li, H., Goodman, A., Sridharan, T., Houde, M., Li, Z.-Y., Novak, G., and Tang, K. S. (2014). The link between magnetic fields and cloud/star formation. *Protostars and planets VI*, pages 101–123.

Lii, P. S., Romanova, M. M., Ustyugova, G. V., Koldoba, A. V., and Lovelace, R. V. (2014). Propeller-driven outflows from an mri disc. *Monthly Notices of the Royal Astronomical Society*, 441(1):86–100.

Liu, C.-F. and Shang, H. (2012). Rw aur a from the x-wind point of view: General features. *The Astrophysical Journal*, 761(2):94.

Lodato, G. (2008). Classical disc physics. *New Astronomyr*, 52(2-5):21–41.

López-Martín, L., Cabrit, S., and Dougados, C. (2003). Proper motions and velocity asymmetries in the rw aur jet. *A&A*, 405(1):L1–L4.

Louvet, F., Dougados, C., Cabrit, S., Mardones, D., Ménard, F., Tabone, B., Pinte, C., and Dent, W. (2018). The hh30 edge-on t tauri star-a rotating and precessing monopolar outflow scrutinized by alma. *Astronomy & Astrophysics*, 618:A120.

Lovelace, R., Romanova, M., and Bisnovatyi-Kogan, G. (1999). Magnetic propeller outflows. *The Astrophysical Journal*, 514(1):368.

Lynden-Bell, D. and Pringle, J. E. (1974). The evolution of viscous discs and the origin of the nebular variables. *Monthly Notices of the Royal Astronomical Society*, 168(3):603–637.

Mamatsashvili, G., Chagelishvili, G., Pessah, M. E., Stefani, F., and Bodo, G. (2020). Zero net flux mri turbulence in disks: sustenance scheme and magnetic prandtl number dependence. *The Astrophysical Journal*, 904(1):47.

Manara, C., Rosotti, G., Testi, L., Natta, A., Alcalá, J., Williams, J., Ansdell, M., Miotello, A., Van Der Marel, N., Tazzari, M., et al. (2016). Evidence for a correlation between mass accretion rates onto young stars and the mass of their protoplanetary disks. *A&A*, 591:L3.

Massaglia, S., Bodo, G., Mignone, A., and Rossi, P. (2008). Jets from young stars iii. *Jets From Young Stars III*, 754.

Matsakos, T., Massaglia, S., Trussoni, E., Tsinganos, K., Vlahakis, N., Sauty, C., and Mignone, A. (2009). Two-component jet simulations. II. Combining analytical disk and stellar MHD outflow solutions. *A&A*, 502(1):217–229.

Matsakos, T., Tsinganos, K., Vlahakis, N., Massaglia, S., Mignone, A., and Trussoni, E. (2008). Two-component jet simulations. I. Topological stability of analytical MHD outflow solutions. *A&A*, 477(2):521–533.

Matsakos, T., Vlahakis, N., Tsinganos, K., Karampelas, K., Sauty, C., Cayatte, V., Matt, S. P., Massaglia, S., Trussoni, E., and Mignone, A. (2012). Velocity asymmetries in young stellar object jets. Intrinsic and extrinsic mechanisms. *A&A*, 545:A53.

Matt, S. and Pudritz, R. E. (2005). Accretion-powered stellar winds as a solution to the stellar angular momentum problem. *ApJ*, 632(2):L135.

Matt, S. and Pudritz, R. E. (2008). Accretion-powered Stellar Winds. III. Spin-Equilibrium Solutions. *ApJ*, 681:391–399.

Matt, S. P., MacGregor, K. B., Pinsonneault, M. H., and Greene, T. P. (2012). Magnetic braking formulation for sun-like stars: dependence on dipole field strength and rotation rate. *ApJ*, 754(2):L26.

Mattia, G. and Fendt, C. (2020a). Magnetohydrodynamic accretion–ejection: Jets launched by a nonisotropic accretion-disk dynamo. i. validation and application of selected dynamo tensorial components. *The Astrophysical Journal*, 900(1):59.

Mattia, G. and Fendt, C. (2020b). Magnetohydrodynamic accretion–ejection: Jets launched by a nonisotropic accretion-disk dynamo. ii. a dynamo tensor defined by the disk coriolis number. *The Astrophysical Journal*, 900(1):60.

Mattia, G. and Fendt, C. (2022). Jets from accretion disk dynamos: consistent quenching modes for dynamo and resistivity. *The Astrophysical Journal*, 935(1):22.

Maurri, L., Bacciotti, F., Podio, L., Eislöffel, J., Ray, T., Mundt, R., Locatelli, U., and Coffey, D. (2014). Physical properties of the jet from dg tauri on sub-arcsecond scales with hst/stis. *Astronomy & Astrophysics*, 565:A110.

McElroy, D., Walsh, C., Markwick, A., Cordiner, M., Smith, K., and Millar, T. (2013). The umist database for astrochemistry 2012. *Astronomy & Astrophysics*, 550:A36.

Meheut, H., Fromang, S., Lesur, G., Joos, M., and Longaretti, P.-Y. (2015). Angular momentum transport and large eddy simulations in magnetorotational turbulence: the small pm limit. *Astronomy & Astrophysics*, 579:A117.

Meskini, C., Sauty, C., Marcowith, A., Vlahakis, N., and Brunn, V. (2024). The role of heating in the formation and the dynamics of yso jets-i. a parametric study. *Astronomy & Astrophysics*, 686:A287.

Mignone, A. (2014). High-order conservative reconstruction schemes for finite volume methods in cylindrical and spherical coordinates. *J. Comput. Phys.*, 270:784–814.

Mignone, A., Bodo, G., Massaglia, S., Matsakos, T., Tesileanu, O. e., Zanni, C., and Ferrari, A. (2007). Pluto: a numerical code for computational astrophysics. *ApJS*, 170(1):228.

Miller, K. A. and Stone, J. M. (1997). Magnetohydrodynamic simulations of stellar magnetosphere-accretion disk interaction. *The Astrophysical Journal*, 489(2):890.

Miotello, A., Kamp, I., Birnstiel, T., Cleeves, L., and Kataoka, A. (2023). Setting the stage for planet formation: Measurements and implications of the fundamental disk properties. In *Astronomical Society of the Pacific Conference Series*, volume 534, page 501.

Mirabel, I., Dhawan, V., Chaty, S., Rodríguez, L., Martí, J., Robinson, C., Swank, J., and Geballk, T. (1998). Accretion instabilities and jet formation in grs 1915+ 105. *A&A*, 330(1):L9–L12.

Mishra, B., Begelman, M. C., Armitage, P. J., and Simon, J. B. (2020). Strongly magnetized accretion discs: structure and accretion from global magnetohydrodynamic simulations. *Monthly Notices of the Royal Astronomical Society*, 492(2):1855–1868.

Mitchner, M. and Kruger Jr, C. H. (1973). *Partially ionized gases*. John Wiley and Sons, Inc., New York.

Miyoshi, T. and Kusano, K. (2005). A multi-state hll approximate riemann solver for ideal magnetohydrodynamics. *Journal of Computational Physics*, 208(1):315–344.

Mohanty, S., Jankovic, M. R., Tan, J. C., and Owen, J. E. (2018). Inside-out planet formation. v. structure of the inner disk as implied by the mri. *The Astrophysical Journal*, 861(2):144.

Montmerle, T., Grosso, N., Tsuboi, Y., and Koyama, K. (2000). Rotation and x-ray emission from protostars. *The Astrophysical Journal*, 532(2):1097.

Mouschovias, T. C. (1976). Nonhomologous contraction and equilibria of self-gravitating, magnetic interstellar clouds embedded in an intercloud medium: Star formation. ii-results. *ApJ*, 207:141–158.

Murphy, G. C., Ferreira, J., and Zanni, C. (2010). Large scale magnetic fields in viscous resistive accretion disks-i. ejection from weakly magnetized disks. *Astronomy & Astrophysics*, 512:A82.

Murphy, G. C. and Pessah, M. E. (2015). On the anisotropic nature of mri-driven turbulence in astrophysical disks. *The Astrophysical Journal*, 802(2):139.

Nagai, T., Inutsuka, S.-i., and Miyama, S. M. (1998). An origin of filamentary structure in molecular clouds. *The Astrophysical Journal*, 506(1):306.

Nelson, R. P., Gressel, O., and Umurhan, O. M. (2013). Linear and non-linear evolution of the vertical shear instability in accretion discs. *Monthly Notices of the Royal Astronomical Society*, 435(3):2610–2632.

Nisini, B., Antoniucci, S., Alcalá, J., Giannini, T., Manara, C., Natta, A., Fedele, D., and Biazzo, K. (2018). Connection between jets, winds and accretion in t tauri stars-the x-shooter view. *Astronomy & Astrophysics*, 609:A87.

Nisini, B., Gangi, M., Giannini, T., Antoniucci, S., Biazzo, K., Frasca, A., Alcalá, J. M., Manara, C. F., and Weber, M. L. (2024). Giarps high-resolution observations of t tauri stars (ghost)-v. new insights into disk winds from 3 km s- 1 resolution spectroscopy. *Astronomy & Astrophysics*, 683:A116.

Öberg, K. I., Qi, C., Wilner, D. J., and Andrews, S. M. (2011). The ionization fraction in the dm tau protoplanetary disk. *The Astrophysical Journal*, 743(2):152.

Offner, S. S. R., Gaches, B. A. L., and Holdship, J. R. (2019). Impact of Cosmic-Ray Feedback on Accretion and Chemistry in Circumstellar Disks. *Astrophysical Journal*, 883(2):121.

Opher, M., Drake, J., Swisdak, M., Schoeffler, K., Richardson, J., Decker, R., and Toth, G. (2011). Is the magnetic field in the heliosheath laminar or a turbulent sea of bubbles? *The Astrophysical Journal*, 734(1):71.

Ouyed, R. and Pudritz, R. E. (1997a). Numerical simulations of astrophysical jets from keplerian disks. i. stationary models. *ApJ*, 482(2):712.

Ouyed, R. and Pudritz, R. E. (1997b). Numerical simulations of astrophysical jets from keplerian disks. ii. episodic outflows. *ApJ*, 484(2):794.

Padoan, P., Kritsuk, A., Norman, M. L., and Nordlund, Å. (2005). A solution to the pre-main-sequence accretion problem. *The Astrophysical Journal*, 622(1):L61.

Padovani, M., Galli, D., and Glassgold, A. E. (2009). Cosmic-ray ionization of molecular clouds. *Astronomy and Astrophysics*, 501(2):619–631.

Padovani, M., Ivlev, A. V., Galli, D., and Caselli, P. (2018). Cosmic-ray ionisation in circumstellar discs. *Astronomy and Astrophysics*, 614:A111.

Padovani, M., Ivlev, A. V., Galli, D., Offner, S. S. R., Indriolo, N., Rodgers-Lee, D., Marcowith, A., Girichidis, P., Bykov, A. M., and Kruijssen, J. M. D. (2020). Impact of Low-Energy Cosmic Rays on Star Formation. *Space Science Reviews*, 216(2):29.

Padovani, M., Marcowith, A., Hennebelle, P., and Ferrière, K. (2016). Protostars: Forges of cosmic rays? *Astronomy and Astrophysics*, 590:A8.

Palla, F. and Stahler, S. W. (1999). Star formation in the orion nebula cluster. *The Astrophysical Journal*, 525(2):772.

Pantellini, F., Solanki, S., and Stenflo, J. (1988). Velocity and temperature in solar magnetic fluxtubes from a statistical centre-to-limb analysis. *A&A*, 189:263–276.

Pantolmos, G. and Matt, S. P. (2017). Magnetic braking of sun-like and low-mass stars: dependence on coronal temperature. *The Astrophysical Journal*, 849(2):83.

Pantolmos, G., Zanni, C., and Bouvier, J. (2020). Magnetic torques on t tauri stars: Accreting versus non-accreting systems. *Astronomy & Astrophysics*, 643:A129.

Parkin, E. (2014). Global simulations of magnetorotational turbulence–iii. influence of field configuration and mass injection. *Monthly Notices of the Royal Astronomical Society*, 441(3):2078–2093.

Pelletier, G. and Pudritz, R. E. (1992). Hydromagnetic disk winds in young stellar objects and active galactic nuclei. *ApJ*, 394:117–138.

Perez-Becker, D. and Chiang, E. (2011). Surface Layer Accretion in Conventional and Transitional Disks Driven by Far-ultraviolet Ionization. *Astrophysical Journal*, 735(1):8.

Petrov, P., Romanova, M., Grankin, K., Artemenko, S., Babina, E., and Gorda, S. Y. (2021). Modulated accretion in the t tauri star ry tau–a stable mhd propeller or a planet at 0.2 au? *Monthly Notices of the Royal Astronomical Society*, 504(1):871–877.

Petrov, P. P., Grankin, K. N., Gameiro, J. F., Artemenko, S. A., Babina, E. V., Albuquerque, R. M. G. d., Djupvik, A. A., Gahm, G. F., Shenavrin, V. I., Irsmambetova, T. R., Fernandez, M., Mkrtichian, D. E., and Gorda, S. Y. (2019). Dynamics of wind and the dusty environments in the accreting T Tauri stars RY Tauri and SU Aurigae. *MNRAS*, 483(1):132–146.

Petrov, P. P., Zajtseva, G. V., Efimov, Y. S., Duemmler, R., Ilyin, I. V., Tuominen, I., and Shcherbakov, V. A. (1999). Brightening of the T Tauri star RY Tauri in 1996. Photometry, polarimetry and high-resolution spectroscopy. *A&A*, 341:553–559.

Podio, L., Bacciotti, F., Nisini, B., Eislöffel, J., Massi, F., Giannini, T., and Ray, T. P. (2006). Recipes for stellar jets: results of combined optical/infrared diagnostics. *Astronomy & Astrophysics*, 456(1):189–204.

Polko, P., Meier, D. L., and Markoff, S. (2010). Determining the optimal locations for shock acceleration in magnetohydrodynamical jets. *ApJ*, 723(2):1343.

Popham, R. and Narayan, R. (1992). Supersonic infall and causality in accretion disk boundary layers. *Astrophysical Journal, Part 1 (ISSN 0004-637X), vol. 394, no. 1, July 20, 1992, p. 255-260.*, 394:255–260.

Porth, O. and Fendt, C. (2010). Acceleration and collimation of relativistic magnetohydrodynamic disk winds. *ApJ*, 709(2):1100.

Powell, K. G. (1997). An approximate riemann solver for magnetohydrodynamics: (that works in more than one dimension). In *Upwind and high-resolution schemes*, pages 570–583. Springer.

Pringle, J. E. (1981). Accretion discs in astrophysics. *In: Annual review of astronomy and astrophysics. Volume 19.(A82-11551 02-90) Palo Alto, CA, Annual Reviews, Inc., 1981, p. 137-162.*, 19:137–162.

Pudritz, R., Ouyed, R., Fendt, C., and Brandenburg, A. (2007). Disk winds, jets, and outflows: Theoretical and computational foundations. *Protostars and Planets V*, page 277.

Pudritz, R. E., Rogers, C. S., and Ouyed, R. (2006). Controlling the collimation and rotation of hydromagnetic disc winds. *MNRAS*, 365(4):1131–1148.

Purser, S., Ainsworth, R., Ray, T., Green, D., Taylor, A., and Scaife, A. (2018). Constraining the nature of dg tau a's thermal and non-thermal radio emission. *MNRAS*, 481(4):5532–5542.

Pyo, T.-S., Kobayashi, N., Hayashi, M., Terada, H., Goto, M., Takami, H., Takato, N., Gaessler, W., Usuda, T., Yamashita, T., et al. (2003). Adaptive optics spectroscopy of the [fe ii] outflow from dg tauri. *ApJ*, 590(1):340.

Rab, C., Güdel, M., Padovani, M., Kamp, I., Thi, W.-F., Woitke, P., and Aresu, G. (2017). Stellar energetic particle ionization in protoplanetary disks around t tauri stars. *A&A*, 603:A96.

Rab, C., Güdel, M., Woitke, P., Kamp, I., Thi, W.-F., Min, M., Aresu, G., and Meijerink, R. (2018). X-ray radiative transfer in protoplanetary disks-the role of dust and x-ray background fields. *A&A*, 609:A91.

Raga, A. and Bohm, K. (1986). Predicted long-slit, high-resolution emission-line profiles from interstellar bow shocks. ii-arbitrary bow shock orientation. *Astrophysical Journal, Part 1 (ISSN 0004-637X), vol. 308, Sept. 15, 1986, p. 829-835.*, 308:829–835.

Rankine, W. J. M. (1870). Xv. on the thermodynamic theory of waves of finite longitudinal disturbance. *Philosophical Transactions of the Royal Society of London*, pages 277–288.

Ray, T., Dougados, C., Bacciotti, F., Eislöffel, J., and Chrysostomou, A. (2007). Protostars and planets v.

Ray, T. and Ferreira, J. (2021). Jets from young stars. *New A Rev.*, 93:101615.

Reames, D. V. (2015). What Are the Sources of Solar Energetic Particles? Element Abundances and Source Plasma Temperatures. *Space Science Reviews*, 194(1-4):303–327.

Rebull, L., Wolff, S., and Strom, S. (2004). Stellar rotation in young clusters: the first 4 million years. *AJ*, 127(2):1029.

Reedy, R. (2012). Update on solar-proton fluxes during the last five solar activity cycles. In *43rd Annual Lunar and Planetary Science Conference*, page 1285.

Reipurth, B. (2000). Disintegrating multiple systems in early stellar evolution. *The Astronomical Journal*, 120(6):3177.

Reipurth, B. and Bally, J. (2001). Herbig-haro flows: Probes of early stellar evolution. *Annual Review of Astronomy and Astrophysics*, 39(1):403–455.

Rekowski, M. v., Rüdiger, G., and Elstner, D. (2000). Structure and magnetic configurations of accretion disk-dynamo models. *A&A*, 353:813–822.

Roberts, D. A., Goldstein, M. L., Matthaeus, W. H., and Ghosh, S. (1992). Velocity shear generation of solar wind turbulence. *Journal of Geophysical Research: Space Physics*, 97(A11):17115–17130.

Robitaille, T. P., Whitney, B. A., Indebetouw, R., Wood, K., and Denzmore, P. (2006). Interpreting spectral energy distributions from young stellar objects. i. a grid of 200,000 yso model seds. *The Astrophysical Journal Supplement Series*, 167(2):256.

Rodenkirch, P. J. and Dullemond, C. P. (2022). Dust entrainment in magnetically and thermally driven disk winds. *Astronomy & Astrophysics*, 659:A42.

Rodenkirch, P. J., Klahr, H., Fendt, C., and Dullemond, C. P. (2020). Global axisymmetric simulations of photoevaporation and magnetically driven protoplanetary disk winds. *Astronomy & Astrophysics*, 633:A21.

Rodgers-Lee, D., Taylor, A. M., Ray, T. P., and Downes, T. P. (2017). The ionizing effect of low-energy cosmic rays from a class II object on its protoplanetary disc. *Monthly Notices of the RAS*, 472(1):26–38.

Roe, P. L. (1986). Characteristic-based schemes for the euler equations. *Annual review of fluid mechanics*, 18(1):337–365.

Romanova, M., Ustyugova, G., Koldoba, A., and Lovelace, R. (2012). Mri-driven accretion on to magnetized stars: global 3d mhd simulations of magnetospheric and boundary layer regimes. *MNRAS*, 421(1):63–77.

Romanova, M., Ustyugova, G., Koldoba, A., and Lovelace, R. V. (2002). Magnetohydrodynamic simulations of disk-magnetized star interactions in the quiescent regime: funnel flows and angular momentum transport. *The Astrophysical Journal*, 578(1):420.

Romanova, M. M., Long, M., Lamb, F. K., Kulkarni, A. K., and Donati, J. F. (2011). Global 3D simulations of disc accretion on to the classical T Tauri star V2129 Oph. *MNRAS*, 411(2):915–928.

Romanova, M. M., Lovelace, R. V. E., Bachetti, M., Blinova, A. A., Koldoba, A. V., Kurosawa, R., Lii, P. S., and Ustyugova, G. V. (2014). MHD Simulations of Magnetospheric Accretion, Ejection and Plasma-field Interaction. In *European Physical Journal Web of Conferences*, volume 64 of *European Physical Journal Web of Conferences*, page 05001.

Romanova, M. M., Ustyugova, G. V., Koldoba, A. V., and Lovelace, R. V. E. (2009). Launching of conical winds and axial jets from the disc-magnetosphere boundary: axisymmetric and 3D simulations. *MNRAS*, 399:1802–1828.

Rybicki, G. B. and Lightman, A. P. (1991). *Radiative processes in astrophysics*. John Wiley & Sons.

Saigo, K., Tomisaka, K., and Matsumoto, T. (2008). Evolution of first cores and formation of stellar cores in rotating molecular cloud cores. *The Astrophysical Journal*, 674(2):997.

Salvesen, G., Simon, J. B., Armitage, P. J., and Begelman, M. C. (2016). Accretion disc dynamo activity in local simulations spanning weak-to-strong net vertical magnetic flux regimes. *Monthly Notices of the Royal Astronomical Society*, 457(1):857–874.

Sauty, C. (2019). *JET Simulations, Experiments, and Theory*. Springer.

Sauty, C., Cayatte, V., Lima, J., Matsakos, T., and Tsinganos, K. (2012). Counterrotation in magnetocentrifugally driven jets and other winds. *The Astrophysical Journal Letters*, 759(1):L1.

Sauty, C., de Albuquerque, R., Cayatte, V., Lima, J., and Gameiro, J. (2022). Nonradial and nonpolytropic astrophysical outflows-xi. simulations of the circumstellar environment of ry tauri. *A&A*, 664:A176.

Sauty, C., Meliani, Z., Lima, J. J. G., Tsinganos, K., Cayatte, V., and Globus, N. (2011). Nonradial and nonpolytropic astrophysical outflows. IX. Modeling T Tauri jets with a low mass-accretion rate. *A&A*, 533:A46.

Sauty, C., Trussoni, E., and Tsinganos, K. (2002). Nonradial and nonpolytropic astrophysical outflows-v. acceleration and collimation of self-similar winds. *Astronomy & Astrophysics*, 389(3):1068–1085.

Sauty, C., Trussoni, E., and Tsinganos, K. (2004). Nonradial and nonpolytropic astrophysical outflows-vi. overpressured winds and jets. *Astronomy & Astrophysics*, 421(3):797–809.

Sauty, C. and Tsinganos, K. (1994). Nonradial and nonpolytropic astrophysical outflows III. A criterion for the transition from jets to winds. *A&A*, 287:893–926.

Schekochihin, A., Cowley, S. C., Dorland, W., Hammett, G., Howes, G. G., Quataert, E., and Tatsuno, T. (2009). Astrophysical gyrokinetics: kinetic and fluid turbulent cascades in magnetized weakly collisional plasmas. *The Astrophysical Journal Supplement Series*, 182(1):310.

Schlickeiser, R. (2013). *Cosmic ray astrophysics*. Springer Science & Business Media.

See, V., Lehmann, L., Matt, S. P., and Finley, A. J. (2020). How much do underestimated field strengths from zeeman-doppler imaging affect spin-down torque estimates? *The Astrophysical Journal*, 894(1):69.

See, V., Matt, S. P., Folsom, C. P., Saikia, S. B., Donati, J.-F., Fares, R., Finley, A. J., Hébrard, É. M., Jardine, M. M., Jeffers, S. V., et al. (2019). Estimating magnetic filling factors from zeeman–doppler magnetograms. *The Astrophysical Journal*, 876(2):118.

Semenov, D., Wiebe, D., and Henning, T. (2004). Reduction of chemical networks. II. Analysis of the fractional ionisation in protoplanetary discs. *Astronomy and Astrophysics*, 417:93–106.

Shakura, N. I. and Sunyaev, R. A. (1973). Black holes in binary systems. Observational appearance. *Astronomy and Astrophysics*, 24:337–355.

Shakura, N. I. and Sunyaev, R. A. (1976). A theory of the instability of disk accretion on to black holes and the variability of binary X-ray sources, galactic nuclei and quasars. *Monthly Notices of the RAS*, 175:613–632.

Sheikhnezami, S., Fendt, C., Porth, O., Vaidya, B., and Ghanbari, J. (2012). Bipolar jets launched from magnetically diffusive accretion disks. i. ejection efficiency versus field strength and diffusivity. *The Astrophysical Journal*, 757(1):65.

Shoda, M., Suzuki, T. K., Matt, S. P., Cranmer, S. R., Vidotto, A. A., Strugarek, A., See, V., Réville, V., Finley, A. J., and Brun, A. S. (2020). Alfvén-wave-driven magnetic rotator winds from low-mass stars. i. rotation dependences of magnetic braking and mass-loss rate. *The Astrophysical Journal*, 896(2):123.

Shu, C. (1991). *Generalized differential-integral quadrature and application to the simulation of incompressible viscous flows including parallel computation*. University of Glasgow (United Kingdom).

Shu, F., Najita, J., Ostriker, E., Wilkin, F., Ruden, S., and Lizano, S. (1994). Magnetocentrifugally driven flows from young stars and disks. 1: A generalized model. *The Astrophysical Journal, vol. 429, no. 2, pt. 1, p. 781-796*, 429:781–796.

Shu, F., Najita, J., Ostriker, E., Wilkin, F., Ruden, S., and Lizano, S. (1994). Magnetocentrifugally driven flows from young stars and disks. 1: A generalized model. *ApJ*, 429:781–796.

Shu, F. H. (1977). Self-similar collapse of isothermal spheres and star formation. *ApJ*, 214:488–497.

Shu, F. H., Adams, F. C., and Lizano, S. (1987). Star formation in molecular clouds-observation and theory. *IN: Annual review of astronomy and astrophysics. Volume 25 (A88-13240 03-90). Palo Alto, CA, Annual Reviews, Inc., 1987, p. 23-81. NASA-sponsored research.*, 25:23–81.

Shu, F. H., Najita, J., Ostriker, E. C., and Shang, H. (1995). Magnetocentrifugally driven flows from young stars and disks. v. asymptotic collimation into jets. *The Astrophysical Journal*, 455(2):L155.

Shu, F. H., Najita, J. R., Shang, H., and Li, Z.-Y. (2000). X-winds theory and observations. *Protostars and planets IV*, 789:31–32.

Sicilia-Aguilar, A., Henning, T., and Hartmann, L. W. (2010). Accretion in evolved and transitional disks in cep ob2: looking for the origin of the inner holes. *The Astrophysical Journal*, 710(1):597.

Simon, J. B., Bai, X.-N., Armitage, P. J., Stone, J. M., and Beckwith, K. (2013). Turbulence in the outer regions of protoplanetary disks. ii. strong accretion driven by a vertical magnetic field. *The Astrophysical Journal*, 775(1):73.

Simon, M., Guilloteau, S., Beck, T. L., Chapillon, E., Di Folco, E., Dutrey, A., Feiden, G. A., Grosso, N., Piétu, V., Prato, L., et al. (2019). Masses and implications for ages of low-mass pre-main-sequence stars in taurus and ophiuchus. *The Astrophysical Journal*, 884(1):42.

Somers, G., Cao, L., and Pinsonneault, M. H. (2020). The spots models: a grid of theoretical stellar evolution tracks and isochrones for testing the effects of starspots on structure and colors. *The Astrophysical Journal*, 891(1):29.

Spezzi, L., Vernazza, P., Merín, B., Allen, L. E., Evans, N. J., Jørgensen, J. K., Bourke, T. L., Cieza, L. A., Dunham, M. M., Harvey, P. M., et al. (2011). The spitzer survey of interstellar clouds in the gould belt. iv. lupus v and vi observed with irac and mips. *The Astrophysical Journal*, 730(2):65.

Spruit, H., Stehle, R., and Papaloizou, J. (1995). Interchange instability in and accretion disc with a poloidal magnetic field. *Monthly Notices of the Royal Astronomical Society*, 275(4):1223–1231.

St-Onge, G. and Bastien, P. (2008). A Jet Associated with the Classical T Tauri Star RY Tauri. *ApJ*, 674:1032–1036.

Stahler, S. W. and Palla, F. (2008). *The formation of stars*. John Wiley & Sons.

Stelzer, B., Flaccomio, E., Briggs, K., Micela, G., Scelsi, L., Audard, M., Pillitteri, I., and Güdel, M. (2007). A statistical analysis of x-ray variability in pre-main sequence objects of the taurus molecular cloud. *Astronomy & Astrophysics*, 468(2):463–475.

Stepanovs, D. and Fendt, C. (2014). Modeling mhd accretion–ejection—from the launching area to propagation scales. *ApJ*, 793(1):31.

Stepanovs, D. and Fendt, C. (2016). An extensive numerical survey of the correlation between outflow dynamics and accretion disk magnetization. *The Astrophysical Journal*, 825(1):14.

Stepanovs, D., Fendt, C., and Sheikhnezami, S. (2014). Modeling mhd accretion–ejection: episodic ejections of jets triggered by a mean-field disk dynamo. *ApJ*, 796(1):29.

Stone, J. M., Hawley, J. F., Gammie, C. F., and Balbus, S. A. (1996). Three-dimensional magnetohydrodynamical simulations of vertically stratified accretion disks. *Astrophysical Journal v. 463, p. 656*, 463:656.

Stute, M., Gracia, J., Vlahakis, N., Tsinganos, K., Mignone, A., and Massaglia, S. (2014). 3d simulations of disc winds extending radially self-similar mhd models. *MNRAS*, 439(4):3641–3648.

Stute, M., Tsinganos, K., Vlahakis, N., Matsakos, T., and Gracia, J. (2008). Stability and structure of analytical mhd jet formation models with a finite outer disk radius. *A&A*, 491(2):339–351.

Sun, X. and Bai, X.-N. (2023). The magnetohydrodynamic-particle-in-cell module in athena++: implementation and code tests. *Monthly Notices of the Royal Astronomical Society*, 523(3):3328–3347.

Suriano, S. S., Li, Z.-Y., Krasnopolsky, R., and Shang, H. (2017). Rings and gaps produced by variable magnetic disc winds and avalanche accretion streams - I. Axisymmetric resistive MHD simulations. *MNRAS*, 468(4):3850–3868.

Suzuki, T. K. and Inutsuka, S.-i. (2009). Disk winds driven by magnetorotational instability and dispersal of protoplanetary disks. *The Astrophysical Journal*, 691(1):L49.

Suzuki, T. K. and Inutsuka, S.-i. (2014). Magnetohydrodynamic simulations of global accretion disks with vertical magnetic fields. *The Astrophysical Journal*, 784(2):121.

Tabone, B., Cabrit, S., Bianchi, E., Ferreira, J., Des Forêts, G. P., Codella, C., Gusdorf, A., Gueth, F., Podio, L., and Chapillon, E. (2017). Alma discovery of a rotating so/so2 flow in hh212-a possible mhd disk wind? *Astronomy & Astrophysics*, 607:L6.

Takami, M., Beck, T. L., Schneider, P. C., Günther, H. M., White, M., Grankin, K., Karr, J. L., Ohyama, Y., Coffey, D., Liu, H. B., et al. (2020). Possible time correlation between jet ejection and mass accretion for rw aur a. *ApJ*, 901(1):24.

Takami, M., Günther, H. M., Schneider, P. C., Beck, T. L., Karr, J. L., Ohyama, Y., Galván-Madrid, R., Uyama, T., White, M., Grankin, K., et al. (2022). Time-variable jet ejections from rw aur a, ry tau, and dg tau. *ApJS*, 264(1):1.

Takasao, S., Tomida, K., Iwasaki, K., and Suzuki, T. K. (2018). A three-dimensional simulation of a magnetized accretion disk: fast funnel accretion onto a weakly magnetized star. *The Astrophysical Journal*, 857(1):4.

Takasao, S., Tomida, K., Iwasaki, K., and Suzuki, T. K. (2022). Three-dimensional simulations of magnetospheric accretion in a t tauri star: Accretion and wind structures just around the star. *The Astrophysical Journal*, 941(1):73.

Teague, R., Semenov, D., Guilloteau, S., Henning, T., Dutrey, A., Wakelam, V., Chapillon, E., and Pietu, V. (2015). Chemistry in disks-ix. observations and modelling of hco+ and dco+ in dm tauri. *Astronomy & Astrophysics*, 574:A137.

Telleschi, A., Güdel, M., Briggs, K. R., Audard, M., and Palla, F. (2007). X-ray emission from t tauri stars and the role of accretion: inferences from the xmm-newton extended survey of the taurus molecular cloud. *Astronomy & Astrophysics*, 468(2):425–442.

Teşileanu, O., Mignone, A., Massaglia, S., and Bacciotti, F. (2012). Numerical simulations of radiative magnetized herbig–haro jets: The influence of pre-ionization from x-rays on emission lines. *The Astrophysical Journal*, 746(1):96.

Teyssier, R. and Commerçon, B. (2019). Numerical methods for simulating star formation. *Frontiers in Astronomy and Space Sciences*, 6:51.

Thi, W., Lesur, G., Woitke, P., Kamp, I., Rab, C., and Carmona, A. (2019). Radiation thermo-chemical models of protoplanetary disks-grain and polycyclic aromatic hydrocarbon charging. *Astronomy & Astrophysics*, 632:A44.

Thi, W. F., Mathews, G., Ménard, F., Woitke, P., Meeus, G., Riviere-Marichalar, P., Pinte, C., Howard, C. D., Roberge, A., Sandell, G., Pascucci, I., Riaz, B., Grady, C. A., Dent, W. R. F., Kamp, I., Duchêne, G., Augereau, J. C., Pantin, E., Vandenbussche, B., Tilling, I., Williams, J. P., Eiroa, C., Barrado, D., Alacid, J. M., Andrews, S., Ardila, D. R., Aresu, G., Brittain, S., Ciardi, D. R., Danchi, W., Fedele, D., de Gregorio-Monsalvo, I., Heras, A., Huelamo, N., Krivov, A., Lebreton, J., Liseau, R., Martin-Zaidi, C., Mendigutía, I., Montesinos, B., Mora, A., Morales-Calderon, M., Nomura, H., Phillips, N., Podio, L., Poelman, D. R., Ramsay, S., Rice, K., Solano, E., Walker, H., White, G. J., and Wright, G. (2010). Herschel-PACS observation of the 10 Myr old T Tauri disk TW Hya. Constraining the disk gas mass. *Astronomy and Astrophysics*, 518:L125.

Timmes, F. X., Woosley, S. E., Hartmann, D. H., Hoffman, R. D., Weaver, T. A., and Matteucci, F. (1995). 26Al and 60Fe from Supernova Explosions. *Astrophysical Journal*, 449:204.

Tsinganos, K., Sauty, C., Surlantzis, G., Trussoni, E., and Contopoulos, J. (1996). Critical points and separatrix characteristics in solar and astrophysical mhd flows. In *Solar and Astrophysical Magnetohydrodynamic Flows*, pages 427–458. Springer.

Tzeferacos, P., Ferrari, A., Mignone, A., Zanni, C., Bodo, G., and Massaglia, S. (2009). On the magnetization of jet-launching discs. *MNRAS*, 400(2):820–834.

Tzeferacos, P., Ferrari, A., Mignone, A., Zanni, C., Bodo, G., and Massaglia, S. (2013). Effects of entropy generation in jet-launching discs. *MNRAS*, 428(4):3151–3163.

Umebayashi, T. and Nakano, T. (1981). Fluxes of energetic particles and the ionization rate in very dense interstellar clouds. *Publications of the Astronomical Society of Japan, Vol. 33, P. 617, 1981*, 33:617.

Umebayashi, T. and Nakano, T. (2009). Effects of Radionuclides on the Ionization State of Protoplanetary Disks and Dense Cloud Cores. *Astrophysical Journal*, 690(1):69–81.

Ustyugova, G., Koldoba, A., Romanova, M., Chechetkin, V., and Lovelace, R. (1995). Magnetohydrodynamic simulations of outflows from accretion disks. *Astrophysical Journal, Part 2-Letters (ISSN 0004-637X), vol. 439, no. 2, p. L39-L42*, 439:L39–L42.

Ustyugova, G., Koldoba, A., Romanova, M., Chechetkin, V., and Lovelace, R. (1999). Magnetocentrifugally driven winds: comparison of mhd simulations with theory. *The Astrophysical Journal*, 516(1):221.

Ustyugova, G., Koldoba, A., Romanova, M. M., and Lovelace, R. (2006). "propeller" regime of disk accretion to rapidly rotating stars. *The Astrophysical Journal*, 646(1):304.

van Dishoeck, E. F. (2014). Astrochemistry of dust, ice and gas: introduction and overview. *Faraday Discussions*, 168:9.

Van Kempen, T., van Dishoeck, E., Salter, D., Hogerheijde, M., Jørgensen, J., and Boogert, A. (2009). The nature of the class i population in ophiuchus as revealed through gas and dust mapping. *Astronomy & Astrophysics*, 498(1):167–194.

Van Leer, B. (1977). Towards the ultimate conservative difference scheme iii. upstream-centered finite-difference schemes for ideal compressible flow. *Journal of Computational Physics*, 23(3):263–275.

Van Leer, B. (1979). Towards the ultimate conservative difference scheme. v. a second-order sequel to godunov's method. *Journal of computational Physics*, 32(1):101–136.

Vasconcelos, M., Jatenco-Pereira, V., and Opher, R. (2000). Alfvénic heating of protostellar accretion disks. *The Astrophysical Journal*, 534(2):967.

Vidotto, A., Opher, M., Jatenco-Pereira, V., and Gombosi, T. (2009). Simulations of winds of weak-lined t tauri stars: the magnetic field geometry and the influence of the wind on giant planet migration. *The Astrophysical Journal*, 703(2):1734.

Viñas, A. F. and Goldstein, M. L. (1991). Parametric instabilities of circularly polarized large-amplitude dispersive alfvén waves: excitation of obliquely-propagating daughter and side-band waves. *Journal of plasma physics*, 46(1):129–152.

Vlahakis, N., Tsinganos, K., Sauty, C., and Trussoni, E. (2000). A disc-wind model with correct crossing of all magnetohydrodynamic critical surfaces. *MNRAS*, 318(2):417–428.

Wang, L., Bai, X.-N., and Goodman, J. (2019). Global simulations of protoplanetary disk outflows with coupled non-ideal magnetohydrodynamics and consistent thermochemistry. *ApJ*, 874(1):90.

Wang, L. and Goodman, J. (2017a). Hydrodynamic photoevaporation of protoplanetary disks with consistent thermochemistry. *The Astrophysical Journal*, 847(1):11.

Wang, L. and Goodman, J. J. (2017b). Wind-driven accretion in transitional protostellar disks. *The Astrophysical Journal*, 835(1):59.

Wardle, M. (1999). The balbus-hawley instability in weakly ionized discs. *Monthly Notices of the Royal Astronomical Society*, 307(4):849–856.

Wardle, M. and Königl, A. (1993). The structure of protostellar accretion disks and the origin of bipolar flows. *Astrophysical Journal, Part 1 (ISSN 0004-637X), vol. 410, no. 1, p. 218-238.*, 410:218–238.

Wardle, M. and Ng, C. (1999). The conductivity of dense molecular gas. *Monthly Notices of the Royal Astronomical Society*, 303(2):239–246.

Wasserburg, G. J., Busso, M., Gallino, R., and Nollett, K. M. (2006). Short-lived nuclei in the early Solar System: Possible AGB sources. *Nuclear Physics A*, 777:5–69.

Watanabe, Y., Nishimura, Y., Harada, N., Sakai, N., Shimonishi, T., Aikawa, Y., Kawamura, A., and Yamamoto, S. (2017). Molecular-cloud-scale chemical composition. i. a mapping spectral line survey toward w51 in the 3 mm band. *The Astrophysical Journal*, 845(2):116.

Waterfall, C. O. G., Browning, P. K., Fuller, G. A., and Gordovskyy, M. (2019). Modelling the radio and X-ray emission from T-Tauri flares. *Monthly Notices of the RAS*, 483(1):917–930.

Waugh, R. F., Jardine, M. M., Morin, J., and Donati, J.-F. (2021). Slingshot prominences: a hidden mass loss mechanism. *Monthly Notices of the Royal Astronomical Society*, 505(4):5104–5116.

Weizsäcker, C. F. (1948). Die rotation kosmischer gasmassen. *Zeitschrift für Naturforschung A*, 3(8-11):524–539.

White, R., Greene, T., Doppmann, G., Covey, K., and Hillenbrand, L. (2007). Stellar properties of embedded protostars. *Protostars and Planets V*, page 117.

White, R. J. and Hillenbrand, L. A. (2004). On the evolutionary status of class i stars and herbig-haro energy sources in taurus-auriga. *The Astrophysical Journal*, 616(2):998.

Williams, J. P. and Best, W. M. (2014). A parametric modeling approach to measuring the gas masses of circumstellar disks. *The Astrophysical Journal*, 788(1):59.

Wilms, J., Allen, A., and McCray, R. (2000). On the absorption of x-rays in the interstellar medium. *The Astrophysical Journal*, 542(2):914.

Woitas, J., Ray, T. P., Bacciotti, F., Davis, C. J., and Eislöffel, J. (2002). Hubble space telescope space telescope imaging spectrograph observations of the bipolar jet from rw aurigae: tracing outflow asymmetries close to the source. *The Astrophysical Journal*, 580(1):336.

Woitke, P. (2015). Heating and cooling processes in disks. In *EPJ Web of Conferences*, volume 102, page 00011. EDP Sciences.

Woitke, P., Kamp, I., and Thi, W.-F. (2009). Radiation thermo-chemical models of protoplanetary disks-i. hydrostatic disk structure and inner rim. *A&A*, 501(1):383–406.

Woitke, P., Min, M., Pinte, C., Thi, W.-F., Kamp, I., Rab, C., Anthonioz, F., Antonellini, S., Baldovin-Saavedra, C., Carmona, A., et al. (2016). Consistent dust and gas models for protoplanetary disks-i. disk shape, dust settling, opacities, and pahs. *A&A*, 586:A103.

Wood, B. E., Müller, H.-R., Redfield, S., Konow, F., Vannier, H., Linsky, J. L., Youngblood, A., Vidotto, A. A., Jardine, M., Alvarado-Gómez, J. D., et al. (2021). New observational constraints on the winds of m dwarf stars. *The Astrophysical Journal*, 915(1):37.

Wood, B. E., Müller, H.-R., Zank, G. P., Linsky, J. L., and Redfield, S. (2005). New mass-loss measurements from astrospheric lyα absorption. *The Astrophysical Journal*, 628(2):L143.

Wurster, J. and Li, Z.-Y. (2018). The role of magnetic fields in the formation of protostellar discs. *Frontiers in Astronomy and Space Sciences*, 5:39.

Xu, R., Bai, X.-N., Öberg, K., and Zhang, H. (2019). Chemical Network Reduction in Protoplanetary Disks. *Astrophysical Journal*, 872(1):107.

Young, A. K. (2023). Insights into the first and second hydrostatic core stages from numerical simulations. *Frontiers in Astronomy and Space Sciences*, 10:1288730.

Zanni, C., Ferrari, A., Rosner, R., Bodo, G., and Massaglia, S. (2007). Mhd simulations of jet acceleration from keplerian accretion disks-the effects of disk resistivity. *A&A*, 469(3):811–828.

Zanni, C. and Ferreira, J. (2009). Mhd simulations of accretion onto a dipolar magnetosphere-i. accretion curtains and the disk-locking paradigm. *A&A*, 508(3):1117–1133.

Zanni, C. and Ferreira, J. (2010). Observational limits on the spin-down torque of accretion powered stellar winds. *The Astrophysical Journal Letters*, 727(1):L22.

Zanni, C. and Ferreira, J. (2013). MHD simulations of accretion onto a dipolar magnetosphere. II. Magnetospheric ejections and stellar spin-down. *A&A*, 550:A99.

Zhu, Z. and Stone, J. M. (2018). Global evolution of an accretion disk with a net vertical field: coronal accretion, flux transport, and disk winds. *The Astrophysical Journal*, 857(1):34.

Zimniak, N., Ferreira, J., and Jacquemin-Ide, J. (2024). The accretion-ejection paradigm : Unveiling the role of turbulent magnetic pressure on magnetically driven outflows from Jet Emitting Disks. In *EAS2024*, page 2287.

Appendix A

A map of jet and wind tracers

From the map shown in Fig.A.1, we deduce the opening angle of the dark purple region. In cases where the spine varies slightly during the evolution, we do a time-average of the measured opening angles.

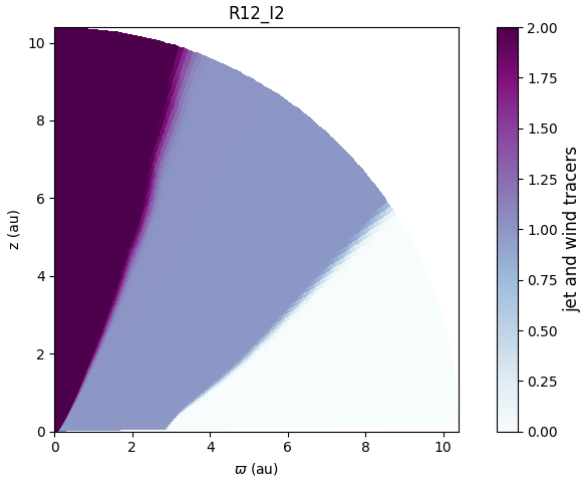

Figure A.1: 2D map of jet and wind tracers. The dark purple indicates the evolution of the spine and the light purple shows the disk wind coming from below 3au of the disk surface. We plot the final time.

Appendix B

Additional tables

To gauge how simulations evolve with different disk densities, we tried three cases as presented in Tab.B.1. More details about the results are given in Sec.4.5.2

name	l_ρ	l_B	d_m	α_m	$\dot{M}_{wind}(10^{-9} M_\odot\,\mathrm{yr}^{-1})$	$\dot{M}_{acc}(10^{-8} M_\odot\,\mathrm{yr}^{-1})$	$\lvert\dot{M}_{wind}/\dot{M}_{acc}\rvert$	$\dot{M}_{stel}/\dot{M}_{wind}$
R3A1	0.004	0.013	2	1	6.9	-1.3	0.53	0.43
R3A2	0.014	0.025	2	1	3.0	-1.3	0.23	1
R3A3	0.044	0.044	2	1	1.8	-1.3	0.14	1.7

Table B.1: Table of the mass-loss and wind to accretion ratio for different density normalization factors at $t = 0$. The mass loss of the star in all cases is $3.0 \cdot 10^{-9}\ M_\odot\,\mathrm{yr}^{-1}$. The ratio of stellar mass loss rate to accretion rate is, also, common to the three cases, $|\dot{M}_{stel}/\dot{M}_{acc}| \simeq 0.23$.

Sim ID	R_c (au)	I_h	Avg. Disk Heating (erg cm^{-3} s^{-1})	$\dot{M}_{JED}$ ($M_\odot$ yr^{-1})	$\dot{M}_{stel}/\dot{M}_{tot}$	R_{JED} (au)
R0_I1	0	10^{-1}	$6.2 \cdot 10^{-7}$	$6.8 \cdot 10^{-9}$	0.31	0.42
R0_I2	0	10^{-2}	$1.7 \cdot 10^{-7}$	not steady	only stellar - 0.15	no JED - 3 au
R05_I1	0.052	10^{-1}	$1.8 \cdot 10^{-6}$	$1.2 \cdot 10^{-9}$	0.69	0.21
R05_I2	0.052	10^{-2}	$2.9 \cdot 10^{-7}$	not steady	only stellar - 0.23	no JED - 1 au
R1_I1	0.104	10^{-1}	$5.6 \cdot 10^{-6}$	$6.5 \cdot 10^{-10}$	0.82	0.19
R1_I12	0.104	$0.5\ 10^{-1}$	$2.9 \cdot 10^{-6}$	$1.3 \cdot 10^{-9}$	0.74	0.21
R1_I2	0.104	10^{-2}	$5.4 \cdot 10^{-7}$	$7.5 \cdot 10^{-9}$	0.24	0.63
R1_I22	0.104	$0.5\ 10^{-2}$	$4.7 \cdot 10^{-7}$	$9.7 \cdot 10^{-9}$	0.21	0.63
R1_I23	0.104	$0.3\ 10^{-2}$	$3.7 \cdot 10^{-7}$	$1.1 \cdot 10^{-8}$	0.21	0.63
R12_I12	0.156	$0.5\ 10^{-1}$	$3.6 \cdot 10^{-6}$	$6.4 \cdot 10^{-10}$	4.6	0.19
R12_I2	0.156	10^{-2}	$8.7 \cdot 10^{-7}$	$1.5 \cdot 10^{-9}$	0.51	0.20
R12_I3	0.156	10^{-3}	$2.6 \cdot 10^{-7}$	$1.0 \cdot 10^{-8}$	0.29	0.60
R2_I13	0.208	$0.3\ 10^{-1}$	$2.8 \cdot 10^{-6}$	$1.1 \cdot 10^{-9}$	0.81	0.20
R2_I2	0.208	10^{-2}	$1.0 \cdot 10^{-6}$	$2.3 \cdot 10^{-9}$	0.61	0.26
R2_I22	0.208	$0.5 \cdot 10^{-2}$	$5.9 \cdot 10^{-7}$	$3.5 \cdot 10^{-9}$	0.42	0.32
R2_I3	0.208	10^{-3}	$2.2 \cdot 10^{-7}$	$4.6 \cdot 10^{-9}$	0.28	0.37
R2_I32	0.208	$0.5 \cdot 10^{-3}$	$1.7 \cdot 10^{-7}$	$6.2 \cdot 10^{-9}$	0.24	0.41
R3_I13	0.312	$0.33 \cdot 10^{-1}$	$3.6 \cdot 10^{-6}$	$7.0 \cdot 10^{-10}$	0.85	0.19
R3_I2	0.312	10^{-2}	$1.6 \cdot 10^{-6}$	$2.0 \cdot 10^{-9}$	0.66	0.25
R3_I22	0.312	$0.5 \cdot 10^{-2}$	$7.0 \cdot 10^{-7}$	$3.4 \cdot 10^{-9}$	0.54	0.28
R3_I3	0.312	10^{-3}	$2.7 \cdot 10^{-7}$	$5.5 \cdot 10^{-9}$	0.34	0.36
R3_I32	0.312	$0.5 \cdot 10^{-3}$	$2.5 \cdot 10^{-7}$	$6.5 \cdot 10^{-9}$	0.29	0.48
R3_I4	0.312	10^{-4}	$1.4 \cdot 10^{-7}$	$9.6 \cdot 10^{-9}$	0.23	0.52
R4_I3	0.416	10^{-3}	$3.2 \cdot 10^{-7}$	$5.7 \cdot 10^{-9}$	0.35	0.35
R4_I4	0.416	10^{-4}	$1.5 \cdot 10^{-7}$	$8.0 \cdot 10^{-9}$	0.26	0.42

Table B.2: List of the simulations performed with analytical radial boundary conditions. Except for R0_I2 and R05_I2, all simulations reach a steady state. The heating rate is computed by considering its mean value at the disk atmosphere up to 1 au. All the values presented here are extracted at the final time of the simulations. R_{JED} is the last radius at which the disk launches a jet.

Appendix C

ADO-ASO models

Assuming axi-symmetry, steady state, and self-similarity, the ideal magnetohydrodynamics (MHD) equations reduce to a system of coupled ordinary differential equations (ODEs) in spherical coordinates. The equations are then solved by providing the values of key functions for each analytical model.

For the analytical disk outflow (ADO) solution, physical quantities are provided by key functions $G_d(\theta)$, $M_d(\theta)$and $\Psi_d(\theta)$,

$$\frac{\rho_D}{\rho_{D_\star}} = \alpha_D^{x-3/2}\frac{1}{M^2}, \tag{C.1}$$

$$\frac{P_D}{P_{D_\star}} = \alpha_D^{x-2}\frac{1}{M_D^{2\gamma}}, \tag{C.2}$$

$$\frac{\boldsymbol{B}_{D_p}}{B_{D_\star}} = -\alpha_D^{\frac{x}{2}-1}\frac{1}{G_D^2}\frac{\sin\theta}{\cos\left(\psi+\theta\right)}\left(\sin\left(\psi+\theta\right)\hat{\boldsymbol{r}}+\cos\left(\psi+\theta\right)\hat{\boldsymbol{\theta}}\right), \tag{C.3}$$

$$\frac{\boldsymbol{V}_{D_p}}{V_{D_\star}} = -\alpha_D^{-1/4}\frac{M_D^2}{G_D^2}\frac{\sin\theta}{\cos\left(\psi+\theta\right)}\left(\sin\left(\psi+\theta\right)\hat{\boldsymbol{r}}+\cos\left(\psi+\theta\right)\hat{\boldsymbol{\theta}}\right), \tag{C.4}$$

$$\frac{B_{D_\varphi}}{B_{D_\star}} = -\lambda_D{\alpha_D}^{\frac{x}{2}-1}\frac{1-G_D^2}{G_D\left(1-M_D^2\right)}, \tag{C.5}$$

$$\frac{V_{D_\varphi}}{V_{D_\star}} = \lambda_D{\alpha_D}^{-1/4}\frac{G_D^2-M_D^2}{G_D\left(1-M_D^2\right)}, \tag{C.6}$$

$M_D^2(\theta)$ is defined as the square of the poloidal Alfvén Mach number and is given by,

$$M_D^2(\theta) = 4\pi\rho\frac{\boldsymbol{V}_{D_p}^2}{\boldsymbol{B}_{D_p}^2}, \tag{C.7}$$

The next key function is $G_D(\theta)$, the cylindrical cross section of a flux tube defined by the flux function α_D. Finally, $\Psi(\theta)$ is the angle between a particular poloidal field line

and the radial cylindrical axis. The nondimensional magnetic flux function α_D is given by,

$$\alpha_D = \frac{\varpi^2}{\varpi_\star^2 G_D^2} \tag{C.8}$$

The analytical stellar outflow (ASO) solution is, on the other hand, described with the help of the following functions, $G_s(R)$, $M_s(R)$, $F_s(R)$and $\Pi_s(R)$,

$$P_S(R,\alpha) = \frac{1}{2}\rho_* V_*^2 \Pi[1+\kappa_S \alpha] + P_{naught} \tag{C.9}$$

$$\rho_S(R,\alpha) = \frac{\rho_*}{M_S^2}(1+\delta\alpha) \tag{C.10}$$

$$\frac{\boldsymbol{B}_{Sp}}{B_{S_*}} = \frac{1}{G_S^2}(\cos\theta\ \hat{\boldsymbol{r}} - \frac{F}{2}\sin\theta\ \hat{\boldsymbol{\theta}}) \tag{C.11}$$

$$\frac{\boldsymbol{V}_{Sp}}{V_{S_*}} = \frac{M_S^2}{G_S^2}\frac{1}{\sqrt{1+\delta\alpha(R,\theta)}}(\cos\theta\ \hat{\boldsymbol{r}} - \frac{F}{2}\sin\theta\ \hat{\boldsymbol{\theta}}) \tag{C.12}$$

$$\frac{V_{S\varphi}}{V_{S_*}} = \frac{\lambda_S}{G_S^2}\frac{G_S^2 - M_S^2}{1-M_S^2}\frac{R\sin\theta}{\sqrt{1+\delta\alpha(R,\theta)}} \tag{C.13}$$

$$\frac{B_{S\varphi}}{B_{S_*}} = -\frac{\lambda_S}{G_S^2}\frac{1-G_S^2}{1-M_S^2}R\sin\theta \tag{C.14}$$

This model also uses certain key functions to provide a solution for the stellar jet component. These functions are $M_S(R)$, $G_S(R)$, $F(R)$, and $\Pi(R)$. Similarly to the ADO model $M_S(R)$ and $G_S(R)$ have the same definitions, but depend on R. $\Pi(R)$ is the dimensionless pressure. $F(R)$ is analogous to $\Psi_D(\theta)$ as it represents a logarithmic expansion factor, which measures the angle of a field line projected on the poloidal plane along the radial direction. It is written as,

$$F(R) = \frac{\partial\ \ln\alpha_S}{\partial\ \ln R} = 2\left(1 - \frac{\partial\ \ln G_S}{\partial\ \ln R}\right)\ . \tag{C.15}$$

The nondimensional magnetic flux function α_S is given by,

$$\alpha_S = \frac{\varpi^2}{r_\star^2 G_S^2} \tag{C.16}$$

The parameters used can be linked to the solutions as follows,

$$\mu = \frac{2P_D}{B_D}, \quad \lambda_s = \frac{G_a^2}{G^2(R_{ss})}, \quad \lambda_d = \frac{G_a^2}{G^2(R_{ds})}, \tag{C.17}$$

on the Alfvén surface the key function G is equal to zero. The subscripts a, ss, and ds are for Alfvén surface, stellar surface, and disk surface, respectively.